DEBRIS FLOWS AND GENERAL STEEP SLOPE SHALLOW WATER FLOWS NUMERICAL SIMULATION

By

Vicente Medina Iglesias

Research Supervisor:

Allen Bateman

SUBMITTED IN PARTIAL FULFILLMENT OF THE
REQUIREMENTS FOR THE DEGREE OF
DOCTOR OF PHILOSOPHY
AT
UNIVERSITAT POLITECNICA DE CATALUNYA
BARCELONA, SPAIN
JUNE 2010

A book is never finished, only abandoned.
Rewriting means refusing to capitulate in front
of the overwhelming imperfection.

No hay obras acabadas, sólo obras abandonadas.
Reescribir es negarse a capitular
ante la avasalladora imperfeccion.

(J. E. Pacheco citing Paul Valery)

Table of Contents

Abstract

The main target of this research is to develop a numerical model for debris flow simulations. As it is known, in general, this kind of flows occur in steeped mountain slopes. When dealing with the complete 3D physic system of equations that model the phenomenon this singular characteristic has not special effect.

To simulate large events (typical scales in real world) is not possible to use the complete equations (three dimensional, variable density, non-hydrotactic...) so a spacial dimension reduction is necessary combined with several simplifications to reduce the complexity of the system, along the present text previous works references are introduced to justify the selected simplifying hypothesis.

During the mathematical manipulation of the equations, performed in order to reduce the spacial dimension (3D $\rightarrow$ 2D), the real complexity of the problem emerges, important consequences on the coordinate system appear. This means that, to obtain a simpler version of the physical model of the phenomenon, complex mathematical operations are needed.

In the approach presented in this work the complexity of the problem is reduced in to manners:

- Applying direct physical hypothesis on the flow characteristics.
- Applying mathematical hypothesis.

An example of these physical simplifications could be the monophasic fluid hypothesis. An example of the mathematical simplifications could be the fact of the

curvature terms neglecting.

In this work the coordinate system selected for the model is named Proposed Coordinates System (PCS), this coordinates system is based on the work of Bouchut and Westdickenberg (2004) and Berger and Carey (1998*a*). The metric characteristics of the system are calculated and important conclusions are extracted from the analysis of the curvature terms. A link exist between the curvatures and the Christoffel symbols, if the curvatures are discarded also the Christoffel symbols should be discarded for model consistency. In the model governing differential equations, the use of curvilinear coordinates (PCS) provokes the existence of metric source terms defined as a Christoffel symbols functions. So, neglecting these terms the equations become simplified.

Strictly talking the model is valid for steep but slowly varying slopes, where the curvatures are very small, although in the real test cases used for validating the model, the curvatures does not fit this condition. The rough approximation to the debris flow process through simplified physics used in the model probably hides the low accuracy of the model in strongly curved areas. Many other different coordinates system choices exist in the scientific literature, in this work some of them are commented and analyzed.

Along the development of the model different problems appear and different strategies and methodologies are proposed in order to overcome them. The first important problem is related to the physics of the process, the debris flows tend to naturally develop flow pulses, the flowing mixture stops and later is remobilized. The model includes what is called "stop and go" mechanism to capture this behavior.

The second problem is related with the boundary conditions, standard debris flow hydrograph includes sharp gradients which can become flow shocks, in this work a new methodology is proposed to introduce the boundary conditions in a way that shocks are correctly solved also in the boundary of the computational domain, contrary to the standard method of characteristics (Henderson, 1966; Abbott, 1966).

The general family of the numerical methods selected to solve the resulting system is the Finite Volume Method (FVM) using the Riemann solver. This approach is extensively used in the debris flow simulation framework, so its selection is justified. In order to fit the special requirements of the PCS coordinates system the methodology developed by Rossmanith et al. (2004) and Rossmanith (2006) is used. This approach solves the problem of the non-orthogonal coordinates in the FVM framework.

To validate the code analytical, experimental and real test cases are selected. The model validation process is partial because the lack in analytical solutions, specially for complex geometries.

Acknowledgements/Agradecimientos

This research work was funded by the the Spanish Research and Technology Ministry, contract BTE2002-0375. The research was carried out in the 2003-2007 period. The main reason of this work is Professor Bateman, his interest in the debris flow phenomenon and in science in general is the engine that moves all the research machine inside UPC-GITS research group. A wish to thank also David Velasco because all along the research process he was one of the keystones.

The research process includes laboratory experiments in which a lot of people was involved, I wish to thank all of them, professors and degree students.

The field data and real cases were provided by Professor Marcel H"urlimann, his point of view guide several aspects of the developed model.

La investigación realizada en esta tesis doctoral ha estado financiada por el proyecto BTE2002-0375 del Ministerio de Ciencia y Tecnología.

En primer lugar quiero agradecer al Profesor Allen Bateman su soporte en todas las cuestiones profesionales y personales que han surgido a lo largo de este largo periodo de trabajo conjunto. Indudablemente los principales responsables de la realización de este trabajo y de todos los que se realizan dentro de UPC-GITS son él y su empuje.

Tantas horas de aeropuerto y kilómetros entre nubes me han permitido forjar una fuerte amistad con este personaje entrañable y algo quijotesco, situado entre Newton y Darwin.

En segundo lugar querría agradecer al segundo mosquetero del equipo, David Velasco el ser como es. Cualquiera puede ayudar pero nadie con el talante y la disponibilidad de David, quizás su único defecto sea no cocinar como su madre... y me olvidaba, su pijama gris.

En tercer lugar el soporte que nos dio el Profesor Marcel Hürlimann, cuando nos encontró trabajando en un tema que él conocía bien y en el que nosotros apenas entrábamos. Él nos enseño nuestro primer *debris flow*.

Muchos son los estudiantes que han pasado por UPC-GITS estos diez años, muchos de ellos han participado de una manera directa o indirecta en la redacción de esta tesis. Ellos ya saben quienes son, han paleado arena y grava y subido el canal de alta pendiente. Gracias por su ayuda y por las cervezas compartidas.

Gracias a las hadas.

Barcelona,
June 29, 2010

Vicente Medina

Introduction

Normally the numerical modeling starts from a known physical phenomenon described by equations and establish a method to obtain reasonably accurate approaches to the analytical solution. In most of the cases a simplification of the mathematical system is necessary because the complexity of the problem, an example of this process is the solution of hydraulic equations; the general problem is defined by the Navier-Stokes system, due to the computational requirement of this equations in most of the cases a simplified version is used, for example the Reynolds averaged Navier-Stokes (RANS) (Pope, 2000), the Saint Venant equations (Barre de Saint Venant, 1871) or the Bernoulli equations (Clancy, 1975).

The case of the debris flow is different, debris flows are heterogeneous mixtures of sediment air and water, covering a wide range of natural processes, depending on the characteristics and concentration of sediment and water. A great amount of uncertainness exist in the phenomenon, there is no agreement in the detailed behavior of the flow and the name "debris flow" incorporates remarkably different processes. Any classification of debris flow includes this uncertainness (Coussot and Meunier, 1996; Takahashi, 1991). As a result, there does not exist a common physical model to simulate this kind of events, every model is developed under certain hypothesis and is adapted to solve some scenarios. The main classification parameters considered for the models are:

1. Density: One of the most important challenges in debris flow modeling is the simulation of the density evolution along the flow. A debris flow is a mixture of solids and liquids, depending on the concentration, grain size distribution and

solids composition we obtain different densities. Al these parameters change along the flow evolution due to the entrainment (Benda and Cundy, 1990; Hungr and Evans, 2004*a*), water infiltration (Iverson, 1997) and wood incorporation (May, 1998). Recent approaches consider the water and sediment concentration evolution using a biphasic description of the flow (Papa et al., 2004; Fraccarollo and Capart, 2002; Cao et al., 2004; Spinewine and Zech, 2002; Brufau et al., 2000) but, in general, these models are useful to simulate the transition from water flow to debris flow in certain cases, for example dambreak problems. More general models continue using constant density approach (Iverson and Denlinger, 2001; Pitman et al., 2003; McDougall and Hungr, 2004; Rickenmann, Laigle, McArdel and Hbl, 2006; Pudasaini et al., 2005; Pudasaini and Hutter, 2007).

2. Dimension: For a constant density flow, in general, the conservation laws equations system includes at least four conservations laws, three of them express the momentum conservation (Newton second law) applied in spatial three dimensions, and the last equation expresses the mass conservation. For most of the problems it is not possible to solve the full system and some kind of simplification should be done. The first approach is to eliminate vertical or normal momentum conservation equations, then a bidimensional model emerges (Iverson and Denlinger, 2001; Pitman et al., 2003; Pudasaini and Hutter, 2003; Pudasaini et al., 2005), if two momentum equations are eliminated we obtain a one dimensional model results (Pudasaini and Hutter, 2007).

3. Pore pressure: The debris flows are characterized as an heterogeneous mixtures, involving multiphasic flows, containing fluids and solids. The complete analysis of these processes includes the momentum transfer between the different phases (Anderson and Jackson, 1967; Iverson and Denlinger, 2001). In the debris flow there appears a solid fraction pressure and a liquid pressure, called the "pore pressure". Including the pore pressure improves the accuracy in debris flow simulation (Iverson and Denlinger, 2001; Pudasaini et al., 2005).

4. Rheology: The rheology is related to the constitutive equation of the mixture. If a multiphasic model is selected every fraction has its own constitutive equation, more or less accurate. If a monophasic model is selected the problem is more complex, the mixture should be considered as a continuum medium with a homogenous rheology, discarding any interation between different phases. The challenge is to obtain this characteristic rheology.

The model developed in this document has the following characteristics:

- Constant density.
- Bidimensional.
- No pore pressure considered.
- Different rheologies are considered.
- Steep surfaces.
- Low curvature surfaces.

Several efforts have been devoted in order to define similar characteristics models (Iverson et al., 2004; Pudasaini et al., 2005; Quecedo and Pastor, 2003; Bouchut et al., 2003; Mangeney et al., 2007; Pitman et al., 2003). A couple of reasons motivate the present work as an alternative to the previous ones. The model developed in this document was planned as an engineering tool, also useful for research targets. Thus, one of the main requirements was an easy input data definition and simple configuration parameters.

Normally flexible and useful model means reduction in problem complexity and multiple approximations. A large number of fluid dynamic problems are usually solved using this kind of approximations. The ideal flow hypothesis is used for airfoils simulation or Boussinesq hypotheses is used for buoyancy-driven flows. To avoid any

loss of important physics in the debris flow description the simplifications should be selected carefully and physically reasonable.

Dealing with debris flow normally means to deal with steep and slope topographies, so the metrics in the model became one of the crucial points. How to introduce such metrics and its relation to the topography has been one of the keystones of the model presented here. In this sense the requirement was the use of simple DEM's (Digital Elevation Model) to define the topography. Several models are rigorously developed from the mathematical point of view (Pudasaini and Hutter, 2003; Pudasaini et al., 2005; Quecedo and Pastor, 2003) but this reduces the flexibility in the model used, because they are adapted to a very specific scenario.

The constitutive equations are the second challenge in the model, in Iverson et al. (2004) a complete description of the rheology is included, but a combined finite volume/finite element model is used for the stresses tensor. Such complexity goes beyond the scope of the model presented here.

The topography and metrics analysis developed in this thesis follows the works of Bouchut and Westdickenberg (2004) in the coordinate system adopted and Berger and Carey (1998*a*) in the equation system simplification. The point of view adopted in the rheologies question is classical (Rickenmann et al., 2003), considering the basal friction as the main acting force on the flow.

After the model definition (equation system set) the next step is the discretization. The FVM (Finite Volume Method) is adopted, in particular the Godunov (1959) approach, based on the Riemann solvers (Toro, 1999; Roe, 1981; Harten, 1983; Harten et al., 1983). This choice is typical in the context of hyperbolic equations and lot of literature exists on the topic (LeVeque, 2002; Toro et al., 1994; Toro, 2001), also for sediment-water mixtures (Brufau et al., 2000; Fraccarollo and Capart, 2002; Fraccarollo et al., 2003; Ferreira et al., 2003).

As was commented previously in this text, the main target of this work is to obtain a model useful for engineering calculations and research. Following these ideas some

special features should be implemented in the model, first of all a new methodology to introduce hydrographs as boundary conditions. This methodology should be able to deal with shock waves (LeVeque, 2002) as boundary conditions. The standard procedure for boundary conditions in hyperbolic equations is the MOC (Method Of Characteristics) (Abbott, 1966) and is not able to deal with discontinuous solutions.

The second feature is the inclusion of internal boundary conditions in the calculation domain. Internal boundary conditions, in the context of SWE (Shallow Water Equations), are any kind of control structures, weirs, gates, orifices, culverts, etc. To be able to introduce these kind of elements in the hyperbolic equations framework it's necessary to define a new accuracy criterium, since the Courant one is not useful for internal boundary conditions where the time doesn't appear in the equations (weir discharge equation, orifice flow equation, etc.).

Another element of central importance in debris flow is the entrainment (Egashira et al., 2001; Rickenmann et al., 2003). The initial volume of a debris flow is usually increased along the flow path. The basal erosion that triggers this phenomenon is known as entrainment. In one of the real cases presented in this document (Pal catchment) the initial volume was 500 m^3 and the final deposition was around 5000m^3. This means that the ratio between initiation and deposition volumes could be typically 10 (Hungr and Evans, 2004*a*).

To try to include this phenomenon in the model a new approach is proposed following the ideas presented in Fraccarollo and Capart (2002). A real test case is included to validate this approach. Although the entrainment is considered as one of the main problems in debris flow, it has not yet been used to classify the models in the beginning of this section. This was due to the fact that almost none of them includes this feature.

To validate the complete model several analytical and experimental test cases are used. The problem concerning these validation cases is the lack in the existence of completely bidimensional debris flow analytical solution. After the model validation three different real cases are used to test the model.

Collecting all the previously commented ideas the corresponding chapter structure is:

1 Coordinate System Definition: Description of the reference coordinates system adopted for the model, comparison to other alternatives. Description of the metric elements necessary for the model.

2 Equations System Definition: Development from the conservation laws to the selected equations system for the model.

3 Numerical Methods: Discretization of the equations using the FVM and Godunov method.

4 Boundary conditions: A new approach to introduce the boundary conditions, able to deal with discontinuous flows.

5 Accuracy Condition For Internal Boundary Conditions Alternative to Courant stability criterium for internal boundary conditions.

6 Special Features of the Debris Flow Modeling: First for the entrainment calculation a new approach is described. In the second place a method to adapt internal friction angle to the static or dynamic value is presented. The third feature is the Stop and Go mechanism used to simulate flow remobilizing.

7 Validation Test Cases: Analytical and experimental test cases.

8 Real Cases: Three different debris flow real test cases.

Chapter 1

Coordinate System Definition

In this chapter we will discuss the selection of a coordinate system that is useful for steep slope flow computation. Different proposals from several authors will be commented upon and finally, a curvilinear, local, non-orthogonal coordinates will be proposed (Pudasaini and Hutter, 2007). All the metrics related to these coordinates will be analyzed. In the proposed coordinates a link between curvatures and Christoffel symbols will be found.

Some general characteristics of the steep slope terrain surfaces will be analyzed to ensure the applicability of the proposed computations, these characteristics will be related to the smoothness of the surface.

To demonstrate the qualities of the proposed coordinate system an example will carried on. First a torus will be exposed, later steep slopes will be introduced achieving a steep slope high curvature surface. To evidence the reactions between curvature and metrics a new surface will be introduced, distinguished by a high slope and low curvature.

1.1 The Coordinate System Challenge

The debris flow phenomenon belongs to the multiphysics problems. This means that different branches of the physics converges in the definition of the problem. In the

present case, the fluid mechanics and solid mechanics are included, among others. Normally in this kind of problems it is possible to write the complete equation system but, as many other fluid problems, is not possible to numerically attack the solution. So it's necessary to reduce the complexity of the system in order to model it. One of the typical techniques used in fluids to simplify the problem is the dimension reducing.

This procedure is based on decreasing the freedom degrees number of the problem, using less independent variables, for example, it's possible to find symmetry axes, free jets problems (Pope, 2000) could be solved using axisymmetric coordinate systems, with two dimensions instead of three.

Another typical method to suppress one dimension is to integrate along it, the shallow water equations (Whitman, 1974) is a classical example. Before this integration process is carried on, it's necessary to define some hypothesis on the system, that guarantees the dependance of the removable coordinate on the remain ones. To formulate this hypothesis is necessary to accomplish some conditions, and most of them are related with the coordinate system definition.

For example, in the commented free jet case, if we want to use axisymmetric coordinates is necessary to have a longitudinal coordinate coincident with the jet axis. In the debris flow case, the main constrain in axes selection is related to the hydrostatic pressure gradient, the integration coordinate should be parallel to the pressure gradient, otherwise the equations are not easily simplified (Pudasaini et al., 2005; Wang et al., 2004; Iverson and Denlinger, 2001; Bouchut et al., 2003; Sivakumaran and Dressler, 1989; Quecedo and Pastor, 2003), although other approaches have been proposed (Denlinger and Iverson, 2004).

In the classical shallow water framework the integration coordinate is the vertical direction, this is a consequence of the mild slopes of the terrain. In the steep slope flows the hydrostatic pressure gradient is supposed to be in the terrain surface normal direction (Iverson and Denlinger, 2001; Bouchut and Westdickenberg, 2004; Hungr, 1995; Pitman et al., 2003; Bouchut et al., 2003). The classification as *steep slope flows* does not depend only in the terrain surface geometric slopes, it depends also in the

flow condition. In Figure 1.1 is possible to see a case where coexist the steep slope flow and the mild slope flow in the same topography.

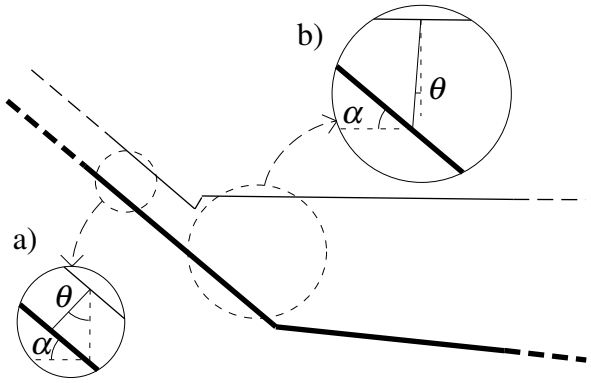

Figure 1.1: Representation of a steep slope stream flowing into lake, along the upper part of the stream a steep slope flow is found. In the lower part the reach bed is underwater.

In Figure 1.1 the stream slope angle is defined as α and the angle defined between the vertical and the hydrostatic pressure gradient is θ. In the figure, mild slope and steep slope situations are found, in a) the slope angle α and pressure gradient θ are presented and, as is shown, both are roughly equal and θ perpendicular to the free surface. This is due to the fact that the free surface flow and the terrain surface are almost parallel.

In b) different situation is shown, the free surface and bottom are not parallel, the angle θ is near vertical, and the angle α is still steep. The integration coordinate should be defined by θ not by α. As a consequence, the integration direction depends on the flow situation. Following these ideas the integration coordinate evolves along the simulation depending on the flow conditions.

It does not seem reasonable to continuously change the coordinates, as a function of the flow state, so, to simplify the problem a constant integration direction is defined.

1. In shallow water models: (situation b) in Figure 1.1) the vertical direction is selected, it's based upon the hypothesis that the free surface and the streamlines are almost horizontal, so vertical accelerations could be neglected.

2. In steep slope flows: (situation a) in Figure 1.1) the direction normal to terrain surface is selected as an integration direction.

Is not easy to establish where to use these different approaches, mainly because the choice depends on the result of the simulation. It is responsibility of the modeler to analyze the results in other to check the selected model hypothesis.

Recall that, as it was exposed, the *mild slopes* or shallow water conditions, are not only related to topography, in the typical prismatic crossection found in a stream, Figure 1.2, is possible to see in a) that the crossection bank slope α_t is high, but the longitudinal stream slope (α_l) shown in b) is small. So in the typical shallow water cases we also find steep geometric slopes.

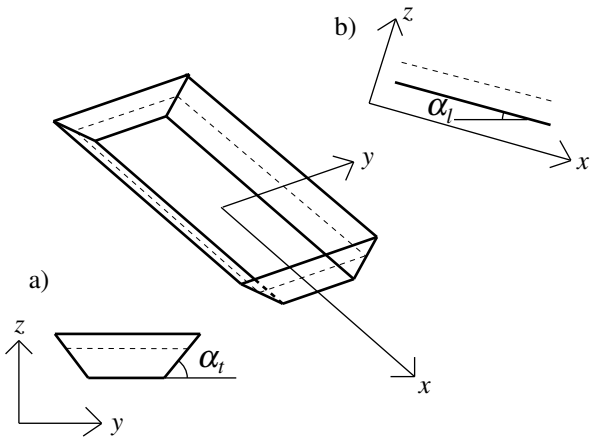

Figure 1.2: Typical small slope channel where the shallow water hypothesis are valid, but the transversal slopes α_t are high.

Following the exposed ideas, from the theoretical point of view, it is possible to define an algorithm to capture the right integration direction at every space point and time, but it will be computationally too expensive. So, as it was explained, in general, in step slope flows, the local terrain normal will be used as integration direction.

As a first conclusion of this chapter, the integration direction used will be the terrain surface normal.

1.2 Terrain Surface Smoothness

To compute local coordinates is not a trivial process, some advanced differential geometry are necessary (Misner et al., 1973; do Carmo, 1976). All the techniques developed in this chapter need to require the regularity of the topographic surface. At least all the second derivatives are required to compute the metric elements, first of all the terrain surface will be defined:

$$S(X,Y) \in C^2 \; \forall (X,Y) \in [X_{\min}, X_{\max}] \times [Y_{\min}, Y_{\max}] \tag{1.2.1}$$

where $\Omega = [X_{\min}, X_{\max}] \times [Y_{\min}, Y_{\max}]$ is the problem domain expressed in the global cartesian coordinates X, Y. In real world cases, the coordinates X, Y could be understood as the projected UTM coordinates (Universal Transverse Merkator), these coordinates are planar in front of the geographic coordinates (latitude, longitude), that are curvilinear. In most of the recent debris flow simulations (*International Forum on Landslide Disaster Management 2007 Hong Kong*), the terrain topography is introduced as a DEM (Digital Elevation Model), this means a square uniform distributed grid, so the terrain surface is not continuous, it's formed by discrete values. The model equations will include terrain surface first and second derivative, to use a coherent terrain description we need a continuous and smooth surface. So, if the terrain surface description is introduced by a DEM (e.g. in the model described here), a methodology to convert it in a continuous surface it's necessary.

It's common to use directly the DEM as a computational mesh, the governing equations will be discretizated based on it. Some components of the equations, as the gradients, should be computed at the cell centers (known values in the DEM) and many others at the cell interfaces (unknown values in the DEM). This means that interpolated values for the terrain should be used, so, again, the defined interpolation is a central question.

1.2.1 Global Interpolation Approach

To achieve this surface smooth characteristic is not trivial. In one-dimensional problems it is possible to use any interpolation technique that fits the points and belongs to C^2. For example a cubic spline interpolation to compute the slopes and curvatures, but in multi dimensional problems it is not enough to use function defined by the product of the one-dimensional interpolations along the different axes, is necessary to implement a method like the RST (Regularized Spline Tension) defined by Mitasova and Mitas (1993). In the RST method the the target of the proposed interpolation is to fit two conditions:

The first condition is to guarantee that the interpolation fits the grid values $Z_{int}(X_i, Y_i) = Z_i$ where Z_{int} is the terrain surface interpolated value and X_i, Y_i, Z_i are the coordinates of the grid points.

The second condition is related to the smoothness of the interpolation and is expressed as the minimization of E_{int}, computed as the integral of the first, second and third derivatives:

$$\begin{aligned} E_{\text{int}} = & \int_{\Omega} \left(\left(\frac{\partial Z_{\text{int}}}{\partial X} \right)^2 + \left(\frac{\partial Z_{\text{int}}}{\partial Y} \right)^2 \right) dX dY + \\ & \int_{\Omega} \left(\left(\frac{\partial^2 Z_{\text{int}}}{\partial X^2} \right)^2 + 2 \left(\frac{\partial^2 Z_{\text{int}}}{\partial X \partial Y} \right)^2 + \left(\frac{\partial^2 Z_{\text{int}}}{\partial Y^2} \right)^2 \right) dX dY + \\ & \int_{\Omega} \left(\left(\frac{\partial^3 Z_{\text{int}}}{\partial X^3} \right)^2 + 3 \left(\frac{\partial^3 Z_{\text{int}}}{\partial X^2 \partial Y} \right)^2 + 3 \left(\frac{\partial^3 Z_{\text{int}}}{\partial X \partial Y^2} \right)^2 + \left(\frac{\partial^3 Z_{\text{int}}}{\partial Y^3} \right)^2 \right) dX dY. \end{aligned} \tag{1.2.2}$$

These conditions are fulfilled with the interpolation:

$$\begin{aligned} Z_{int}(\mathbf{X}) &= a + \sum_{j=1}^{N} \lambda_j R(\mathbf{X}, \mathbf{X_j}) \\ R(\mathbf{X}, \mathbf{X_j}) &= - \left\{ \ln \left[\left(\frac{|\mathbf{X} - \mathbf{X_j}|}{2} \right)^2 \right] + E_1 \left(\frac{|\mathbf{X} - \mathbf{X_j}|}{2} \right)^2 + C_E \right\}. \end{aligned} \tag{1.2.3}$$

Where E_1 is the exponential integral function, C_E is the Euler constant (0.577...) and $\mathbf{X} = (X, Y)$. The computation of first and second derivatives is straight. As is shown in Equation 1.2.3, the RST is a global interpolation, so, to solve it, it is necessary to solve a linear equations system, being the number of unknowns λ_j equal to the total number of points in the grid N, and being the size of the matrix $N \times N$. Of course, for large grids it is almost impossible to solve the system, although being linear equations interpolation. If the topography is modified during the calculations, for example, to include basal erosion/deposition effects, the system should be solved once again.

So, although the proposed interpolation is simple and very useful for the purposes of this chapter, only in limited cases is an interesting alternative, because the interpolation computation takes more time than the hydrodynamic computation. This solution is included as a standard curvature calculator inside the extended software "GNU GRASS GIS".

1.2.2 Local Interpolation Approach

Discarding the use of this exact solution for computation of first and second derivatives of the terrain surfaces, a simpler solution is used (Travis et al., 1975), this solution is useful for topographies available as DEM. The surface interpolation is based on a local fitting function:

$$Z_{\text{int}}(X, Y) = aX^2 + bY^2 + cXY + dX + eY + f. \tag{1.2.4}$$

As is clear, there are six different fitting parameters. So, in order to compute the value of these adjustment coefficients, it is enough to use the local D8 neighborhood, also known as Moore neighborhood, Figure 1.3.

The local point where the interpolation will be carried on is Z_5, in this approach, the fitting function could not accomplish $Z_{int}(X_i, Y_i) = Z_i$ in all the local cells (D8

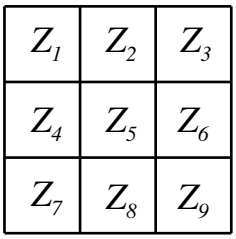

Figure 1.3: D8 Neighborhood.

domain), because we have 9 cell values and the interpolation function has 6 freedom degrees. It is possible to solve the optimization problem defined in 1.2.4 using the minimum squares approximation, and the obtained results for the D8 neighborhood are:

$$\begin{aligned}
a &= \frac{Z_1 + Z_3 + Z_4 - Z_6 - Z_7 - Z_9}{6\Delta X^2} - \frac{Z_2 + Z_5 - Z_8}{3\Delta X^2}, \\
b &= \frac{Z_1 + Z_2 + Z_3 - Z_7 - Z_8 - Z_9}{6\Delta Y^2} - \frac{Z_4 + Z_5 - Z_6}{3\Delta Y^2}, \\
c &= \frac{Z_3 + Z_7 - Z_1 - Z_9}{4\Delta X \Delta Y}, \\
d &= \frac{Z_3 + Z_6 + Z_9 - Z_1 - Z_4 - Z_7}{6\Delta X}, \\
e &= \frac{Z_1 + Z_2 + Z_3 - Z_7 - Z_8 - Z_9}{6\Delta Y}, \\
f &= \frac{2\left(Z_2 + Z_4 + Z_6 - Z_8\right) - \left(Z_1 + Z_3 + Z_7 - Z_9\right) + 5Z_5}{9},
\end{aligned} \tag{1.2.5}$$

where $\Delta X, \Delta Y$ are the cell size in X, Y directions. Now the locally interpolated surface is defined and also the associated derivatives. Although we have an unique value for the derivatives at the D8 center (Z_5), the weakness of the approach emerges if we try to compute the interpolated value at the interface between Z_5 and Z_2, we could use the interpolation function centered at Z_5, but also is possible to use the interpolation function centered at Z_2, the values obtained in both cases will be different. So it is clear that the weakness of this approach is related to the lack of uniqueness, compared to the global approach.

First and second derivatives

In the following chapters the values of the terrain surface slopes and curvatures will be used. To compute its values the *terrain height function* $h(X,Y)$ will be introduced. In this section Z_{int} was defined as a local interpolated function centered in Z_5, but for metrics calculations the continuous and smooth h function will be considered. In the model the first and second derivatives of h are calculated centered on the computational grid nodes, so the local interpolated function Z_{int} could be used:

$$\underline{Z_{\text{int}}(X,Y)}\Big|_{(X_i,Y_j)} \equiv \underline{h(X,Y)}\Big|_{(X_i,Y_j)} \tag{1.2.6}$$

Computing the first and the second derivatives is trivial, for example the obtained values for the slopes in the center ($Z_5, X \equiv 0, Y \equiv 0$) are:

$$\begin{aligned} \underline{\frac{\partial h}{\partial X}}\Big|_{Z_5} &= h_X = d = \frac{Z_3 + Z_6 + Z_9 - Z_1 - Z_4 - Z_7}{6\Delta X}, \\ \underline{\frac{\partial h}{\partial Y}}\Big|_{Z_5} &= h_Y = e = \frac{Z_1 + Z_2 + Z_3 - Z_7 - Z_8 - Z_9}{6\Delta Y}. \end{aligned} \tag{1.2.7}$$

If the weighting matrix is drawn, we obtain for the $\partial h/\partial X$ the matrix (Figure 1.4).

-ΔX	*0*	ΔX
-ΔX	*0*	ΔX
-ΔX	*0*	ΔX

Figure 1.4: D8 X first derivative weighting.

Also, the computation of $h(X,Y)$ second derivatives, used in metrics, is straight:

$$\frac{\partial^2 h}{\partial^2 X} = h_{XX} = a, \ \frac{\partial^2 h}{\partial^2 Y} = h_{YY} = b, \ \frac{\partial^2 h}{\partial X \partial Y} = h_{XY} = c. \tag{1.2.8}$$

In Table 1.1 a summary table is presented:

Derivative	Value
h_X	d
h_Y	e
h_{XX}	a
h_{YY}	b
h_{XY}	c

Table 1.1: First and second derivatives of $h(X, Y)$ using the local interpolation approach.

1.3 Definition of Local Coordinate System

In this section, different coordinate systems will be described. Previously, to introduce the model equations, a reference system was used. A suitable coordinate system simplifies the obtained equation system.

1.3.1 Coordinate Systems Used In Debris Flow Simulations

For a complete review of the coordinate system problem see Pudasaini and Hutter (2007). One of the first attempts to define coordinate system useful for this problem was proposed by Savage and Hutter (1989, 1991), in the original proposal the equations were adequate for plane flow down inclined planes (Figure 1.5, a) case), the x, y, z axes define the local coordinates.

This model was improved to compute straight channel with a slope varying bed (Greve et al., 1994) in Figure 1.5, in the b) case, the improvement is shown, and finally the model was modified to include transverse curvatures in the basal topography (Gray et al., 1999; Pudasaini and Hutter, 2007), in Figure 1.5, in c) case, a general example is shown.

As is clear in Figure 1.5, in the a), b) cases the integration coordinate (z) is normal to the terrain surface. In the c) case the integration coordinate is normal just in the channel axe. A big effort has been carried on to improve the model for dealing with curved and twisted channels (Pudasaini and Hutter, 2003; Pudasaini et al., 2005).

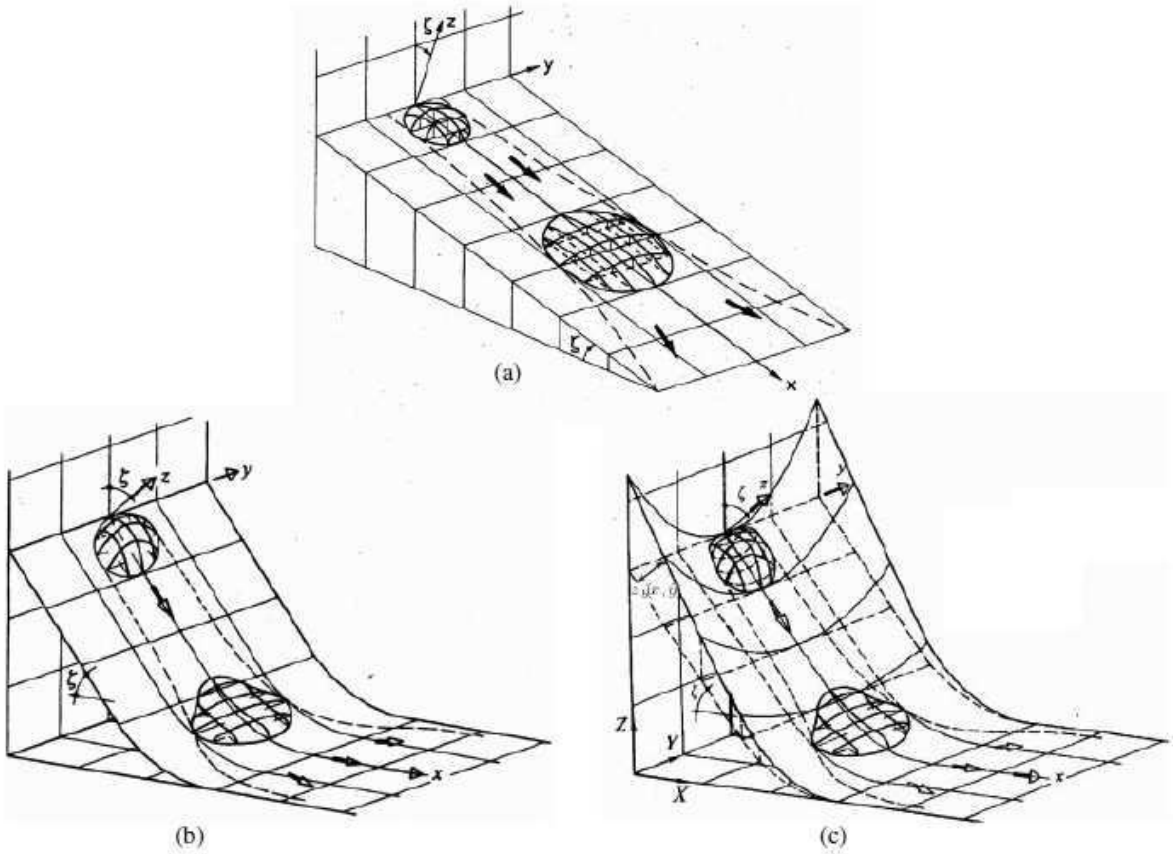

Figure 1.5: Three different approaches of the Savage and Hutter (1989) model (image extracted from Gray et al. (1999)).

In Figure 1.6 the coordinate system is shown. In this case a *Frenet Frame* is used (do Carmo, 1976), using the thalweg tangent as x direction, curvature as normal z and the binormal as the third coordinate direction y. In that model the metric curvatures of the longitudinal and lateral axes are considered. A complete review of the different approaches to Savage-Hutter approach could be found in Wang et al. (2004); Hutter et al. (2005); Pudasaini and Hutter (2007).

Another different approach is proposed by Quecedo and Pastor (2003), in that work a natural topography is considered, and the coordinate system considered is the *Principal Directions Coordinate System*. This coordinate system is defined using the direction of the lines of curvature and the surface normal. As is known the lines of

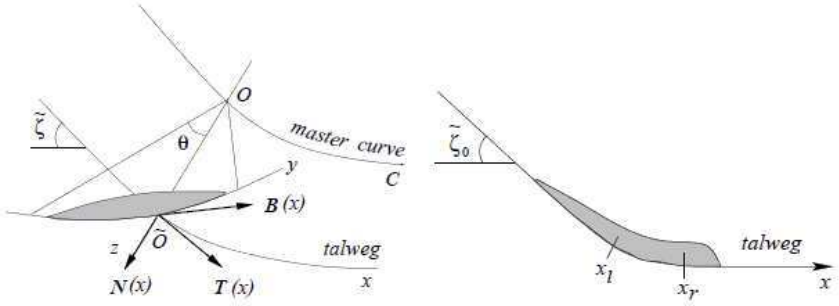

Figure 1.6: Coordinate system used by Pudasaini et al. (2005) (image extracted from the reference).

curvature are defined by the eigenvectors of the curvature matrix (do Carmo, 1976), and in a natural topography, using a DEM, is possible to approximate this directions using numerical methods (Hameiri and Shimshoni, 2003).

In contrast with the Pudasaini et al. (2005) approach, where the *Frenet Trihedron* was used, in the principal directions approach the coordinate system defined is called *Darboux Frame*, and is also a classical approach. Anyway, in the Quecedo and Pastor (2003) work, the principal directions are considered as constant along the proposed test case, not depending on the local topography. A similar approach, but considering the evolution of the principal direction could be found in Berger and Carey (1998*a*) and in Sivakumaran and Dressler (1989).

One of the main reasons to use the principal directions as coordinates is that the directions are orthogonal and also the metrics are simplified because curvature tensor becomes a diagonal matrix. On the other hand, these curvilinear coordinates are strongly dependent on the local topography details, so small modifications on the terrain surface motive large distortions in coordinate directions.

The minimum curvature direction could be rotated notoriously due to the presence on a small topography sink or hill, these coordinate directions sudden evolution provoke the formation of large valued terms in the curvilinear differential equations

systems. An example of principal directions coordinate system will be shown in Section 1.6.

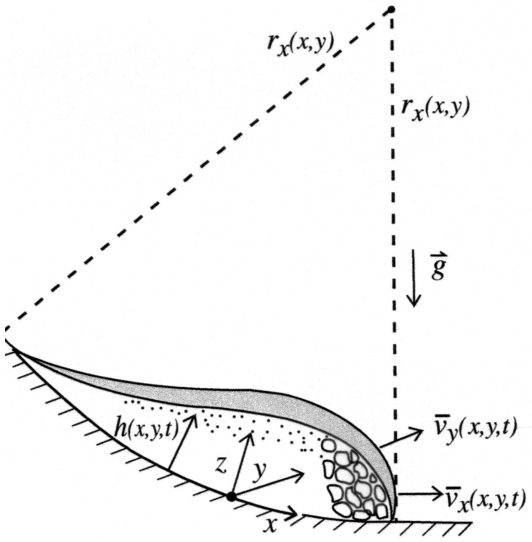

Figure 1.7: Coordinate system used by Iverson and Denlinger (2001) (image extracted from the reference).

Deserve study also, the proposal for coordinate systems in debris flow founded in Iverson and Denlinger (2001), using again a longitudinal curved coordinate and a transversal constant direction. This approach for the coordinate system definition is similar to the one proposed by Greve et al. (1994). In Figure 1.7 it is possible to see the defined coordinate system, again the local coordinates are defined as x, y, z, only a curved x is considered, and the curvature radius expressed as r_x.

The main limitation of these kind of approaches is the lack of versatility, the range of application its far from natural topographies.

In dealing with general geometries, one of the most successful recent approaches could be found in Bouchut and Westdickenberg (2004), also used in Bouchut et al. (2003); Mangeney et al. (2007), in this approach a general coordinate system is defined, with a wide range of applicability. The coordinate system proposed in this work could be considered as a case of the general coordinate proposed by Bouchut

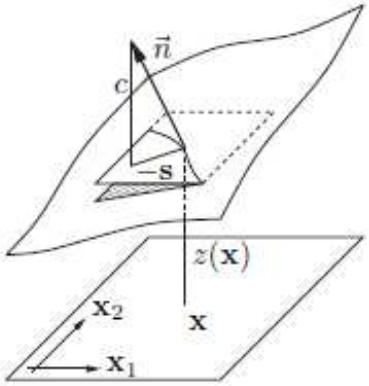

Figure 1.8: Coordinate system defined by Bouchut and Westdickenberg (2004) (image extracted from the reference).

and Westdickenberg (2004). In Figure 1.8 the coordinate system is presented, but is a general description valid for a wide range of proposals. An interesting analysis of Bouchut et al. (2003) could be found in Keller (2003).

Another completely different approach was carried out by Denlinger and Iverson (2004); Iverson et al. (2004), a general cartesian coordinates systems was proposed, avoiding the introduction of the complex metrics inherent to the curvilinear coordinates, all the conservation system will be defined in the general cartesian coordinates, with considerations related to the fact of the shallowness of the flow.

In Figure 1.9 the coordinate system is shown, the x, y, z coordinate system is not local but global, so its the *Cartesian Coordinate System*, in our notation should be presented as X, Y, Z. One of the main particularities of the coordinate system proposed in Denlinger and Iverson (2004) is related to the fact that the integration direction is the cartesian Z, so unlike the previous cases where the integration direction was always the terrain surface normal z.

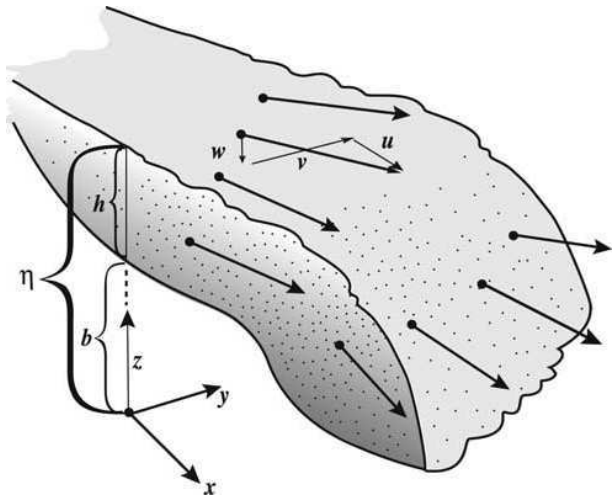

Figure 1.9: General coordinate system defined by Denlinger and Iverson (2004), (image extracted from the reference).

1.3.2 Proposed Coordinate System (PCS)

As was commented previously, in the present work a particular case of the Bouchut et al. (2003) general coordinate system is used. The coordinates are local and are defined through the projection of the cartesian coordinates X, Y in the terrain surface. This projection is carried by using the Z direction.

In this manner a local coordinates x, y are obtained, and, as will be commented later, these local coordinates are not orthogonal, but at least are easily obtained. The third local coordinate z is obtained as the normal to the local space defined by x, y.

In Figure 1.10 the PCS is shown. The terrain surface S is defined in cartesian coordinates X, Y, Z. The coordinate direction X is projected over the surface S along the direction Z, the result of this projection is the curve s_1. Moreover the coordinate Y is projected over the surface defining the curve s_2.

Both surface curves s_1, s_2, are obtained projecting the global cartesian coordinates X, Y. These curves, also, intersect in the surface point $p\,(X, Y)$. In this point ($p \in$ S) a local curvilinear coordinates x, y are defined, x is the tangent to curve s_1 and y is the tangent to curve s_2.

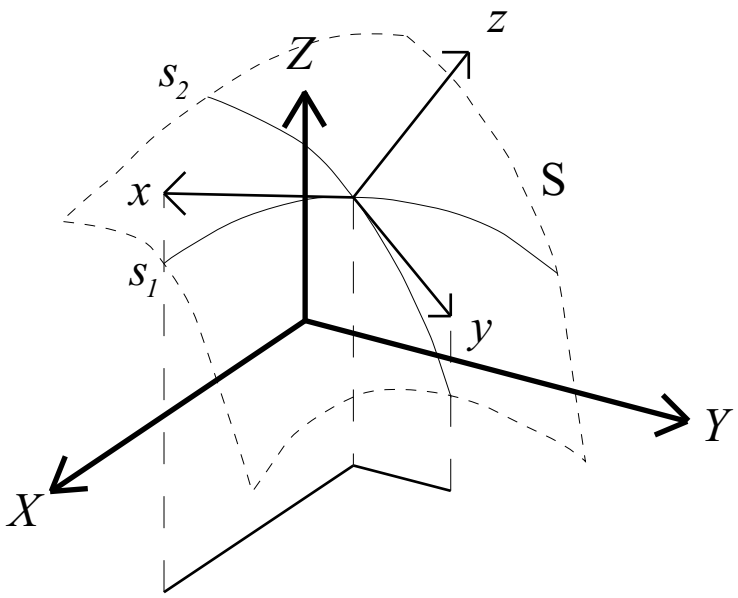

Figure 1.10: Proposed coordinate system.

So, both local tangent curves x, y and the normal direction z form the local coordinate system (PCS). As was commented previously, most of the times, in real cases the terrain topography is provided as an structured topographic grid (DEM), a kind of uniformly distributed matrix were terrain height value is found. The strength of the PCS is that follows the row/colum structure of a DEM.

In Figure 1.11 the DEM is presented over the Cartesian axes. The X, Y axis define the rows and columns of the topographic grid defined by the Z_i values. In PCS when the first and the second derivatives need to be calculated, the local interpolation approach defined in Section 1.2.2 could be used, the Table 1.1 summarizes the main values.

One of the targets of the present model is to be simple and easy to use as an engineering tool, it also includes the way how the topography is used. This chapter analyzes the features of this simple coordinate system named PCS.

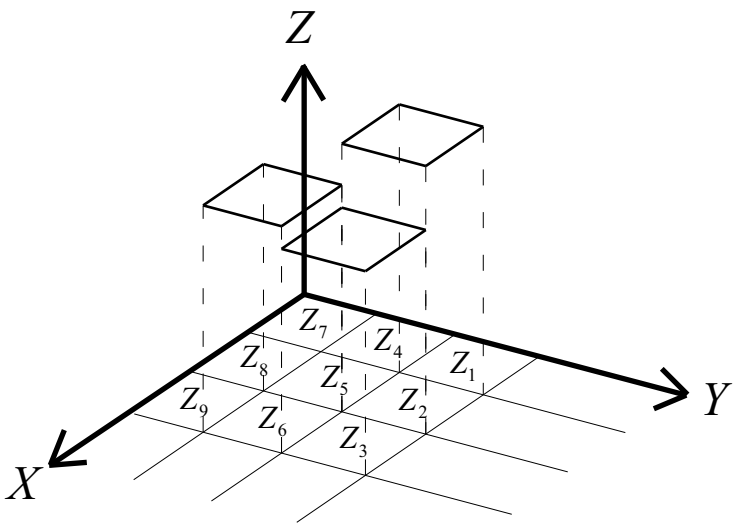

Figure 1.11: Relation between DEM's and PCS.

1.4 PCS Metrics

The differential geometry analyzes and describes all the elements necessary to define coordinate systems. In this section the classical approach will be followed (do Carmo, 1976; Misner et al., 1973), different steps will be carried out:

- Tangent space
- First fundamental form
- Second fundamental form
- Curvature tensor
- Christoffel symbols

The reason to finalize at Christoffel symbols step will be clarified in the next chapter.

1.4.1 Tangent Space

The terrain surface is considered as a regular surface existing in three dimensional space ($\mathrm{S} \in \mathbb{R}^3$). The smoothness of this surface has been analyzed in Section 1.2, also an isomorphism is considered between the geographic coordinates (longitude, latitude, UTM...) and the terrain surface height, this means that at every geographic coordinate only one elevation is found. Under these requirements a parametrization is defined following the conditions established in Section 1.4:

$$\mathbf{X} : \mathrm{U} \subset \mathbb{R}^2 \rightarrow \mathrm{S}, \;\; \mathbf{X}\left(u, v\right) = \left(X(u,v), Y(u,v), Z(u,v)\right) \qquad (u,v) \in \mathrm{U} \tag{1.4.1}$$

As has been defined previously X, Y, Z are the Cartesian coordinates, the curvilinear coordinates u, v are defined, in our proposed system, as $u = X$ and $v = Y$. Obtaining finally the parametrization:

$$\mathbf{X} = \left(X, Y, h\left(X,Y\right)\right), \quad h\left(X,Y\right) \in C^2\left(\mathrm{U}\right) \tag{1.4.2}$$

Where $h\left(X,Y\right)$ is the terrain height function. At every point $p \in \mathrm{S}$, a tangent space $\mathrm{T_p}$ is defined by the subspace generated by the vectors:

$$\mathbf{X}_u \equiv \mathbf{X}_X = \left(1, 0, \frac{\partial h}{\partial X}\right), \quad \mathbf{X}_v \equiv \mathbf{X}_Y = \left(0, 1, \frac{\partial h}{\partial Y}\right) \tag{1.4.3}$$

Henceforth the partial derivatives of h will be defined using subscripts, for example $\frac{\partial h}{\partial X} \equiv h_X$. As was defined in Section 1.2, the vectors $\mathbf{X}_X, \mathbf{X}_Y$ define the directions of the tangents to the local curvilinear coordinates x, y. The third direction z is obtained as the normal to the tangent space.

1.4.2 First Fundamental Form I_p

The first fundamental form I_p is related to the dot product of the curvilinear coordinates tangents, it defines the covariant metric tensor g_{ij}, and also the inverse o

contravariant metric tensor $g^{ij} = (g_{ij})^{-1}$, in the present case the components of this tensor in PCS are:

$$\begin{aligned} g_{11} &= E = \langle \mathbf{X}_X | \mathbf{X}_X \rangle = \left(1 + h_X^2\right) \\ g_{12} &= F = \langle \mathbf{X}_X | \mathbf{X}_Y \rangle = h_X h_Y \\ g_{21} &= F = \langle \mathbf{X}_Y | \mathbf{X}_X \rangle = h_Y h_X \\ g_{22} &= G = \langle \mathbf{X}_Y | \mathbf{X}_Y \rangle = \left(1 + h_Y^2\right). \end{aligned} \tag{1.4.4}$$

As is obvious the tensor is symmetric, also an important question should be noted, F is not zero, this means that the defined coordinate system is not orthogonal, this fact has an essential importance in the future development of the equations system. The components can be grouped in the tensor:

$$\bar{\bar{g}} = \begin{pmatrix} (1 + h_X^2) & h_X h_Y \\ h_X h_Y & (1 + h_Y^2) \end{pmatrix}. \tag{1.4.5}$$

The angle between both coordinates could be computed as:

$$\cos\alpha = \frac{\langle \mathbf{X}_X | \mathbf{X}_Y \rangle}{|\mathbf{X}_X|\,|\mathbf{X}_Y|} = \frac{F}{\sqrt{EG}} = \frac{h_X h_Y}{\left(1 + h_Y^2 + h_X^2 + h_X^2 h_Y^2\right)^{1/2}} \tag{1.4.6}$$

Where the metric norm $|\cdot|$ is defined as the square root of the dot product $\langle\cdot\rangle$. So, the system will be non orthogonal if $h_X h_Y$ is non zero; i.e. when either one or both h_X, h_Y are non zero. The area element is defined using the cross product as:

$$|X_X \times X_Y| = \sqrt{EG - F^2} = \sqrt{1 + h_X^2 + h_Y^2} \tag{1.4.7}$$

1.4.3 Second Fundamental Form II_p

The second fundamental form II_p is related to the second derivatives of the curvilinear coordinates, as a starting point we need to compute them:

$$\begin{aligned}\mathbf{X}_{XX} &= (0,0,h_{XX})\\ \mathbf{X}_{YY} &= (0,0,h_{YY})\\ \mathbf{X}_{XY} &= (0,0,h_{XY})\,.\end{aligned} \tag{1.4.8}$$

The second step is to compute the vector normal to the tangent space:

$$\left.\begin{aligned}\mathbf{N} &= \frac{X_X \times X_Y}{|X_X \times X_Y|},\\ X_X \times X_Y &= (-h_X,-h_Y,1)\end{aligned}\right\} \mathbf{N} = \frac{(-h_X,-h_Y,1)}{(1+h_X^2+h_Y^2)^{1/2}}. \tag{1.4.9}$$

The second fundamental form it is obtained by quantifying the evolution of the normal vector $\mathbf{N}$ along the tangent space:

$$\begin{aligned}e &= \langle \mathbf{N}|\mathbf{X}_{XX}\rangle = -\langle \mathbf{N}_X|\mathbf{X}_X\rangle = \frac{h_{XX}}{(1+h_X^2+h_Y^2)^{1/2}},\\ f &= \langle \mathbf{N}|\mathbf{X}_{XY}\rangle = -\langle \mathbf{N}_X|\mathbf{X}_Y\rangle = \frac{h_{XY}}{(1+h_X^2+h_Y^2)^{1/2}},\\ g &= \langle \mathbf{N}|\mathbf{X}_{YY}\rangle = -\langle \mathbf{N}_Y|\mathbf{X}_Y\rangle = \frac{h_{YY}}{(1+h_X^2+h_Y^2)^{1/2}}.\end{aligned} \tag{1.4.10}$$

1.4.4 Curvature Tensor

Now with all these values it is possible to compute the curvature tensor a_{ij}, which defines the normal vector ($\mathbf{N} \equiv z$) at certain point $p \in \mathrm{S}$ ($\mathbf{N}_\mathrm{p}$) evolution along a curve, $d\mathbf{N}_\mathrm{p} : \mathrm{T_p(S)} \to \mathrm{T_p(S)}$, being and self-adjoint operator (do Carmo, 1976), so there's an orthonormal basis where the tensor becomes diagonal.

$$d\mathbf{N}\begin{pmatrix} u' \\ v' \end{pmatrix} = \begin{pmatrix} a_{11} & a_{12} \\ a_{21} & a_{22} \end{pmatrix}\begin{pmatrix} u' \\ v' \end{pmatrix} \tag{1.4.11}$$

Where (u', v') are the curve tangent components in coordinates (u, v). A relation exist linking the tensor a_{ij} and the first and second fundamental forms (do Carmo, 1976):

$$-\begin{pmatrix} e & f \\ f & g \end{pmatrix} = \begin{pmatrix} a_{11} & a_{12} \\ a_{21} & a_{22} \end{pmatrix} \begin{pmatrix} E & F \\ F & G \end{pmatrix} \tag{1.4.12}$$

When the system 1.4.12 is solved, the results obtained in Equation 1.4.4,1.4.10 could be applied (do Carmo, 1976):

$$\begin{aligned} a_{11} &= \frac{fF - eG}{EG - F^2} = \frac{h_{XY}h_X h_Y - h_{XX}\left(1 + h_Y^2\right)}{\left(1 + h_X^2 + h_Y^2\right)^{3/2}} \\ a_{12} &= \frac{gF - fG}{EG - F^2} = \frac{h_{YY}h_X h_Y - h_{XY}\left(1 + h_Y^2\right)}{\left(1 + h_X^2 + h_Y^2\right)^{3/2}} \\ a_{12} &= \frac{eF - fE}{EG - F^2} = \frac{h_{XX}h_X h_Y - h_{XY}\left(1 + h_X^2\right)}{\left(1 + h_X^2 + h_Y^2\right)^{3/2}} \\ a_{22} &= \frac{fF - gE}{EG - F^2} = \frac{h_{XY}h_X h_Y - h_{YY}\left(1 + h_X^2\right)}{\left(1 + h_X^2 + h_Y^2\right)^{3/2}} \end{aligned} \tag{1.4.13}$$

The curvature tensor has a great importance in this work, it has been one of the most relevant terms not only in the steep slope but the general flow modeling research and discussion (Bouchut and Westdickenberg, 2004; Denlinger and Iverson, 2004; Mangeney et al., 2007; Pudasaini et al., 2005; Berger and Carey, 1998*a*). Several main geometric parameters are obtained from this tensor, (e.g. Gaussian Curvature $\mathrm{K_G}$, Mean Curvature $\mathrm{K_M}$, Principal curvatures k_1, k_2).

The eigenvalues (k_1, k_2) of the curvature tensor (a_{ij}) define the directions of the principal curvatures (eigenvectors), being both directions orthogonal, and, also, defining a reference coordinate system known as *principal directions*. This system will be used in next sections, is also important to recall the fact that the curvatures in any directions are always between (k_1, k_2), so principal curvatures are extreme values.

There are two principal values related to curvature, one of them is the principal curvatures product, known as *Gaussian curvature* ($\mathrm{K_G} = k_1 k_2$), also equal to the determinant of the curvature tensor ($\mathrm{K_G} = \det(a_{ij})$). The second important value is the *mean curvature*, defined as $\mathrm{K_M} = 1/2(k_1 + k_2)$, also obtained as curvature tensor trace. As is known, both elements, the determinant and the trace, are invariant, so

are not depending on the selected coordinate system, are surface intrinsic values. The values obtained for both curvatures in the PCS are:

$$\mathrm{K_G} = \frac{h_{XX}h_{YY} - h_{XY}^2}{\left(1 + h_X^2 + h_Y^2\right)^2} \tag{1.4.14}$$

$$\mathrm{K_M} = \frac{h_{XX}\left(1 + h_Y^2\right) - 2h_{XY}h_Xh_Y + h_{YY}\left(1 + h_X^2\right)}{\left(1 + h_X^2 + h_Y^2\right)^{3/2}} \tag{1.4.15}$$

Observing these equations it is clear that a surface with large slopes (first derivative) and small slope variation, result in a very low values for both curvatures, Gaussian and mean. And also we could relate both curvatures with the principal curvatures:

$$\begin{aligned} k_1 &= \mathrm{K_M} + \sqrt{\mathrm{K_{M^2}} - \mathrm{K_G}}, \\ k_2 &= \mathrm{K_M} - \sqrt{\mathrm{K_{M^2}} - \mathrm{K_G}}. \end{aligned} \tag{1.4.16}$$

So, a low value of Gaussian and mean curvature results in a low value of principal curvatures and viceversa ($\mathrm{K_G}$,$\mathrm{K_M} \simeq 0 \;\; \Leftrightarrow \;\; k_1, k_2 \simeq 0$). As a conclusion of this section it's clear that small second derivatives and large first derivatives imply low curvature values. This describes a surface where the slopes evolve slowly, defining a smooth plane, equivalent to a mountain slope.

1.4.5 Christoffel Symbols

The last step in this section is to compute the second kind Christoffel symbols (Γ_{ij}^k), this tensor is symmetric in the lower subindexes. There are several ways to compute the values of this tensor (do Carmo, 1976; Misner et al., 1973), for example using the metric tensor (Section 1.4.2):

$$\Gamma_{ij}^k = \frac{1}{2}g^{\alpha k}\left(\frac{\partial g_{\alpha i}}{\partial x^j} + \frac{\partial g_{\alpha j}}{\partial x^i} - \frac{\partial g_{ij}}{\partial x^\alpha}\right) \tag{1.4.17}$$

Being $g^{\alpha k}$ the inverse of the metric tensor $g_{\alpha k}$. For a better understanding of the obtained values, another approach will be used, relating the evolution of the curvilinear coordinates to the tangent space. The starting point will be the three compatibility equations:

$$\begin{aligned}\mathbf{X}_{XX} &= \Gamma^X_{XX}\mathbf{X}_X + \Gamma^Y_{XX}\mathbf{X}_Y - e\mathbf{N},\\ \mathbf{X}_{XY} &= \Gamma^X_{XY}\mathbf{X}_X + \Gamma^Y_{XY}\mathbf{X}_Y - f\mathbf{N},\\ \mathbf{X}_{YY} &= \Gamma^X_{YY}\mathbf{X}_X + \Gamma^Y_{YY}\mathbf{X}_Y - g\mathbf{N}.\end{aligned} \tag{1.4.18}$$

The next step is to compute the derivatives of the tangent space vectors:

$$\mathbf{X}_{XX} = \begin{pmatrix} 0\\ 0\\ h_{XX}\end{pmatrix},\ \mathbf{X}_{XY} = \begin{pmatrix} 0\\ 0\\ h_{XY}\end{pmatrix},\ \mathbf{X}_{YY} = \begin{pmatrix} 0\\ 0\\ h_{XY}\end{pmatrix}. \tag{1.4.19}$$

Then the the values obtained for $\mathbf{X}_X, \mathbf{X}_Y$ in the Section 1.4.1 and the values for $e, f, g, \mathbf{N}$ obtained in Section 1.4.3, are substituted, becoming the first equation:

$$\begin{pmatrix} 0\\ 0\\ h_{XX}\end{pmatrix} = \Gamma^X_{XX}\begin{pmatrix} 1\\ 0\\ h_X\end{pmatrix} + \Gamma^Y_{XX}\begin{pmatrix} 0\\ 1\\ h_Y\end{pmatrix} - h_{XX}\begin{pmatrix} -h_x\\ -h_Y\\ 1\end{pmatrix}\frac{1}{(1+h_X^2+h_Y^2)} \tag{1.4.20}$$

And operating:

$$\Gamma^X_{XX} = \frac{h_{XX}h_X}{(1+h_X^2+h_Y^2)},\ \Gamma^Y_{XX} = \frac{h_{XX}h_Y}{(1+h_X^2+h_Y^2)}. \tag{1.4.21}$$

The same operation are carried out with the second equation:

$$\begin{pmatrix} 0\\ 0\\ h_{XY}\end{pmatrix} = \Gamma^X_{XY}\begin{pmatrix} 1\\ 0\\ h_X\end{pmatrix} + \Gamma^Y_{XY}\begin{pmatrix} 0\\ 1\\ h_Y\end{pmatrix} - h_{XY}\begin{pmatrix} -h_X\\ -h_Y\\ 1\end{pmatrix}\frac{1}{(1+h_X^2+h_Y^2)}. \tag{1.4.22}$$

And also the results are obtained:

$$\Gamma^X_{XY} = \frac{h_{XY}h_X}{(1+h_X^2+h_Y^2)},\ \ \Gamma^Y_{XY} = \frac{h_{XY}h_Y}{(1+h_X^2+h_Y^2)}. \tag{1.4.23}$$

And finally with the third equation:

$$\begin{pmatrix} 0 \\ 0 \\ h_{YY} \end{pmatrix} = \Gamma^X_{YY}\begin{pmatrix} 1 \\ 0 \\ h_X \end{pmatrix} + \Gamma^Y_{YY}\begin{pmatrix} 0 \\ 1 \\ h_Y \end{pmatrix} - h_{YY}\begin{pmatrix} -h_X \\ -h_Y \\ 1 \end{pmatrix}\frac{1}{(1+h_X^2+h_Y^2)}. \tag{1.4.24}$$

With the results:

$$\Gamma^X_{YY} = \frac{h_{YY}h_X}{(1+h_X^2+h_Y^2)},\ \ \Gamma^Y_{YY} = \frac{h_{YY}h_Y}{(1+h_X^2+h_Y^2)}. \tag{1.4.25}$$

Grouping all the tensor together is possible to observe an interesting phenomenon:

$$\begin{aligned} &\Gamma^X_{XX} = \frac{h_{XX}h_X}{(1+h_X^2+h_Y^2)},\ \ \Gamma^Y_{XX} = \frac{h_{XX}h_Y}{(1+h_X^2+h_Y^2)},\ \ \Gamma^X_{XY} = \frac{h_{XY}h_X}{(1+h_X^2+h_Y^2)}, \\ &\Gamma^Y_{XY} = \frac{h_{XY}h_Y}{(1+h_X^2+h_Y^2)},\ \ \Gamma^X_{YY} = \frac{h_{YY}h_X}{(1+h_X^2+h_Y^2)},\ \ \Gamma^Y_{YY} = \frac{h_{YY}h_Y}{(1+h_X^2+h_Y^2)}. \end{aligned} \tag{1.4.26}$$

Again we can conclude that small second derivatives and large first derivatives of $h(XY)$ give very low Christoffel symbols, as was found in the curvatures section. The components could be ordered defining matrix:

$$\begin{aligned} \Gamma^X &= \begin{pmatrix} \frac{h_{XX}h_x}{(1+h_X^2+h_Y^2)} & \frac{h_{XY}h_x}{(1+h_X^2+h_Y^2)} \\ \frac{h_{XY}h_x}{(1+h_X^2+h_Y^2)} & \frac{h_{YY}h_x}{(1+h_X^2+h_Y^2)} \end{pmatrix}, \\ \Gamma^Y &= \begin{pmatrix} \frac{h_{XX}h_y}{(1+h_X^2+h_Y^2)} & \frac{h_{XY}h_y}{(1+h_X^2+h_Y^2)} \\ \frac{h_{XY}h_y}{(1+h_X^2+h_Y^2)} & \frac{h_{YY}h_y}{(1+h_X^2+h_Y^2)} \end{pmatrix}. \end{aligned} \tag{1.4.27}$$

This result will be very useful in the next chapter when the terms of the equations will be discussed.

1.5 Existing Relation Between Curvatures and Christoffel Symbols in PCS

Two results will be presented linking in the PCS (Section 1.4) the curvatures to the Christoffel symbols. The target of this proposition is to demonstrate that, under certain assumptions related to the steepness, when curvatures are discarded, also Christoffel symbols could be discarded. The second result will be presented demonstrating that small curvatures imply small Christoffel symbols, while being the slopes (first derivatives) not small.

Proposition 1.5.1. *In the PCS, if the values of the Gaussian Curvature K_G and Mean Curvature K_M vanish, being the terrain slopes not zero, then the second derivatives of the terrain surface (h_{XX}, h_{YY}, h_{XY}) are zero, and, therefore, Christoffel symbols are also zero:*

$$(K_G, K_M = 0) \Leftrightarrow (h_{XX}, h_{YY}, h_{XY} = 0) \Leftrightarrow \left(\Gamma_{ij}^{k} = 0\right) \tag{1.5.1}$$

Proof. The second implication is obvious, just looking the the Christoffel symbols values in our PCS (Equation 1.4.26) it is clear that when the first derivatives are not zero, the values of the second derivatives and Christoffel symbols are strongly linked.

The first implication is more complex. The left going sense is simple, just substituting in Equation 1.4.14 and in Equation 1.4.15:

$$(h_{XX}, h_{YY}, h_{XY} = 0) \Rightarrow (\mathrm{K}_G, \mathrm{K}_M = 0) \tag{1.5.2}$$

The right going sense should be demonstrated, first both curvature definitions have to be recalled:

$$\begin{aligned} \mathrm{K_G} &= \frac{h_{XX}h_{YY} - h_{XY}^2}{\left(1 + h_X^2 + h_Y^2\right)^2} \\ \mathrm{K_M} &= \frac{h_{XX}\left(1 + h_Y^2\right) - 2h_{XY}h_Xh_Y + h_{YY}\left(1 + h_X^2\right)}{\left(1 + h_X^2 + h_Y^2\right)^{3/2}} \end{aligned} \tag{1.5.3}$$

To obtain zero values the numerator should be zero, so:

$$\begin{cases} 0 = h_{XX}h_{YY} - h_{XY}^2 \\ 0 = h_{XX}\left(1 + h_Y^2\right) - 2h_{XY}h_Xh_Y + h_{YY}\left(1 + h_X^2\right) \end{cases} \tag{1.5.4}$$

And operating with the first term:

$$h_{XY}^2 = h_{XX}h_{YY} \rightarrow h_{XY} = \pm\sqrt{h_{XX}h_{YY}} \tag{1.5.5}$$

The product $\sqrt{h_{XX}h_{YY}}$ is real, so there are two options, both are positive or both derivatives are negative.

1. Both are positive:

   First Equation 1.5.5 is substituted in the second equation of Equation 1.5.4, obtaining:

$$0 = h_{XX}\left(1 + h_Y^2\right) \mp 2\sqrt{h_{XX}h_{YY}}h_Xh_Y + h_{YY}\left(1 + h_X^2\right) \tag{1.5.6}$$

   And operating:

$$\begin{aligned} 0 &= h_{XX} + h_{XX}h_Y^2 \mp 2\sqrt{h_{XX}h_{YY}}h_Xh_Y + h_{YY} + h_{YY}h_X^2; \\ 0 &= (h_{XX} + h_{YY}) + h_{XX}h_Y^2 \mp 2\sqrt{h_{XX}h_{YY}}h_Xh_Y + h_{YY}h_X^2; \\ 0 &= (h_{XX} + h_{YY}) + \left(h_Y\sqrt{h_{XX}} \mp h_X\sqrt{h_{YY}}\right)^2; \end{aligned} \tag{1.5.7}$$

And due to the values of second derivatives:

$$0 = \underbrace{(h_{XX} + h_{YY})}_{\geqslant 0} + \underbrace{\left(h_Y\sqrt{h_{XX}} \mp h_X\sqrt{h_{YY}}\right)^2}_{\geqslant 0} \tag{1.5.8}$$

The unique solution for this equation is $h_{XX}, h_{YY} = 0$, and using Equation 1.5.5 the result is $h_{XY} = 0$.

2. Both are negative (thanks to A. Herrero):

   The starting point of the demonstration is similar:

$$\begin{aligned} 0 &= h_{XX} + h_{XX}h_Y^2 \mp 2\sqrt{h_{XX}h_{YY}}h_X h_Y + h_{YY} + h_{YY}h_X^2; \\ 0 &= \underbrace{(h_{XX} + h_{YY})}_{\leqslant 0} + \boxed{\underbrace{h_{XX}h_Y^2 + h_{YY}h_X^2 \mp 2\sqrt{h_{XX}h_{YY}}h_X h_Y}_{\geqslant 0}}; \end{aligned} \tag{1.5.9}$$

   Let's begin moving the positive part to the left side of the equality:

$$-h_{XX}h_Y^2 - h_{YY}h_X^2 \pm 2\sqrt{h_{XX}h_{YY}}h_X h_Y = h_{XX} + h_{YY} \tag{1.5.10}$$

   Then introduce negative signs in the square root:

$$-h_{XX}h_Y^2 - h_{YY}h_X^2 \pm 2\sqrt{(-h_{XX})\,(-h_{YY})}h_X h_Y = h_{XX} + h_{YY} \tag{1.5.11}$$

   And finally rearranging:

$$\left(\sqrt{-h_{XX}}h_Y^2 \pm \sqrt{-h_{YY}}h_X^2\right)^2 = h_{XX} + h_{YY} \leqslant 0 \tag{1.5.12}$$

   As a consequence, $h_{XX}, h_{YY}, h_{XY} = 0$, using 1.5.9.

□

So as an important conclusion of this section, if the curvatures are discarded (flat area), also the Christoffel symbols should be discarded.

Here the second result will be introduced, linking the magnitude of curvatures to the magnitude of Christoffel symbols.

Proposition 1.5.2. *In the PCS, being the terrain slopes not negligible, if the values of the terrain height second derivatives $h_{ij}\,\forall i,j \in \{X,Y\}$ are much smaller than the first derivatives $h_i \forall i \in \{X,Y\}$ then values of the Gaussian Curvature K_G and Mean Curvature K_M are close to zero, and Christoffel symbols are also close to zero:*

$$(K_G, K_M \simeq 0) \Leftrightarrow h_{ij} \ll h_k \;\; \forall i,j,k \in \{X,Y\} \Leftrightarrow \Gamma_{ij}^k \simeq 0 \;\; \forall i,j,k \in \{X,Y\} \quad (1.5.13)$$

Proof. The proof is similar to the previous one, the first step is to modify the Christoffel symbols in order to express the dependence into the terrain surface derivatives:

$$\begin{aligned}
\Gamma_{22}^1 &= \frac{h_{YY}}{\left(1+h_X^2+h_Y^2\right)^{1/2}} \frac{h_X}{\left(1+h_X^2+h_Y^2\right)^{1/2}}, \;\; \Gamma_{22}^2 = \frac{h_{YY}}{\left(1+h_X^2+h_Y^2\right)^{1/2}} \frac{h_Y}{\left(1+h_X^2+h_Y^2\right)^{1/2}}, \\
\Gamma_{11}^1 &= \frac{h_{XX}}{\left(1+h_X^2+h_Y^2\right)^{1/2}} \frac{h_X}{\left(1+h_X^2+h_Y^2\right)^{1/2}}, \;\; \Gamma_{11}^2 = \frac{h_{XX}}{\left(1+h_X^2+h_Y^2\right)^{1/2}} \frac{h_Y}{\left(1+h_X^2+h_Y^2\right)^{1/2}}, \\
\Gamma_{12}^1 &= \frac{h_{XY}}{\left(1+h_X^2+h_Y^2\right)^{1/2}} \frac{h_X}{\left(1+h_X^2+h_Y^2\right)^{1/2}}, \;\; \Gamma_{12}^2 = \frac{h_{XY}}{\left(1+h_X^2+h_Y^2\right)^{1/2}} \frac{h_Y}{\left(1+h_X^2+h_Y^2\right)^{1/2}}.
\end{aligned} \quad (1.5.14)$$

Also the curvatures will presented in the same manner:

$$\begin{aligned}
\mathrm{K} &= \frac{h_{XX}}{\left(1+h_X^2+h_Y^2\right)} \frac{h_{YY}}{\left(1+h_X^2+h_Y^2\right)} - \left(\frac{h_{XY}}{\left(1+h_X^2+h_Y^2\right)} \right)^2, \\
\mathrm{K_M} &= \frac{h_{XX}}{\left(1+h_X^2+h_Y^2\right)} \frac{\left(1+h_Y^2\right)}{\left(1+h_X^2+h_Y^2\right)^{1/2}} - \frac{h_{XY}}{\left(1+h_X^2+h_Y^2\right)} \frac{2h_X h_Y}{\left(1+h_X^2+h_Y^2\right)^{1/2}} \\
&\quad + \frac{h_{YY}}{\left(1+h_X^2+h_Y^2\right)} \frac{\left(1+h_X^2\right)}{\left(1+h_X^2+h_Y^2\right)^{1/2}}.
\end{aligned} \quad (1.5.15)$$

The second implication of Equation1.5.16 is obvious, just looking the the Christoffel symbols values in our PCS (Equation 1.5.14) it is clear that when the first derivatives are far from zero ($\gg 0$), then the ratio between second and first derivatives should be close to zero.

The first implication of Equation1.5.16 is more complex. The left going sense is simple, just substituting in Equation 1.5.15:

$$(\mathrm{K}_G, \mathrm{K}_M \simeq 0) \Leftarrow h_{ij} \ll h_k \quad \forall i,j,k \in \{X,Y\}\,. \tag{1.5.16}$$

For the right going sense the process used in the Proposition1.5.1 will be followed. The Equation1.5.4 becomes:

$$\begin{cases} 0 \simeq \dfrac{h_{XX}h_{YY} - h_{XY}^2}{\left(1 + h_X^2 + h_Y^2\right)^2} \\ 0 \simeq \dfrac{h_{XX}\left(1 + h_Y^2\right) - 2h_{XY}h_Xh_Y + h_{YY}\left(1 + h_X^2\right)}{\left(1 + h_X^2 + h_Y^2\right)^{3/2}} \end{cases} \tag{1.5.17}$$

The analysis carried out in second derivative terms h_{XX}, h_{YY} sign becomes:

1. Both are positive:

   The unique solution is

$$\frac{h_{XX}}{\left(1 + h_X^2 + h_Y^2\right)^{1/2}} \simeq 0, \frac{h_{YY}}{\left(1 + h_X^2 + h_Y^2\right)^{1/2}} \simeq 0. \tag{1.5.18}$$

   And as a consequence of the first part of Equation1.5.17:

$$\frac{h_{XY}}{\left(1 + h_X^2 + h_Y^2\right)^{1/2}} \simeq 0. \tag{1.5.19}$$

As was commented in the proposition this result is obtained with the constrainment in the first derivatives:

$$\frac{h_X}{(1+h_X^2+h_Y^2)} \gg 0, \frac{h_Y}{(1+h_X^2+h_Y^2)} \gg 0. \tag{1.5.20}$$

2. Both are negative:

   The unique solution is

$$\frac{h_{XX}}{(1+h_X^2+h_Y^2)^{1/2}} \simeq 0, \frac{h_{YY}}{(1+h_X^2+h_Y^2)^{1/2}} \simeq 0, \frac{h_{XY}}{(1+h_X^2+h_Y^2)^{1/2}} \simeq 0. \tag{1.5.21}$$

□

The Proposition1.5.1 is useful for steep but not curved slopes, the requirements in terms of slope in non zero first derivatives. The Proposition1.5.2 is useful for steep, slow varying slopes, the requirements in terms of slope is non small first derivatives. In general, for a mountain surface the curvature could not be neglected, it is a very rough approximation.

1.6 Application Examples, Revolution Surfaces

In this section there are two examples, the first one is a real case application of all the differential elements introduced in this chapter. A simple value for the terrain height function $h(X,Y)$ will be provided and all the analytic equations obtained along the chapter for metric elements will be used. In the second part of the section a steep slope geometric example will be used, but considering two cases, low curvature and high curvature.

As it is clear, the first example is used to validate the analytic equations obtained in the chapter, but this example is not adapted to debris flow conditions due to the low slope. The purpose of the second example is to consider a "steep slope" cases. An slope modified torus will constitute the "high curvature" scenario and a new revolution shape will be the "low curvature" scenario. In this second case, the Gaussian Curvatures will be reduced, the Chrisstoffel symbols obtained with the PCS also will be reduced, as was concluded in the previous section. Nevertheless, using the Principal Curvatures Coordinate system, the results are quite different, the value of the different Chrisstoffel symbols does not decrease as it does in PCS. **The vanishing linking between curvatures and the Christoffel symbols is a feature of the PCS, and it is not a general characteristic for coordinate systems**.

The aim of these cases is to demonstrate that in the PCS if the curvatures are negligible the Christoffel symbols too.

1.6.1 First Example: Torus

In the first part of this section, a torus geometry will be considered, all the metrics of this element will be computed, using two different coordinate systems. First the one proposed in this chapter, and the second will be the lines of curvature coordinate system, so using principal directions as coordinates. The target of this step is to show the application of the metrics to a real case. All the differential elements of this surface are computed and plotted in Appendix A, an small part of this elements is included in this section for text comprehension.

Torus Metrics in PCS

Here the metric elements will be applied on the torus geometry, the curvatures and Chrisstoffel symbols will be computed. The equations used for torus parametrization are:

$$\begin{cases} x = X \\ y = Y \\ z = h(X,Y) = -\sqrt{r_2^2 - \left(r_1 - \sqrt{X^2+Y^2}\right)^2} \end{cases}, \tag{1.6.1}$$

where r_1, r_2 are the bend radius and the crossection shape radius. In Figure 1.12 the typical torus shape is shown, as was commented the surface reproduces a stream bed only the bottom of the torus is considered.

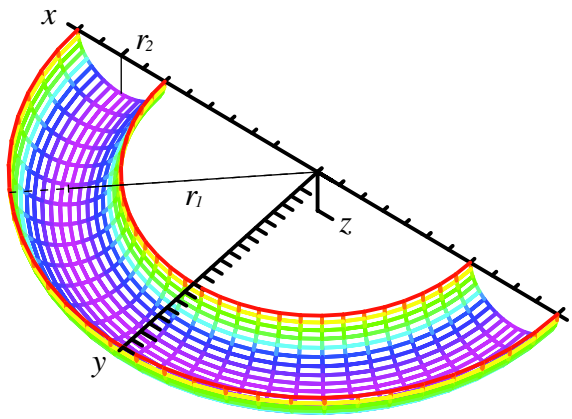

Figure 1.12: Torus geometry, with $r_1 = 0.9$ and $r_2 = 0.2$.

Following Equation 1.4.14 is possible to compute the Gauss Curvature for the torus using the PCS:

$$\mathrm{K}_G = -\frac{-X^2 + r_1\sqrt{X^2+Y^2} - Y^2}{r_2\left(X^2+Y^2\right)}. \tag{1.6.2}$$

Also in Equation 1.4.15 the Mean Curvature is found, and the results for the torus using the PCS are:

$$\begin{aligned} \mathrm{K}_M = & -\frac{1}{2}\frac{-5r_1X^2 + 2X^2\sqrt{X^2+Y^2} - 5r_1Y^2}{\sqrt{r_2\left(X^2+Y^2\right)}\left(r_2 - r_1^2 + 2r_1\sqrt{X^2+Y^2} - X^2 - Y^2\right)} \cdot \\ & \frac{-2r_2\sqrt{X^2+Y^2} - r_1^3 + 4r_1^2\sqrt{X^2+Y^2} + r_1r_2 + 2Y^2\sqrt{X^2+Y^2}}{\sqrt{r_2\left(X^2+Y^2\right)}\left(r_2 - r_1^2 + 2r_1\sqrt{X^2+Y^2} - X^2 - Y^2\right)}. \end{aligned} \tag{1.6.3}$$

The plot for both curvatures can be found in the Appendix A. The next group of metric elements are the Christoffel symbols, the results are too long to bee presented here, as a sample, the result for the first symbol is:

$$\Gamma^X_{XX} = -\frac{X\left(-r_1+\sqrt{X^2+Y^2}\right)}{r_2\left(X^2+Y^2\right)^2\left(r_2-{r_1}^2+2\,r_1\sqrt{X^2+Y^2}-X^2-Y^2\right)} \cdot \left(\begin{array}{c} -3\,r_1X^2Y^2+X^2\sqrt{X^2+Y^2}Y^2-X^2\sqrt{X^2+Y^2}r_2-3\,r_1Y^4+ \\ +3\,\sqrt{X^2+Y^2}{r_1}^2Y^2-{r_1}^3Y^2+Y^4\sqrt{X^2+Y^2}+r_1Y^2r_2-\sqrt{X^2+Y^2}r_2Y^2 \end{array} \right). \tag{1.6.4}$$

As is clear, this result is not simple. The graphical representation of this values and are presented in the Figure 1.13.

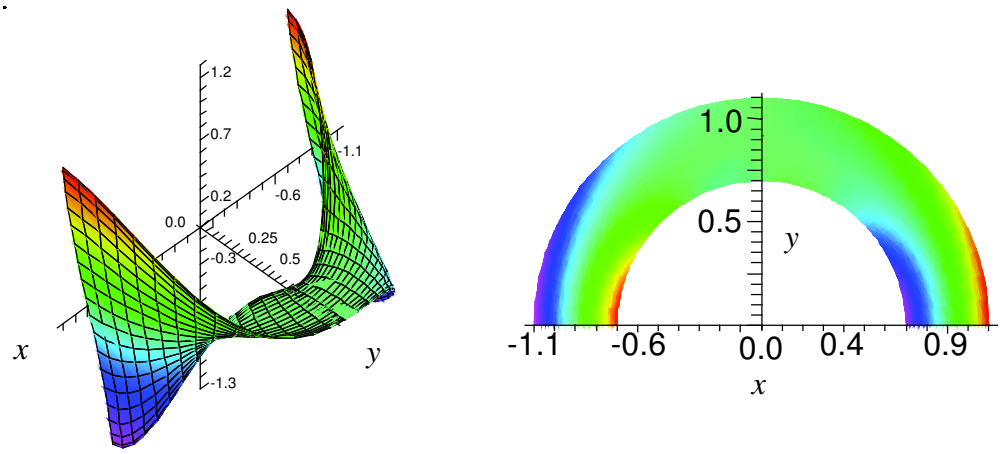

Figure 1.13: Γ^X_{XX} values for torus geometry, with $r_1 = 0,2$ and $r_2 = 0,9$.

As it's known, principal curvatures are intrinsic properties, so the results are the same in the principal directions reference system (see next section).

Torus Metrics in Principal Curvatures Coordinates

As was commented before two coordinate systems are considered, the first one is the PCS, just using the directions of he cartesian coordinates. The second coordinate

system is defined by the principal directions, so the coordinate axes are the lines of curvature. The torus and the revolution surface are selected because it is trivial to find the principal curvatures. In a general surface it is not trivial, in the case of the torus, the parameterizations that define the curvature lines is obtained though the conversion of Equation1.6.1 into polar coordinates:

$$\begin{cases} \mathrm{x} = (\mathrm{r}_1 + \mathrm{r}_2 \cos(\phi)) \cos(\theta) \\ \mathrm{y} = (\mathrm{r}_1 + \mathrm{r}_2 \cos(\phi)) \sin(\theta) \\ z = \mathrm{r}_2 \sin(\phi) \end{cases}, \tag{1.6.5}$$

where $\theta \in (0, \pi)$ and $\phi \in (\pi, 2\pi)$. These two coordinates define the curvature lines (revolution surface), in Figure 1.14 is possible to see both curvature lines.

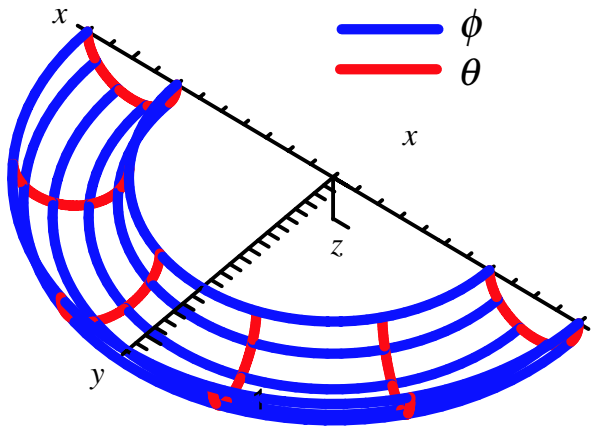

Figure 1.14: Coordinates defined by lines of curvature ($r_1 = 0.2$, $r_2 = 0.9$).

In the principal directions coordinate system the Gaussian Curvature is:

$$\mathrm{K}_G = \frac{\cos(\phi)}{r_2 (r_1 + r_2 \cos(\phi))}. \tag{1.6.6}$$

In the Figure 1.15 the value of the Gauss curvature is presented, as is shown, the maximum values are achieved near the boundary. The curvature values are intrinsic, so the figure is representative of both coordinate systems, the proposed one (Equation A.4.1) and the principal curvatures one (A.4.2).

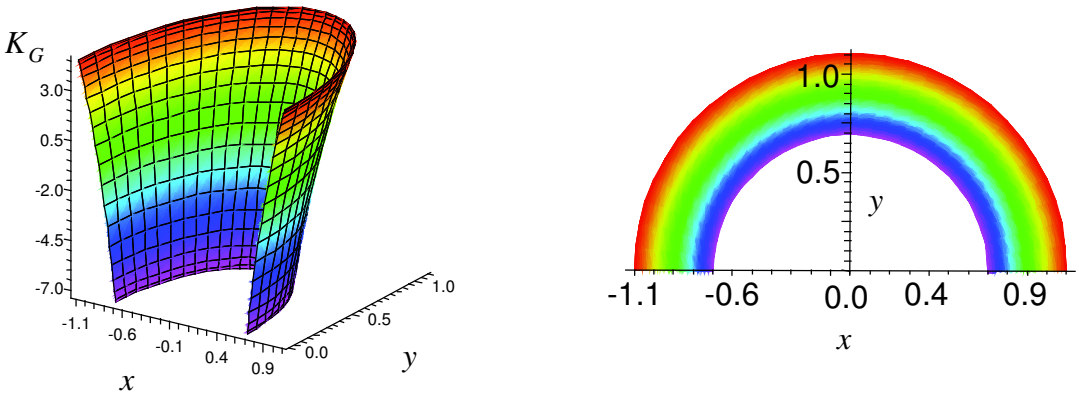

Figure 1.15: Gauss curvature of the torus ($r_1 = 0.2$, $r_2 = 0.9$).

The Mean Curvature in the principal directions is:

$$\mathrm{K}_M = \frac{1}{2}\frac{2r_2\cos(\phi) + r_1}{r_2\left(r_1 + r_2\cos(\phi)\right)}. \tag{1.6.7}$$

In the Appendix A, in the Figure A.10 the value of the Mean Curvature is presented, as is shown, the maximum values are achieved near the boundary. As in the previous case, it is an intrinsic property, so the results are the same in both coordinate systems (A.4.3, A.4.4).

The values of the principal curvatures obtained are:

$$\begin{aligned} k_1 &= \frac{1}{r_2}, \\ k_2 &= \frac{\cos(\phi)}{r_1 + r_2\cos(\phi)}. \end{aligned} \tag{1.6.8}$$

One of the principal curvatures is related to the crossection shape radius (r_2), and the other to the radius of curvature of the bend (r_1). In the Appendix A, in the Figure A.11 the values of both principal curvatures are shown, it's important to note that the extreme values are in the shape boundary.

As in the PCS also the Christoffel symbols are analyzed, in this case only two are different from zero, $\Gamma^{\phi}_{\theta\theta}, \Gamma^{\theta}_{\theta\phi}$, in Figure 1.16 the first one values are shown in the

whole torus, for a determined case.

$$\Gamma^{\phi}_{\theta\,\theta} = \frac{(r_1 + r_2\cos(\phi))\sin(\phi)}{r_2},$$
$$\Gamma^{\theta}_{\theta\,\phi} = -\frac{r_2\sin(\phi)}{r_1 + r_2\cos(\phi)}. \tag{1.6.9}$$

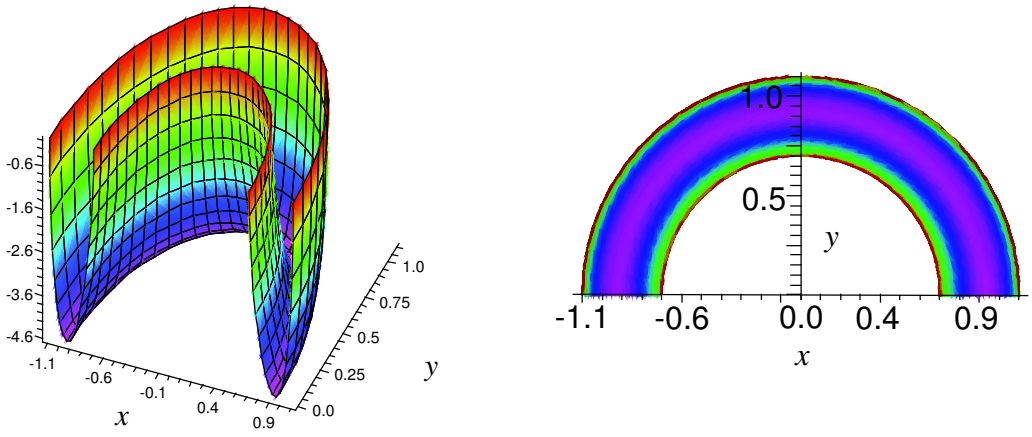

Figure 1.16: Values of $\Gamma^{\phi}_{\theta\,\theta}$ in the torus $r_1 = 0.9$, $r_2 = 0.2$.

The sense of this term is the centripetal force along the longitudinal coordinate, it's clear that depends on the curvatures radius.

1.6.2 Second Example: Steep Slope Revolution Surfaces

In the second part of this section, along the bend (torus), in the longitudinal direction, a slope will be introduced, to guarantee the "steep slope" condition in the geometry. With this longitudinal slope a "steep slope" and "high curvature" geometry will be obtained. The geometry of this modified torus will be compared to a "steep slope" and "small curvature" surface, in this case the a cubic revolution surface is selected. Only several metric elements of this surface are included in this chapter, unlike the previous example there is not an appendix collecting all the differential elements, but the process to obtain them it's clear.

In this subsection the steep slope will be introduced in the torus to achieve "steep slope" condition with "high curvature" and a new revolution geometry will created, with the same slope but with "small curvature", in order to compare the results between both surfaces. The small curvature surface is created as a revolution surface using a cubic polynomial. The coordinate transformation function for the torus with slope are:

$$\begin{cases} x = X \\ y = Y \\ z = h(X,Y) = -\sqrt{r_2^2 - \left(r_1 - \sqrt{X^2+Y^2}\right)^2} - S_0 \arctan\left(\frac{Y}{X}\right) r_1 \end{cases}, \tag{1.6.10}$$

where S_0 is the slope of the channel, and in the principal directions coordinates:

$$\begin{cases} \mathrm{x} = (\mathrm{r}_1 + \mathrm{r}_2 \cos(\phi)) \cos(\theta) \\ \mathrm{y} = (\mathrm{r}_1 + \mathrm{r}_2 \cos(\phi)) \sin(\theta) \\ z = \mathrm{r}_2 \sin(\phi) - S_0 r_1 \theta \end{cases}, \tag{1.6.11}$$

where $\theta \in (0, \pi)$ and $\phi \in (\pi, 2\pi)$. In Figure 1.17 the geometry of the modified torus is shown, it is clear the longitudinal slope and also the semicircular crossection.

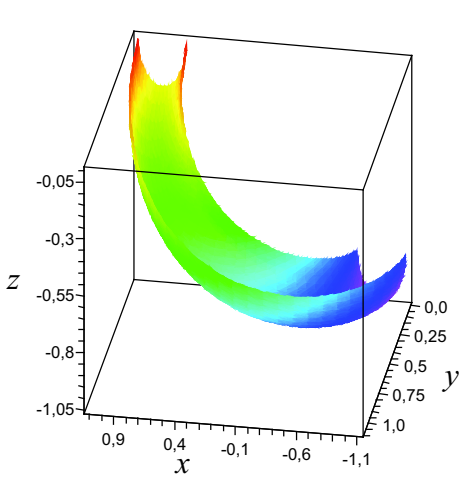

Figure 1.17: Torus modified to include steep slope, in this case $r_1 = 0.9$, $r_2 = 0.2$ and $S_0 = 0.3$.

As has been explained previously, a low curvature surface will be introduced to compare the values of the metric elements. In this case a revolution surface is proposed, to guarantee the low curvature values a polynomial function is used, in this case a cubic. The surface function in PCS is:

$$\begin{cases} x = X \\ y = Y \\ z = h(X,Y) = \left(r_1 - \sqrt{X^2+Y^2}\right)^3 - r_2^3 - S_0 \arctan\left(\frac{Y}{X}\right) r_1 \end{cases} . \tag{1.6.12}$$

And the surface in the principal directions is:

$$\begin{cases} \mathrm{x} = (\mathrm{r}_1 + \mathrm{r}_2 \cos(\phi)) \cos(\theta) \\ \mathrm{y} = (\mathrm{r}_1 + \mathrm{r}_2 \cos(\phi)) \sin(\theta) \\ z = (\mathrm{r}_2 \cos(\phi))^3 - r_2^3 - S_0 r_1 \theta \end{cases} . \tag{1.6.13}$$

Where $\theta \in (0, \pi)$ and $\phi \in (\pi, 2\pi)$. In Figure 1.18 the low curvature surface is shown, the crossection is a cubic polynomial.

As in the standard torus case, now the principal directions coordinate system is presented for both surfaces, the modified torus and the revolution surface, in the

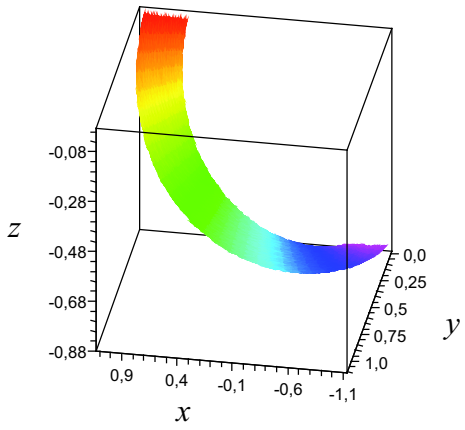

Figure 1.18: Low curvature surface defined by a revolution surface produced with a cubic polynomial, $r_1 = 0.9$, $r_2 = 0.2$ and $S_0 = 0.3$.

Figure 1.19 both coordinate systems are presented.

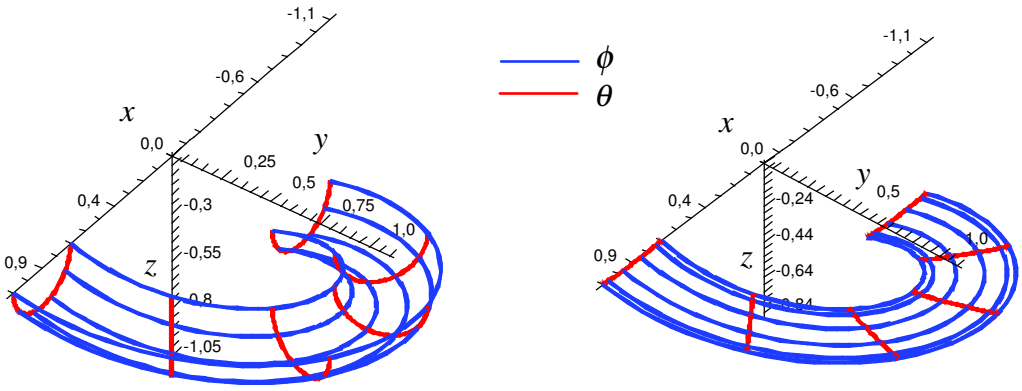

Figure 1.19: Principal directions coordinate systems for both surfaces, high curvature torus in the left, and low curvature revolution surface in the right ($r_1 = 0.9$, $r_2 = 0.2$ and $S_0 = 0.3$).

For the presented steep slope surfaces the metrics are computed, including, tangent space, metric tensor, curvature tensor, principal curvatures and Christoffel symbols. As was demonstrated in Section 1.5, for the PCS, if the curvatures are small, necessary the Christoffel symbols are also small. But this is not true for other coordinate

systems, for the principal directions coordinate system in Figure 1.20 is possible to see the $\Gamma^{\phi}_{\theta\,\theta}$, as is clear the values are no small. This is due to the fact that the centripetal force is strong due to bend curvature radius, on the other hand, in the PCS the values are small.

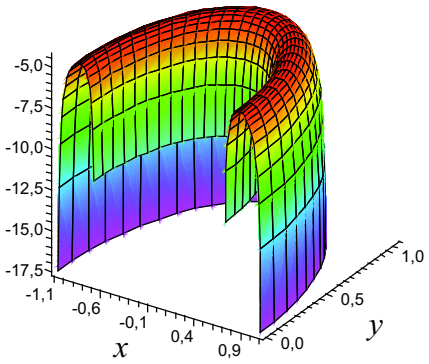

Figure 1.20: $\Gamma^{\phi}_{\theta\,\theta}$ results for the low curvature surface in the principal directions reference system ($r_1 = 0.9$, $r_2 = 0.2$ and $S_0 = 0.3$).

1.6.3 Example Conclusions

To compare the both coordinate systems (PCS and *Principal Curvatures coordinates*), a table is presented (Table 1.2), the first column results correspond to the modified torus, the second column corresponds to the low curvature surface, the polynomial revolution surface.

In the Table 1.2 the combined results from PCS and principal directions are shown. As is known curvatures are intrinsic parameters, so are equal for both coordinates systems, the Christoffel symbols with X, Y, Z subindex refer to PCS, and symbols with θ, ϕ refer to principal directions.

Based on the table its clear a curvature reduction, presented as Gauss curvature and mean curvature reduction ($\mathrm{K_G}, \mathrm{K_M}$), changing the Gauss curvature to a less

	High curvature	Low curvature
K_G	(-6.5, 4.4)	(-0.4, 0.0)
K_M	(2.0, 3.0)	(-0.6, 0.5)
k_1	(4.7, 5.5)	(-1.2, 0.1)
k_2	(-1.2, 0.9)	(0.2, 1.2)
Γ^X_{XY}	(-40, 40)	(-0.1, 0.4)
Γ^Y_{XY}	(-18, 17)	(-0.4, 0.4)
Γ^X_{YY}	(-14, 18)	(-0.2, 1.7)
Γ^Y_{YY}	(-40, 40)	(-0.1, 0.4)
Γ^X_{XY}	(-17, 16)	(-0.3, 0.2)
Γ^Y_{XY}	(-17, 14)	(-0.3, 0.2)
$\Gamma^\phi_{\theta\theta}$	(-4.6, 1.2)	(-17, -4)

Table 1.2: Curvatures and Chrisstoffel symbols for the PCS and principal curvatures coordinate system. Two scenarios are evaluated, low curvatures geometry and high curvatures one.

off the 10 percent of the original value. Also the principal curvatures are strongly reduced. In the PCS the Christoffel symbols are very low, in contrast, in the principal directions coordinate system the Christoffel symbols are higher than in high curvature surface ($\Gamma^\phi_{\theta\theta}$), from -4.6 to -17.

So, as was concluded before, in the PCS the link between curvatures and Christoffel symbols is strong. So, again is tested that in PCS a low curvature surface will have also small Christoffel symbols value, and is not a general property, the principal curvature directions were used to prove it.

Chapter 2

Equations System Definition

In this chapter the adopted equations system will be defined, the target of this model is to simulate debris flow, maybe equations definition is the most important work in modeling steep slope flows. A large quantity of approaches exist, they go from simple one dimensional models to biphasic three dimensional ones, eulerian and lagrangian, in local coordinates and in global coordinates, from simple rheologies to complex constitutive laws, etc.

As was described in the thesis introduction, in this work a monophasic approach is considered, several different existing models for monophasic approach will be commented within this chapter. Every model includes its own equation system, with particularities that differentiate from the other existing models. Several elements of the presented approach come from other existing models, along the text these similarities will be commented.

2.1 Introduction

Following the work carried out in the previous chapter, now a equations system will be defined. It's clear that, this definition in debris flow, is a challenge. Still there are big unknowns and uncertainty in the mechanics of the phenomenon, as was commented in the thesis introduction, in the present model, a simplified version of the physics is

considered.

Monophasic, constant density flow is modeled, simply considering the debris flow as a continuum. This is a strong hypothesis. The test cases presented in this work belong to the granular debris flows family. To model this kind of problems a completely different approach could be carried out using the available granular lagrangian methods (Delannay et al., 2007; Azanza et al., 1999; MiDi, 2004), also complex multiphysics flows models exist as MFIX (**M**ultiphase **F**low with **I**nterphase e**X**changes), (Anderson and Jackson, 1967) developed by NETL (National Energy Technology Laboratory), including most of the elements present in the physics of the phenomenon, solid fluid interaction, granular temperature, chemical reactions among other *state of art* features.

The problem regarding these physical models is the requirement of a deep knowledge on the material properties. In real cases, the nature of the debris materials is not homogeneous, and neither the exact conditions in the moment of occurrences are known. So, in controlled situations, as in the laboratory experiments, it is useful to use the sophisticated multiphysics models. In real cases, perhaps the reasonable limit is on the hydrostatic biphasic models (water phase also as pore pressure), used for high sediment concentration (Iverson and Denlinger, 2001; Pitman and Le, 2005; Pudasaini et al., 2005) and also for medium concentration (Spinewine and Zech, 2002; Fraccarollo and Capart, 2002).

All these elements give sense to the implementation an use of simplified models, as the one presented in this work. Once the medium is considered as homogeneous, it remains the complexity of the constitutive laws in debris flows. Supposing the solid liquid mixing as a special material implies the existence of a rheology relating deformation tensor and stresses tensor. In many cases the behavior of the flow is considered simply as Coulombian (Iverson, 1997; Savage and Hutter, 1989; Pudasaini et al., 2005; Pudasaini and Hutter, 2007; Mangeney et al., 2007; Pitman et al., 2003), obtaining enough accurate results.

2.2 Methodology Description

The equations system will be based on the definition of the conservations laws. These conservation equations will be the classic ones used in computational fluid dynamics (CFD). As is known, in CFD, the complexity of the simulations restricts the application of complete equation system to a small scale problems, far from the real natural hazard scale.

To overcome this limitation a simplified model should be used, this simplification implies the reduction of problem dimensions. To achieve this goal some hypothesis should be used. For shallow flows the classic process to carry on the simplification is through the flow depth integration (Whitman, 1974; Vreugdenhil, 1990; Abbott, 1979).

As has been commented, this described process is classic, but the particular use to debris flow problems is not so simple. The main problem is related to the geometry, normally shallow water flows are defined for mild slopes. On the other hand, in debris flow problems, the geometries are terrain surfaces in mountain areas.

In Chapter 1 the coordinate system has been defined (PCS), this selected system should be useful for steep slopes situations. One of the main research lines in debris flow modeling is related to topography complexity (Pudasaini and Hutter, 2007; Iverson et al., 2004; Bouchut and Westdickenberg, 2004; Gray et al., 1999; Bouchut et al., 2003), in most of these works different approaches are used to include terrain curvature effects.

The standard procedure for equations derivation implies:

1. Definition of the complete conservation laws as a equations system.
2. Application of the defined coordinate system to the equations.
3. Depth integration of the equations system.
4. Non-dimensionalizing equations using characteristic magnitudes.

5. Simplification of the equations using the non-dimensional parameters.

6. Transform the equations back to dimensional form.

In this work, during the equations system derivation process, the coordinate system used will be *Principal Directions Coordinate System* (see Chapter 1) and once the system becomes defined, the proposed coordinate system (PCS) will be used. This approach is selected in order to reduce the number of terms in the equations (an orthogonal coordinates are preferable).

The reason for this methodology is that, in real debris flow test cases, it is difficult to define principal curvatures directions, but is easy to define the PCS. But for differential equations manipulation is easier to use the principal directions because the coordinates are orthogonal and also the curvature tensor is diagonal.

2.3 Definition of the Conservation Laws

In this section, the conservation laws will be defined using appropriated curvilinear coordinates. The differential geometry defines the exact process for transformation of differential equations between different coordinates systems, also including curvilinear ones. The conservation laws used in this work will be mass conservation (continuity) and momentum conservation (Newton second law of motion).

The central point in PDE (partial derivative equations) in curvilinear coordinates is the *covariant derivative*. This element is equivalent to a partial derivative in cartesian coordinates (do Carmo, 1976; Aris, 1962), and it's named the covariant derivative of the contravariant vector field $u^i(\mathbf{X})$. In our case the contravariant vector field is the velocity field of the flow:

$$u^i_{,j} = \frac{\partial u^i}{\partial x^j} + \Gamma^i_{kj} u^k, \tag{2.3.1}$$

where u_i are the velocities in the curvilinear coordinate system, the k index it is a dummy index and follows the Einstein convention. The methodology consist in substitution of the partial derivatives with the covariant ones.

$$\left.\frac{\partial U^i}{\partial X^j}\right|_{Cartesian} \equiv \left.\underline{u^i_{,j}}\right|_{Curvilinear}, \tag{2.3.2}$$

where X^j are the cartesian coordinates, also presented as (X, Y, Z), U_i are the velocities in cartesian coordinates and x^j are the curvilinear coordinates (u, v, w). For the tensors ($\mathbf{T}$) the procedure is similar, the covariant derivative for a tensor is obtained:

$$T^{ji}_{,j} = \frac{\partial T^{ji}}{\partial x^j} + \Gamma^j_{kj} T^{ki} + \Gamma^i_{kj} T^{jk}, \tag{2.3.3}$$

with varying indexes (j, k), so the transformation is:

$$\left.\frac{\partial T^{ij}}{\partial X^j}\right|_{Cartesian} \equiv \left.\underline{T^{ij}_{,j}}\right|_{Curvilinear}. \tag{2.3.4}$$

2.3.1 Continuity Equation

The first conserved property is the mass, expressed as the continuity equation:

$$\nabla \cdot \mathbf{U} = 0 \quad \rightarrow \quad \frac{\partial U^1}{\partial X} + \frac{\partial U^2}{\partial Y} + \frac{\partial U^3}{\partial Z} = 0, \tag{2.3.5}$$

where $\mathbf{U}$ is the velocity vector, U^1, U^2, U^3 are the components in 3D Cartesian coordinates and u^1, u^2, u^3 are the components in curvilinear coordinates. The Equation 2.3.2 is introduced in Equation 2.3.5.

$$\frac{\partial U^1}{\partial X} + \frac{\partial U^2}{\partial Y} + \frac{\partial U^3}{\partial Z} = 0 \quad \rightarrow \quad u^1_{,1} + u^2_{,2} + u^3_{,3} = 0. \tag{2.3.6}$$

And introducing Equation 2.3.1 the obtained result is:

$$\frac{\partial u^1}{\partial x^1} + \Gamma^1_{k1} u^k + \frac{\partial u^2}{\partial x^2} + \Gamma^2_{k2} u^k + \frac{\partial u^3}{\partial x^3} + \Gamma^3_{k3} u^k = 0. \tag{2.3.7}$$

This result could be arranged regrouping terms to obtain:

$$\nabla \cdot \mathbf{u} = \frac{\partial u^i}{\partial x^i} + \Gamma^j_{ij} u^i = 0. \tag{2.3.8}$$

This is the classical form of the continuity equation in curvilinear coordinates. After some operations it is possible to transform this equation into more useful form (Aris, 1962):

$$\nabla \cdot \mathbf{u} = \frac{1}{\sqrt{|g|}} \frac{\partial \left(u^i \sqrt{|g|} \right)}{\partial x^i} = 0, \tag{2.3.9}$$

where $\sqrt{|g|}$ is the determinant of the covariant metric tensor g_{ij}.

2.3.2 Momentum Equation

A constant density, monophasic flow is considered. The constitutive equation will be analyzed later to introduce the friction laws, so the momentum conservation is expressed as:

$$\frac{\partial \mathbf{U}}{\partial t} + (\mathbf{U} \cdot \nabla)\, \mathbf{U} + \frac{\nabla \cdot \boldsymbol{\tau}}{\rho} = \mathbf{g}, \tag{2.3.10}$$

where $\boldsymbol{\tau}$ is the stresses tensor. The constitutive equation is not considered yet. So a system equivalent to perfect fluid is used:

$$\frac{\partial \mathbf{U}}{\partial t} + (\mathbf{U} \cdot \nabla)\, \mathbf{U} = \frac{-\nabla \mathrm{P}}{\rho} + \mathbf{g}, \tag{2.3.11}$$

where P is the pressure, ρ is the density and $\mathbf{g}$ the gravity vector $(\mathrm{g}_1, \mathrm{g}_2, \mathrm{g}_3)$. This equation is vectorial so it incudes three component equations, one for every cartesian axis. In cartesian coordinates:

$$\boldsymbol{\tau} = \tau_{ii} = P. \tag{2.3.12}$$

To transform the system to curvilinear coordinates, the tensor $\boldsymbol{\tau}$ in curvilinear coordinates is defined as:

$$\boldsymbol{\tau} = \tau_{ij} = g^{ij}P, \tag{2.3.13}$$

where the pressure is expressed in physical units, so the term g^{ij} is necessary for units consistency. Applying the same methodology used for continuity, the obtained result for curvilinear coordinates is:

$$\frac{\partial u^i}{\partial t} + u^j u^i_{,j} = -\frac{1}{\rho}\left(g^{ij}P\right)_{,j} + \mathrm{g}_i. \tag{2.3.14}$$

Introducing the definition of the covariant derivative (Equation 2.3.1,2.3.3):

$$\frac{\partial u^i}{\partial t} + u^j\left(\frac{\partial u^i}{\partial x_j} + \Gamma^i_{kj}u^k\right) = -\frac{1}{\rho}g^{ij}\frac{\partial P}{\partial x_j} + \mathrm{g}_i. \tag{2.3.15}$$

It is interesting to note that all the Christoffel terms related to pressure terms are canceled out to the presence of g^{ij}, so the equations include only one pressure term.

Should be notice also, that now the gravity components $(\mathrm{g}_1, \mathrm{g}_2, \mathrm{g}_3)$ are defined in the curvilinear coordinates. This coordinates transformation is not a trivial process (Pudasaini and Hutter, 2007), in AppendixB an example for PCS is presented.

The equation system defined by Equations 2.3.8 and 2.3.15 constitutes the starting point for the model development.

A useful identity formally related to Equation 2.3.9 could be defined here, to be applied with tensors. The stresses existing in momentum equation are a second order tensor $\boldsymbol{\tau} = \tau_{ij}$, when the momentum conservation is written in conservative form, also the convective term could be defined as tensor, joining convective term and stresses the $\mathbf{T}$ tensor is defined, and the momentum equation becomes:

$$\frac{\partial \mathbf{U}}{\partial t} + \nabla \cdot \mathbf{T} = \mathbf{g}. \tag{2.3.16}$$

It is possible to compute the tensor divergence in curvilinear coordinates, using the covariant derivative for tensors (Equation 2.3.3) a vectorial identity is obtained (Aris, 1962), defined in the curvilinear coordinates space:

$$\begin{aligned} \nabla \cdot \mathbf{T} = & \left(\frac{\partial T^{ji}}{\partial x^k} + \Gamma^j_{kj} T^{ki} + \Gamma^i_{kj} T^{jk} \right) \mathbf{X}_i = \\ & \left(\frac{1}{\sqrt{|g|}} \frac{\partial}{\partial x^j} \left(\sqrt{|g|} T^{ji} \right) + \Gamma^i_{kj} T^{jk} \right) \mathbf{X}_i. \end{aligned} \tag{2.3.17}$$

This important identity will be used later, as will be shown in next sections, the final equations system could be expressed in Equation 2.3.16 form, so the identity will be very useful.

2.4 Conservation Laws in Principal Directions Coordinate System

In the previous chapter a coordinate system has been proposed (PCS), this system uses the projection of the cartesian coordinates into the terrain surface. As is known, the curvatures are intrinsic properties, not depending on the coordinate system, just on surface shape.

In the present section, the equations system describing the conservation laws of the phenomenon will be defined based on the *Principal Directions Coordinate System*, the reason for the use of these coordinates as auxiliary reference system is to facilitate the integration of the equations and simplification processes that will be carried out later in this chapter.

2.4.1 Metrics of the Principal Directions Coordinate System

The goal of this section is the application of Equations 2.3.8 and 2.3.15, so all the metric elements included in the equations should be computed. The scheme of this section is similar to that of the Section 1.4.

1. Coordinates definition.
2. Tangent space.
3. First fundamental form.
4. Second fundamental form.
5. Curvature tensor.
6. Christoffel symbols.

So the explanation will not be detailed. The first step is to define the coordinates transformation functions, in this case a 3D coordinate system should be defined in the flow volume ($\Omega \in \mathbb{R}^3$), but this flow volume will be located over the terrain surface ($\mathrm{S} \in \mathbb{R}^3$), that will be defined using the same function used in the previous chapter:

$$\mathbf{X} : \mathrm{U} \subset \mathbb{R}^2 \rightarrow \mathrm{S}, \;\; \mathbf{X}\,(u,v) = (X(u,v), Y(u,v), h(u,v)) \qquad (u,v) \in \mathrm{U}. \tag{2.4.1}$$

Being u, v the curvilinear coordinates in principal directions (how to calculate it for a general topography could be found in Hameiri and Shimshoni (2003)) and requiring $h\,(u,v) \in C^2\,(\mathrm{U})$, over this terrain surface, the 3D transformation function will be constructed:

$$\widehat{\mathbf{X}} : \mathrm{W} \subset \mathbb{R}^3 \rightarrow \Omega, \;\; \widehat{\mathbf{X}}\,(u,v,w) = (X(u,v,w), Y(u,v,w), Z(u,v,w)) \qquad (u,v,w) \in \mathrm{W}. \tag{2.4.2}$$

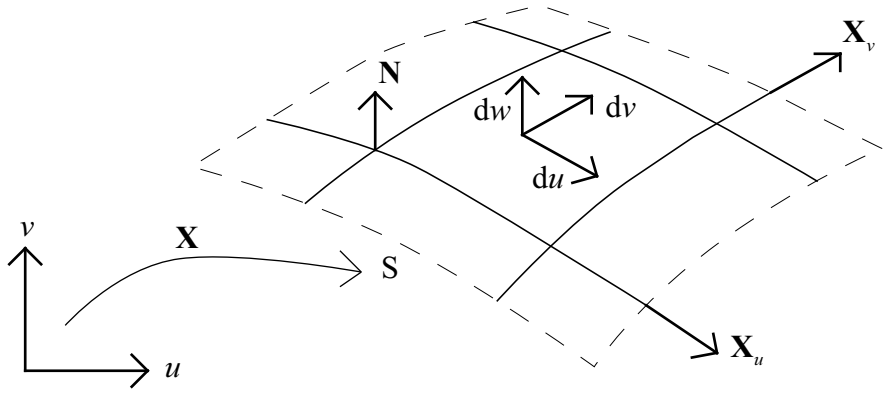

Figure 2.1: Coordinates transformation function $\mathbf{X}$ definition.

So at the end, two different functions have been defined, $\widehat{\mathbf{X}}$ to transform the three dimensional space and $\mathbf{X}$ to transform the terrain surface. Introducing the surface as the flow volume bed surface, the transformation $\widehat{\mathbf{X}}$ becomes defined adding the depth coordinate w in the surface normal vector direction $\mathbf{N}$:

$$\begin{aligned} \widehat{\mathbf{X}} &= (\mathbf{X} + w\mathbf{N}) \\ \widehat{\mathbf{X}} &= \big((X(u,v), Y(u,v), h\,(u,v)) + w\mathbf{N}\big), \quad (u,v,w) \in \mathrm{W} \end{aligned} \tag{2.4.3}$$

$\mathbf{N}$ is the terrain surface normal vector (defined in the previous chapter). The u, v coordinates are defined as principal directions, implying this that the normal derivatives along vector (u', v') in basis $(\mathbf{X}_u, \mathbf{X}_v)$ are computed as:

$$d\mathbf{N} \begin{pmatrix} u' \\ v' \end{pmatrix} = k_1 \mathbf{X}_u + k_2 \mathbf{X}_v. \tag{2.4.4}$$

Here $\mathbf{X}_u, \mathbf{X}_v$ are the surface S tangent vectors, in the principal directions u, v and k_1, k_2 principal curvatures. Using the previous result and Equation 2.4.3, is possible to define the tangent space for the 3D transformation ($\widehat{\mathbf{X}}$):

$$
\begin{aligned}
\widehat{\mathbf{X}}_u &= \frac{\partial \widehat{\mathbf{X}}}{\partial u} = \frac{\partial \mathbf{X}}{\partial u} - k_1 w \frac{\partial \mathbf{X}}{\partial u} = \mathbf{X}_u \left(1 - k_1 w\right) \\
\widehat{\mathbf{X}}_v &= \frac{\partial \widehat{\mathbf{X}}}{\partial v} = \frac{\partial \mathbf{X}}{\partial v} - k_2 w \frac{\partial \mathbf{X}}{\partial v} = \mathbf{X}_v \left(1 - k_2 w\right) \\
\widehat{\mathbf{X}}_w &= \frac{\partial \widehat{\mathbf{X}}}{\partial w} = \mathbf{N}.
\end{aligned}
\tag{2.4.5}
$$

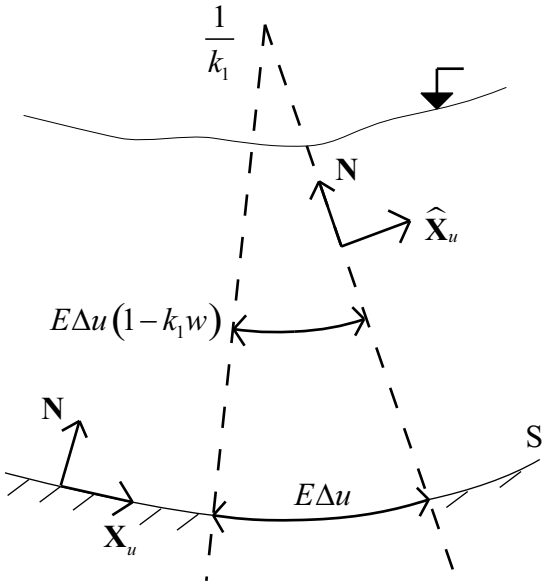

Figure 2.2: Detail of axes and metrics in principal direction u.

In Figure 2.2 the curvilinear axes in u crossection are shown. As is shown the tangent vectors $(\mathbf{X}_u, \mathbf{X}_v)$ change along the depth as functions of $1 - k_1 w$ and $1 - k_2 w$.

The *First Fundamental Form* I_p for the surface transformation $(\mathbf{X})$ is computed:

$$
\begin{aligned}
g_{11} &= E = \langle \mathbf{X}_u | \mathbf{X}_u \rangle \\
g_{12} &= F = \langle \mathbf{X}_u | \mathbf{X}_v \rangle = 0 \\
g_{21} &= F = \langle \mathbf{X}_v | \mathbf{X}_u \rangle = 0 \\
g_{22} &= G = \langle \mathbf{X}_v | \mathbf{X}_v \rangle
\end{aligned}
\tag{2.4.6}
$$

And also for the volume, taking into account the orthogonality of the coordinates and obtaining the 3x3 symmetric tensor:

$$
\begin{aligned}
\widehat{g}_{11} &= \widehat{E} = \langle \widehat{\mathbf{X}}_u | \widehat{\mathbf{X}}_u \rangle = E\,(1 - k_1 w)^2 \\
\widehat{g}_{12} &= \widehat{F} = \langle \widehat{\mathbf{X}}_u | \widehat{\mathbf{X}}_v \rangle = 0 \\
\widehat{g}_{13} &= \langle \widehat{\mathbf{X}}_u | \widehat{\mathbf{X}}_w \rangle = 0 \\
\widehat{g}_{21} &= \widehat{F} = \langle \widehat{\mathbf{X}}_v | \widehat{\mathbf{X}}_u \rangle = 0 \\
\widehat{g}_{22} &= \widehat{G} = \langle \widehat{\mathbf{X}}_v | \widehat{\mathbf{X}}_v \rangle = G\,(1 - k_2 w)^2 \\
\widehat{g}_{23} &= \langle \widehat{\mathbf{X}}_v | \widehat{\mathbf{X}}_w \rangle = 0 \\
\widehat{g}_{31} &= \langle \widehat{\mathbf{X}}_w | \widehat{\mathbf{X}}_u \rangle = 0 \\
\widehat{g}_{32} &= \langle \widehat{\mathbf{X}}_w | \widehat{\mathbf{X}}_v \rangle = 0 \\
\widehat{g}_{13} &= \langle \widehat{\mathbf{X}}_u | \widehat{\mathbf{X}}_w \rangle = 1
\end{aligned}
\tag{2.4.7}
$$

It is immediate to compute the contravariant tensor:

$$
\widehat{g}_{ij} = \begin{pmatrix} \widehat{E} & 0 & 0 \\ 0 & \widehat{F} & 0 \\ 0 & 0 & 1 \end{pmatrix}, \quad \widehat{g}^{ij} = \begin{pmatrix} 1/\widehat{E} & 0 & 0 \\ 0 & 1/\widehat{F} & 0 \\ 0 & 0 & 1 \end{pmatrix}
\tag{2.4.8}
$$

For simplicity in the notation, also metric scaling elements for u, v are defined:

$$
\begin{aligned}
h_1(w) &= \sqrt{\widehat{E}} = \sqrt{E}\,(1 - k_1 w) \\
h_2(w) &= \sqrt{\widehat{G}} = \sqrt{G}\,(1 - k_2 w)
\end{aligned}
\tag{2.4.9}
$$

Then the covariant metric tensor determinant is easily computed $\sqrt{|\widehat{g}|} = h_1 h_2$. Finally the Christoffel symbols are computed.

$$
\begin{cases}
\Gamma^u_{uu} = \dfrac{1}{h_1}\dfrac{\partial h_1}{\partial u} \\
\Gamma^v_{uu} = -\dfrac{h_1}{h_2^2}\dfrac{\partial h_1}{\partial v} \\
\Gamma^w_{uu} = h_1 k_1 E
\end{cases}
\tag{2.4.10}
$$

$$\begin{cases} \Gamma^u_{vv} = -\dfrac{h_2}{h_1^2}\dfrac{\partial h_2}{\partial v} \\ \Gamma^v_{vv} = \dfrac{1}{h_2}\dfrac{\partial h_2}{\partial v} \\ \Gamma^w_{vv} = h_2 k_2 G \end{cases} \tag{2.4.11}$$

$$\begin{cases} \Gamma^u_{uv} = \dfrac{1}{h_1}\dfrac{\partial h_1}{\partial v} \\ \Gamma^v_{uv} = \dfrac{1}{h_2}\dfrac{\partial h_2}{\partial u} \\ \Gamma^w_{uv} = 0 \end{cases} \tag{2.4.12}$$

$$\begin{cases} \Gamma^u_{ww} = 0 \\ \Gamma^v_{ww} = 0 \\ \Gamma^w_{ww} = 0 \end{cases} \tag{2.4.13}$$

$$\begin{cases} \Gamma^u_{uw} = -\dfrac{k_1 E}{h_1} \\ \Gamma^v_{uw} = 0 \\ \Gamma^w_{uw} = 0 \end{cases} \tag{2.4.14}$$

$$\begin{cases} \Gamma^u_{vw} = 0 \\ \Gamma^v_{vw} = -\dfrac{k_2 G}{h_2} \\ \Gamma^w_{vw} = 0 \end{cases} \tag{2.4.15}$$

The components could be ordered as matrix:

$$\Gamma^u = \begin{pmatrix} \frac{1}{h_1}\frac{\partial h_1}{\partial u} & \frac{1}{h_1}\frac{\partial h_1}{\partial v} & -\frac{k_1 E}{h_1} \\ \frac{1}{h_1}\frac{\partial h_1}{\partial v} & -\frac{h_2}{h_1^2}\frac{\partial h_2}{\partial v} & 0 \\ -\frac{k_1 E}{h_1} & 0 & 0 \end{pmatrix} \tag{2.4.16}$$

$$\Gamma^v = \begin{pmatrix} -\frac{h_1}{h_2^2}\frac{\partial h_1}{\partial v} & \frac{1}{h_2}\frac{\partial h_2}{\partial u} & 0 \\ \frac{1}{h_2}\frac{\partial h_2}{\partial u} & \frac{1}{h_2}\frac{\partial h_2}{\partial v} & -\frac{k_2 G}{h_2} \\ 0 & -\frac{k_2 G}{h_2} & 0 \end{pmatrix} \tag{2.4.17}$$

$$\Gamma^w = \begin{pmatrix} h_1 k_1 E & 0 & 0 \\ 0 & h_1 k_1 G & 0 \\ 0 & 0 & 0 \end{pmatrix} \tag{2.4.18}$$

2.4.2 Continuity Equation in the Principal Directions Coordinate System

In this section all the computed metrics will be applied into the continuity equation (Equation 2.3.9).

$$\frac{1}{h_1 h_2}\left(\frac{\partial}{\partial u}\left(h_1 h_2 u^1\right) + \frac{\partial}{\partial v}\left(h_1 h_2 u^2\right) + \frac{\partial}{\partial w}\left(h_1 h_2 u^3\right)\right) = 0. \tag{2.4.19}$$

And arranging:

$$\frac{\partial}{\partial u}\left(h_1 h_2 u^1\right) + \frac{\partial}{\partial v}\left(h_1 h_2 u^2\right) + \frac{\partial}{\partial w}\left(h_1 h_2 u^3\right) = 0. \tag{2.4.20}$$

2.4.3 Momentum Equation in the Principal Directions Coordinates System

The complete substitution of metric terms in momentum conservation equation (Equation 2.3.15) implies more than 15 terms for every momentum component, so just the final simplified version is shown. First the momentum conservation in $\mathbf{X}_u$ direction:

$$h_1 \frac{\partial u^1}{\partial t} + u^1 \frac{\partial u^1 h_1}{\partial u} + u^2 \frac{\partial u^1 h_1}{\partial v} + u^3 \frac{\partial u^1 h_1}{\partial w}$$

$$= \frac{h_2 u^2 u^2}{h_1}\frac{\partial h_2}{\partial u} - u^1 u^2 \frac{\partial h_1}{\partial v} + k_1 E u^1 u^3 - \frac{1}{h_1 \rho}\frac{\partial P}{\partial u} + h_1 \mathrm{g}_1. \tag{2.4.21}$$

The first and second term in the R.H.S (Right Hand Side) correspond to centripetal acceleration. The $\mathbf{X}_v$ component of the system is:

$$h_2\frac{\partial u^2}{\partial t} + u^1\frac{\partial u^2 h_2}{\partial u} + u^2\frac{\partial u^2 h_2}{\partial v} + u^3\frac{\partial u^2 h_2}{\partial w} =$$

$$= \frac{h_1 u^1 u^1}{h_2}\frac{\partial h_1}{\partial v} - u^1 u^2\frac{\partial h_2}{\partial u} + k_2 G u^2 u^3 - \frac{1}{h_2\rho}\frac{\partial P}{\partial v} + h_2 \mathrm{g}_2. \tag{2.4.22}$$

And finally the $\mathbf{X}_w$ component:

$$\frac{\partial u^3}{\partial t} + u^1\frac{\partial u^3}{\partial u} + u^2\frac{\partial u^3}{\partial v} + u^3\frac{\partial u^3}{\partial w} + E k_1 h_1 u^1 u^1 + G k_2 h_2 u^2 u^2 + \frac{1}{\rho}\frac{\partial P}{\partial w} - \mathrm{g}_3 = 0 \tag{2.4.23}$$

2.5 Dimensionless Equations System

Once the equation system is defined, simplifications should be applied. This simplifications are always related to dimensionless parameters analysis. In the steep slope flows, traditionally it is possible to find two main parameters, in debris flow models the parameter ε is the typical maximum depth-to-length H/L aspect ratio of a flow, a purely geometric factor, first defined by Savage and Hutter (1989) and in most cases the parameter is considered to be $0 < \varepsilon \ll 1$ (Iverson and Denlinger, 2001; Pudasaini et al., 2005; Quecedo and Pastor, 2003; Bouchut and Westdickenberg, 2004).

In hydraulic models with curvature, the classical non-dimensional parameter ε is defined by the maximum depth-to-curvature radius H/r ratio (Sivakumaran et al., 1981; Sivakumaran and Dressler, 1989; Berger and Carey, 1998*a*) and considering it as small or large value is possible to define models useful for low or high curvatures.

This apparent difference between hydraulic and debris flow models is not so deep, to apply the debris flow ε to the equations terms involving curvature is also necessary

to perform hypotheses on the scale of curvature. As example, in Bouchut and Westdickenberg (2004), in the *small slope variation* model presented, it is possible to find $d\mathbf{N}_{\mathrm{p}} \simeq O(\varepsilon)$, meaning that the curvatures are very small, so the curvature radius are larger than depths, in a similar manner to the definition of ε used in curved hydraulic models.

In the same direction, in Pudasaini et al. (2005) is possible to found $\lambda = O(\varepsilon^{\alpha})$, meaning λ the depth-to-curvature radius H/r ratio, so, at last, using a parametrization similar to the one used in curved hydraulic models.

In this work the method proposed by Berger and Carey (1998*a*) will be followed, so as has been explained the non-dimensional parameter ε will be the square of typical maximum depth-to-curvature radii $(H/r)^2$. Once the equations are in non-dimensional form the perturbation method in the solution will be applied.

2.5.1 Dimensionless Variables

As has been commented, the flow characteristic dimensions are: H the characteristic depth and r the curvature radius, and also the relation between them ε. Selecting the most suitable dimension for each variable the non dimensional variables are defined in Table 2.1, where d is the flow depth, the distance from the bottom to the free surface following the terrain normal direction.

The horizontal coordinates (u, v) are transformed into dimensionless form using the curvature radius (r), but the vertical coordinate (w) is converted into dimensionless form using the characteristic depth H. The horizontal velocities (u^1, u^2) get dimensionless using the characteristic celerity $(\sqrt{\mathrm{g}H})$. The pressure is scaled with the hydrostatic pressure.

The next step in the dimensionless conversion i.e., the substitution of the values of the table in the equations (Equation 2.4.20-2.4.23). First the continuity equation, after some arrange the equation becomes:

	Non dimensional variable	Definition
Coordinate	α	u/r
Coordinate	γ	v/r
Coordinate	β	w/H
Depth	Y	d/H
Velocity	$\tilde{u}^1$	$u^1/\sqrt{\mathrm{g}H}$
Velocity	$\tilde{u}^2$	$u^2/\sqrt{\mathrm{g}H}$
Velocity	$\tilde{u}^3$	$u^3 H/r\sqrt{\mathrm{g}H}$
Metric	$\tilde{E}$	E
Metric	$\tilde{G}$	G
Pressure	π	$P/\rho H\mathrm{g}$
Curvature	$\tilde{k}_1$	$k_1 H$
Curvature	$\tilde{k}_2$	$k_2 H$
Time	τ	$t\sqrt{\mathrm{g}H}/H$
Metric	$\tilde{h}_1$	$\sqrt{\tilde{E}}\left(1-\tilde{k}_1\beta\right)$
Metric	$\tilde{h}_2$	$\sqrt{\tilde{G}}\left(1-\tilde{k}_2\beta\right)$
Parameter	ε	$(H/r)^2$

Table 2.1: Non-dimensional variables.

$$\varepsilon\left\{\frac{\partial}{\partial\alpha}\left(\tilde{h}_1\tilde{h}_2\tilde{u}^1\right)+\frac{\partial}{\partial\gamma}\left(\tilde{h}_1\tilde{h}_2\tilde{u}^2\right)\right\}+\frac{\partial}{\partial\beta}\left(\tilde{h}_1\tilde{h}_2\tilde{u}^3\right)=0. \tag{2.5.1}$$

And also in the three momentum equations:

$$\varepsilon\left\{\tilde{h}_1\frac{\partial\tilde{u}^1}{\partial\tau}+\tilde{u}^1\frac{\partial\tilde{u}^1\tilde{h}_1}{\partial\alpha}+\tilde{u}^2\frac{\partial\tilde{u}^1\tilde{h}_1}{\partial\gamma}-\frac{\tilde{h}_2\tilde{u}^2\tilde{u}^2}{\tilde{h}_1}\frac{\partial\tilde{h}_2}{\partial\alpha}+\tilde{u}^1\tilde{u}^2\frac{\partial\tilde{h}_1}{\partial\gamma}+\frac{1}{\tilde{h}_1}\frac{\partial\pi}{\partial\alpha}-\tilde{h}_1\tilde{\mathrm{g}}_1\right\}+$$

$$+\tilde{u}^3\frac{\partial\tilde{u}^1\tilde{h}_1}{\partial\beta}-\tilde{k}_1\tilde{E}\tilde{u}^1\tilde{u}^3=0, \tag{2.5.2}$$

$$\varepsilon\left\{\tilde{h}_2\frac{\partial\tilde{u}^2}{\partial\tau}+\tilde{u}^1\frac{\partial\tilde{u}^2\tilde{h}_2}{\partial\alpha}+\tilde{u}^2\frac{\partial\tilde{u}^2\tilde{h}_2}{\partial\gamma}-\frac{\tilde{h}_1\tilde{u}^1\tilde{u}^1}{\tilde{h}_2}\frac{\partial\tilde{h}_1}{\partial\gamma}+\tilde{u}^1\tilde{u}^2\frac{\partial\tilde{h}_2}{\partial\alpha}+\frac{1}{\tilde{h}_2}\frac{\partial\pi}{\partial\gamma}-\tilde{h}_1\tilde{\mathrm{g}}_2\right\}+$$

$$+\tilde{u}^3\frac{\partial\tilde{u}^2\tilde{h}_2}{\partial\gamma}-\tilde{k}_2\tilde{G}\tilde{u}^2\tilde{u}^3=0, \quad (2.5.3)$$

$$\varepsilon\left\{\frac{\partial\tilde{u}^3}{\partial\tau}+\tilde{u}^1\frac{\partial\tilde{u}^3}{\partial\alpha}+\tilde{u}^2\frac{\partial\tilde{u}^3}{\partial\gamma}+\tilde{E}\tilde{k}_1\tilde{h}_1\tilde{u}^1\tilde{u}^1+\tilde{G}\tilde{k}_2\tilde{h}_2\tilde{u}^2\tilde{u}^2+\frac{\partial\pi}{\partial\beta}-\tilde{\mathrm{g}}_3\right\}+$$

$$+\tilde{u}^3\frac{\partial\tilde{u}^3}{\partial\beta}=0. \quad (2.5.4)$$

The last two terms in Equations 2.5.2 and 2.5.3 when arranged are:

$$\begin{array}{l}\ldots\tilde{u}^3\left(\frac{\partial\tilde{u}^1\tilde{h}_1}{\partial\beta}-\tilde{k}_1\tilde{E}\tilde{u}^1\right),\\ \ldots\tilde{u}^3\left(\frac{\partial\tilde{u}^2\tilde{h}_2}{\partial\beta}-\tilde{k}_2\tilde{G}\tilde{u}^2\right).\end{array} \quad (2.5.5)$$

The terms into the parenthesis could be linked, through the continuity equation, to the vorticity of the flow in the u, v directions, in shallow flows the vorticity in these directions is considered to be zero, see the details in Berger and Carey (1998*a*). In the following analysis they will be neglected.

Over this non-dimensional system a perturbation analysis can be performed (Hinch, 1991), in vanish all the variables are expanded in terms of the parameter ε. This way is easier to establish the importance of the curvature. The typical expansion of a non dimensional variable is:

$$\tilde{u}^1(\alpha,\gamma,\beta,\tau)=u_0^1(\alpha,\gamma,\beta,\tau)+\varepsilon u_1^1(\alpha,\gamma,\beta,\tau)+\varepsilon^2u_2^1(\alpha,\gamma,\beta,\tau)+\ldots \quad (2.5.6)$$

Where the subindexes are to indicate the order of the term in the powers expansion. The complete process will not be reproduced here, for the details check Berger and Carey (1998*a*), where similar process using *physical coordinates* (Aris, 1962) is

carried out. Once the terms have been grouped in powers of ε, several conclusions could be achieved using the zero powers of ε.

1. From the continuity equation, along with the boundary condition that imposes null vertical velocities in the bottom ($\underline{u^3}|_{\beta=0} = 0$), is obtained: $u_0^3 = 0$, so in order zero the vertical (strictly speaking is defined as the surface normal) velocities are zero.

2. Also is obtained $\tilde{u}_0^1 = \hat{u}^1 \Big/ \left(1 - \tilde{k}_1\beta\right)$, where $\hat{u}^1$ is the velocity in the bottom. This result means that in order zero, the velocity distribution of $\tilde{u}^1$ is linear in the depth.

3. And finally is obtained $\tilde{u}_0^2 = \hat{u}^2 \Big/ \left(1 - \tilde{k}_2\beta\right)$, where $\hat{u}^2$ is the velocity in the bottom. This result means that in order zero, the velocity distribution of $\tilde{u}^2$ is linear in the depth.

The next step is to work with the first order ε terms, in the continuity equation the obtained result is:

$$\frac{\partial}{\partial\alpha}\left(\tilde{h}_1\tilde{h}_2\tilde{u}_0^1\right) + \frac{\partial}{\partial\gamma}\left(\tilde{h}_1\tilde{h}_2\tilde{u}_0^2\right) + \frac{\partial}{\partial\beta}\left(\tilde{h}_1\tilde{h}_2\tilde{u}_1^3\right) = 0. \tag{2.5.7}$$

So, the term relative to vertical component of the velocity (u^3) is of order 1, while the remain velocity variables are of order 0 in powers of ε. The same process for momentum equations in α, γ gives:

$$\tilde{h}_1\frac{\partial\tilde{u}_0^1}{\partial\tau} + \tilde{u}_0^1\frac{\partial\tilde{u}_0^1\tilde{h}_1}{\partial\alpha} + \tilde{u}_0^2\frac{\partial\tilde{u}_0^1\tilde{h}_1}{\partial\gamma} - \frac{\tilde{h}_2\tilde{u}_0^2\tilde{u}_0^2}{\tilde{h}_1}\frac{\partial\tilde{h}_2}{\partial\alpha} + \tilde{u}_0^1\tilde{u}_0^2\frac{\partial\tilde{h}_1}{\partial\gamma} + \frac{1}{\tilde{h}_1}\frac{\partial\pi_0}{\partial\alpha} - \tilde{h}_1\tilde{\mathrm{g}}_1 = 0, \tag{2.5.8}$$

$$\tilde{h}_2\frac{\partial\tilde{u}_0^2}{\partial\tau} + \tilde{u}_0^1\frac{\partial\tilde{u}_0^2\tilde{h}_2}{\partial\alpha} + \tilde{u}_0^2\frac{\partial\tilde{u}_0^2\tilde{h}_2}{\partial\gamma} - \frac{\tilde{h}_1\tilde{u}_0^1\tilde{u}_0^1}{\tilde{h}_2}\frac{\partial\tilde{h}_1}{\partial\gamma} + \tilde{u}_0^1\tilde{u}_0^2\frac{\partial\tilde{h}_2}{\partial\alpha} + \frac{1}{\tilde{h}_2}\frac{\partial\pi_0}{\partial\gamma} - \tilde{h}_2\tilde{\mathrm{g}}_2 = 0. \tag{2.5.9}$$

It is clear that all the variables terms are of order 0. The third momentum equation is obtained discarding the first order vertical velocities ($u_0^3 = 0$), as was concluded from the continuity equation:

$$\tilde{E}\tilde{k}_1\tilde{h}_1\tilde{u}_0^1\tilde{u}_0^1 + \tilde{G}\tilde{k}_2\tilde{h}_2\tilde{u}_0^2\tilde{u}_0^2 + \frac{\partial \pi_0}{\partial \beta} - \tilde{\mathrm{g}}_3 = 0. \tag{2.5.10}$$

Again all the terms are of order 0. Two different parts appear, the first two terms are the centripetal effects (dynamic), and the last one the hydrostatic contribution (static). This equation will be integrated in order to obtain the pressure distribution equation.

2.6 Depth Integration

The depth integration is the essential process to reduce equations system complexity. First the integration is performed in the continuity equation and pressures. The depth integration is a classical process and details could be found in Vreugdenhil (1990); Whitman (1974), essentially, the methodology consists in successive application of the Leibnitz rule. It's interesting to note that the metric scaling elements h_1, h_2 are functions of w coordinate, so also should be integrated along β. The results obtained for continuity equation, expressed again in dimensional variables, are:

$$\begin{aligned} &h_1(d)h_2(d)\frac{\partial d}{\partial t} + \frac{\partial}{\partial u}\left[\frac{h_2(0)h_1(0)\hat{u}^1}{k_1}\left\{\left(\frac{k_2 - k_1}{k_1}\right)\log\left(1 - k_1 d\right) + k_2 d\right\}\right] + \\ &+\frac{\partial}{\partial v}\left[\frac{h_1(0)h_2(0)\hat{u}^2}{k_2}\left\{\left(\frac{k_1 - k_2}{k_2}\right)\log\left(1 - k_2 d\right) + k_1 d\right\}\right] = 0. \end{aligned} \tag{2.6.1}$$

As was previously defined, d is the depth and it's a function of $d(u, v, t)$, $\hat{u}^1, \hat{u}^2$ are the flow velocity components in the terrain surface. Notice that $h_1(0), h_2(0)$ are the metrics at the bottom. This result (Berger and Carey, 1998*b*) clearly includes the effects of curvature as shown in Figure 2.2. It is obvious that the curvature influences the capacity of flow accumulation along the depth, positive curvatures reduce the

capacity and negative ones increases it. The conclusions 2,3 in Page 67 are also used, describing a linear velocity profile, at least in a first order approximation.

This result includes the one obtained by Bouchut et al. (2003) for 1D model with curvatures, although the non-dimensionalization is carried on based on the characteristic flow length L instead curvature radius r. The notation is noticeably different but when the Berger and Carey (1998a) result is simplified for one dimensional geometries the demonstration is straight.

The result for the pressure is:

$$\begin{aligned} P(w) = &\frac{\rho}{2}\left(h_1(0)\hat{u}^1\right)^2\left\{\left(\frac{1}{1-k_1 d}\right)^2-\left(\frac{1}{1-k_1 w}\right)^2\right\}+ \\ &+\frac{\rho}{2}\left(h_2(0)\hat{u}^2\right)^2\left\{\left(\frac{1}{1-k_2 d}\right)^2-\left(\frac{1}{1-k_2 w}\right)^2\right\}+\rho \mathrm{g}_3\left(d-w\right). \end{aligned} \tag{2.6.2}$$

The centripetal effects are included on pressure, and, in agreement to the theoretically predicted values, proportional to the velocity square values. It should also be notice that $(h_1(0)\hat{u}^1, h_2(0)\hat{u}^2)$ are the physical components of the velocity at the surface, transformed from curvilinear units to (m/s).

Before defining the model horizontal momentum equations some considerations will be performed in order to simplify the problem conditions and to simplify the numerical methods used to solve it.

2.7 Equations System Simplification

The Equation 2.6.1 exhibits the complexity of continuity equation in curvilinear coordinates. The mass flux is affected by curvature and the model is far from the *shallow water equations* (SWE). Also the pressure term introduces new nonlinearities in momentum fluxes.

It is very interesting to propose a model similar to SWE. An important background exists in the numerical solution of SWE. There is an vast knowledge on solution strategies for SWE. The finite volume methods based on Godunov (1959) have great success in numerical modeling (LeVeque, 2002; Toro, 2001) and have become widespread methods.

To remove the differences between the obtained model and SWE, in order to develop a simpler equation model, the curvatures are considered small so the curvature radii is considered large. This simplification is not so clear, there's no evidence of small curvatures in real topographies, as Bouchut and Westdickenberg (2004) affirm, neglecting the curvatures defines a model valid only for *small slope variations*.

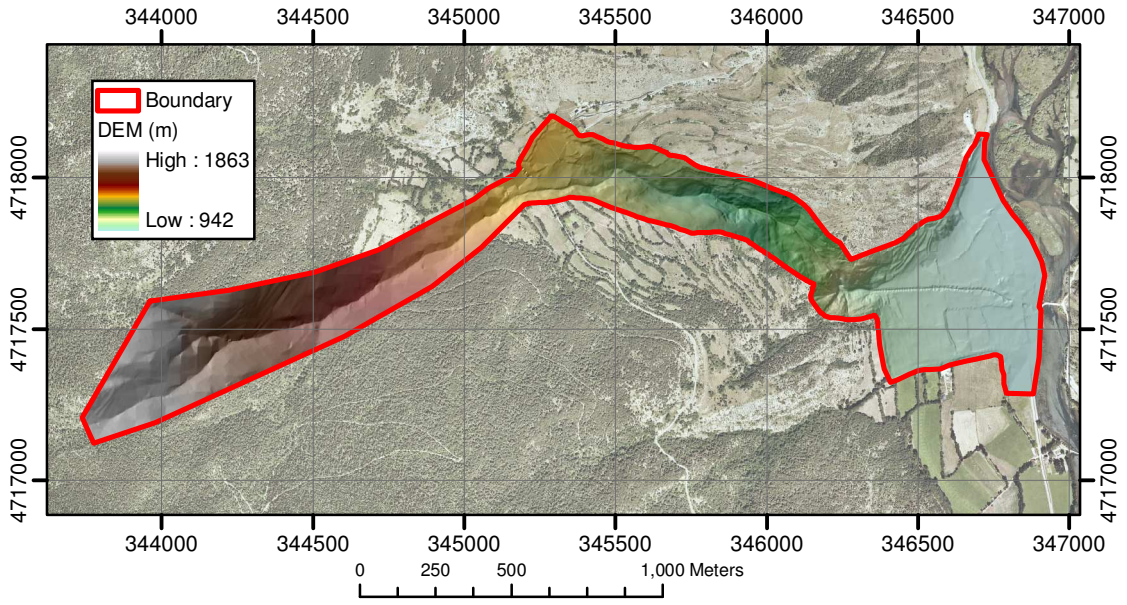

Figure 2.3: La Guingueta test basin in Northern Pirinees.

In Figure 2.3 a real debris flow event basin is shown, it's true that the characteristic length of the event L (around one kilometer) is longer than the characteristic depth H (around 1 meter), defining $H/L \simeq 0.001$, but this is not enough to guarantee the low curvatures.

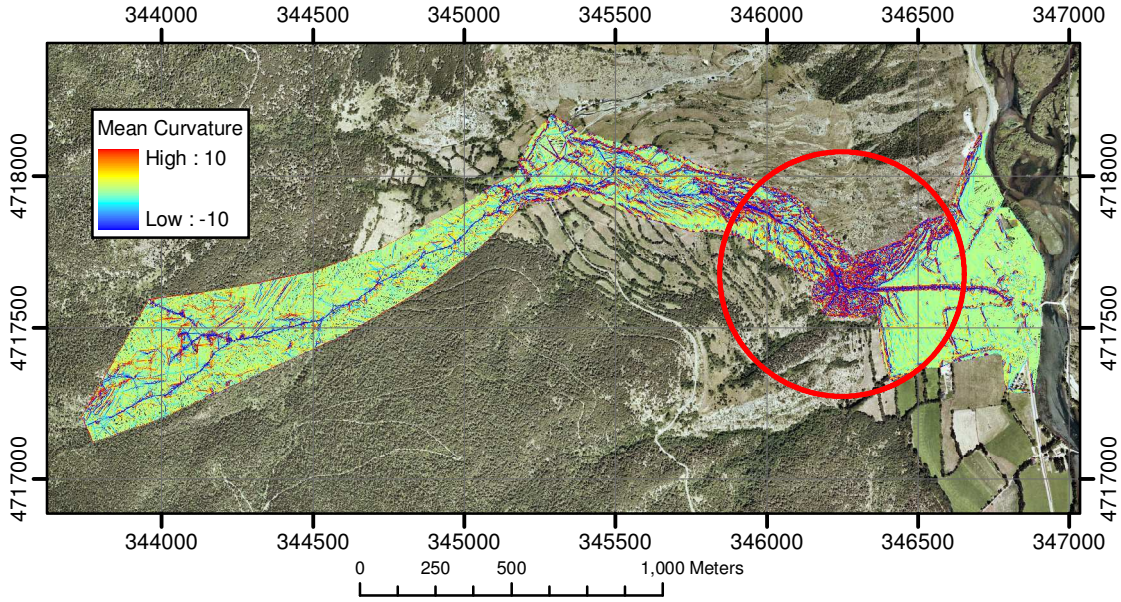

Figure 2.4: Mean curvatures in La Guingueta basin.

A simplified curvature values are calculated $(1/2\,(h_{XX} + h_{YY}))$, the results are shown in Figure 2.4. This simplified approximation computes the Hessian matrix trace. In the figure it is clear that the spatial variability of metrics in real topographies is large. It's not possible to guarantee low values for curvatures. In this case it is not possible to affirm that the extreme curvature values are real or topographic mistakes.

The red circle in Figure 2.4 shows the apex of the deposition cone, and the values in that area are high, but it should be taken into account that an artificial encroachment exists, modifying the natural values.

Neglecting the curvatures means to consider negligible principal curvatures k_1, k_2. Important consequences come for this simplification, the linear velocity profile described in conclusions 2, 3 in Page 67 turns into a constant velocity $u^1 = \hat{u}^1$, $u^2 = \hat{u}^2$, equal to bed velocity. Also all the metric scales of the 3D transformation $\hat{\mathbf{X}}$ become equal to the 2D surface transformation $\mathbf{X}$ metrics, then h_1, h_2 become constant in depth $\widehat{E} = E$, $\widehat{G} = G$, $\hat{g}_{ij} = g_{ij}$.

The effect over the pressure profile is immediate:

$$P(w) = \rho \mathrm{g}_3 \left(d - w\right). \tag{2.7.1}$$

The pressure becomes the classical hydrostatic result, neglecting the centripetal acceleration effects. The main difference with the SWE pressures is the corrected gravity, instead $\mathbf{g}$ the pressure is computed using g_3 the projected value into the $\mathbf{N}$ axis.

2.7.1 Continuity Simplification

Discarding curvatures in Equation 2.5.7 depth integration makes the continuity equation become formally equal to the SWE, but using curvilinear metrics:

$$h_1 h_2 \frac{\partial d}{\partial t} + \frac{\partial \left(h_2 h_1 \hat{u}^1 d\right)}{\partial u} + \frac{\partial \left(h_2 h_1 \hat{u}^2 d\right)}{\partial v} = 0. \tag{2.7.2}$$

Several considerations could be carried on this equation:

Proposition 2.7.1. *Discarding the curvature effects converts the definition of the equation system in the direct application of covariant derivative to the SWE.*

Proof. First lets recall the value of the metric determinant $\sqrt{|\hat{g}|} = h_1 h_2$, introducing this equivalence in Equation 2.7.2 we obtain:

$$\sqrt{|\hat{g}|} \frac{\partial d}{\partial t} + \frac{\partial \left(\sqrt{|\hat{g}|} \hat{u}^1 d\right)}{\partial u} + \frac{\partial \left(\sqrt{|\hat{g}|} \hat{u}^2 d\right)}{\partial v} = 0. \tag{2.7.3}$$

And rearranging:

$$\frac{\partial d}{\partial t} + \frac{1}{\sqrt{|\hat{g}|}} \frac{\partial \left(\sqrt{|\hat{g}|} \hat{u}^k d\right)}{\partial x^k} = 0. \tag{2.7.4}$$

Comparing this result to the Equation 2.3.9 it is clear that the obtained equation is equal to the result of applying covariant derivative to the SWE continuity equation:

$$\frac{\partial d}{\partial t} + \frac{\partial \left(U^k d\right)}{\partial X^k} = 0 \quad \rightarrow \quad \frac{\partial d}{\partial t} + \frac{1}{\sqrt{|\hat{g}|}} \frac{\partial \left(\sqrt{|\hat{g}|}\hat{u}^k d\right)}{\partial x^k} = 0. \tag{2.7.5}$$

□

It is possible to go farther, using the continuity equation form described by Equation 2.3.8 to SWE we obtain:

$$\frac{\partial d}{\partial t} + \frac{\partial \left(u^i d\right)}{\partial x^i} + \Gamma^j_{ij} \left(u^i d\right) = 0. \tag{2.7.6}$$

Now, using PCS (Proposed Coordinate System), it is possible to apply the Proposition 1.5.1 obtained in the Chapter 1 to simplify the equation:

$$\frac{\partial d}{\partial t} + \frac{\partial \left(u^i d\right)}{\partial x^i} = 0. \tag{2.7.7}$$

Being this result equal to the application of PCS to Bouchut and Westdickenberg (2004) *small slope variation* continuity equation.

The physical justification for the equivalence of Equations 2.7.7,2.7.4 is due to the fact that conservation could be defined over any projected version of topography and fluxes, and PCS defines the projection of the problem in cartesian X, Y plane.

The continuity version finally used in the model is Equation 2.7.2, a physical interpretation is now given.

The first step is to transform the equation into discrete form, substituting ∂ with Δ and arranging it:

$$\Delta d + \frac{\Delta t}{(h_1 h_2 \Delta v \Delta u)} \left(\Delta v \Delta \left(h_2 h_1 \hat{u}^1 d\right) + \Delta u \Delta \left(h_2 h_1 \hat{u}^2 d\right)\right) = 0. \tag{2.7.8}$$

Now some considerations should be applied, $(h_1 h_2 \Delta v \Delta u) = A$ is the control volume area (Figure 2.5), $h_1 \hat{u}^1 d = F^1, h_2 \hat{u}^2 d = F^2$ are the physical mass flows, and $h_1 \Delta u = L^1, h_2 \Delta v = L^2$ are the physical length of the control volume (Figure 2.5), so substituting in the equation, the classical conservation law is obtained:

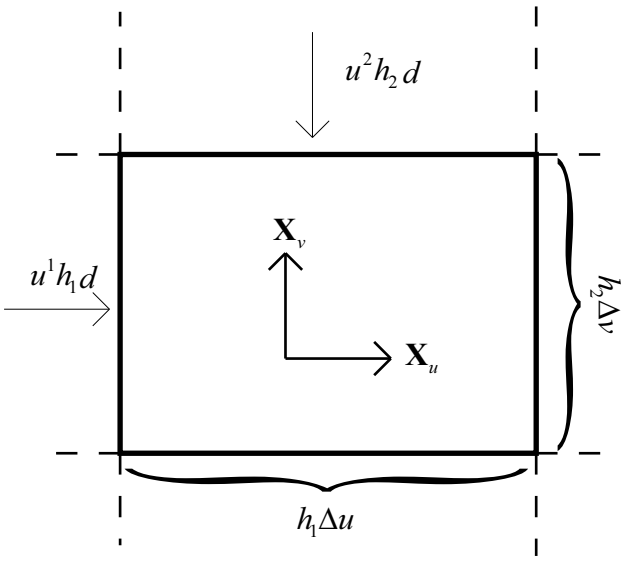

Figure 2.5: Control volume metrics and flows.

$$\Delta d = -\frac{\Delta t}{A}\left(\Delta\left(L^1 F^1\right) + \Delta\left(L^2 F^2\right)\right). \tag{2.7.9}$$

Taking into account the metrics simplification, the continuity equation implemented in the model is:

$$\frac{\partial d}{\partial t} + \frac{1}{\sqrt{|g|}}\frac{\partial\left(\sqrt{|g|}u^k d\right)}{\partial x^k} = 0. \tag{2.7.10}$$

2.7.2 Momentum Simplification

As has been concluded in the previous section, discarding curvatures transforms the velocity profile in a constant, equal to the bottom velocity $\hat{u}^1, \hat{u}^2$, also the pressure becomes hydrostatic, with this considerations it is simple to obtain the u coordinate momentum equation from Equation 2.5.8, recovering the dimensional form:

$$h_1\frac{\partial \hat{u}^1}{\partial t} + \hat{u}^1\frac{\partial \hat{u}^1 h_1}{\partial u} + \hat{u}^2\frac{\partial \hat{u}^1 h_1}{\partial v} - \frac{h_2\hat{u}^2\hat{u}^2}{h_1}\frac{\partial h_2}{\partial u} + \hat{u}^1\hat{u}^2\frac{\partial h_1}{\partial v} + \frac{1}{h_1\rho}\frac{\partial P}{\partial u} - h_1 \mathrm{g}_1 = 0. \tag{2.7.11}$$

The first step is to check the hypothesis developed in the previous section, the equality between the obtained equation and the direct application of covariant derivative to the SWE. In this case the starting point is the X momentum conservation in SWE, it should be necessary to consider that the hydrostatic pressure comes from the g_3 component of the gravity.

$$\frac{\partial dU^i}{\partial t} + \frac{\partial \left(dU^i U^j\right)}{\partial X^j} + \frac{1}{2}\frac{\partial \left(\mathrm{g}_3 d^2\right)}{\partial X^i} = -\mathrm{g}_i d. \tag{2.7.12}$$

Let's transform the momentum equation into the non-conservative version:

$$U^i \frac{\partial d}{\partial t} + d\frac{\partial U^i}{\partial t} + U^i \frac{\partial \left(dU^j\right)}{\partial X^j} + dU^j \frac{\partial U^i}{\partial X^j} + \mathrm{g}_3 d\frac{\partial d}{\partial X^i} = -\mathrm{g}_i d. \tag{2.7.13}$$

And rearranging terms:

$$U^i \left(\frac{\partial d}{\partial t} + \frac{\partial \left(dU^j\right)}{\partial X^j}\right) + d\frac{\partial U^i}{\partial t} + dU^j \frac{\partial U^i}{\partial X^j} = -d\left(\mathrm{g}_3 \frac{\partial d}{\partial X^i} + \mathrm{g}_i\right). \tag{2.7.14}$$

The first part of the equation is the continuity equation, so it's equal to zero.

$$d\left(\frac{\partial U^i}{\partial t} + U^j \frac{\partial U^i}{\partial X^j}\right) = -d\left(\mathrm{g}_3 \frac{\partial d}{\partial X^i} + \mathrm{g}_i\right). \tag{2.7.15}$$

And simplifying:

$$\frac{\partial U^i}{\partial t} + U^j \frac{\partial U^i}{\partial X^j} = -\mathrm{g}_3 \frac{\partial d}{\partial X^i} - \mathrm{g}_i. \tag{2.7.16}$$

The next step is to express it in curvilinear coordinates using the covariant derivative:

$$\frac{\partial u^i}{\partial t} + u^j u^i_{,j} + \mathrm{g}_3 d_{,i} = -\mathrm{g}_i. \tag{2.7.17}$$

The gravity components $(\mathrm{g}_1, \mathrm{g}_2, \mathrm{g}_3)$ now are defined in curvilinear basis, recall that the third component g_3 is equal in both basis. Now the values for the covariant derivative (Equation 2.3.1) are substituted. Again the process involves a large

quantity of terms due to the Christoffel symbols, at the end the simplified expression obtained is:

$$\frac{\partial u^i}{\partial t} + \frac{u^j}{h_i}\frac{\partial u^i h_i}{\partial x^j} = \frac{h_j u^j u^i}{h_i^2}\frac{\partial h_j}{\partial x^j} - \frac{1}{h_i^2}\mathrm{g}_3\frac{\partial d}{\partial x_i} + \mathrm{g}_j. \tag{2.7.18}$$

Considering the hydrostatic pressure Equation 2.7.1 and the constant velocity profile ($\hat{u}^i = u^i$) the result corresponds to Equation 2.7.11 when $i = 1$. So again the momentum equation is the direct transformation of SWE using covariant derivatives for surface curvilinear coordinates.

The final version of momentum equation adopted in the model is the conservative form, as has been shown, to apply the curvilinear coordinates it's only necessary to use the covariant derivative in the SWE. In the case of momentum the equation, it could be expressed as tensor function (Equation 2.3.16), and then the tensor identity Equation 2.3.17 could be used. First the SWE tensor should be defined:

$$T^{ij} = dU^i U^j + \frac{\mathrm{g}_3}{2} d^2 g^{ij}. \tag{2.7.19}$$

And introducing the identity into the the momentum equation:

$$\frac{\partial\left(du_i\right)}{\partial t} + \frac{1}{\sqrt{|g|}}\frac{\partial}{\partial x^j}\left(\sqrt{|g|}T^{ji}\right) + \Gamma^i_{kj}T^{jk} = d\mathrm{g}_i. \tag{2.7.20}$$

Now the last simplification could be applied, as has been concluded in the previous chapter, when the PCS is used, discarding the curvature imply discarding also the Christoffel symbols, so if the coordinate system selected is PCS the momentum equation could be written as:

$$\frac{\partial\left(du_i\right)}{\partial t} + \frac{1}{\sqrt{|g|}}\frac{\partial}{\partial x^j}\left(\sqrt{|g|}T^{ji}\right) = d\mathrm{g}_i. \tag{2.7.21}$$

2.7.3 Model Equations

The equation system defined to use in agreement with PCS is:

$$\begin{cases} \dfrac{\partial d}{\partial t} + \dfrac{1}{\sqrt{|g|}} \dfrac{\partial \left(\sqrt{|g|} u^k d \right)}{\partial x^k} = 0, \\ \dfrac{\partial \left(du_i \right)}{\partial t} + \dfrac{1}{\sqrt{|g|}} \dfrac{\partial}{\partial x^j} \left(\sqrt{|g|} T^{ji} \right) = d\mathrm{g}_i, \end{cases} \tag{2.7.22}$$
$$T^{ij} = du^i u^j + \frac{\mathrm{g}_3}{2} d^2 g^{ij}.$$

For a inclined ramp all the terrain surface second derivatives are zero ($h_{ij} = 0$ $\forall i, j \in \{X, Y\}$) (case developed in Proposition 1.5.1), the metric tensor g becomes constant and the equation system could be simplified:

$$\begin{cases} \dfrac{\partial d}{\partial t} + \dfrac{\partial \left(u^k d \right)}{\partial x^k} = 0, \\ \dfrac{\partial \left(du_i \right)}{\partial t} + \dfrac{\partial}{\partial x^j} \left(T^{ji} \right) = d\mathrm{g}_i, \end{cases} \tag{2.7.23}$$
$$T^{ij} = du^i u^j + \frac{\mathrm{g}_3}{2} d^2 g^{ij}.$$

But for the small curvatures, or slowly varying slopes (case developed in Proposition 1.5.2) is not possible to consider $\sqrt{|g|}$ as a constant. The proposition just says: $h_{ij} \ll h_k \;\; \forall i, j, k \in \{X, Y\}$. The matrix 1.4.5 collects the components of the metric tensor, and, as it shown, to be constant it requires $h_{ij} = 0 \, \forall i, i \in \{X, Y\}$. So the small curvatures does not fit the inclined ramp condition.

The physical sense of the proposed system is simple (Equation 2.7.22), now the coordinate system is in PCS, this coordinate system is not orthogonal, so the physical explanation of the equations should be adapted to a non orthogonal coordinate system. Let's begin writing the discrete form of the continuity equation:

$$\frac{\Delta d}{\Delta t} + \frac{1}{\sqrt{|g|}} \frac{\Delta \left(\sqrt{g} u^X d \right)}{\Delta X} + \frac{1}{\sqrt{|g|}} \frac{\Delta \left(\sqrt{g} u^Y d \right)}{\Delta Y} = 0. \tag{2.7.24}$$

In PCS the curvilinear coordinates are (X, Y), the scaling metrics are $\sqrt{E}$ for X and $\sqrt{G}$ for Y. The area element is $\sqrt{|g|} = \sqrt{EG - F^2}$, F is the dot product of $\mathbf{X}_X, \mathbf{X}_Y$, so $F = \sqrt{EG}\cos(\alpha)$. Then $\sqrt{|g|} = \sqrt{EG}\sin(\alpha)$, clearly a non orthogonal control volume area.

Now let's multiply all the equation by the area of the discrete volume in PCS coordinates $\Delta X \Delta Y \sqrt{|g|}$, and write the result in a conservative fashion:

$$\frac{\Delta\left(\sqrt{|g|}\Delta Y \Delta X d\right)}{\Delta t} + \left[\Delta Y \sqrt{|g|} u^X d\right]_{X=min}^{X=max} + \left[\Delta X \sqrt{|g|} u^Y d\right]_{Y=min}^{Y=max} = 0. \quad (2.7.25)$$

The first term in the equation is the time evolution of depth inside the control volume. In the Figure 2.6, the control volume measurements are in the X direction $L^X = \Delta X \sqrt{E}$, and in the Y direction $L^Y = \Delta Y \sqrt{G}$. It's clear that the X components of fluxes in continuity equation (Equation 2.7.25) are:

$$\Delta Y \sqrt{|g|} u^X d = \left(\Delta Y \sqrt{G}\right) \sin(\alpha) \left(\sqrt{E} u^X\right) d.$$

And substituting:

$$\Delta Y \sqrt{|g|} u^X d = L^Y \sin(\alpha) \left(\sqrt{E} u^X\right) d.$$

Recall that $\sqrt{E} u^X$ is the physical magnitude of X velocity component. So the X component of the continuity equation is the normal flux of d through the control volume boundary L^Y.

In the same manner the Y component of the continuity equation expresses the normal flux of depth d through the ΔX faces of the control volume. As it's clear the continuity equation in Equation 2.7.22 expresses the mass conservation in a control volume defined by a non-orthogonal coordinates and with fluxes expressed in non physical units. The same process could be carried on in the momentum equations.

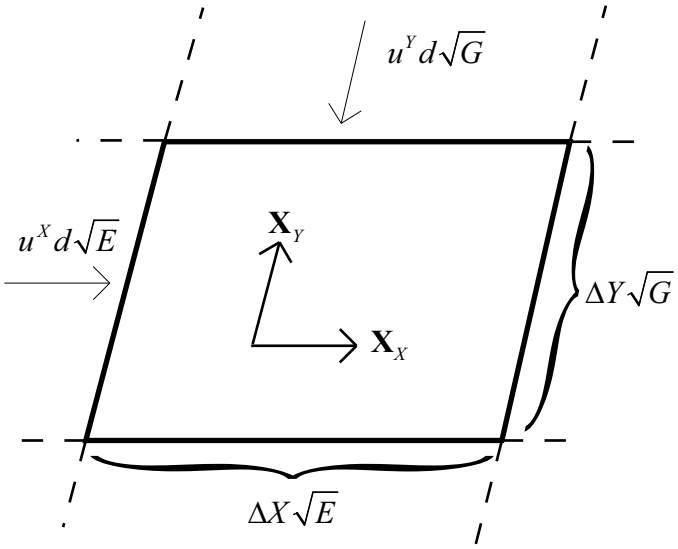

Figure 2.6: Control volume metrics and flows for PCS (non orthogonal).

2.8 Rheologies

In the previous section the equations system has been established supposing the flow to be ideal. This means discarding the effects of constitutive law of the material. The friction is presented in two fashions:

1. First it appears as an internal friction. From the physical point of view, these internal stresses don't reduce the global momentum of the fluid because it's transferred from point to point, although locally some points loss velocity, another increase it. From the kinetic energy (K.E.) point of view it reduces the energy, because K.E. depends on the velocity square, so, although the momentum is conserved, the new velocity distribution always tend to be more homogeneous (if the velocity gradient is zero no internal stresses appear), and more homogenous means decrease K.E.

2. The second effect of the constitutive law is the basal friction. This comes from the interaction between fluid and the boundaries and it reduces the total momentum of the flow and its energy.

In all the forms it plays an important role on the debris flow process, the justification to discard it along the equations system definition is to avoid its complexity during the definition process.

2.8.1 The Stress Tensor

The rheology is a macroscopic abstraction of the real heterogenous flow physics. The rheology, finally, appears in the conservation equations to replace the stress tensor, to get the depth integrated models, this stress tensor should be also integrated. The integration includes, as usual, the use of dimensional analysis. Through this analysis some terms are discarded.

The first step is to define the stress tensor $\boldsymbol{\tau}$ in cartesian coordinates, considering it as symmetric:

$$\boldsymbol{\tau} = \tau_{ij} = \begin{pmatrix} \sigma_{11} & \tau_{12} & \tau_{13} \\ \tau_{12} & \sigma_{22} & \tau_{23} \\ \tau_{13} & \tau_{23} & \sigma_{33} \end{pmatrix}, \tag{2.8.1}$$

this stress tensor appears in the momentum (Equation 2.3.10) as the term:

$$\nabla \cdot \boldsymbol{\tau} = \frac{\partial \tau_{ij}}{\partial X_i}.$$

The first row of the tensor acts in the X momentum equation, the second row of the tensor acts in the Y momentum equation, and, finally the terms present in the third row are included in the Z momentum conservation equation. The stresses tensor ($\boldsymbol{\tau}$) could be divided into spherical part and deviational one:

$$\tau_{ij} = P \begin{pmatrix} 1 & 0 & 0 \\ 0 & 1 & 0 \\ 0 & 0 & 1 \end{pmatrix} + \begin{pmatrix} \sigma_{11} - P & \tau_{12} & \tau_{13} \\ \tau_{12} & \sigma_{22} - P & \tau_{23} \\ \tau_{13} & \tau_{23} & \sigma_{33} - P \end{pmatrix}, \tag{2.8.2}$$

where P is the thermodynamic pressure used previously in the equations system definition.

2.8.2 Tensor Simplification

The components of the stress tensor are not yet defined, but the simplification could be carried out because it depends on characteristic dimensions of the flow (recall L and H). The first step is to apply Equation 2.3.3 to the stresses tensor, to obtain the curvilinear form:

$$\tau^{ji}_{,j} = \frac{\partial \tau^{ji}}{\partial x^j} + \Gamma^j_{kj}\tau^{ki} + \Gamma^i_{kj}\tau^{jk}. \tag{2.8.3}$$

The curvilinear transformation of the stress tensor (Equation 2.8.3) has three terms, the first is the stress tensor divergence in curvilinear coordinates. Following the previous work carried out to define the equations system, the principal directions (u, v, w) will be used as coordinate system, in principal directions coordinates the tensor becomes:

$$\boldsymbol{\tau} = \tau_{ij} = \begin{pmatrix} \sigma_{uu} & \tau_{uv} & \tau_{uw} \\ \tau_{uv} & \sigma_{vv} & \tau_{vw} \\ \tau_{uw} & \tau_{vw} & \sigma_{ww} \end{pmatrix} \tag{2.8.4}$$

There are two terms of the curvilinear transformation that include the Christoffel symbols. One strategy to deal with this terms is to discard it in PCS. As was stated in Chapter 1, when curvatures are discarded, Christoffel symbols could also be discarded. The second option is to use dimensional analysis to discard them (Pudasaini et al., 2005).

As has been stated previously, the stress tensor appears in the momentum (Equation 2.3.10) inside a divergence term, so its effects depend on the derivatives of the tensor components, when the gradients of these components are low they can be discarded. The characteristic scales of the flow (recall L, H) are used to simplify the

stress tensor (Equation 2.8.4), for example in Iverson et al. (2004) and Pudasaini et al. (2005), the gradients of the components τ_{uw}, τ_{vw} are considered negligible in the w direction momentum equation, so just one term of the tensor survive (σ_{ww}) in this momentum equation.

This last hypothesis allows the depth integration in w direction, obtaining at the end the hydrostatic pressure P as σ_{ww} component. So the result for the w integration is independent on the rheology selected, it depends on the shallow characteristics of the flow. In Pudasaini et al. (2005) using the shallow characteristics of the flow, τ_{uv} is also considered small for the u, v directions, so is discarded. Hypothesis relating longitudinal and transversal velocities, indeed some kind of one dimensional restriction, will ensure this last hypothesis. In Iverson et al. (2004) such hypothesis is not used and a coupled stress model is used including the transversal stresses (τ_{uv}), as a consequence, in that reference a sophisticated model coming from the Finite Elements Method is used to solve the constitutive equation (Zienkiewicz and Taylor, 2000).

An extra hypothesis relating normal stresses is necessary before integration:

$$\sigma_{uu} = \sigma_{ww} = P, \qquad \sigma_{vv} = \sigma_{ww} = P.$$

This last hypothesis about normal stresses is not universally valid, it depends in the rheologic model adopted, for example the hypothesis is valid for inviscid fluid or for newtonian one, but not for Coulomb rheology:

So, when the simplification hypothesis are used, the stresses tensor used is equivalent to:

$$\tau_{ij} = P \begin{pmatrix} 1 & 0 & 0 \\ 0 & 1 & 0 \\ 0 & 0 & 1 \end{pmatrix} + \begin{pmatrix} 0 & 0 & \tau_{uw} \\ 0 & 0 & \tau_{vw} \\ 0 & 0 & 0 \end{pmatrix}. \tag{2.8.5}$$

The resulting matrix is not symmetric because the simplification hypothesis are not symmetric in order to take advantage of the flow shallowness.

The Coulomb rheology has had a great success in depth integrated debris flow modeling (Savage and Hutter, 1989; Iverson, 1997; Pudasaini et al., 2005; Pitman et al., 2003; Pudasaini and Hutter, 2007), because it has interesting features, for example its simplicity allows to carry on all the integration process on it e.g.: see Pudasaini et al. (2005). The main difference over the normal stresses hypothesis when Coulomb rheology is used is:

$$\sigma_{uu} = k_u \sigma_{ww} = k_u P, \qquad \sigma_{vv} = k_v \sigma_{ww} = k_v P,$$

where k_u, k_v are the active/passive pressure coefficients (Savage and Hutter, 1989).

2.8.3 Tensor Depth Integration

Before integration, extra hypothesis is necessary, the free surface stresses are considered zero, no wind effect. This allows to apply again the Leibnitz rule (Vreugdenhil, 1990; Iverson et al., 2004; Pudasaini et al., 2005) and finally obtain some extra terms to add to the momentum equations defined in the model (Section 2.7.3):

$$\begin{cases} \dfrac{\partial d}{\partial t} + \dfrac{1}{\sqrt{|g|}} \dfrac{\partial \left(\sqrt{|g|} u^k d \right)}{\partial x^k} = 0, \\ \dfrac{\partial \left(d u_i \right)}{\partial t} + \dfrac{1}{\sqrt{|g|}} \dfrac{\partial}{\partial x^j} \left(\sqrt{|g|} T^{ji} \right) = d \mathrm{g}_i - \dfrac{1}{\rho} \tau_{bi}, \\ T^{ij} = d u^i u^j + \dfrac{\mathrm{g}_3}{2} d^2 g^{ij}. \end{cases} \tag{2.8.6}$$

The term τ_{bi} is the result of the depth integration of τ_{uw}, τ_{vw} in u, v momentum equations and represents the bed friction (as the velocity, when is expressed in curvilinear coordinates system, the units are not physical ones). As has been defined, pressure P is included in stress tensor (σ_{ii}), so coming from the σ_{uu}, σ_{vv} the pressure terms are found in tensor term T^{ij} as ($\frac{\mathrm{g}_3}{2} d^2 g^{ij}$). The density ρ appearing in the system, if not in physical units, should also consider the metrics of the coordinate

system. Using the active/pasive coefficients the results obtained for the integrated pressure term would be:

$$T^{ij} = du^i u^j + k_i \frac{g_3}{2} d^2 g^{ij}.$$

Other nonlinear approaches to the rheology are non depth integrable problems, useful for complete 3D models but far from the goal of the model presented here. An example of this could be find in the bilinear rheology (Locat, 1997), to be applied in a depth integrated models this rheology needs numerical approximation (Imran et al., 2001).

In other cases the rheology is depth integrable but ends up in an implicit equation without explicit computation, this means an iterative solver to obtain the bed shear stresses values. An example of this situation if found in Bingham (1922), several simplified approaches has been carried out to obtain explicit approximations (Fread, 1988; Pastor et al., 2004).

The approach followed here adds the rheology as a friction law only considering the basal shear stresses, similar to Bouchut and Westdickenberg (2004),

2.8.4 Bed Shear Stresses Definition

Two terms (τ_{bi}) remain to be fix. To define these terms some theoretical considerations will be exposed. For the description several hypothesis will be used.

1. The flow is considered as shallow, so vertical velocities and accelerations are negligible.
2. The velocity will be considered parallel along the depth profile.
3. Only the velocity profile gradients will be taken into account.
4. The computed friction stresses are considered to be in opposition to movement.

This last hypothesis is in disagreement with the hypothesis used in the development of the equations system. During the depth integration of the momentum equation, when the curvature is neglected, the velocity profile obtained is constant and equal to the bottom components $(\hat{u}^1, \hat{u}^1)$. To rectify this point, in the depth integration process is necessary to substitute the bottom velocities $(\hat{u}^i)$ with the depth averaged velocities $(\bar{u}^i)$.

In this section some notation will be introduced, the velocity modulus will be $V = \sqrt{u^i u^j g_{ij}}$, the profile mean velocity velocity will be $\bar{V} = \frac{1}{d}\int_0^d V dw$. Recall that the surface normal coordinate w is arch length, so $g_{ww} = 1$. The stresses τ_{uw}, τ_{vw} module is represented by τ, and should be a function of u, v, w. After the depth integration process, the bed shear stress τ_b will depend just on u, v.

Bingham

This rheology (Bingham, 1922) is useful for mudflows with an important presence of fine fractions. This rheology has a yield stress τ_0, under witch there's no movement. Once this threshold is exceeded a laminar region is found in the velocity profile bottom and a solid body movement in the upper part of the profile.

$$\tau = \tau_0 + \mu_{\mathrm{m}} \left(\frac{\partial V}{\partial w} \right), \tag{2.8.7}$$

where μ_{m} is the Bingham viscosity.

Herschel-Bulkley

The Herschel-Bulkley rheology (Herschel and Bulkley, 1926) as used by OBrien et al. (1993) is similar to the Bingham one, but it uses an exponent:

$$\tau = \tau_0 + k \left(\frac{\partial V}{\partial w} \right)^n, \tag{2.8.8}$$

The value of the index of fluid n exponent is located around 0.33 (Coussot and Piau, 1995; Coussot et al., 1998), k is defined as consistency parameter, which is different from the usual viscosity. From the consistency is possible to define some kind of Herschel-Bulkley viscosity:

$$\mu_{HB} = nk \left(\frac{\partial V}{\partial w} \right)^{n-1}. \tag{2.8.9}$$

This model is useful for clays modeling.

Bagnold

The rheology proposed by Bagnold (1954) is the first approach for the *dispersive pressure*. It is considered as a turbulent rheology, this means that is useful for high Reynolds numbers.

$$\tau = C_{bd}\rho \left[(0.615/C_v)^{(1/3)} - 1 \right]^{-2} d_{50}^2 \left(\frac{\partial V}{\partial w} \right)^2, \tag{2.8.10}$$

where d_{50} is the characteristic sediment diameter, C_{bd} is a constant an C_v is the packed volume.

Coulomb

The Coulomb rheology is characteristic of solid materials (Zienkiewicz and Taylor, 2000), in most of the geomechanics computations these stresses are used. Also in landslides modeling this is a classical approach. It has only one parameter, the internal friction angle ϕ, the shear stresses are computed as a bed normal stress, times $\tan\phi$. The bed normal stress σ_{ww} is hydrostatic, so, in the bed $\sigma_{ww} = \rho g_3 d$, finally the bed shear stress is:

$$\tau_b = \rho g_3 d \tan\phi. \tag{2.8.11}$$

In an improved approach the normal stresses should be corrected with the pressure pore, but the model presented here is considered as monophasic, for example in Iverson and Denlinger (2001) or Pudasaini et al. (2005). The main limitation of Coulomb rheology is to be independent of velocity, so for slope higher that ϕ the flow always accelerates.

Voellmy

Strictly speaking Voellmy approach is not a rheology, its a friction formula, it does not come from the depth integration of a constitutive law, it has an empirical approach. This rheology was introduced by Voellmy (1955), for snow avalanches, it is a combination of Coulomb and turbulent rheologies, so it has two terms:

$$\tau_b = \rho \left(g_3 d \tan(\phi) + g \left(\bar{V}/C \right)^2 \right), \tag{2.8.12}$$

where C is equivalent to Chezy friction factor.

Manning

Manning is a classical friction equation, It originally comes from hydraulics and has something to do with the logarithmic turbulent profile. So, in some sense, it is related to the mixing length theory.

$$\tau_b = \frac{\rho g \bar{V}^2 n^2}{d^{1/3}}, \tag{2.8.13}$$

where n is the Manning friction coefficient.

2.8.5 Stresses depth integration

Some of the rheologic models described in the previous section come directly from friction laws, so the bed shear stresses τ_b could be directly computed, in other cases

the rheology should be integrated to compute bed shear as a function of depth d and mean velocity $\bar{V}$.

Bingham

The integration of Bingham rheology depth integration results in (Chen, 1983):

$$\bar{V} = \frac{\tau_0 d}{3\mu_m}\left(1 - 1.5\frac{\tau_b}{\tau_0} + 0.5\left[\frac{\tau_b}{\tau_0}\right]^3\right). \tag{2.8.14}$$

In this case, is not possible to obtain an explicit form for the basal shear stress, so an approximation should be used. We consider the Jin and Fread (1997) simplification:

$$\tau_b = \tau_0\left[1 + \left(\frac{3\bar{V}}{(0.74 + 0.656)\,(\tau_0/\mu_m)\,d}\right)^{\frac{1}{0.15}}\right]. \tag{2.8.15}$$

The error in this approach is less than 5%, a better fitting is obtained by Pastor et al. (2004), with an error less than 3%:

$$\frac{3}{2}\left(\frac{\tau_0}{\tau_b}\right)^2 - \left(\frac{57}{16} + \frac{6\bar{V}\mu_m}{\tau_0 d}\right)\left(\frac{\tau_0}{\tau_b}\right) + \frac{65}{32} = 0. \tag{2.8.16}$$

Being this last equation a second order polynomial with straight solution. This last approach is used in the present model.

Herschel-Bulkley

For this rheology the same problem exist, the approximation defined by Jin and Fread (1997) is used:

$$\tau_b = \tau_0\left[1 + \left(\frac{(1/n+1)\,(1/n+2)\,\bar{V}}{(0.74 + 0.656/n)\,(\tau_0/k)^{1/n}\,d}\right)^{\frac{1}{1/n+0.15}}\right]. \tag{2.8.17}$$

2.8.6 Rheology Selection

As has been shown a lot of different possibilities for friction law exist. To choose between different options it is necessary to analyze the event. Some non-dimensional parameters had been defined to quantify the influence of the different rheology terms. Three different cases are explained here, the Bagnold number, the Savage number and the friction number. This parameters are different combination of the three possible forces: viscous (Bingham, Herschel-Bulkley), granular (Voellmy) and frictional (Coulomb).

In Table 2.2 the equations for the different non-dimensional numbers are shown, C_s is the solids concentration in the mixture, in the saturated case it is equal to 1 minus the porosity. These formulas link an estimation of the acting forces in the flow, normally debris flow are considered as heterogeneous mixing of water and sediments, the viscous rheology of the water or mud is introduced using the viscosity μ, the frictional character of the solid to solid contact is introduced using the internal friction angle ϕ and finally the granular collisions are estimated using the Bagnold dispersive pressure.

The limit values indicate the threshold beyond which the influence of the numerator force is remarkably dominant, below these values the behavior should be considered dominated by the denominator force.

Number	Equation	Forces Ratio	Limit Value
Bagnold	$N_{BAG} = C_s \rho d_{50}^2 \left(\frac{\bar{V}}{d}\right) \Big/ (1 - C_s)\mu$	Granular - Viscous	100
Savage	$N_S = \rho d_{50}^2 \left(\frac{\bar{V}}{d}\right)^2 \Big/ \rho g_3 d \tan\phi$	Granular - Frictional	0.1
Friction	$N_f = C_s \rho g_3 d \tan\phi \Big/ (1 - C_s) \left(\frac{\bar{V}}{d}\right) \mu$	Frictional - Viscous	2000

Table 2.2: Non-dimensional numbers used to classify the rheology.

Evaluating these parameters it is possible to consider which is dominant force acting in the flow, and choose the most suitable friction law. There is some intuitive

consideration that should be taken into account, the differences that can limit the use of the frictional equations (Voellmy ...) or viscous ones (Bingham ...) are their behavior (Figure 2.7).

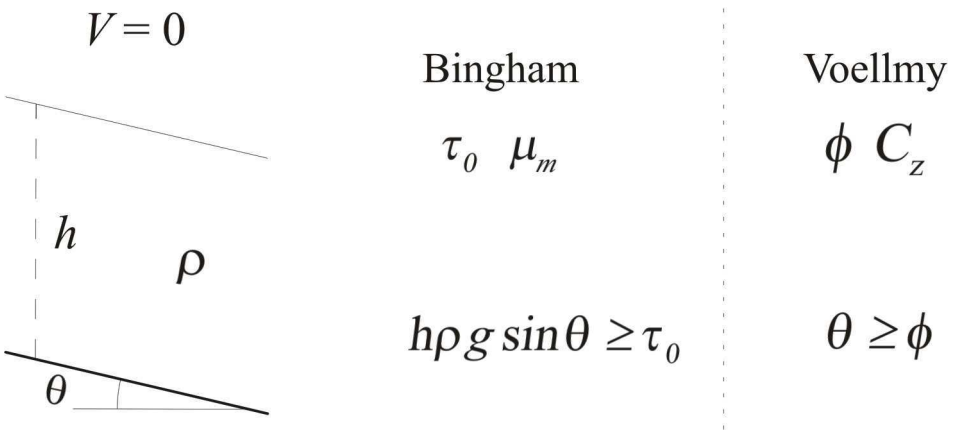

Figure 2.7: Stability criteria for different rheologies.

While the frictional Voellmy model needs a slope to start the motion of the material with independence of the flow height, the Bingham and Herschel-Bulkley model only needs a flow height to start moving; even if the material is in a horizontal plane. This difference is very important, when a debris flow is modeled, and may explain why Bingham rheology did often not fit very well during backanalysis of real events.

Chapter 3

Numerical Methods

In this chapter the numerical methods will be described. The standard *Finite Volume Method* (FVM) is used to numerically solve the equations system defined in the previous chapter. The FVM used here is able to deal with curvilinear coordinates.

An specific version of FVM in curvilinear coordinates could be found in Rossmanith et al. (2004); Rossmanith (2006), this general approach will be followed.

3.1 Introduction

The equations system adopted in the previous chapter (Equations 2.8.6), expressed in PCS is:

$$\begin{cases} \dfrac{\partial h}{\partial t} + \dfrac{1}{\sqrt{|g|}} \dfrac{\partial \left(\sqrt{|g|} u^k h \right)}{\partial x^k} = 0, \\ \dfrac{\partial \left(h u_i \right)}{\partial t} + \dfrac{1}{\sqrt{|g|}} \dfrac{\partial}{\partial x^j} \left(\sqrt{|g|} T^{ji} \right) = h \mathrm{g}_i - \dfrac{1}{\rho} \tau_{bi} \end{cases}, \tag{3.1.1}$$
$$T^{ij} = h u^i u^j + \frac{\mathrm{g}_3}{2} h^2 g^{ij}.$$

Important notation change has been introduced to regularize the nomenclature (LeVeque, 2002; Toro, 2001), in the previous chapter the depth was defined using d, from now to the end the depth will expressed using h. The velocity components

in PCS are $\mathbf{u} = (u, v)$ in (X, Y) coordinates. Recall that these velocities are not in physical coordinates. Also, $\sqrt{|g|}$ is the metric tensor norm, whose components are g_{ij} and g_1, g_2, g_3 are the components of the gravity vector $\mathbf{g}$.

For the FVM the conservative variables vector should be defined. In our case the vector is $\mathbf{q} \equiv \mathbf{q}(X, Y, t)$, and is composed by $\mathbf{q} = (h, hu, hv)$. So the classical conservative variables depth and unit discharge, are now expressed in curvilinear coordinates. The unit discharges hu, hv are presented as the product of the non physical variables h, u, v. This means that the units are not metric, except in the normal to surface coordinate $\mathbf{N}$, so the depth is in physical units.

Developing the equations, the system in PCS becomes:

1. Continuity:

$$\frac{\partial h}{\partial t} + \frac{1}{\sqrt{|g|}}\left[\frac{\partial\left(\sqrt{g}hu\right)}{\partial X} + \frac{\partial\left(\sqrt{g}hv\right)}{\partial Y}\right] = 0 \tag{3.1.2}$$

2. X Momentum:

$$\begin{aligned}&\frac{\partial(hu)}{\partial t} + \frac{1}{\sqrt{|g|}}\left[\frac{\partial}{\partial X}\left(\sqrt{|g|}\left(hu^2 + \frac{g_3}{2}h^2 g^{11}\right)\right) + \frac{\partial}{\partial Y}\left(\sqrt{|g|}\left(huv + \frac{g_3}{2}h^2 g^{12}\right)\right)\right] \\ &= hg_1 - \frac{1}{\rho}\tau_{bX}\end{aligned} \tag{3.1.3}$$

3. Y Momentum:

$$\begin{aligned}&\frac{\partial(hv)}{\partial t} + \frac{1}{\sqrt{|g|}}\left[\frac{\partial}{\partial X}\left(\sqrt{|g|}\left(hvu + \frac{g_3}{2}h^2 g^{21}\right)\right) + \frac{\partial}{\partial Y}\left(\sqrt{|g|}\left(hv^2 + \frac{g_3}{2}h^2 g^{22}\right)\right)\right] \\ &= hg_2 - \frac{1}{\rho}\tau_{bY}\end{aligned} \tag{3.1.4}$$

3.2 Finite Volume Method

The FVM is a classical method to solve fluid problems, its strength comes from the fact that it is based on the conservative form of equations. The classical *control volume* uses the fixed grid to solve the equation, and the fluxes are the physical fluxes.

Inside the FVM family, there are different approaches. However in the SWE numerical methods, in the last years, the Godunov (1959) approach has achieved a great success. This method solves a Riemann differential problem on control volume faces (LeVeque, 2002; Toro, 2001).

3.2.1 Curvilinear Form of Conservation Equations

The starting point is the typical conservation equation used in fluids expressed in integral form:

$$\frac{\partial}{\partial t}\int_{\mathcal{V}} \mathbf{q}\,(X,Y,t)\,\mathrm{d}\mathcal{V} + \int_{\mathrm{d}\mathcal{V}} \mathbf{f}\,(\mathbf{q})\cdot \mathrm{d}\mathcal{S} = 0, \tag{3.2.1}$$

where $\mathcal{V}$ is the control volume, $\mathrm{d}\mathcal{V}$ is the boundary of the control volume, so it is a surface and $\mathrm{d}\mathcal{S}$ is a differential of this boundary surface. The flux function is represented by $\mathbf{f} \equiv \mathbf{f}\,(\mathbf{q})$ and it is a tensor f^{ij}. In this equation the source terms $\mathbf{s}$ are not considered. Applying the divergence theorem, the differential form of the equation is obtained:

$$\frac{\partial}{\partial t}\mathbf{q} + \nabla\cdot\mathbf{f}\,(\mathbf{q}) = 0. \tag{3.2.2}$$

The flux tensor is divided in its curvilinear components $\mathbf{f} = (\mathbf{f}_X, \mathbf{f}_Y)$, and then the conservation equation becomes (Equation 2.3.17):

$$\frac{\partial}{\partial t}\mathbf{q} + \frac{1}{\sqrt{|g|}}\frac{\partial}{\partial X}\mathbf{f}_X\,(X,Y,\mathbf{q}) + \frac{1}{\sqrt{|g|}}\frac{\partial}{\partial Y}\mathbf{f}_Y\,(X,Y,\mathbf{q}) = \boldsymbol{\psi}\,(X,Y,\mathbf{q})\,, \tag{3.2.3}$$

$\boldsymbol{\psi}$ being the source terms due to metrics (the physic source terms are not being considered). In this case the Christoffel symbols, as has been explained in previous chapters, could be discarded in PCS. Comparing this equation to the model equations system (Equation 3.1.1) it is possible to define the fluxes in curvilinear coordinates, including the metrics into the fluxes:

$$\mathbf{f}_X = \begin{pmatrix} \sqrt{|g|}hu \\ \sqrt{|g|}\left(hu^2 + \frac{g_3}{2}h^2 g^{11}\right) \\ \sqrt{|g|}\left(hvu + \frac{g_3}{2}h^2 g^{21}\right) \end{pmatrix}, \qquad \mathbf{f}_Y = \begin{pmatrix} \sqrt{|g|}hv \\ \sqrt{|g|}\left(huv + \frac{g_3}{2}h^2 g^{12}\right) \\ \sqrt{|g|}\left(hv^2 + \frac{g_3}{2}h^2 g^{22}\right) \end{pmatrix}. \tag{3.2.4}$$

The fact of including metrics into fluxes $\left(\sqrt{|g|}\right)$ makes flux function explicitly coordinates dependent, so a spatially varied flux is found $\mathbf{f}(\mathbf{X}, \mathbf{q})$. This fact has important consequences, there are two different approaches to deal with this situation, the *cell-centered flux functions* and the *cell-edge flux functions* (Bale and LeVeque, 2002).

On the one hand, in the *cell-centered flux functions*, the spatially dependent term $\left(\sqrt{|g|}\right)$, is considered as constant in the cell, so discontinuities are found in the cell boundaries. In the other hand, in the *cell-edge flux functions* approach, the spatial dependent term $\left(\sqrt{|g|}\right)$ is considered as constant in the interfaces, so a jump is found in the cell center.

The problem found in the first approach is that a new flux solution should be developed in the interfaces, because new discontinuous terms appear in the flux functions (Bale and LeVeque, 2002). In the second proposal, a discontinuous fluxes appear in cell center due to the $\left(\sqrt{|g|}\right)$ jump, but on the contrary the standard flux solution could be applied in the control volume interfaces.

In the presented model the second approach is used, because the metric derivatives $\frac{\partial\sqrt{|g|}}{\partial X}, \frac{\partial\sqrt{|g|}}{\partial Y}$ are dependent on the Christoffel symbols, so in the PCS are neglected and flux discontinuities in the cell center are not introduced. Recall that the source terms are not being considered, they are grouped as:

$$\mathbf{s} = \begin{pmatrix} hg_1 - \frac{1}{\rho}\tau_{bX} \\ hg_2 - \frac{1}{\rho}\tau_{bY} \end{pmatrix}. \tag{3.2.5}$$

Also the conservative form (Equation 3.2.1) could be obtained in curvilinear coordinates PCS for a control volume $\mathcal{V} = [X_{\min}, X_{\max}] \times [Y_{\min}, Y_{\max}]$:

$$\begin{aligned} \frac{\partial}{\partial t} \iint_{\mathcal{V}} \mathbf{q}\left(X, Y, t\right) \sqrt{|g|} \mathrm{dX} \mathrm{dY} \quad &+ \sum_{X_{\min}, X_{\max}} \int_{\mathrm{d}\mathcal{V}} \mathbf{f}_X\left(X, Y, \mathbf{q}\right) \cdot \mathbf{d}\mathrm{Y} \\ &+ \sum_{Y_{\min}, Y_{\max}} \int_{\mathrm{d}\mathcal{V}} \mathbf{f}_Y\left(X, Y, \mathbf{q}\right) \cdot \mathbf{d}\mathrm{X} = 0. \end{aligned} \tag{3.2.6}$$

3.2.2 Equations Discretization

First of all, the whole domain $\mathcal{V} = [X_{\min}, X_{\max}] \times [Y_{\min}, Y_{\max}]$ is discretized:

$$\begin{aligned} X_i &= X_{\min} + \left(i - \frac{1}{2}\right) \Delta X, \\ Y_j &= Y_{\min} + \left(j - \frac{1}{2}\right) \Delta Y. \end{aligned} \tag{3.2.7}$$

Also the time is discretized:

$$t^n = t_{\min} + n\Delta t. \tag{3.2.8}$$

The Godunov method works with the cell average values for the variables, and in curvilinear metrics, the value is computed using:

$$\mathbf{Q}_{ij}^n \approx \frac{1}{\sqrt{|g|}_{ij} \Delta X \Delta Y} \int_{Y_j - 1/2}^{Y_j + 1/2} \int_{X_i + 1/2}^{X_i + 1/2} \sqrt{|g|} \mathbf{q}\left(\alpha, \beta, t^n\right) \mathrm{d}\alpha \mathrm{d}\beta, \tag{3.2.9}$$

where $\sqrt{|g|}_{ij}$ is considered as the cell average value for $\sqrt{|g|}$. Also the fluxes are discretized using the time average and cell boundary averaging:

$$\begin{aligned}
\mathbf{F}^X_{i-1/2\,j} &\approx \frac{1}{\Delta t \Delta Y} \int_{t^n}^{t^{n+1}} \int_{Y_j-1/2}^{Y_j+1/2} \mathbf{f}_X \left(\mathbf{q}\left(X_{i-1/2}, \alpha, \tau\right)\right) \mathrm{d}\alpha \mathrm{d}\tau, \\
\mathbf{F}^Y_{i\,j-1/2} &\approx \frac{1}{\Delta t \Delta X} \int_{t^n}^{t^{n+1}} \int_{X_i-1/2}^{X_i+1/2} \mathbf{f}_Y \left(\mathbf{q}\left(\beta, Y_{j-1/2}, \tau\right)\right) \mathrm{d}\beta \mathrm{d}\tau.
\end{aligned} \tag{3.2.10}$$

In these equations the dependence of fluxes into coordinates is not explicitly shown. It's important to note that in these integrals the values for the metrics are evaluated in the faces, $\sqrt{|g|}_{i-1/2\,j}$, $\sqrt{|g|}_{i\,j-1/2}$, and are considered constant (*cell-edge flux functions*). The source term could be also defined in discrete form, averaging in the control volume and also in time:

$$\mathbf{S}_{ij} \approx \frac{1}{\sqrt{|g|}_{ij} \Delta t \Delta X \Delta Y} \int_{t^n}^{t^{n+1}} \int_{Y_j-1/2}^{Y_j+1/2} \int_{X_i+1/2}^{X_i+1/2} \sqrt{|g|} \mathbf{s}\left(\mathbf{q}, \alpha, \beta\right) \mathrm{d}\alpha \mathrm{d}\beta \mathrm{d}\tau. \tag{3.2.11}$$

The dependence of the source term on time is not explicit. This is through the variables $\mathbf{q}$. Comparing these results to the conservative form of the Equation 3.2.6, the natural discretization form of the equation is:

$$\begin{aligned}
\mathbf{Q}^{n+1}_{ij} = \mathbf{Q}^n_{ij} &- \frac{\Delta t}{\sqrt{|g|}_{ij} \Delta X} \left(\mathbf{F}^X_{i+1/2\,j} - \mathbf{F}^X_{i-1/2\,j}\right) \\
&- \frac{\Delta t}{\sqrt{|g|}_{ij} \Delta Y} \left(\mathbf{F}^Y_{i\,j+1/2} - \mathbf{F}^Y_{i\,j-1/2}\right) + \Delta t \mathbf{S}_{ij}.
\end{aligned} \tag{3.2.12}$$

As has been commented the metrics are different in the cell center $\sqrt{|g|}_{ij}$ and in the cell boundaries $\sqrt{|g|}_{i\pm1/2 j\pm1/2}$, so terms are not canceled. In the Godunov method the integral fluxes (Equation 3.2.10) are computed using only the cell average values (Equation 3.2.9), in the previous time step, at both sides of the control volume boundary, this means that:

$$\begin{aligned}
\mathbf{F}^X_{i-1/2\,j} &\equiv \mathbf{F}^X_{i-1/2\,j}\left(\mathbf{Q}^n_{i-1\,j}, \mathbf{Q}^n_{i\,j}\right), \\
\mathbf{F}^Y_{i\,j-1/2} &\equiv \mathbf{F}^Y_{i\,j-1/2}\left(\mathbf{Q}^n_{i\,j-1}, \mathbf{Q}^n_{i\,j}\right), \\
\mathbf{S}_{ij} &\equiv \mathbf{S}_{ij}\left(\mathbf{Q}^n_{i\,j}\right).
\end{aligned} \tag{3.2.13}$$

So the basic method is only first order in time and space. It is straight to define higher order time explicit discretizations, using methods as Runge-Kutta. Also second order in space could be achieved using *high resolution TVD methods* (Harten, 1983). Transverse fluxes could be computed to complete the second order accuracy and increase the Courant stability criterion until $C \leq 1$ (Rossmanith et al., 2004; Rossmanith, 2006; LeVeque, 2002). The complete discretization using second order corrections and source term discretization is (Rossmanith et al., 2004):

$$\begin{aligned}
\mathbf{Q}_{ij}^{n+1} &= \mathbf{Q}_{ij}^{n} \\
&\quad -\frac{\Delta t}{\sqrt{|g|}_{ij}\Delta X}\left(\mathcal{A}_X^{-}\Delta\mathbf{Q}_{i+1/2\;j}^{X}+\mathcal{A}_X^{+}\Delta\mathbf{Q}_{i-1/2\;j}^{X}\right) \\
&\quad -\frac{\Delta t}{\sqrt{|g|}_{ij}\Delta Y}\left(\mathcal{A}_Y^{-}\Delta\mathbf{Q}_{i\,j+1/2}^{Y}+\mathcal{A}_Y^{+}\Delta\mathbf{Q}_{i\,j-1/2}^{Y}\right) \\
&\quad -\frac{\Delta t}{\sqrt{|g|}_{ij}\Delta X}\left(\widetilde{\mathbf{F}}_{i+1/2\;j}^{X}-\widetilde{\mathbf{F}}_{i-1/2\;j}^{X}\right)-\frac{\Delta t}{\sqrt{|g|}_{ij}\Delta Y}\left(\widetilde{\mathbf{F}}_{i\,j+1/2}^{Y}-\widetilde{\mathbf{F}}_{i\,j-1/2}^{Y}\right) \\
&\quad -\Delta t\mathbf{S}_{ij}. \qquad (3.2.14)
\end{aligned}$$

The first line of the discretization corresponds to local derivative, the second and the third lines correspond to first order fluxes ($\mathcal{A}_X^{\pm}\Delta\mathbf{Q}_{i\pm1/2\;j}^{X}, \mathcal{A}_Y^{\pm}\Delta\mathbf{Q}_{i\,j\pm1/2}^{Y}$, Section 3.2.2), the fourth line are the spatial second order corrections ($\widetilde{\mathbf{F}}_{i\pm1/2\;j}^{X}, \widetilde{\mathbf{F}}_{i\,j\pm1/2}^{Y}$, Section 3.2.2) and finally the last line is the source term.

In the Godunov method the fluxes are computed solving the *Riemann Problem* in the interface (Godunov, 1959; Toro, 1999), these problems are defined by:

$$\begin{aligned}
&\frac{\partial}{\partial t}\mathbf{q}+\frac{\partial}{\partial X}\mathbf{f}_X\left(X,Y,\mathbf{q}\right)=0, \\
&\mathbf{q}\left(\mathbf{X},t\right)\begin{cases}\mathbf{Q}_{i-1\,j} & \text{if } X<X_{i-1/2}\\ \mathbf{Q}_{i\;j} & \text{if } X<X_{i+1/2}\end{cases}
\end{aligned} \qquad (3.2.15)$$

For the $Y_{\min}, Y_{\max}$ interfaces, and:

$$\begin{aligned} &\frac{\partial}{\partial t}\mathbf{q} + \frac{\partial}{\partial Y}\mathbf{f}_Y\left(X, Y, \mathbf{q}\right) = 0, \\ &\mathbf{q}\left(\mathbf{X}, t\right) \begin{cases} \mathbf{Q}_{i\,j-1} & \text{if } Y < Y_{j-1/2} \\ \mathbf{Q}_{i\,j} & \text{if } Y < Y_{j+1/2} \end{cases} \end{aligned} \tag{3.2.16}$$

For the $X_{\min}, X_{\max}$ interfaces. The values of the first order fluxes are obtained through the solution of these Riemann problems. The methodology to obtain these values depend strongly in the approach selected to solve the Riemann problem. In the present case, the equations system form a non-linear problem, so to achieve the exact solution of the problem, is necessary to implement a non-linear iterative solver.

This kind of solvers are computationally expensive, so the equation system should be linearized in order to reduce the time consuming. There are multiple linearized solvers for Riemann problems, for example Roe (1981), HLLC (Toro et al., 1994), Osher (Engquist and Osher, 1981), HLL (Harten et al., 1983).

Linearized Solver

In case of using a linearized solver the standard wave propagation method is used (Rossmanith et al., 2004), the Riemann problems at the boundaries are substituted by the linearized version, extracting the metrics out of the linearized flux matrix:

$$\begin{aligned} &\frac{\partial}{\partial t}\mathbf{q} + \sqrt{|g|}_{i-1/2\;j}\mathbf{A}_{i-1/2\,j}\frac{\partial}{\partial X}\left(X, Y, \mathbf{q}\right) = 0, \\ &\mathbf{q}\left(\mathbf{X}, t\right) \begin{cases} \mathbf{Q}_{i-1\,j} & \text{if } X < X_{i-1/2} \\ \mathbf{Q}_{i\,j} & \text{if } X > X_{i-1/2} \end{cases} \\ &\sqrt{|g|}_{i-1/2\;j}\mathbf{A}_{i-1/2\,j} \approx \frac{\partial \mathbf{f}_X}{\partial \mathbf{q}}\left(\mathbf{q}\left(X_{i-1/2}, Y_j, t\right)\right). \end{aligned} \tag{3.2.17}$$

Linearized matrix $\mathbf{A}$ should accomplish several conditions (Roe, 1981), the first order fluxes could be defined using:

$$\mathbf{Q}_{i\,j} - \mathbf{Q}_{i-1\,j} = \sum_{p=1}^{M} \alpha^p_{i-1/2\,j}\mathbf{r}^p_{i-1/2\,j} \equiv \sum_{p=1}^{M} \mathcal{W}^p_{i-1/2\,j}, \tag{3.2.18}$$

$$\mathcal{A}_X^- \Delta \mathbf{Q}^X_{i-1/2\ j} = \sqrt{|g|}_{i-1/2\ j} \sum_{p:\ \lambda^p_{i-1/2\ j}>0}^{M} \lambda^p_{i-1/2\ j} \mathcal{W}^p_{i-1/2\, j},$$
$$\mathcal{A}_X^+ \Delta \mathbf{Q}^X_{i-1/2\ j} = \sqrt{|g|}_{i-1/2\ j} \sum_{p:\ \lambda^p_{i-1/2\ j}<0}^{M} \lambda^p_{i-1/2\ j} \mathcal{W}^p_{i-1/2\, j}, \tag{3.2.19}$$

where $\lambda^p_{i\,j}$ are the eigenvalues of the linearized hyperbolic problem (Equation 3.2.17), $\mathbf{r}^p_{i\,j}$ are the eigenvectors, $\alpha^p_{i\,j}$ are the coefficients of the jump across the discontinuity projected in the eigenvectors base, and $\mathcal{W}^p_{i-1/2\,j}$ are the Riemann solution waves, in the non linearized version of the Riemann problem is not possible to assume the existence of these waves (Bale and LeVeque, 2002). All the requirements over eigenvalues and eigenvectors related to hyperbolic problems should be accomplished (LeVeque, 2002; Toro, 2001).

Some considerations should be introduced at this point, as has been shown in Section 2.7.3, $\sqrt{|g|} = \sqrt{EG}\sin(\alpha)$, if we introduce this in Equation 3.2.19

$$\mathcal{A}_X^- \Delta \mathbf{Q}^X_{i-1/2\ j} = \sqrt{E}_{i-1/2\ j} \sqrt{G}_{i-1/2\ j} \sin\left(\alpha_{i-1/2\ j}\right) \sum_{p:\ \lambda^p_{i-1/2\ j}>0}^{M} \lambda^p_{i-1/2\ j} \mathcal{W}^p_{i-1/2\, j}. \tag{3.2.20}$$

And sorting:

$$\mathcal{A}_X^- \Delta \mathbf{Q}^X_{i-1/2\ j} = \sqrt{G}_{i-1/2\ j} \sin\left(\alpha_{i-1/2\ j}\right) \sum_{p:\ \lambda^p_{i-1/2\ j}>0}^{M} \left(\sqrt{E}_{i-1/2\ j} \lambda^p_{i-1/2\ j}\right) \mathcal{W}^p_{i-1/2\, j}. \tag{3.2.21}$$

The term $\left(\sqrt{E}_{i-1/2\ j} \lambda^p_{i-1/2\ j}\right)$ is the wave velocity in physical units $\tilde{\lambda}^p_{i-1/2\ j}$, recall that in curvilinear coordinate systems the values are not in physic units , they should be corrected using metric terms. In the same manner, multiplying both sides with L^Y the total flux through the X control volume boundary is obtained:

$$\Delta Y \mathcal{A}_X^- \Delta \mathbf{Q}^X_{i-1/2\ j} = L^Y \sin\left(\alpha_{i-1/2\ j}\right) \sum_{p:\ \lambda^p_{i-1/2\ j}>0}^{M} \tilde{\lambda}^p_{i-1/2\ j} \mathcal{W}^p_{i-1/2\, j}. \tag{3.2.22}$$

Coinciding with the ideas explained in Section 2.7.3. Of course, due to the non-orthogonality of the coordinates, the angle between axes α, appears as a correction to the flux.

Non-linear Solver

If the non-linear version of the problem is used the situation is a bit different, the eigenvalues and eigenvectors could not be defined, so the waves and their velocities could not be computed. Anyway, the solution to the Riemann problem between two cell could be find, and from this solution, the solution in the interface $\mathbf{Q}^{\perp}$, and the flux solution $\mathbf{F}^{n}_{i+1/2\,j}$ could be found.

$$\mathbf{F}_{i+1/2\,j} = \mathbf{f}_X\left(\mathbf{Q}^{\perp}\left(\mathbf{Q}^{n}_{i\,j}, \mathbf{Q}^{n}_{i+1\,j}\right)\right). \tag{3.2.23}$$

Using this flux solution the first order terms could be computed:

$$\begin{aligned} \mathcal{A}^{-}_{X}\Delta\mathbf{Q}^{X}_{i-1/2\;j} &= \mathbf{f}_X\left(\mathbf{Q}^{\perp}_{i-1/2\;j}\right) - \mathbf{f}_X\left(\mathbf{Q}_{i-1\,j}\right), \\ \mathcal{A}^{+}_{X}\Delta\mathbf{Q}^{X}_{i-1/2\;j} &= \mathbf{f}_X\left(\mathbf{Q}_{i\,j}\right) - \mathbf{f}_X\left(\mathbf{Q}^{\perp}_{i-1/2\;j}\right). \end{aligned} \tag{3.2.24}$$

The problem in this case is related to the waves speed, because these speeds are needed in the second order corrections, as LeVeque (2002) proposes the Rankine-Hugoniot shock speeds could be used with a low error in the solutions and still achieving the second order accuracy in the solution:

$$\begin{aligned} \mathcal{W}_{i-1/2\,j} &= \mathbf{Q}_{i\,j} - \mathbf{Q}_{i-1\,j}, \\ \lambda_{i-1/2\,j} &= \left[\mathbf{f}_X\left(\mathbf{Q}_{i\,j}\right) - \mathbf{f}_X\left(\mathbf{Q}_{i-1\,j}\right)\right] / \left(\mathbf{Q}_{i\,j} - \mathbf{Q}_{i-1\,j}\right). \end{aligned} \tag{3.2.25}$$

In the present model solvers for the linearized and non linear problem are implemented. For real test cases, due to the scale of the problem, a linearized solver is recommended.

Second Order Terms

Regarding to the second order correction terms appearing in Equation 3.2.14, the flux limiting approach is used (LeVeque, 2002), so the correction fluxes are defined through:

$$\widetilde{\mathbf{F}}^{X}_{i-1/2\ j} = \frac{1}{2}\sqrt{|g|}_{i-1/2\ j} \sum_{p=1}^{M} \text{sign}\left(\lambda^{p}_{i-1/2\ j}\right)\left(1 - \frac{\Delta t}{\Delta X}\left|\lambda^{p}_{i-1/2\ j}\right|\right)\widetilde{\mathcal{W}}^{p}_{i-1/2\,j}, \quad (3.2.26)$$

where $\widetilde{\mathcal{W}}_{i\,j}$ are the limited waves:

$$\widetilde{\mathcal{W}}^{p}_{i-1/2\,j} = \mathcal{W}^{p}_{i-1/2\,j}\phi^{p}_{i-1/2\,j}, \quad (3.2.27)$$

where $\phi^{p}_{i\,j}$ is the flux limiter (LeVeque, 2002; Toro, 2001). In the model the Min-mod, Superbee, Van Leer and Monotonized Centered Limiter are implemented.

3.3 Riemann Problem Solution

As has been commented previously, in the presented model, linearized and non-linear Riemann solvers are implemented, there are extensive literature on these solvers (LeVeque, 2002; Toro, 1999, 2001; Roe, 1981; Engquist and Osher, 1981) also applied to debris flow equations (Pitman et al., 2003; Iverson and Denlinger, 2001; Brufau et al., 2000). So it's not necessary to go deeply into the details, but a general description should be carried out, especially taking into account that in the next chapter a boundary conditions approach will be introduced based on the non linear Riemann solver. So in the next section some general details about the Riemann solver for the equations system will be explained.

3.3.1 Orthonormalization

In the equations system definition the goal was to obtain a system similar to the SWE, due to the important background existing in numerically solving this system. Finally the obtained system was close to SWE, but defined in a non-orthogonal coordinate system. So the Riemann problem is more complex than the classical one for SWE, obtaining complicate eigenvectors and eigenvalues.

In order obtain a Riemann problem similar to the SWE, a local orthonormalization is carried on. This operation is locally applied, because the metrics are curvilinear, so the orthogonal basis is dependent on the coordinates. At every cell interface the flows are transformed using orthonormal basis (Rossmanith et al., 2004; Rossmanith, 2006; Pons et al., 1998). Once the transformation is finished, the classical SWE in cartesian basis are obtained, so the Riemann problem could be solved in a simple way.

It's important to note that the transformation is carried on using a rotation matrix, but in general this matrix is not constant, so, the *cell-edge flux functions* hypothesis means to consider this matrix as constant near the interface and discard the derivatives of the rotation matrix in the Riemann problem solution.

Two different rotation matrix are obtained, one for the X axis:

$$\tilde{\mathbf{q}} = \begin{pmatrix} 1 & 0 & 0 \\ 0 & \frac{g_{12}}{\sqrt{g_{22}}} & 0 \\ 0 & \frac{\sqrt{g}}{\sqrt{g_{22}}} & \sqrt{g_{22}} \end{pmatrix} \cdot \mathbf{q} = \begin{pmatrix} 1 & 0 & 0 \\ 0 & \frac{F}{\sqrt{G}} & 0 \\ 0 & \frac{\sqrt{F^2-EG}}{\sqrt{G}} & \sqrt{G} \end{pmatrix} \cdot \begin{pmatrix} h \\ hu \\ hv \end{pmatrix}, \tag{3.3.1}$$

where $\tilde{\mathbf{q}}$ are the variables in the orthonormal basis, so in physic units. In Figure 3.1 the basis defined for X axe is shown, a new coordinate direction $\mathbf{X}_{\tilde{X}}$ is defined orthogonal to $\mathbf{X}_Y$, so orthogonal to the cell interface.

The second matrix is for the Riemann problem in the Y axis:

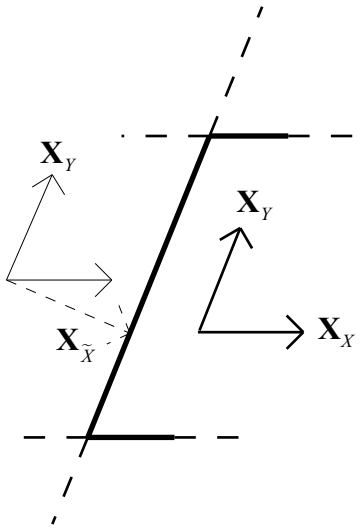

Figure 3.1: Orthonormal basis defined in the X axis, this base is used in the Riemann problem solution.

$$\tilde{\mathbf{q}} = \begin{pmatrix} 1 & 0 & 0 \\ 0 & \sqrt{g_{11}} & \frac{\sqrt{g}}{\sqrt{g_{11}}} \\ 0 & 0 & \frac{g_{12}}{\sqrt{g_{11}}} \end{pmatrix} \cdot \mathbf{q} = \begin{pmatrix} 1 & 0 & 0 \\ 0 & \sqrt{E} & \frac{\sqrt{F^2-EG}}{\sqrt{E}} \\ 0 & 0 & \frac{F}{\sqrt{E}} \end{pmatrix} \cdot \begin{pmatrix} h \\ hu \\ hv \end{pmatrix}, \tag{3.3.2}$$

In the new orthonormal base the flux functions are:

$$\widetilde{\mathbf{f}}_{\widetilde{X}} = \begin{pmatrix} h\tilde{u} \\ h\tilde{u}^2 + \frac{g_3}{2}h^2 \\ h\tilde{v}\tilde{u} \end{pmatrix} \quad \widetilde{\mathbf{f}}_{\widetilde{Y}} = \begin{pmatrix} h\tilde{v} \\ h\tilde{u}\tilde{v} \\ h\tilde{v}^2 + \frac{g_3}{2}h^2 \end{pmatrix}, \tag{3.3.3}$$

$\tilde{u}, \tilde{v}$ being the velocities in the orthonormal coordinates $\widetilde{X}, \widetilde{Y}$, for simplicity the tildes will be omitted in the following sections.

3.3.2 Contact Discontinuity

The Equations 3.3.3 are the classical fluxes in SWE with a corrected gravity, these bidimensional equations are solved with two different Riemann problems, one in the

X direction and the second on the Y direction. As its known (LeVeque, 2002), in the X direction the Y velocity v acts as a *passive tracer*, this means that the v values don't affect the Riemann problem solution. And the same situation occurs with the X velocity in the Y Riemann problem.

These kind of hyperbolic equations that include a *passive tracer*, normally provoke a *contact discontinuity*, this means a wave that is advected with the flow velocity, as a material tracer. The remain Riemann waves are computed solving the traditional one dimensional Riemann problem, so the computation is simplified.

So in the solver the classical SWE Riemann problem will be solved, and a contact discontinuity will be added as an extra wave to include de second dimension in the problem. In case of using a linearized solver, the Harten-Lax-Leer-Contact solver (HLLC) (Toro et al., 1994) is defined to specifically deal with contact discontinuities.

3.3.3 SWE Riemann Problem Solutions

As has been explained, the solver is dimensional splitting, so every dimension is solved with a different Riemann problem, in this section only the X dimension will be exposed. First of all, the interface flux problem will recalled:

$$\begin{aligned}
\mathbf{F}_{i+1/2\,j} &= \mathbf{f}_{\mathbf{X}}\left(\mathbf{q}\left(X_{i+1/2}, Y_j, t\right)\right), \\
\mathbf{F}_{i+1/2\,j} &= \mathbf{f}_{\mathbf{X}}\left(\mathbf{q}^{\perp}\left(\mathbf{Q}^n_{i\,j}, \mathbf{Q}^n_{i+1\,j}\right)\right), \\
\mathbf{F}_{i+1/2\,j} &= \mathbf{f}_{\mathbf{X}}\left(\mathbf{q}^{\perp}\left(\mathbf{q}_l, \mathbf{q}_r\right)\right),
\end{aligned} \tag{3.3.4}$$

$\mathbf{Q}^n_i$ is the vector of dependent variables at cell i at time step n, $\mathbf{q}^{\perp}$ is the dependent variables vector in cell face, and it depends on the values at both sides of the discontinuity $\left(\mathbf{Q}^n_i, \mathbf{Q}^n_{i+1}\right)$, represented as $\mathbf{q}_l, \mathbf{q}_r$ (subscript l and r indicates left side and right side). Finally, the Riemann problem solves the hyperbolic equations system between both side variable values $\mathbf{q}_l, \mathbf{q}_r$, to find the flux solution state $\mathbf{q}^{\perp}\left(\mathbf{q}_l, \mathbf{q}_r\right)$. The boundary conditions are an exception because the dependent variables on either side

of the Riemann problem are unknown. For example, in the downstream boundary, the right values in the discontinuity $\mathbf{q}_r$ are known and the left values $\mathbf{q}_l$ have one unknown dependent variable (subcritical regime).

$$\mathbf{q}_l = \begin{pmatrix} h \\ hu \\ hv \end{pmatrix}_{i\,j}, \quad \mathbf{q}_r = \begin{pmatrix} h \\ hu \\ hv \end{pmatrix}_{i+1\,j}. \tag{3.3.5}$$

In the SWE Riemann problem there are two families of solution waves, the Rankine-Hugoniot waves and the Riemann invariant waves, the first ones are a discontinuous waves, namely shocks and the second one are continuous waves, namely rarefactions. The solution consists of two phase space values $\mathbf{q}_l, \mathbf{q}_r$ connected to a third phase space value $\mathbf{q}_m$ by waves. Thus, a wave connects $\mathbf{q}_l, \mathbf{q}_m$ and a wave connects $\mathbf{q}_m, \mathbf{q}_r$. Every wave must belong to a family of waves. Each family has two waves, thus, in every value in the phase space, we find four different waves: Shock λ_1, Shock λ_2, Riemann λ_1 and Riemann λ_2. However, only some parts of these waves are valid, this condition is imposed by entropy (Lax, 1972). Using the valid solutions from Lax, we construct a solver by combining the different valid waves to obtain a value $\mathbf{q}_m$, which is connected to a 1-wave in the left state of the Riemann problem $\mathbf{q}_l$ and a 2-wave in the right state of the Riemann problem $\mathbf{q}_r$. The valid waves that connect $\mathbf{q}_l$ to $\mathbf{q}_m$ are (1-wave):

$$u_m = \begin{cases} u_l + 2\left(\sqrt{g_3 h_l} - \sqrt{g_3 h_m}\right) & h_m < h_l \\ u_l - (h_m - h_l)\sqrt{\dfrac{g_3}{2}\left(\dfrac{1}{h_m} + \dfrac{1}{h_l}\right)} & h_m > h_l \end{cases} \tag{3.3.6}$$

The valid waves that connect $\mathbf{q}_m$ to $\mathbf{q}_r$ are (2-wave):

$$u_m = \begin{cases} u_r - 2\left(\sqrt{g_3 h_r} - \sqrt{g_3 h_m}\right) & h_m < h_r \\ u_r - (h_m - h_r)\sqrt{\dfrac{g_3}{2}\left(\dfrac{1}{h_m} + \dfrac{1}{h_r}\right)} & h_m > h_r \end{cases} \tag{3.3.7}$$

In Figure 3.2 all the possible waves that pass through a phase space point $\mathbf{q}$ are shown, finally if this state $\mathbf{q}$ inside the phase space belongs to left side $\mathbf{q}_l$ or right side $\mathbf{q}_r$ only two of the curves are valid. And, two accomplish the entropy condition, only a piece of every curve is allowed.

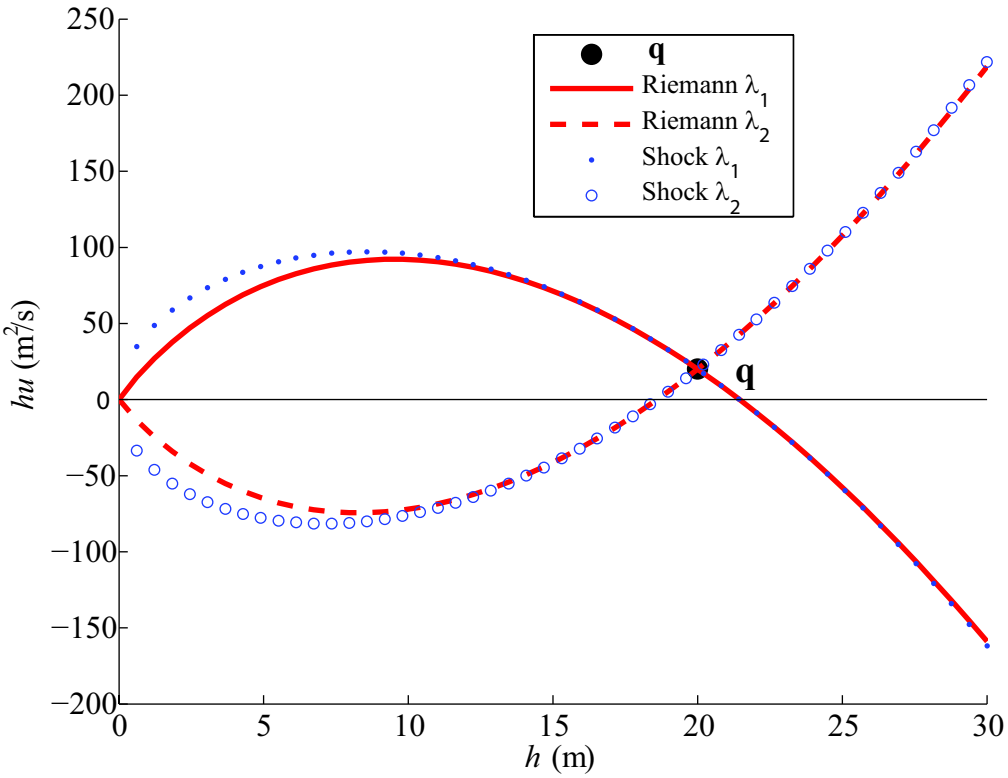

Figure 3.2: All the solution waves existing in a point of the phases space.

If the state is a *left state*, only Shock λ_1, Riemann λ_1 are available, and also one half of these curves is valid. In Figure 3.3 the valid parts of the curves are shown, as its clear combining these curves is always possible to find a crossing point.

It's important to note the difference between $\mathbf{q}_m$ and $\mathbf{q}^{\perp}$, the first one is the

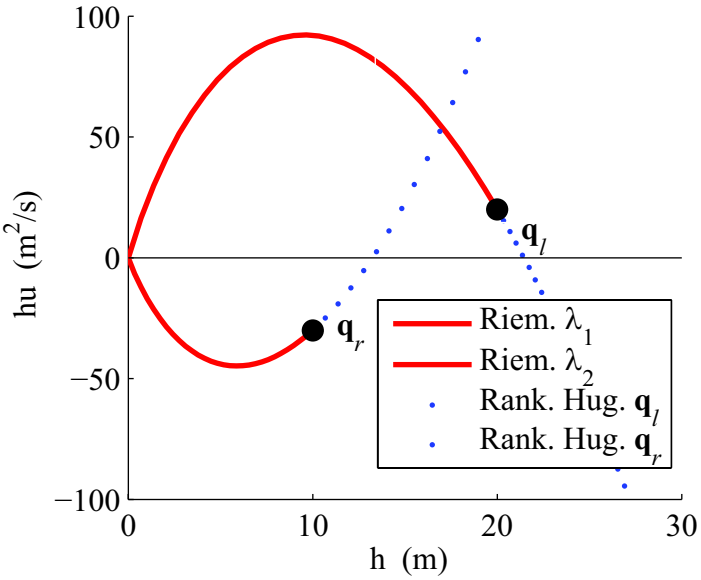

Figure 3.3: Entropically valid waves related to the left state $\mathbf{q}_l$ and right state $\mathbf{q}_r$.

Riemann solution and the second one is the flux solution (flux at the control volume face). This difference is essential for the proposed algorithm to solving boundary conditions, if we solve a typical dambreak problem for $t = 0$, we obtain the (Stoker, 1957) solution, and the flux in the dam is $\mathbf{q}^{\perp} \neq \mathbf{q}_m$.

An example of the solution to the Riemann problem is shown in Figure 3.4, the state $\mathbf{q}_m$ is obtained as the crossing of the valid waves. As has been stated, once the problem is solved, the flux solution $\mathbf{q}^{\perp}$ should be computed.

The computations of $\mathbf{q}^{\perp}$ depends on the structure of the solution, and the solution state that remains on the interface normally corresponds to the piece of the of the resulting waves that has zero velocity. It's important to recall that the hyperbolicity of the system guarantees the self-similarity of the solution, so along the time step Δt the structure of the solution its constant, so the value of $\mathbf{q}^{\perp}$ its constant (if the stability criterion is accomplished) (LeVeque, 2002).

In Figure 3.5 the structure of the solution is shown, the selected variable is the depth, and it's clear the existence of different waves and a standing state $\mathbf{q}^{\perp}$ in the

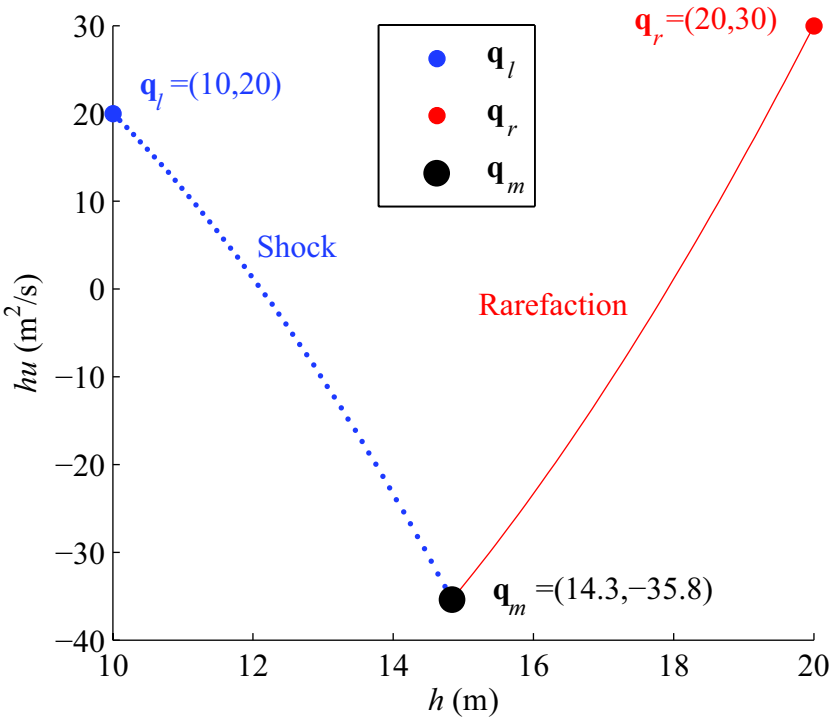

Figure 3.4: Riemann problem solution $\mathbf{q}_m$, connecting left $\mathbf{q}_l$ and right states $\mathbf{q}_r$.

cell interface, different from the problem solution $\mathbf{q}_m$.

The solution estate $\mathbf{q}_m$ it's a vector with three different components:

$$\mathbf{q}_m = \begin{pmatrix} h_m \\ h_m u_m \\ h_m v_m \end{pmatrix}, \tag{3.3.8}$$

the values for h_m, u_m are obtained through Equations 3.3.6, 3.3.7, but v_m it's still undefined, the values for this variables are obtained from the *contact discontinuities* theory, so:

$$v_m = \begin{cases} v_l & u_m < 0 \\ v_r & u_m > 0 \end{cases} \tag{3.3.9}$$

If a linearized solver is used, a wave and a speed are defined for the contact discontinuity:

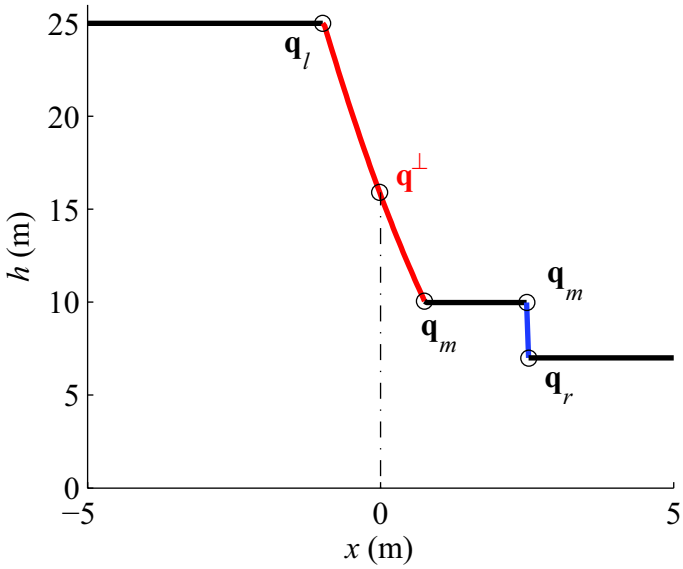

Figure 3.5: Depth solution for Riemann problem at $t = 0.1$, $\mathbf{q}_l = (25, 150)$, $\mathbf{q}_r = (7, 100)$ and the Riemann solution is $\mathbf{q}_m = (9.9, 174.9)$, connecting to left and right states.

$$\lambda^p_{i+1/2\,j} = u_m, \qquad \mathbf{r}^p_{i+1/2\,j} = \begin{pmatrix} 0 \\ 0 \\ 1 \end{pmatrix}, \qquad \mathcal{W}^p_{i+1/2\,j} = \begin{pmatrix} 0 \\ 0 \\ v_r - v_l \end{pmatrix}. \tag{3.3.10}$$

3.3.4 Final Remarks

The complete algorithm of the Godunov flux computation is:

$$\text{Dependent Variables} \begin{cases} \mathbf{q}_l = \mathbf{Q}^n_{i\,j} \\ \mathbf{q}_r = \mathbf{Q}^n_{i+1\,j} \end{cases}$$

$$\downarrow$$

$$\mathbf{q}_m = \text{Riemann Solver}\left(\mathbf{q}_l, \mathbf{q}_r\right)$$

$$\downarrow$$

$$\mathbf{q}^{\perp} = \mathbf{q}^{\perp}(\mathbf{q}_l, \mathbf{q}_r, \mathbf{q}_m)$$

$$\downarrow$$

$$\mathbf{F}^n_{i+1/2\,j} = \mathbf{f}_X\left(\mathbf{q}^{\perp}\right)$$

So the Riemann solver used in FVM must follow these steps, using linear or non linear approach to compute the different elements. The Riemann solvers theory has became classical, so there are a large amount of bibliographic references on the topic (LeVeque, 2002; Toro, 1999, 2001).

Chapter 4

Boundary conditions

One of the central points in debris flow simulation is the introduction of the debris volume. There are two main approaches:

- Introduce the volume as initial condition: useful if the triggering process is a landslide and the initial position and depth is known. The principal restriction is the whole basin simulation requirement, involving large computational resources.
- Introduce the volume as a boundary condition hydrograph: useful for inchannel debris and landslide debris. In the second case it's necessary to transform the landslide volume into discharge.

The first choice is straight, just to introduce the initial conditions and propagate the flow. In the second case the problem is more complicated, the first step is the debris hydrograph creation (Rickenmann, Laigle, McArdell and Hbl, 2006; Nakagawa et al., 1999; Takaoka et al., 2006), and the second is the hydrograph propagation (Scheidl and Rickenmann, 2009; Hübl and Steinwendtner, 2001; Rickenmann, Laigle, McArdell and Hbl, 2006).

The model presented in this work is able to deal with both scenarios, however the challenge is how to introduce debris flow hydrograph boundary condition. The theory for hydrograph input is developed, but in most of the cases to be applied to

continuous flow using the method of characteristics (Sarra, 2003; Henderson, 1966; Abbott, 1966). For debris flow, the rising limb of the hydrograph is steep, and it is not possible to guarantee the absence of shock waves in the boundary. So, a new method is necessary to introduce the hydrograph in the right way.

In this chapter a new approach to introduce the boundary conditions in the FVM framework is described. To illustrate the method the one dimensional version of the SWE is used:

$$\mathbf{q} = \begin{pmatrix} h \\ hu \end{pmatrix},$$
$$\begin{cases} \dfrac{\partial h}{\partial t} + \dfrac{\partial hu}{\partial X} = 0, \\ \dfrac{\partial hu}{\partial t} + \dfrac{\partial \left(u^2 h + g_3 \frac{h^2}{2}\right)}{\partial X} = 0, \end{cases} \tag{4.0.1}$$

where X, t as an independent variables.

4.1 Introduction

The use of the finite volume method in hyperbolic problems has become more widespread. The Godunov method and Riemann solvers have been combined to obtain high-resolution methods capable of solving transcritical regimes (including subcritical and supercritical areas). Simple problems used as test cases have boundary conditions that make mathematical sense, such as reflecting or non-reflecting boundary conditions. Under these conditions, the values of the dependent variables of the boundaries can be found immediately. In real computations the boundary conditions have physical sense and the dependent variables are not so easy to define. The intrinsic characteristics of the hyperbolic problems make complex to define a well posed problem. The boundary conditions imposed should accomplish the hyperbolic structure of the problem.

As an example, in the most typical shallow water equations (SWE) casses (subcritical regimes), the boundary conditions are the upstream discharge value and the downstream water level. To apply boundary conditions, two upstream and two downstream dependent variables are needed. Therefore, the values of the unknown variables (upstream water level and downstream discharge) need to be interpolated. This task is usually performed using the method of characteristics (MOC), but this involves using two different numerical schemes to solve the problem: a finite volume method inside the domain and the MOC at the boundaries. The problem is that MOC is based on the solution of the strong form of the equations, so avoiding transcritical regimes, thus, inside the domain the method can deal with transcritical regimes, and at the boundaries the selected method is not able to deal with discontinuities.

This chapter proposes a new approach to introduce boundary conditions, in a way that is consistent with a Riemann solver, making it unnecessary to use the MOC for the boundaries. With this method, boundary conditions with shocks and rarefactions can be used. This method determines which boundary conditions imply a well-posed hyperbolic problem and which do not. In a similar work by Bateman (1993), the transcritical boundary conditions problem was solved using a modified MOC.

4.2 Description of the Problem

In hyperbolic problems, the definition of boundary conditions is not trivial. The number and application points of the conditions determine whether the problem is well posed. The SWE system has two dependent variables and two equations. In the domain, there are two different boundaries $X_{1-1/2}, X_{n+1/2}$, and two unknowns on every boundary. Depending on the problem it is necessary to impose one, two or none boundary conditions on every domain boundary.

In hyperbolic problems, conditions should be imposed on the upwind side, which is defined by the eigenvalues of the hyperbolic system. For SWE eigenvalues can be both

positive, both negative, or one negative and one positive. These three cases define zones in the phase space, the supercritical regime, inverse regime and subcritical regime. If in a geometric domain we find different regimes we are dealing with a transcritical regime, also it's possible to find eigenvalues with zero value, this define sonic points.

The boundary of the three different regime zones in the phase space is defined by two curves. Crit+ is the boundary between subcritical zone and supercritical one, and Crit- is the boundary between inverse and subcritical zones. These curves are defined by an non-dimensional parameter, the Froude number:

$$\begin{cases} \text{Supercritical-Subcritical boundary Crit+} \\ \lambda_1 = 0 \Rightarrow u - \sqrt{gh} = 0 \\ \Rightarrow u = \sqrt{gh} \Rightarrow \dfrac{u}{\sqrt{gh}} = 1 = \text{Froude number} \\ \\ \text{Subcritical-Inverse boundary Crit}- \\ \lambda_2 = 0 \Rightarrow u + \sqrt{gh} = 0 \\ \Rightarrow u = -\sqrt{gh} \Rightarrow \dfrac{-u}{\sqrt{gh}} = -1 \end{cases}$$

In a supercritical regime, boundary conditions should be defined on the upstream boundary. In an inverse regime, boundary conditions should be imposed on the downstream boundary. In the subcritical regime, one condition should be imposed on the upstream boundary and one on the downstream boundary.

In a transcritical regime the number of conditions imposed on every boundary depends on the regime zone were the boundary belongs. As mentioned above, to solve a Riemann problem, we need to know the values of the dependent variables on both sides of the problem.

In a supercritical or inverse regime, we find a boundary with all the conditions imposed, the solution of the Riemann problem in this boundary should be the imposed

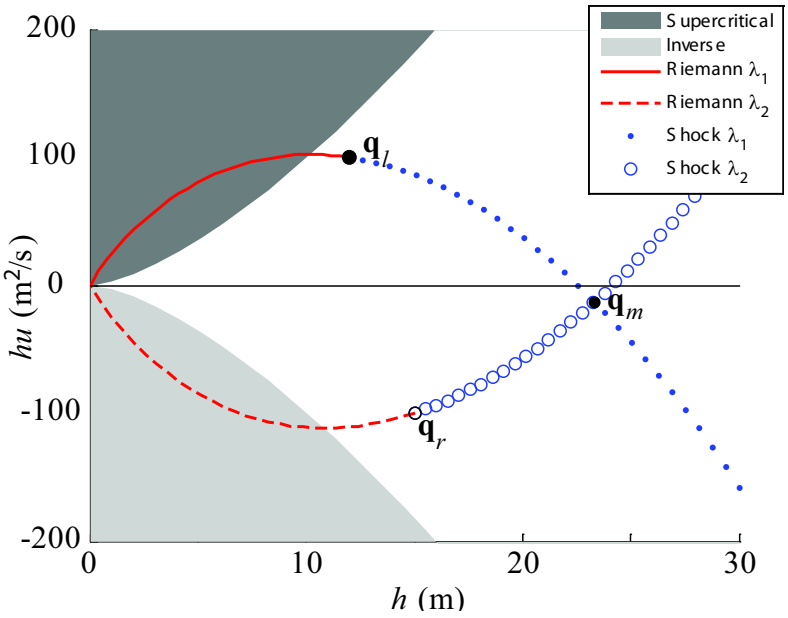

Figure 4.1: Phase space with the zones defined for every regime, supercritical (dark grey), inverse (grey) and subcritical (remain), in the figure we see and example of Riemann problem and solution with all the values in the subcritical zone.

boundary conditions:

$$\mathbf{q}_{cc} = (h_{cc}, (hu)_{cc}) \,, \tag{4.2.1}$$

where $\mathbf{q}_{cc}$ is boundary conditions vector, composed by the imposed dependent variables, depth h_{cc} and unit discharge $(hu)_{cc}$, to simplify the notation, in the next, the brackets in the unit discharge will be omitted $(hu)_{cc} \rightarrow hu_{cc}$. So to fulfill the boundary condition, the Riemann flux solution should be $\mathbf{q}^{\perp} = \mathbf{q}_m = \mathbf{q}_{cc}$, otherwise is a not a well posed problem. The other boundary side has no boundary conditions imposed; the Riemann problem solution should not depend on the unknown values. This defines the well-posed problem condition.

The subcritical regime is different. In order to solve the Riemann problem, we have one side of the problem with only one boundary condition imposed, so the other one must be interpolated. A complete boundary conditions method should find

the unknown dependent variable value. It should be consistent with the imposed boundary condition and the domain dependent variables.

First, the method should test the well-posed condition. Second, the method should interpolate the values of the incomplete dependent variables. These problems have traditionally been solved with the MOC, but this is not consistent with a Godunov method capable of dealing with transcritical regimes.

4.3 General Description of the Solution Method

This method uses the Riemann problem solution structure to introduce the boundary conditions in the domain. The method will use the Riemann solution structure to test whether the boundaries are well posed, and it will use this structure to compute the values of the incomplete boundary conditions (subcritical).

For supercritical and inverse regimes, is required the complete boundary with two imposed conditions (h_{cc}, hu_{cc}) to belong to the supercritical or inverse zone of the phase space. Is also needed that the Riemann problem solution state $\mathbf{q}_m$, fulfills another condition, depending on the regime, in order to guarantee that the flux solution $\mathbf{q}^{\perp} = (h_{cc}, hu_{cc})$ is equal to the imposed boundary values.

For subcritical regimes, one dependent variable is imposed on each side of the domain and the other needs to be interpolated. To find this unknown variable, the method will impose that it belongs to the phases connected by valid waves to the inside domain dependent variables values. Figure 4.2 shows an example of a subcritical regime with a unit discharge hu_{cc} imposed in the upstream and the other dependent variable h_{cc} interpolated. The state (h_c, hu_{cc}) is connected to the inside state $\mathbf{q}_r$ by a Riemann λ_2 rarefaction.

The dependent variables values at both sides of the Riemann problem are:

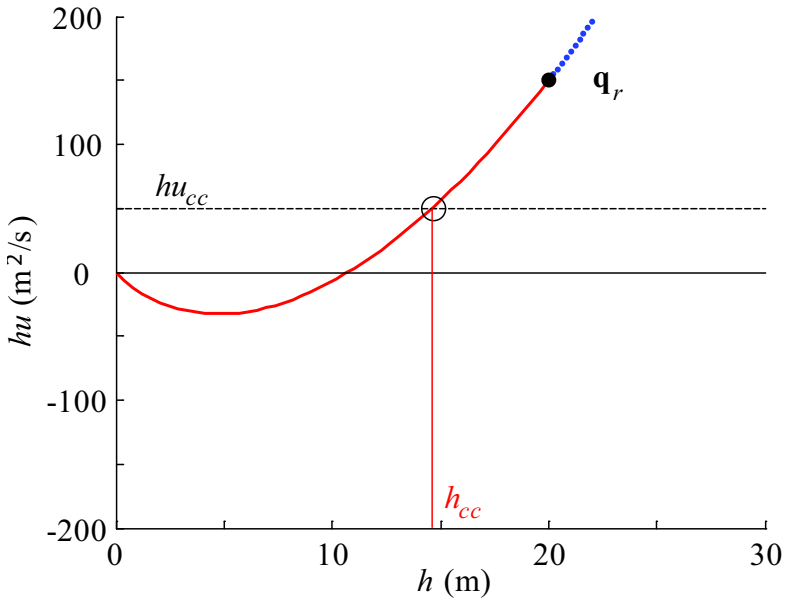

Figure 4.2: Interpolation of the boundary condition h_{cc} from the inside state $\mathbf{q}_r$ and the imposed boundary condition hu_{cc}.

$$\mathbf{q}_r = \mathbf{Q}_1^n,$$
$$\mathbf{q}_l = \begin{pmatrix} h? \\ hu_{cc} \end{pmatrix}.$$

Conceptually, this method finds the Riemann solution $\mathbf{q}_m$, but for the Godunov method we need the flux solution $\mathbf{q}^\perp$. However, as we will see:

Proposition 4.3.1. *In a subcritical regime, boundary conditions are well posed only if $\boldsymbol{q}^\perp = \boldsymbol{q}_m$ is fulfilled.*

Proof. The demonstration is simple, if we impose a unique boundary condition (h_{cc} or hu_{cc}), the resulting flux should depend on the inside value ($\mathbf{q}_l, \mathbf{q}_r$) and on the boundary condition value itself (h_{cc}, hu_{cc}). The phase values connected by valid waves to the inside state ($\mathbf{q}_l, \mathbf{q}_r$) have one degree of freedom, so by imposing one boundary condition

(h_{cc}, hu_{cc}), the value of the solution state $\mathbf{q}_m$ is defined exactly As we will see, in some cases the solution is undefined, but these cases are not mathematically well posed.

So the flux solution $\mathbf{q}^{\perp}$ should therefore fulfill $\mathbf{q}^{\perp} \in [\mathbf{q}_m, \mathbf{q}_l]$ or $\mathbf{q}^{\perp} \in [\mathbf{q}_m, \mathbf{q}_r]$, depending on the case (downstream or upstream conditions). In some cases, we will find $\mathbf{q}^{\perp} = \mathbf{q}_m$. However, other cases fulfill $\mathbf{q}^{\perp} \in (\mathbf{q}_m, \mathbf{q}_l]$ or $\mathbf{q}^{\perp} \in (\mathbf{q}_m, \mathbf{q}_r]$, such as transcritical rarefactions. In these cases, the problem is not well posed because $\mathbf{q}^{\perp} \neq (h_{cc}, hu_{cc})$, so the boundary condition is not imposed.

□

4.4 Figures Used To Describe The Cases

To illustrate different situations in which this method can be applied, two different figures will be used: one with the phase space (Figure 4.3) and another with a dependent variable in the space domain (Figure 4.4). The latter will reproduce time evolution of the waves produced in the phase space.

The graphs will contain the Riemann problem states $\mathbf{q}_l, \mathbf{q}_r$, the solution state $\mathbf{q}_m$and the flux state $\mathbf{q}^{\perp}$. The valid waves connected to these states will also be drawn. The continuous waves represent the rarefactions; $\mathbf{q}_l$ connects to Riemann λ_1 and $\mathbf{q}_r$ connects to Riemann λ_2.

The discontinuous lines represent the shocks; $\mathbf{q}_l$ connects to Shock λ_1 and $\mathbf{q}_r$ connects to Shock λ_2. We will also find two curves, Crit+ and Crit-, which define the boundaries of the supercritical and inverse regime zones respectively (Figure 4.1), are the eigenvalues of the hyperbolic system.

The result figure combining phase space and spatial domain is:

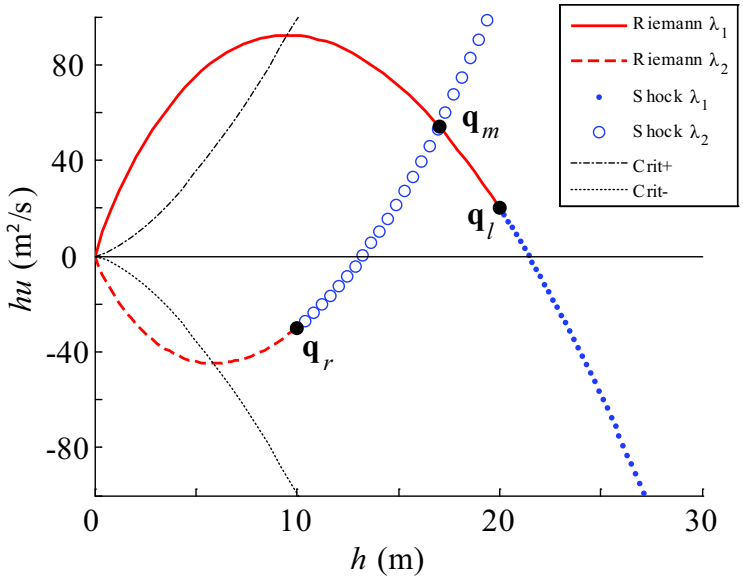

Figure 4.3: Phase space figure with the Riemann problem phase values $\mathbf{q}_l, \mathbf{q}_r$, the solution state $\mathbf{q}_m$, the waves and the supercritical and inverse zones boundaries Crit+, Crit-.

In the Figure 4.4, in the phase space the left state $\mathbf{q}_l$ is a supercritical right going flow, and the right state $\mathbf{q}_r$ is a subcritical left going flow. After the collision the resulting waves are presented in lower part, corresponding to t=0.1 s. The phase space just show the paths, but is independent on the time, so to evidence the dynamics is necessary to introduce the waves plot.

In the remainder analysis we will only consider upstream boundary because the problem is symmetric for the downstream boundary, the upstream supercritical regime is symmetric to the downstream inverse regime.

4.5 Supercritical And Inverse Regimes

The supercritical and inverse regimes implies imposing both dependent variable values in the boundary, as we said before, we will deal with the upstream boundary. If we

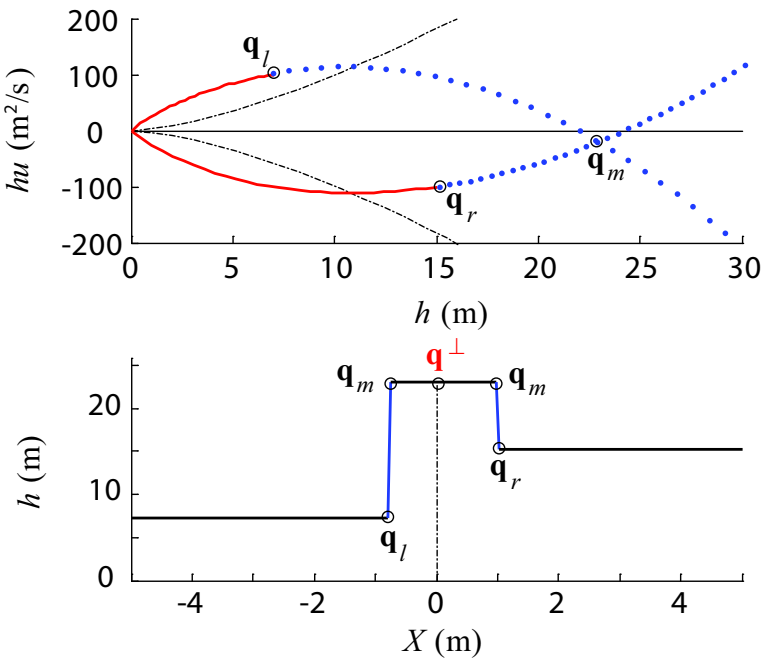

Figure 4.4: Phase space and waves obtained at t=0.1s.

find a supercritical regime, we obtain the left Riemann variables values from the boundary conditions and the right Riemann values from the domain values.

$$\begin{aligned} \mathbf{q}_r &= \mathbf{Q}_1^n, \\ \mathbf{q}_l &= \begin{pmatrix} h_{cc} \\ hu_{cc} \end{pmatrix}. \end{aligned} \tag{4.5.1}$$

With all this information is possible to compute the Riemann solution and test its validity. In Figure 4.5 is possible to see the Riemann solution for a upstream supercritical boundary conditions, as a result we obtain $\mathbf{q}^{\perp} = \mathbf{q}_{cc}$, so it's a well posed problem.

In Figure 4.6 we see an invalid supercritical upstream boundary condition; the flow solution obtained in the upstream boundary $\mathbf{q}^{\perp}$ is not equal to the imposed boundary conditions values $\mathbf{q}_{cc}$, its equal to $\mathbf{q}_m$ instead, so this would not be a valid boundary condition, supposed to be supercritical one. So it is not a well posed problem.

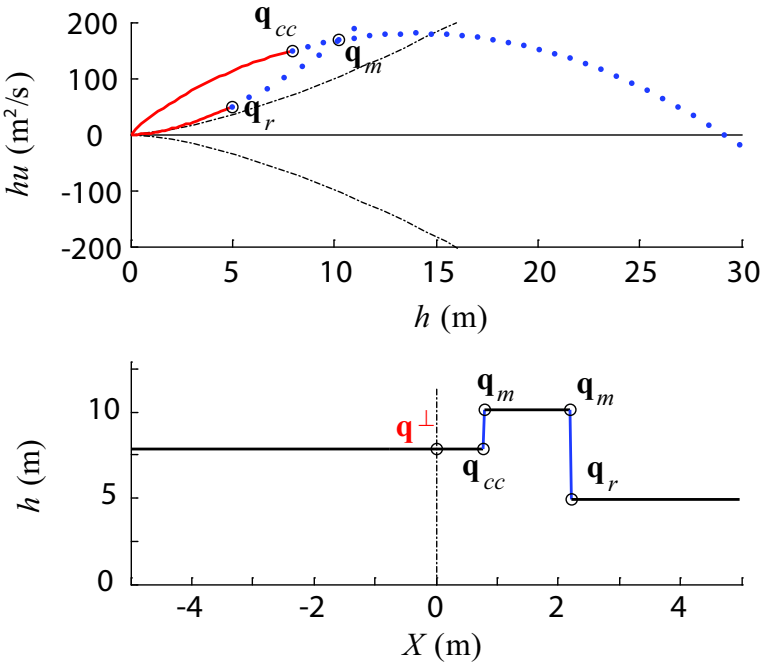

Figure 4.5: Riemann problem solution for upstream supercritical regime obtained at t=0.1s.

The imposed boundary condition is only valid if the Riemann solution $\mathbf{q}_m$ accomplishes the positive shock speed condition:

$$\frac{hu_m - hu_{cc}}{h_m - h_{cc}} > 0. \tag{4.5.2}$$

So the slope of the line connecting $\mathbf{q}_{cc}$ and $\mathbf{q}_m$ should be positive.

In the inverse regime boundary conditions applied to upstream boundary, the right Riemann problem values should be inside the inverse regime zone (Figure 4.1), if this condition is fulfilled is not necessary to impose boundary conditions in this boundary.

If the inverse regime is imposed in the downstream boundary condition the condition is:

$$\frac{hu_m - hu_{cc}}{h_m - h_{cc}} < 0. \tag{4.5.3}$$

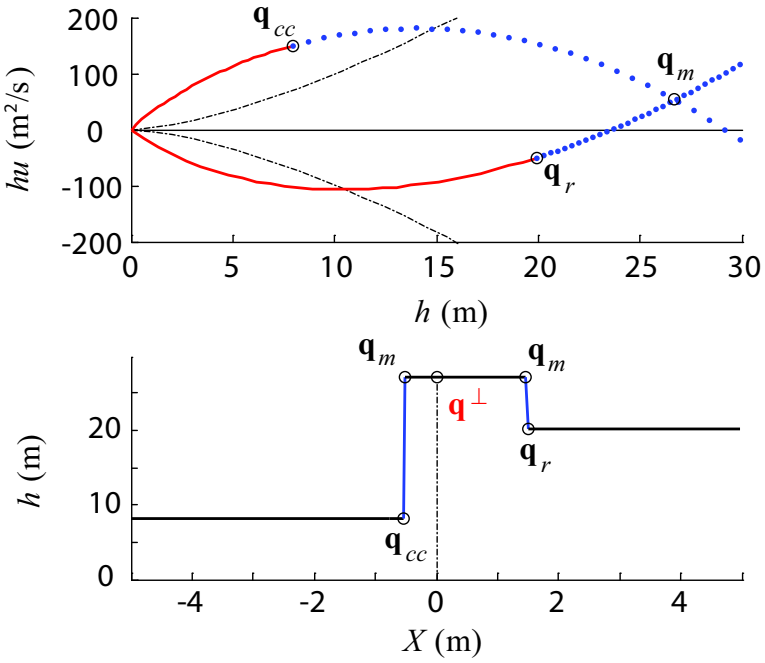

Figure 4.6: Invalid upstream supercritical boundary condition $\mathbf{q}^{\perp} \neq \mathbf{q}_{cc}$ (waves at t=0.1s).

4.6 Subcritical Regimes

As explained in Section 4.3 and described in Figure 4.2, applying subcritical boundary conditions, means that only one of the dependent variables value is imposed, so the other value should be interpolated from the valid Riemann problem curves. In the upstream boundary the guest value should be obtained from the curves connecting to $\mathbf{q}_r$ (Figure 4.2). With the imposed value and the interpolated one we construct $\mathbf{q}_{cc}$, and this point is in $\mathbf{q}_r$ curves, so is the Riemann problem solution $\mathbf{q}_{cc} = \mathbf{q}_m$.

In Figure 4.7 is imposed an upstream boundary condition $hu_{cc} = 100m^2/s$, interpolating this value in the $\mathbf{q}_r$ curves is obtained the depth $h_{cc} = 20\,\text{m}$, these two values form the boundary values vector $\mathbf{q}_{cc}$. When we solve the Riemann problem $(\mathbf{q}_{cc}, \mathbf{q}_r)$, is obtained the Riemann solution $\mathbf{q}_m = \mathbf{q}_{cc}$. To be a well posed problem is necessary $\mathbf{q}^{\perp} = \mathbf{q}_m = \mathbf{q}_{cc}$, in the problem solved in Figure 4.7 this is achieved. If $\mathbf{q}^{\perp} \neq \mathbf{q}_{cc}$ then the discharge or the depth are not the imposed ones so is not a well posed problem.

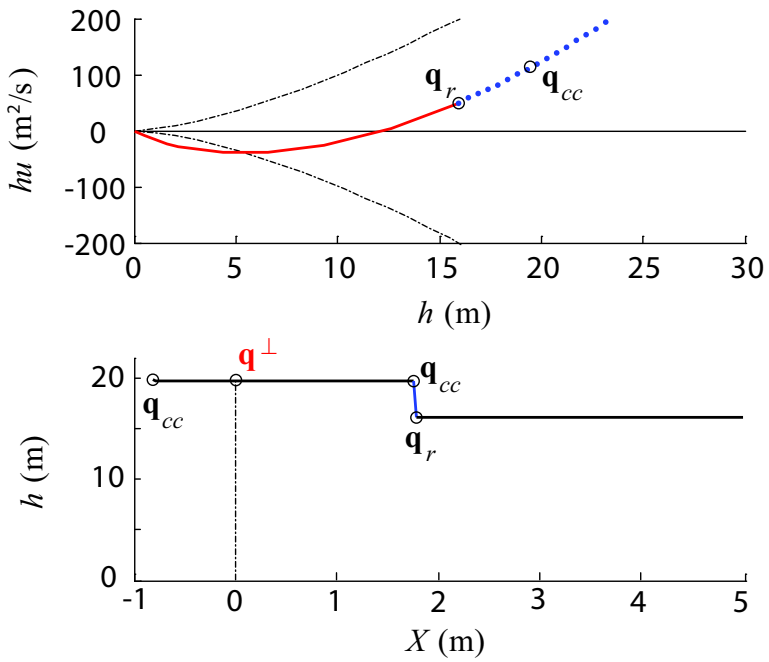

Figure 4.7: Upstream subcritical boundary condition imposed (waves at t=0.1s).

Figure 4.8 shows another upstream subcritical boundary condition $h_{cc} = 10\,\mathrm{m}$, the interpolated condition is $hu_{cc} = -22\mathrm{m}^2/\mathrm{s}$. Now the solution is connected using a rarefaction instead a shock (Figure 4.7). Is a well posed problem because $\mathbf{q}^{\perp} = \mathbf{q}_{cc}$.

As the previous case is possible to find invalid boundary conditions, in subcritical regime it occurs when $\mathbf{q}^{\perp} \neq \mathbf{q}_m$, in Figure 4.9 is possible to see an example, the imposed boundary value is $h_{cc} = 14\,\mathrm{m}$, the interpolated one is $hu_{cc} = 125\mathrm{m}^2/\mathrm{s}$.

As it's shown in the figure $\mathbf{q}^{\perp} \neq \mathbf{q}_m$ so $\mathbf{q}^{\perp} \neq \mathbf{q}_{cc}$, this is not well posed problem case. The condition to achieve $\mathbf{q}_{cc} = \mathbf{q}_m = \mathbf{q}^{\perp}$ in subcritical regimes is:

$$\frac{hu_{cc} - hu_r}{h_{cc} - h_r} > 0. \tag{4.6.1}$$

So the line connecting the right values and the boundary values $\mathbf{q}_{cc}$ should have positive slope. For the downstream boundary this condition is:

$$\frac{hu_{cc} - hu_l}{h_{cc} - h_l} < 0. \tag{4.6.2}$$

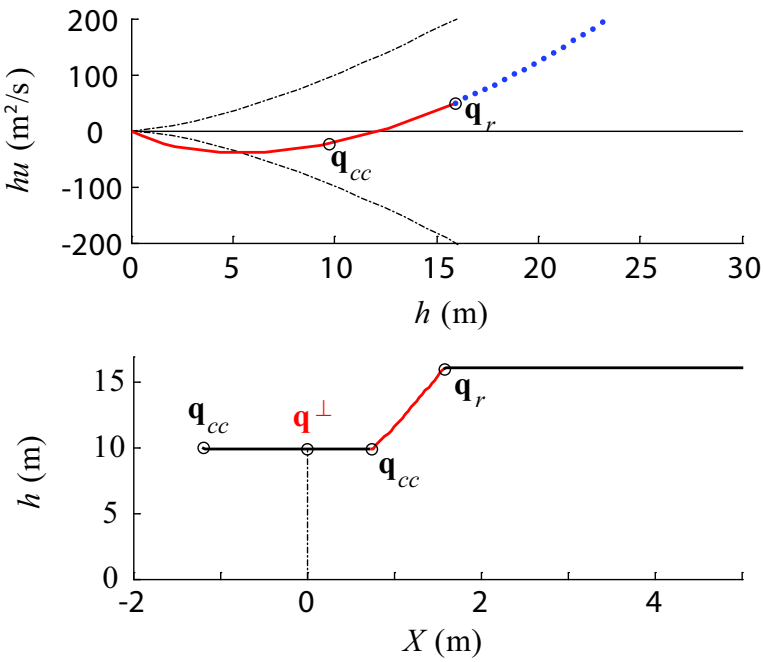

Figure 4.8: Upstream subcritical boundary conditions (waves at t=0.1s).

4.7 Solution Algorithm

The type of algorithm depends on the type of boundary condition to be imposed. It does not depend on the regime inside the domain.

4.7.1 Supercritical Regime

If the supercritical boundary condition is imposed in the downstream boundary, it's only necessary to check that the inside domain values $\mathbf{q}_l$ are inside the supercritical regime zone (Figure 4.1).

If this condition is imposed in the upstream boundary the steps are:

1. Check that the imposed values of the dependent variables $\mathbf{q}_{cc}$ are included in the supercritical regime zone in the phase space.

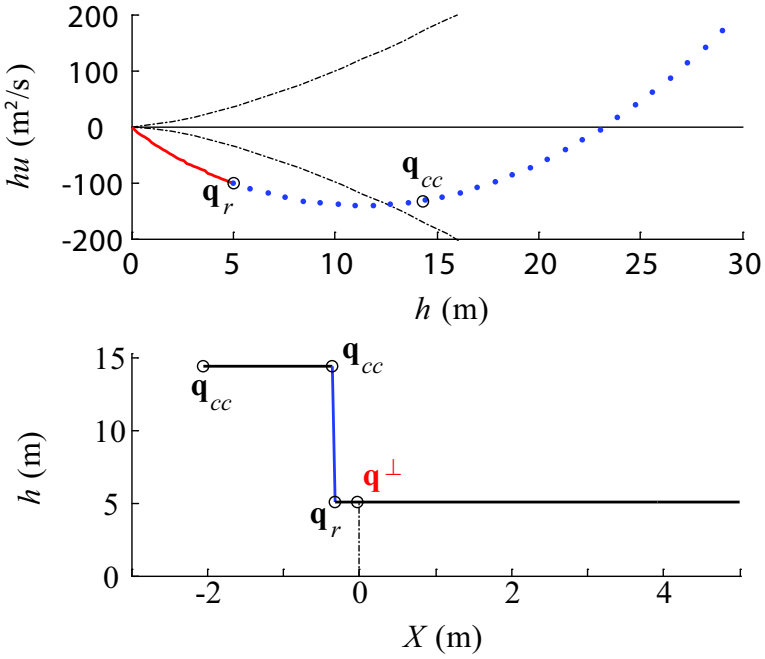

Figure 4.9: Invalid upstream subcritical boundary condition (waves at t=0.1s).

2. Impose the boundary conditions ($\mathbf{q}_l = \mathbf{q}_{cc}$) and solve the Riemann problem $(\mathbf{q}_l, \mathbf{q}_r)$ and find $\mathbf{q}_m$.

3. Check condition 4.5.2 to test $\mathbf{q}^{\perp} = \mathbf{q}_l = \mathbf{q}_{cc}$.

4.7.2 Inverse Regime

If the inverse boundary condition is imposed in the downstream boundary, it's only necessary to check that the inside domain values $\mathbf{q}_r$ are inside the inverse regime zone (Figure 4.1).

If this condition is imposed in the upstream boundary the steps are:

1. Check the imposed values of the dependent variables $\mathbf{q}_{cc}$ are included in the inverse regime zone in the phase space.

2. Impose the boundary conditions ($\mathbf{q}_r = \mathbf{q}_{cc}$) and solve the Riemann problem ($\mathbf{q}_l, \mathbf{q}_r$) and find $\mathbf{q}_m$.

3. Check condition 4.5.2 to test $\mathbf{q}^{\perp} = \mathbf{q}_r = \mathbf{q}_{cc}$.

4.7.3 Subcritical Regime

To define the subcritical regime algorithm, previous steps must be carried out. In this regime, we impose one boundary condition with a dependent variable (h_{cc} or hu_{cc}) and we interpolate the other dependent variable (hu_{cc} or h_{cc}). To interpolate the unknown dependent variable, we use the waves that connect the known variables (Figure 4.2). However, the curves are not injective (the shapes are parabolic), so a new criteria is necessary to select the right choice.

This new criteria comes from a limitation; the interpolated state must not be inside the supercritical or inverse regime zones, because if it were it would not be a subcritical condition. Excluding the zones that correspond to supercritical or inverse regimes, the remaining part of the curves is injective. Thus, the mathematical and hydraulic problems are coupled. The limit state is the intersection between the state solution curves and the Crit+ and Crit- curves. This intersection defines the points (h_c,hu_c).

For an upstream condition, our boundary condition dependent variables must fulfill (Figure 4.10):

$$\begin{aligned} h_{cc} &> h_c, \\ hu_{cc} &> hu_c. \end{aligned} \tag{4.7.1}$$

Fulfilling this condition the boundary variable values are therefore outside of the inverse regime zone.

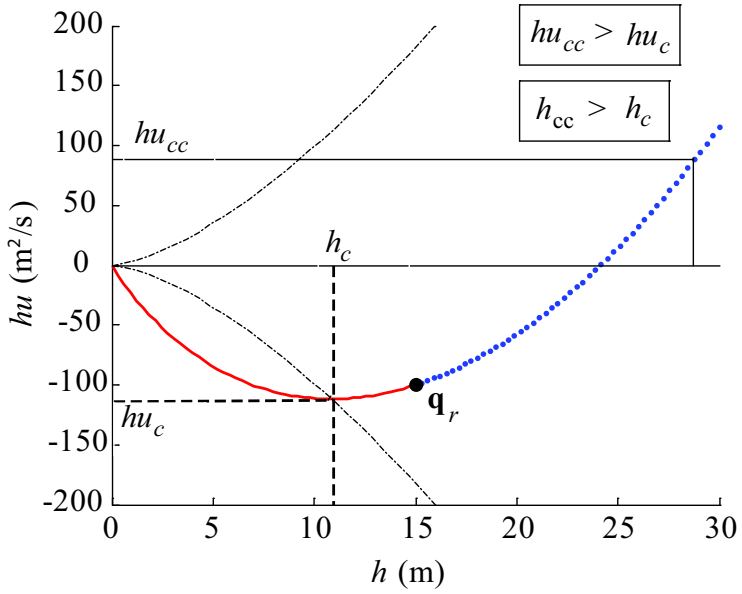

Figure 4.10: Threshold values for boundary values interpolation.

If we impose a downstream boundary condition, the dependent variables must fulfill the symmetric condition, now computing h_c,hu_c as intersection between the valid wave's curves and the Crit- curve:

$$\begin{aligned} h_{cc} &> h_c, \\ hu_{cc} &< hu_c. \end{aligned} \tag{4.7.2}$$

This limitation imposes a maximum for the negative discharges for upstream and positive discharge for downstream boundary conditions. If we try to impose a upstream boundary condition inside the forbidden zone, we don't obtain a well posed problem $\mathbf{q}^{\perp} \neq \mathbf{q}_m \Rightarrow \mathbf{q}^{\perp} \neq \mathbf{q}_{cc}$ (Figure 4.11).

In hydraulic terms, this condition means that neither the upstream outflow discharge may exceed the critical discharge.

The algorithm is as follows:

1. Determine the values of h_c and hu_c as interpolation limits.

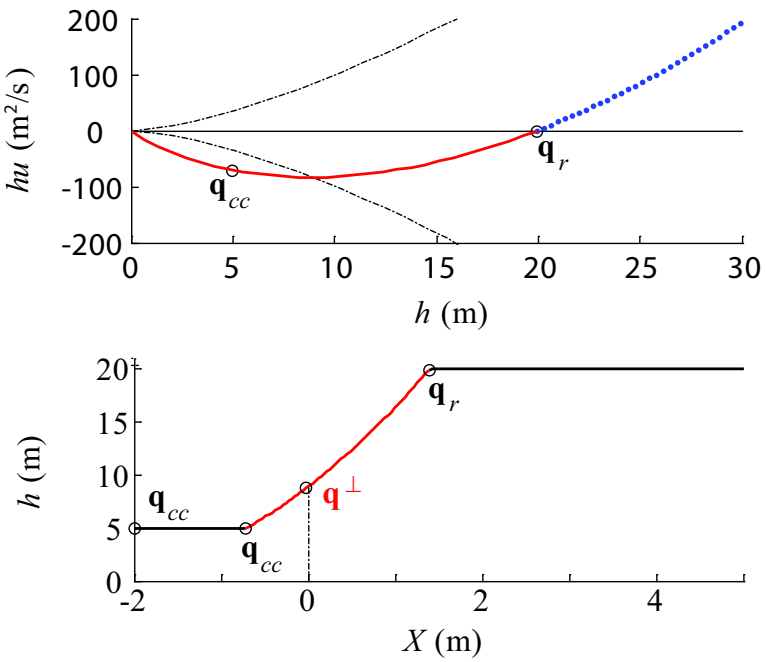

Figure 4.11: Invalid upstream subcritical boundary condition (waves at t=0.1s).

2. Considering these limitations, find the unknown dependent variable that corresponds to the known dependent variable imposed as a boundary condition. The result of this step is $\mathbf{q}_m$.

3. Check that state $\mathbf{q}_m$ is not in the supercritical or subcritical zone, because that would indicate a compatible but complete boundary condition (which is only valid for supercritical and inverse regimes).

4. At this point, we know that $\mathbf{q}^\perp \in [\mathbf{q}_m, \mathbf{q}_r]$ or $\mathbf{q}^\perp \in [\mathbf{q}_m, \mathbf{q}_l]$. We only need to check that $\mathbf{q}_m = \mathbf{q}^\perp$.

Sufficient conditions to fulfill 4) are the conditions 4.6.1 and 4.6.2 defined in Section 4.6.

Let us conceptually interpret these limitations. Condition 1) imposes that the boundary conditions at least have an influence inside the domain (upwind). Condition 3) imposes that the condition may not be complete, because that would imply

imposing two values for dependent variables, which is not valid for subcritical regimes.

4.8 Results

In this section we compare the results obtained simulating channel flow with the new boundary conditions method and using the traditional method of characteristics (MOC). This test case involves a channel 10 meters long and 1 meter wide. The initial conditions are water at rest, 1 meter depth. The boundary conditions are an upstream discharge of 1 cubic meter per second and a downstream water level of 2 meters. When the simulation starts the channel shows two different waves coming from channel boundaries, upstream wave due to instantaneous inflow increasing and downstream wave due to water level instantaneous rising.

4.8.1 Subcritical Regime

The upstream inflow originates a water level rising and the downstream water level rising originates a downstream inflow (negative discharges).

Figure 4.12 and Figure 4.13 are different time results showing the commented behaviors. It's possible to see both waves traveling along the channel, the wave originated by the downstream boundary condition is stronger than upstream originated one. At time 1.3 s we find the collision between both waves near the channel center.

In the next time step profiles is possible to see the depth fixed at the downstream boundary but the downstream discharge changes in a big range because it's not a fixed boundary condition.

When the boundary conditions are imposed, shocks come from the boundaries, and keep unaltered until the wave traveling from the opposite node arrives. Figure 4.14 shows the changes over time in the depth and discharge in the upstream boundary

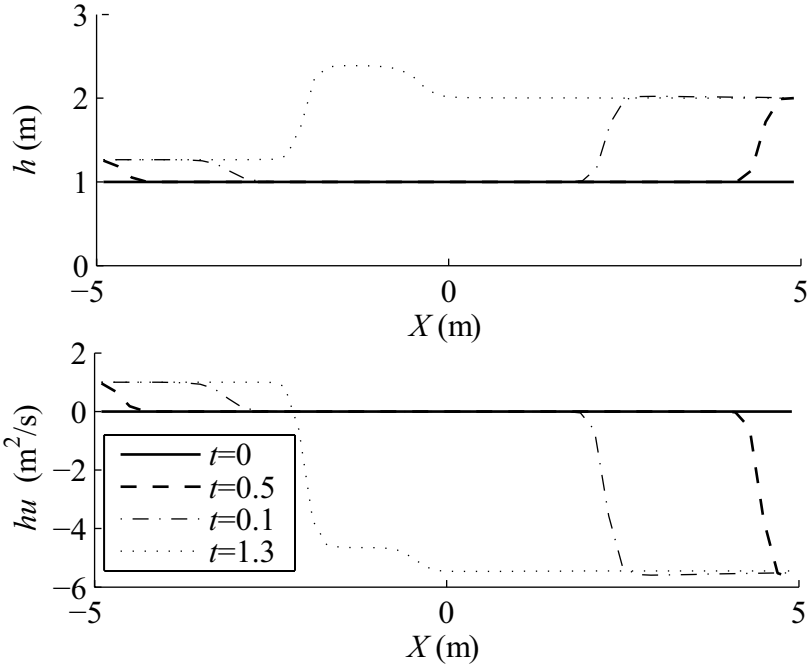

Figure 4.12: Depth and discharge in the channel at four different times.

and in the first node next to the boundary. In the upper axes are showed the values at the upstream boundary and in the lower axes are showed the values in the internal node. The upstream boundary keeps the imposed discharge boundary condition while the depth changes and the internal node follows these values.

Figure 4.15 shows the time evolution of the variables in the upstream boundary. There are two curves, the red one are the values in the boundary, and the blue one are the values in the internal node next to boundary. The boundary curve is always at 1 cubic meter per second discharge because it is imposed, and it changes the depth to adapt to the inside domain situation. The blue line changes over time until it reaches a steady state, as does the whole channel, in the imposed boundary conditions, discharge 1 m^3/s and depth 2 m. It could happen that along the simulation (transient) the imposed boundary conditions are wrong because the hyperbolic problem becomes not well posed, in this situation the computation should stop or use special condition like critical depth.

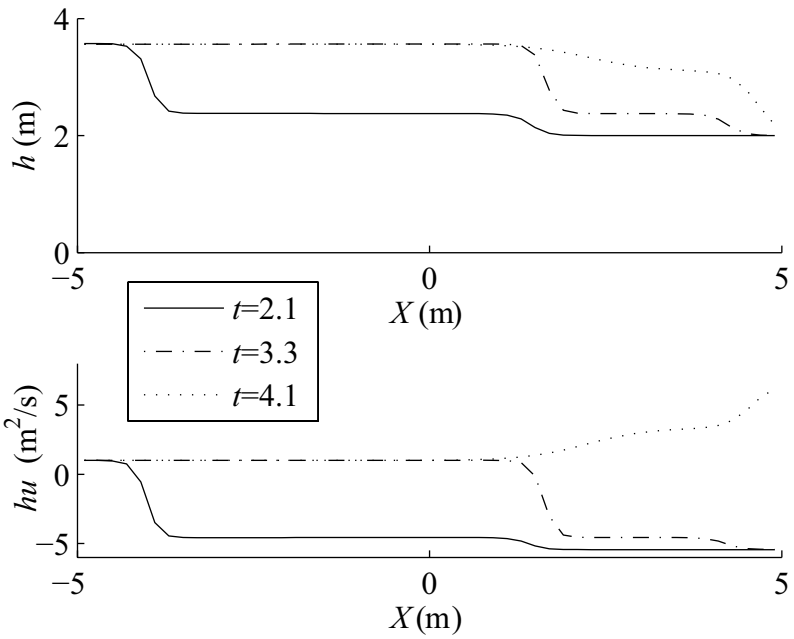

Figure 4.13: Three states of the channel in the first seconds.

4.8.2 MOC Boundary Conditions Approach

To compare the results obtained using the traditional MOC and the values obtained using the new approach, we compare the time evolution of depth and discharge in the upstream boundary. In Figure 4.16 the values in the boundary and in the internal node are showed, as in the previous section. Is possible to see a instability when the first wave coming from downstream collides to the upstream boundary, this is due to the fact that MOC don't considers shock waves, so is not able to deal with these kind of situation. Along the time, when the flow becomes smooth the differences are less important, but this confirms the hypothesis that the proposed method is useful to impose boundary conditions in shock situations.

In Figure 4.17 we see the comparison of the values obtained in the first node using both methods. The differences between the new approach and the classical MOC are clear; there are some instabilities in the depth and discharge values.

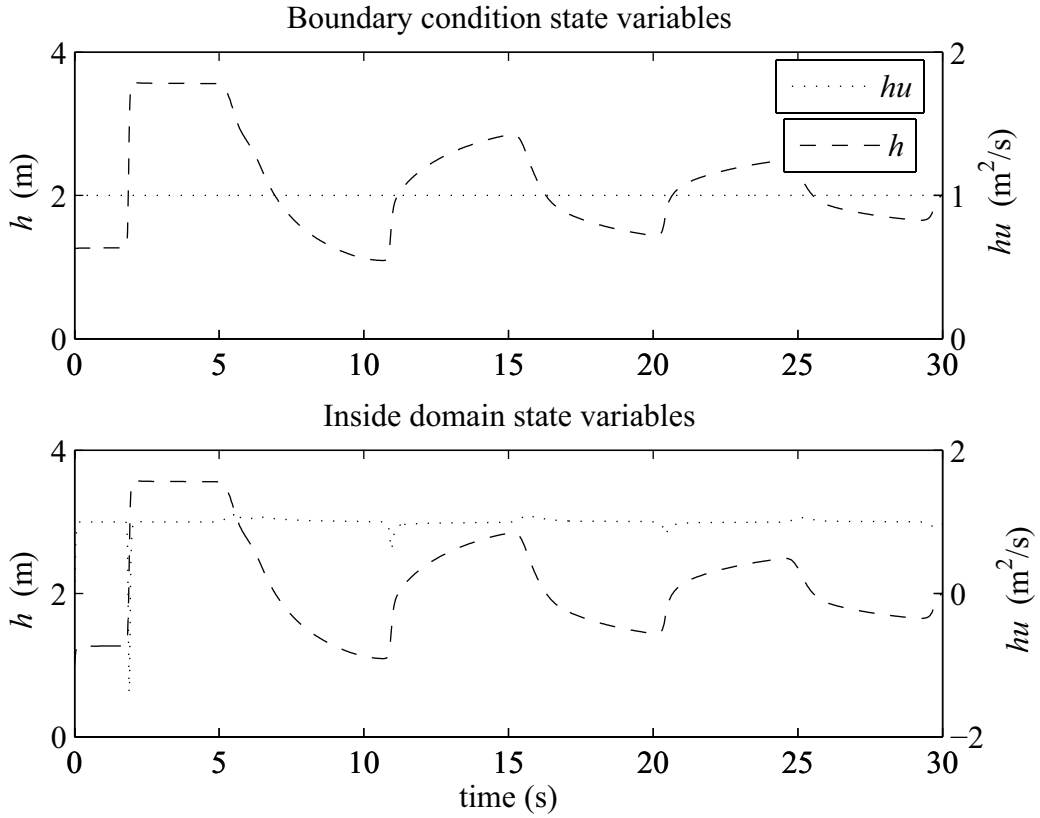

Figure 4.14: Time evolution in the variables in the upstream boundary and in the node next to the upstream boundary.

4.9 Conclusions Of The Chapter

The proposed method combines a filter, which ensures that only well-posed problems are defined, and a method for interpolating the unknown dependent variables in partial boundary conditions (subcritical regimes). The method is based on the Riemann problem solution and is optimal for the Godunov method, it allows discontinuities as boundary conditions to be introduced.

The method can immediately be extended to one-dimensional Euler equations, but more research is required before it can be extended to multidimensional problems. The method is computed using an exact Riemann solver because is not computationally expensive, so the combination with approximate Riemann solvers should be

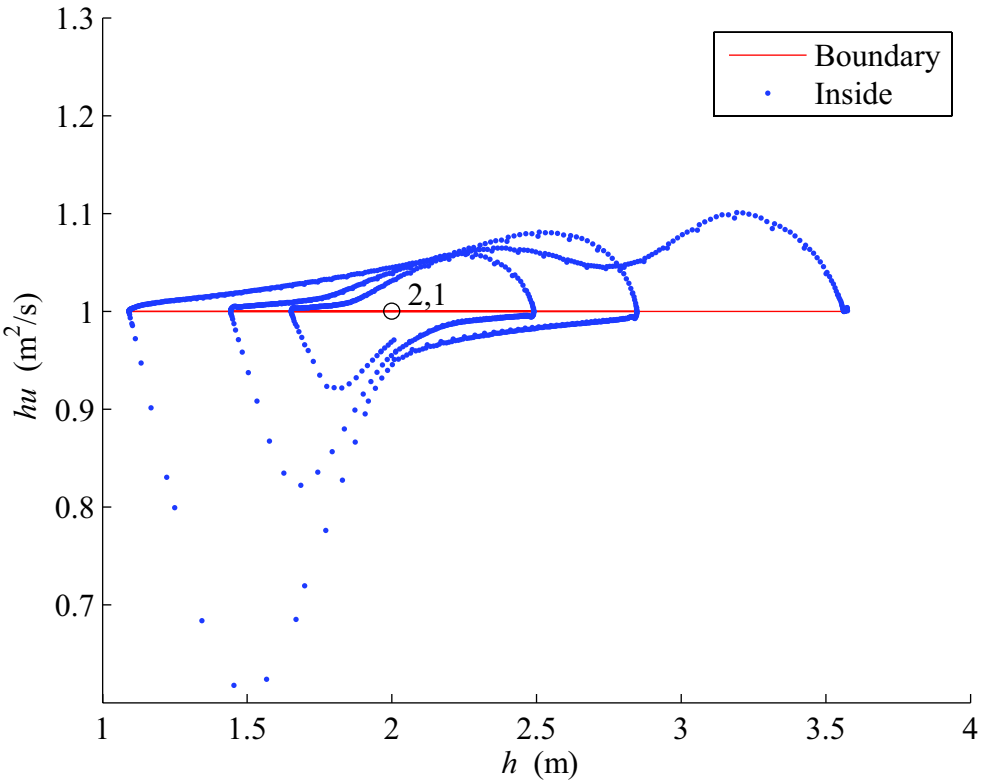

Figure 4.15: Phase space variables evolution in the upstream boundary condition and in the inside domain node next to boundary, both are converging to boundary conditions, $h = 2$ m , $hu = 1\text{m}^3/\text{s}$.

researched.

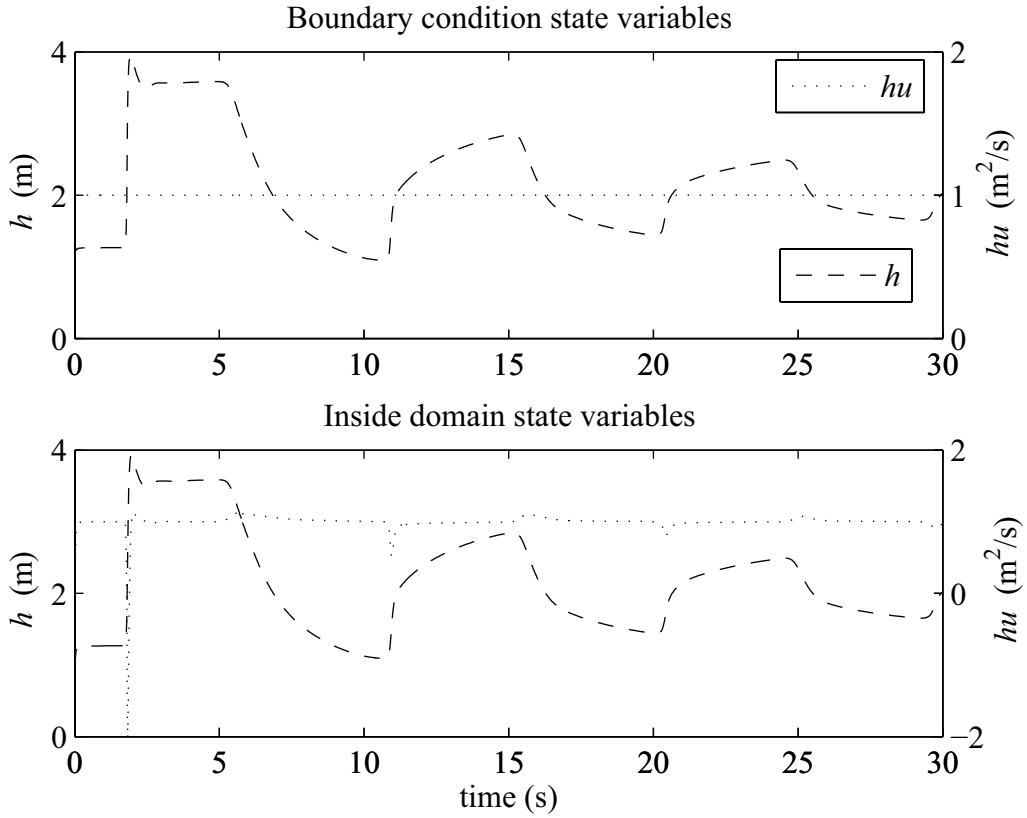

Figure 4.16: Time evolution in the variables in the upstream boundary and in the node next to the upstream boundary.

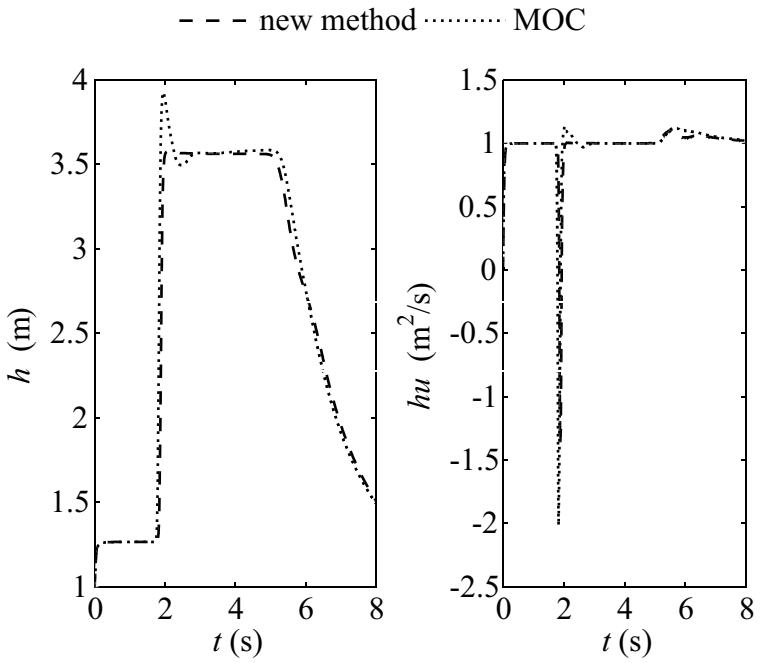

Figure 4.17: Depth and discharge values obtained in the first upstream node using the new method and the MOC.

Chapter 5

Accuracy Condition For Internal Boundary Conditions

Sometimes in the computational domain special elements are found, these special elements are not governed by the differential equations system, they follow closure relations, i.e. in hydraulics, inside the computational mesh structures like walls, weir, bridges, gates... could be found. Closure relations normally link the values of the different dependant variables without using differential equations. For example in the $k-\epsilon$ model the turbulent viscosity ν_t is defined using the closure relation:

$$\nu_t \;=\; C_\mu \frac{k^2}{\epsilon}, \tag{5.0.1}$$

where k the turbulent kinetic energy and ϵ the viscous dissipation. In hydraulics, multiple closure relations could be found. For example for a gate flow the relation:

$$hu = C_d \left(\Delta h\right)^{1/2}, \tag{5.0.2}$$

where the discharge (hu) is related to the water level drop (Δh), it fixes the discharge through the gate.

In hyperbolic problems, such as the one presented in the present thesis, a stability criterium has been defined for the numerical solution, i.e. CFL limit (Courant-Friedichs-Lewy) in the maximum time step. The solution to a hyperbolic problem is

self-similar, this means that during the time step the solution in the interfaces does not evolve, obtaining a first order in time scheme in the Godunov (1959) approach.

The closure relations are different, the shape of the functions is not established and the smoothness of the relations is not clear, the time does not appear explicitly so, due to the mathematical form of the closure relations, an accuracy criteria for closure relations should be defined, to guarantee that the closure relation is fulfilled along the time step.

Through the *Lax equivalence theorem* (Lax and Richtmyer, 1956) its clear that a link exist connecting the convergence, stability and consistency. The accuracy in convergence is therefore related to the stability in the solution. This stability link will be revealed with an example in 5.3.

5.1 Introduction

The proposed method is based on the connection of the dependant variables to the time, so the presence of the variables in the closure relation provokes an implicit relation to the time. To guarantee the fitting of the closure relation (accuracy) during the time step the smoothness of the function is necessary. The main question is "How smooth should be the closure relation to guarantee the fitting during one time step?". Or on the other hand, the question could be "How short should be the time step to guarantee the fitting of the closure function shape?".

So, as a first idea, a link exist between the smoothness of the closure relation and the time step used. Following this idea a new criterium to fix the maximum time step is proposed and an example will be shown, applying the method to a hydraulic control structure represented by a complex closure relation.

5.2 Accuracy Criterium

In the model there are independent variables time and space $(x, y, z, t) \in \mathbb{R}$. Let us suppose that there are two different dependent variables $(p(x, y, z, t), q(x, y, z, t)) \in \mathbb{R}$. A computational grid is defined on the independent variables, under this assumptions a closure relation $q = f(p)$ is defined at some cell interface. Let's suppose that the spectrum of the relation is defined by $F(k)$, where $k \in \mathbb{R}$ is the wave number $(2\pi/\lambda)$, where λ is the wave length, and the spectrum is computed using the Fourier transform:

$$F(k) = \int_{-\infty}^{+\infty} f(p)\, e^{-ikp} \mathrm{d}p \tag{5.2.1}$$

Proposition 5.2.1. *The closure relation f is fulfilled only if the difference in the values of p at both sides of time step (Δp) is less than π/k_{MAX}, where k_{MAX} is the maximum wave number of the Fourier spectrum:*

$$\Delta p \leqslant \frac{\pi}{k_{MAX}} \tag{5.2.2}$$

Proof. The proof is obtained by applying the *Shannon-Nyquist Sampling Theorem* (Shannon, 1949), this theorem fixes a minimum sampling frequency to reproduce a signal.

> "...If a function $x(t)$ contains no frequencies higher than B hertz, it is completely determined by giving its ordinates at a series of points spaced $1/(2B)$ seconds apart...."

The k_{MAX} is equivalent to the maximum frequency B existing in the closure relation function f:

$$k_{MAX} = 2\pi B, \tag{5.2.3}$$

here the frequency should be understand not in time coordinate t, but in the dependent variable p instead. Substituting this in Equation 5.2.2, the proof is finished. This theorem provides a *sufficient condition* to fit the closure relation. Using a time step Δt short enough to guarantee Equation 5.2.2, the accuracy of the simulation is fulfilled.

□

So its necessary to known which is the maximum wave number k_{MAX} existing in the function f, and as high this value is as short the time step should be to guarantee the accuracy in the function fitting. In most of the functions the spectrum is almost continuous, so there's not limit in the wave number k, to avoid

5.2.1 Methodology To Fulfill Accuracy

Once the condition has been stated an algorithm is proposed to accomplish it.

1. Define the closure equation function $f \equiv f\,(p)$.
2. Compute the Fourier spectrum of the function $F(k)$.
3. Define a maximum frequency threshold for the function k_{MAX} (Equation 5.2.3).
4. Fix the maximum variable step to reach the defined frequency Δp.
5. Use a lowpass filter with the frequency threshold (k_{MAX}) to modify the closure function f obtaining the filtered version $\bar{f}$.
6. During the simulation compute the maximum time step Δt to obtain Δp.

7. Compare the Δt to the Courant stability time step, select the most restrictive one.

8. Along the simulation the filtered function $\bar{f}$ could be exactly reconstructed from the sampled values using the *Whittaker Shannon interpolation formula* (Whittaker, 1935):

$$\operatorname{sinc}(x) = \begin{cases} 1, & t = 0 \\ \frac{\sin(\pi x)}{\pi x}, & t \neq 0 \end{cases} \tag{5.2.4}$$

5.2.2 Local Time Stepping

When the most restrictive time step is found in the closure relation accuracy criterium, the local time step could be used. This means that in the whole model the Courant stability time step is used, but in the elements in the neighborhood of the closure relation a different time step is used. This last time step is the one that allows to guarantee the accuracy in the closure function computation.

This technic avoids the new restriction in time step to be extended to the whole domain, increasing dramatically the computation cost of the modeling.

Also more sophisticated techniques could be used, the frequency filter could be applied in a piecewise fashion, this means to apply different thresholds to different parts of the closure function, allowing the maximum time step to be adapted to the requirements of the function smoothness.

5.2.3 Bivariate Closure Relations Extension

The theory has been explained for a closure relation depending in one variable, for example the free weir discharge (Figure 5.1), hu is computed using the upstream depth of the weir h, so $hu = f(h)$.

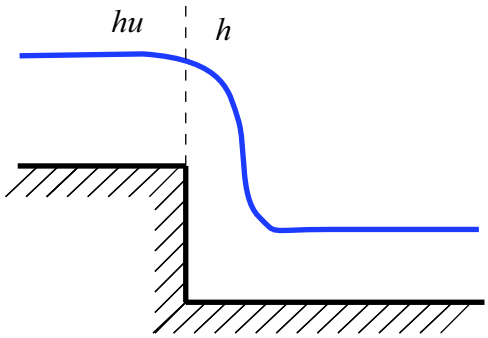

Figure 5.1: Step in channel, it behaves as a weir.

In hydraulics bi-dimensional closure relations are classical, for example a submerged weir (Figure 5.2, left side), where the discharge through the structure depends on the water level upstream and downstream of the structure. In the right part of the Figure 5.2 the closure equations are shown, every line corresponds to different h_2 values, so for every upstream water level a curve is defined.

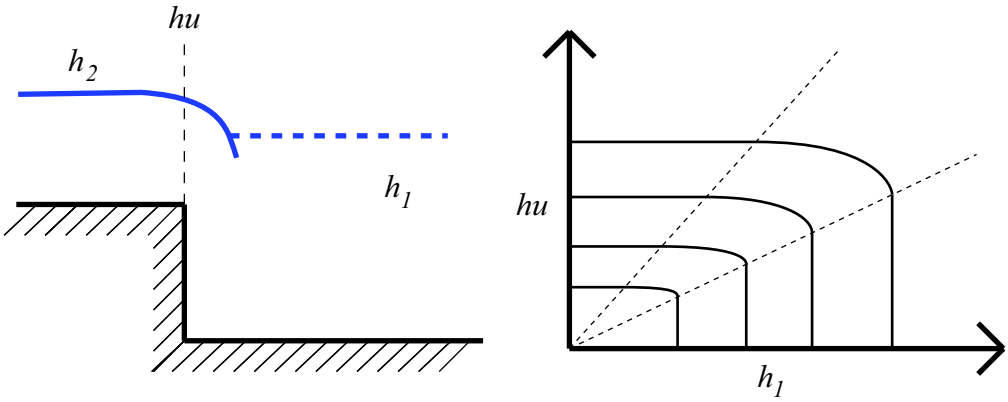

Figure 5.2: Step in channel, it behaves as a weir.

This means that the relation is $hu = f(h_1, h_2)$, so the accuracy condition should be extended to include these bivariate relations. The modification is direct, first the bi-dimensional Fourie transform should be introduced, using the variables p, q:

$$F(\mathbf{k}_1, \mathbf{k}_2) = \int_{-\infty}^{+\infty} \int_{-\infty}^{+\infty} f(p, q)\, e^{-i\mathbf{k}_1 p} e^{-i\mathbf{k}_2 q} \mathrm{d}p\mathrm{d}q\,. \tag{5.2.5}$$

And now the accuracy condition is equal to the previous one but imposing different restrictions on the time step depending on the maximum frequency of every variable.

$$\begin{cases} \Delta p \leqslant \frac{\pi}{k_{1\,MAX}}, \\ \Delta q \leqslant \frac{\pi}{k_{2\,MAX}}, \end{cases} \tag{5.2.6}$$

where $k_{1\,MAX}, k_{2\,MAX}$ are the maximum wave numbers for the dependent variables respectively.

5.3 Practical Example

In this section an example of the proposed algorithm will exposed. In this case the one-dimensional SWE will be used:

$$\begin{gathered} \mathbf{q} = \begin{pmatrix} h \\ hu \end{pmatrix}, \\ \begin{cases} \dfrac{\partial h}{\partial t} + \dfrac{\partial hu}{\partial X} = 0, \\ \dfrac{\partial hu}{\partial t} + \dfrac{\partial \left(u^2 h + g_3 \frac{h^2}{2} \right)}{\partial X} = 0, \end{cases} \end{gathered} \tag{5.3.1}$$

where X, t are an independent variables and h, hu are the dependent variables. This equation will be applied in the whole domain except in a cell interface, where a modified weir equation will be used:

$$hu = f(h) = \sin(4\pi(h-3))\left(1.3^{h-3} - 1\right) + \left|1.3^{h-3} - 1\right|. \tag{5.3.2}$$

The modifications of the equation are introduced to obtain a complex, nonlinear equation, to demonstrate the effect of the proposed algorithm. In Figure 5.3 the graph of the Equation 5.3.2 is shown. Its clear that the shape of the curve is not simple.

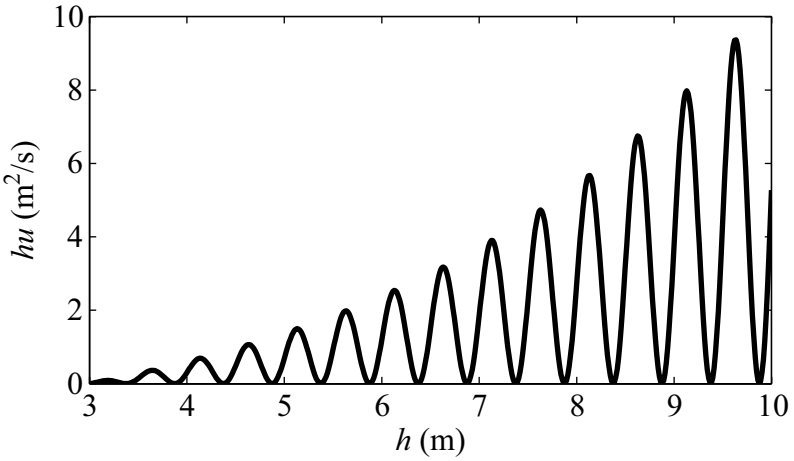

Figure 5.3: Discharge equation for the hypothetic weir.

As has been stated in the methodology description, once the function is defined, the spectrum of the equation should be analyzed. In this case, in Figure 5.4, the result is shown. Here the spectrum's upper limit is 30 Hz. However the cutting frequency is selected to be 2.5 Hz, because most of the information is considered to be in the lower part of the spectrum, below this frequency.

Once the threshold frequency is selected the sampling of the signal at double frequency is carried on, the result of this sampling is shown in Figure 5.5. The output is a series of values, at 5 Hz, i.e. this means 5 values per depth meter (h).

Once the sampling is finished the new filtered closure function $\bar{f}\,(h)$ will be constructed, for this construction the Equation 5.2.4 is used.

In Figure 5.6 the filtered function $\bar{f}$ is shown, the construction of $\bar{f}$ using the *sinc* functions is carried on as a sum of infinite terms, in the figure, the blue line is the reconstructed function using the first 21 samples, and the red line is the next *sinc* function associated to the sample number 22, this last function should be added to the blue line, and move to the next sample (23).

In the lower part of Figure 5.6 the reconstructed function $\bar{f}$ is presented. The

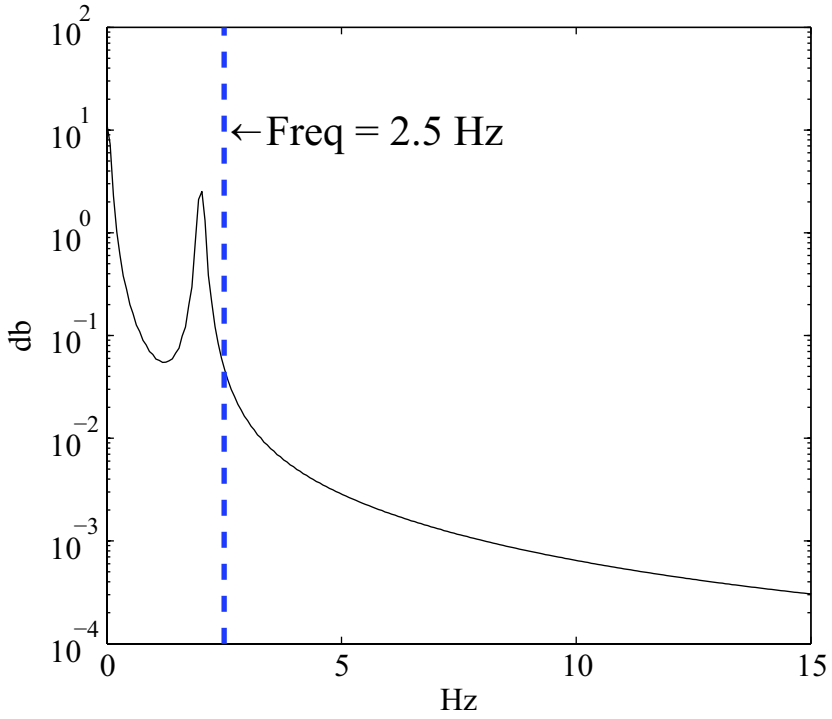

Figure 5.4: Energy spectrum of the discharge equation.

reconstruction uses the first 21 function f samples. The original function f is compared. It is clear that the filtered version of the function fits well the original equation, although it is created using a few amount of discrete samples.

The Figure 5.7 shows the existing error between the filtered version and the original one, recall that only the first 21 terms of the series are used in the reconstruction of the shown function.

With the original function f and the filtered version $\bar{f}$ a test case will be carried on, first using the standard version with the Courant time step restriction and the f weir equation, and the second case will be computed using the proposed algorithm and the filtered weir equation $\bar{f}$. Recall that the threshold frequency was 2.5 Hz, this means that the accuracy criterium is fulfilled with a double frequency, so 5 Hz, therefore, as agreed in Equation 5.2.2, the maximum depth increments per time step should be 0.2 meters.

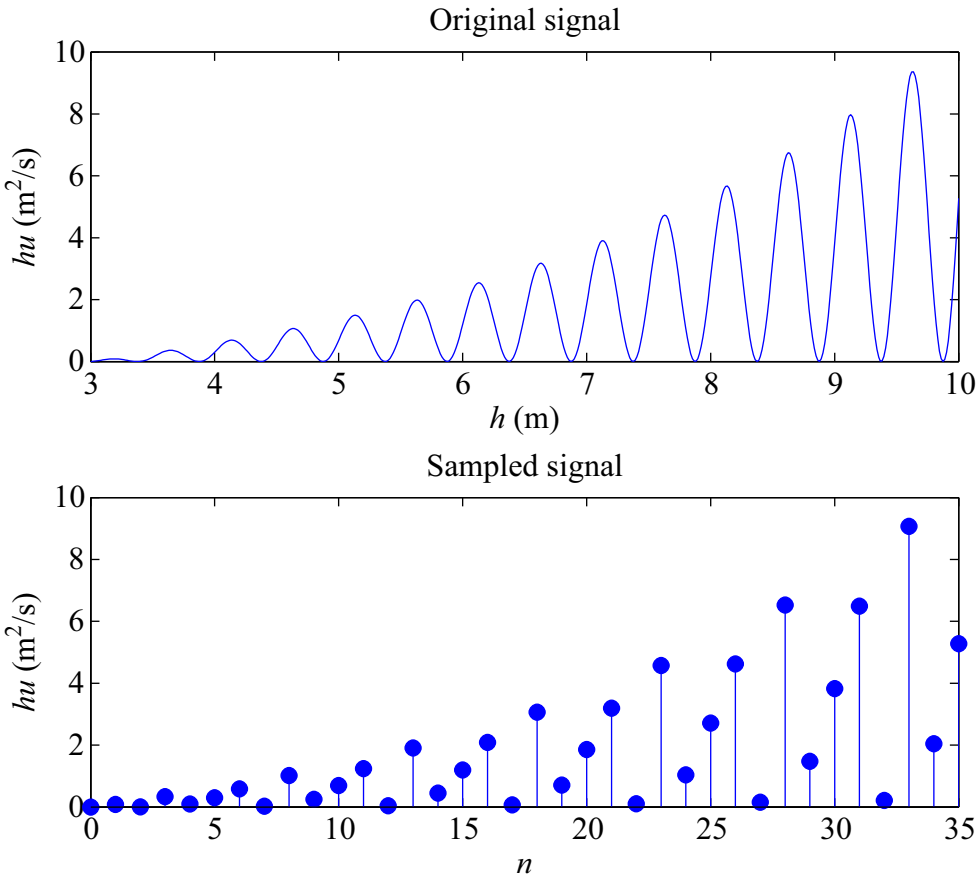

Figure 5.5: Sampling of the discharge equation using a 5 Hz frequency.

The test case is a ten meters long channel, with an initial condition of water at rest with a 2 meters depth. The weir is introduced in the middle of the channel, with 5 meters upstream and 5 meters downstream. The boundary conditions are corresponding to a subcritical regime, downstream 2 meters depth and upstream 5 m^2/s.

In Figure 5.8 the channel scheme with the weir is shown, also the results obtained at $t = 0.6s$ are shown. The boundary conditions have a constant discharge of 5 m^2/s, so as it's shown in the results, a wave is coming from the upper part of the channel, because the initial conditions were water at rest.

In the time evolution of the solution, the wave achieves the weir and when the

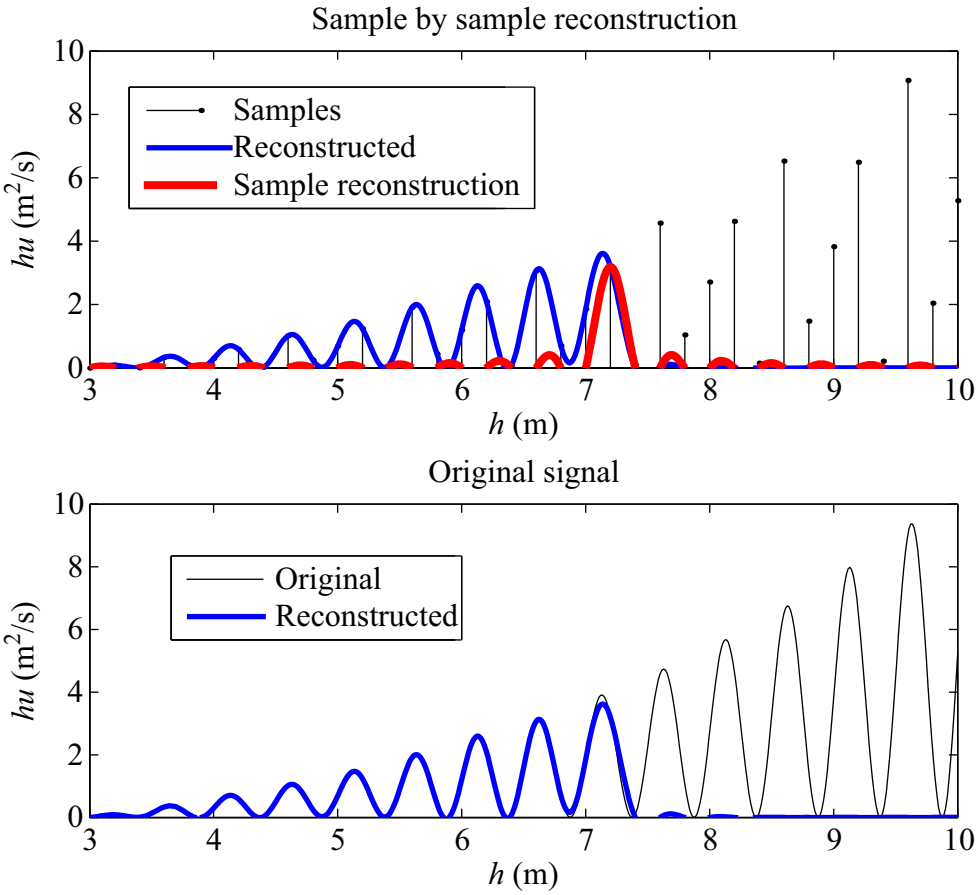

Figure 5.6: Reconstruction of the signal using a low pass filter. The red line is the sample reconstruction using *sinc* function and the blue line is the cumulative signal obtained adding the previous samplings (created with "Samprecon", developed by Tor Ramstad, Anders Gjendemsjo, 2003).

water level is below 3 m the discharge is null, so a filling process is carried on in the weir upstream part, until it reaches 3 meters. When this value is reached the discharge initiates, always fitting the weir discharge equation.

In the first case, as was commented, the new accuracy criterium is not used, then the time step is defined using the CFL condition. The discharge over the weir is computed using the original function equation f, at some time steps, the depth step is larger than 0.3 meters (> 0.2m), this means fail to fulfill the accuracy criterium, and also for this especial test case instability.

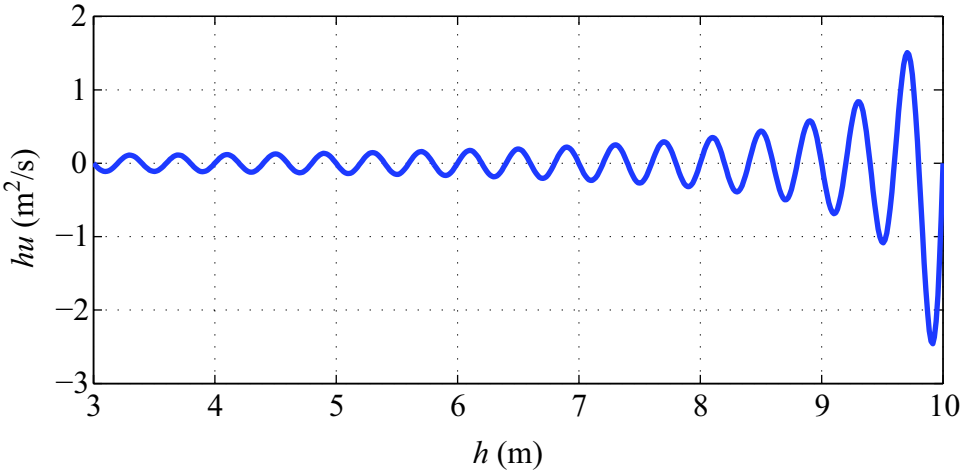

Figure 5.7: Error in the discharge equation reconstructed using a low pass filter.

This instability is due to the fact that a bat curve fitting implies jumps between different periods in the discharge equation (Figure 5.3) and a strongly discontinuous discharge, so, at the end, a instable discharge is obtained.

In Figure 5.9 the different results in the weir are shown, in the upper part the depths time series is shown, the instability is evident, continuous jumps appear in the depth. In the middle graph the discharge appears, its clearly unstable, with strong jumps and discontinuities. To try to analyze the discharge curve fitting a plot of depth vs. discharge is done in the lower part of the figure. The shape of the line recalls vaguely to the original curve (Figure 5.3), but with strong mistakes.

On the other hand, in the second test case the proposed accuracy algorithm is used, the results could be found in the Figure 5.10, the results are completely different, in this case the depth and the discharges are stable and continuous and the modified curve $\hat{f}$ its perfectly fitted.

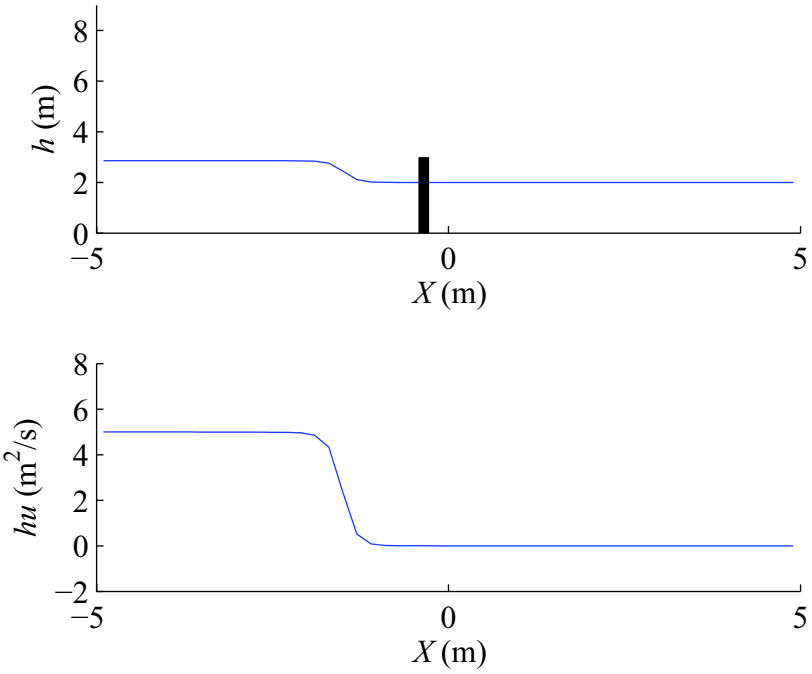

Figure 5.8: Test case results obtained at $t = 0.6s$, the black thick line is the weir position.

5.4 Conclusion Of The Chapter

The proposed accuracy criterium improves the computation in the internal boundary conditions, its straight to adapt it to multidimensional equations and could also avoid the instabilities due to the internal boundary condition.

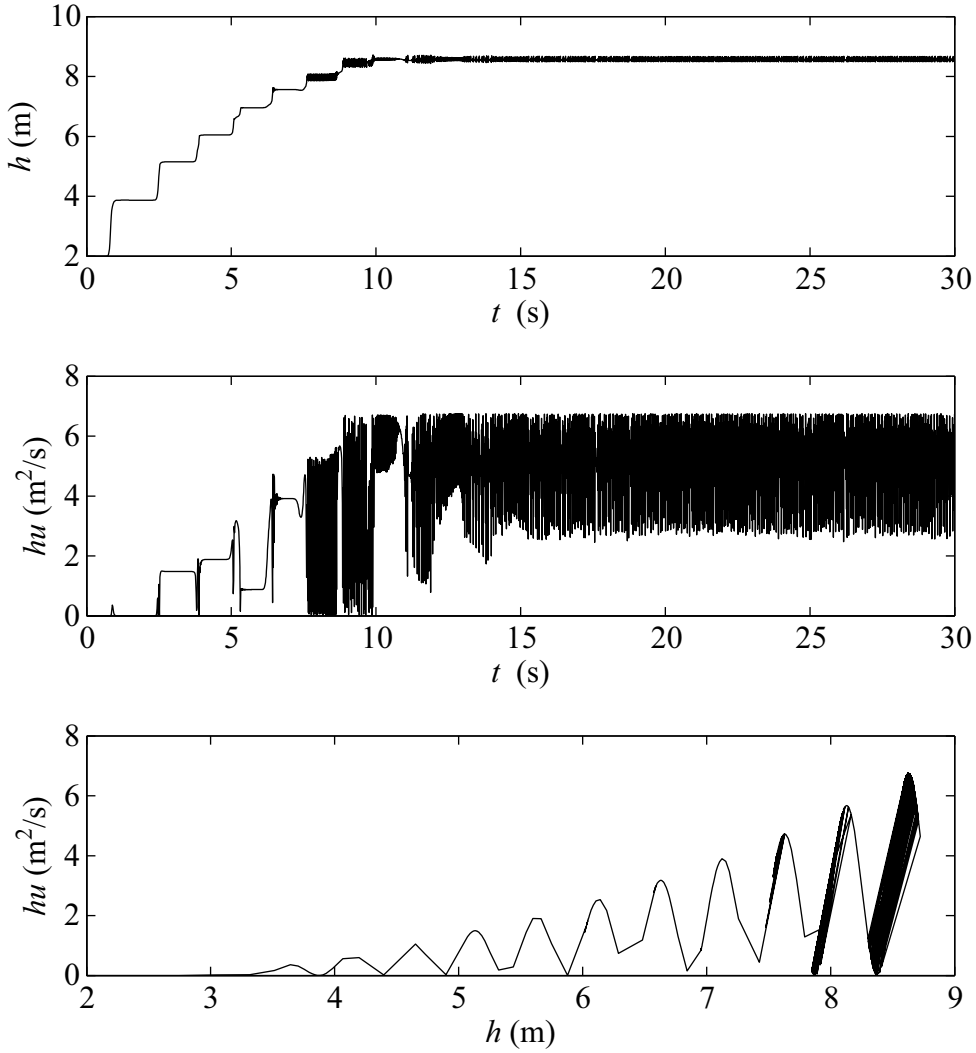

Figure 5.9: Results for discharge equation using the non corrected stability criterion.

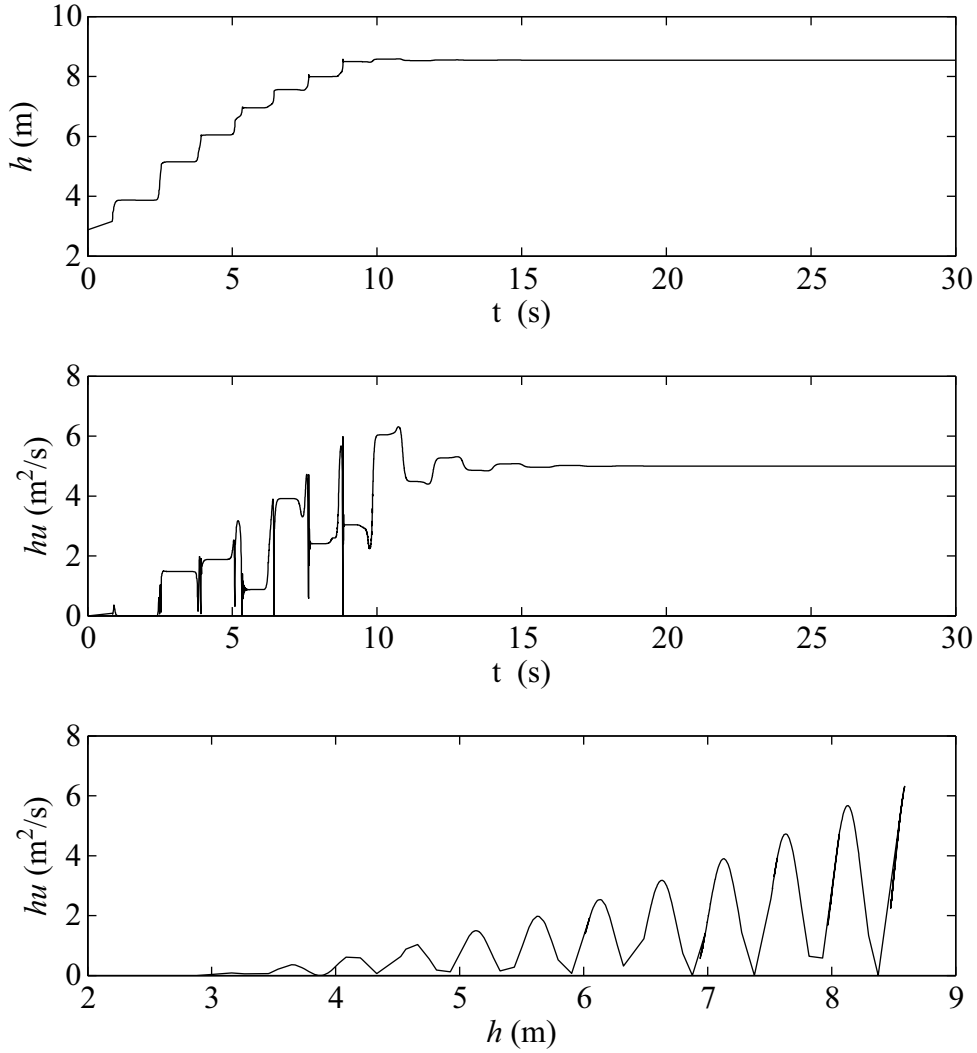

Figure 5.10: Results for discharge equation using the corrected stability criterion.

Chapter 6

Special Features of the Debris Flow Modeling

The main governing equation of the debris flow modeling have been defined in Chapter 2. Also the rheology details have been stated. However there are still some special elements related to the steep slope flow modeling that should be implemented in the model to increase the performance of the results. This chapter includes a couple of these different elements.

6.1 Introduction

In this chapter we consider three main aspects of debris flow modeling. They are:

1. Stop and go mechanism
2. Entrainment process
3. Rheology adaptation

The first one, the "Stop and Go" mechanism is the implemented method to simulate the deposition of the material during the flow. Rheologies that imply *yield stress* (e.g. Bingham, Voellmy, Herschell Bulkley...), characterize the stop and go mechanism in debris flow.

Once the fluxes are computed, maybe the results make us thought that a cell was not moving. So, the material was deposited. In this case the computations have to be repeated until the fluxes are only computed in moving cells.

This creates a problem of iterating numerical method. As it is clear, to iterate means to increase the computational time. However there is no guarantee of success or convergence. To avoid this additional load an algorithm is developed and implemented in the model.

The second feature refers to the entrainment process, this is one of the major unknowns in the debris low modeling. Although it plays an important role in the process. Several references could be found in Hungr and Evans (2004*b*), the total material mobilized in a debris flow event could be the 6 or 7 times the initial volume. A very basic approaches are introduced in the model as a first step in the entrainment modeling research.

The third question is related to the rheology evolution. In granular media mechanics, it is known that the friction laws may depend on the velocity of the process, at least the static internal friction and the dynamic one are considered (Da Cruz, 2004; MiDi, 2004). This fact is introduced in the friction laws, the internal friction angle existing in granular rheologies (Coulomb, Voellmy) evolves with the velocity, following the previous idea. In Pudasaini and Kr
"oner (2008) is shown that the rheology depends on the flow configuration and flow dynamics.

6.2 Stop and Go

Due to the dynamics of the flow and the rheology, the material may stop its motion due to friction, or, start the motion again influenced by the surrounding activities. This is not easily handled in an explicit scheme, and it is important to apply some numerical restrictions in order to have a good evaluation. The problem is to define:

the meaning of cell repose state. It is not only a zero velocity cell. In an explicit method the fluxes at the cell faces are evaluated first, and then the frictional term is calculated. If the friction force is sufficient to stop the flow at the cell, it should stop. However, in this calculation process the cell moves and the material flows.

To avoid this numerical problem we have to define which cells are in repose state. The model presented operates in the following way: the model determines which cell is in motion or repose state, and calculates only those cells that really are in motion. Whether a cell with a zero velocity will be in motion or repose state depends on the surrounding cells flow dynamics. For this, a cell is in motion if the following three conditions are satisfied:

1. The cell was in motion in the last time step,

2. If the cell was stopped: Some of the neighborhood cells were in motion in the last time step. The presented model uses an explicit scheme controlled by the Courant number. Any wave or information that enters in a cell is incapable to flow throughout the front face of the same cell, because of the Courant restriction. This means that, any motion in a neighborhood cell can activate a zero velocity cell until the next time step. This is a chain process that activates cells through the neighborhood cell.

3. If the cell was stopped, a second check: The geometric slope of the free surface of the material is greater than the internal friction angle of the material. When the numerical models uses frictional rheologies the material tends to stop with higher slopes than the internal friction angle of the bed. The model incorporates a recalculation of zones in which the angle of the material is greater than the internal friction angle, until all the surfaces have less or equal slope to that of the material friction angle.

With this technique it is possible to in motion cells that had been stop before but receive material with sufficient momentum from the neighborhood cells. In a

Figure 6.1: La Guingueta case. "Stop and Go" example initial conditions.

complicated process a cell can be moved and stopped more than once; close to real phenomena.

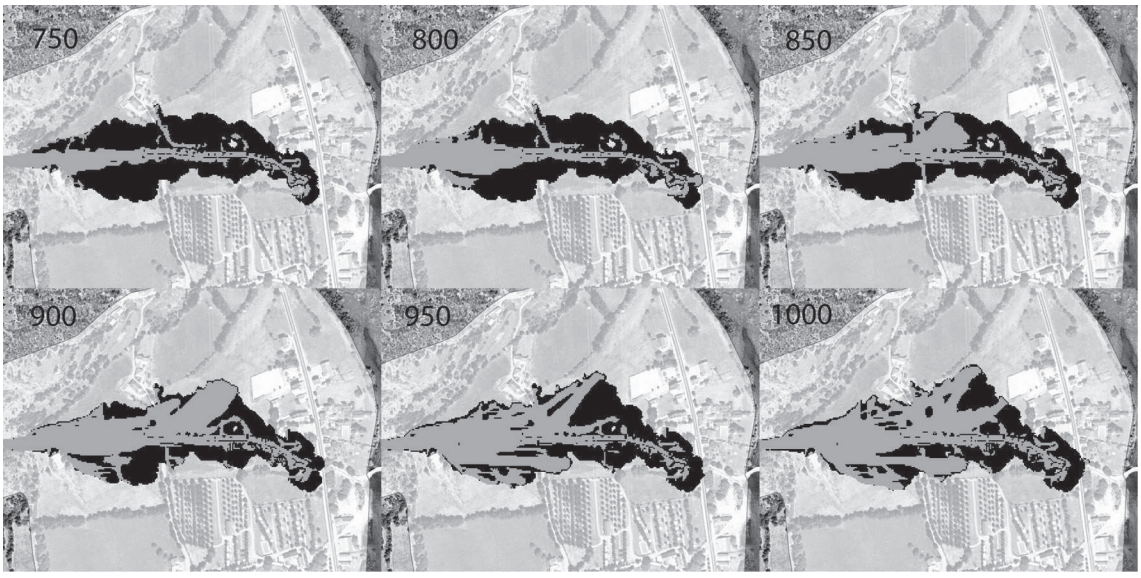

Figure 6.2: Time evolution of the stopped cells, the black color are stopped cells and the grey color are moving cells.

To illustrate the operation of the algorithm we will see an example, some results

of "La Guingueta" event, which will be explained later. In this simulation there's a first pulse that runs until it stops in the fan. Over this deposition we introduce a new pulse (Figure 6.1). This new pulse runs until the fan apex and collides with the first deposition. In this collision we observe a remobilization of the first pulse deposit. In Figure 6.2 it is possible to see different times for the collision. The time 0 seconds is the release time of the second pulse. The black color are the cells that contains stopped material, and the gray ones contains flowing material. As is shown in the figure the contact with flowing material changes the state of the cells from "stopped" to "flowing", the total amount of moving material is increased until it stops again.

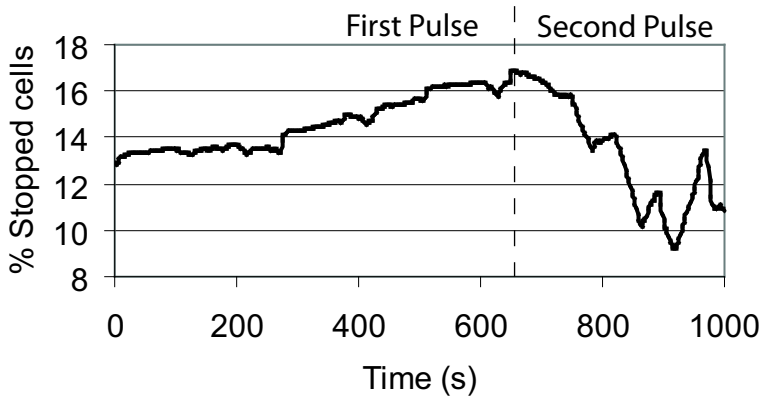

Figure 6.3: Time evolution of the stopped cells in the fan area.

In the Figure 6.3 a graph of the remobilization evolution is presented. The stopped cells are presented as % of the total fan area. As mentioned before the time 0 s. is the release time of the second pulse. As it is shown in the figure, until the 650 s. the first pulse is still stopping, the 17% of the fan area becomes stopped. After that time, the second pulse arrives and remobilizes the 50% of the previously stopped cells, being the new stopped area less than the 8.5%. The second pulse arrives with different waves. After the 900 s. the stopped area increases again, until the end of the simulation (2000 s.).

It is important to note that this method is strictly conservative, the change in

material state does not introduce new momentum or volume.

6.3 Entrainment Implementation

One of the most important factors that characterize debris flows is the basal incorporation or entrainment (Rickenmann et al., 2003). A volume of a few cubic meters of initial mass motion can incorporate, in some circumstances of slope and types of material, ten times or more the initial volume mobilized (Egashira et al., 2001). The bed stress of the flow can be sufficiently higher to incorporate part of the bed into the flow. We used two different approximations: static and dynamic.

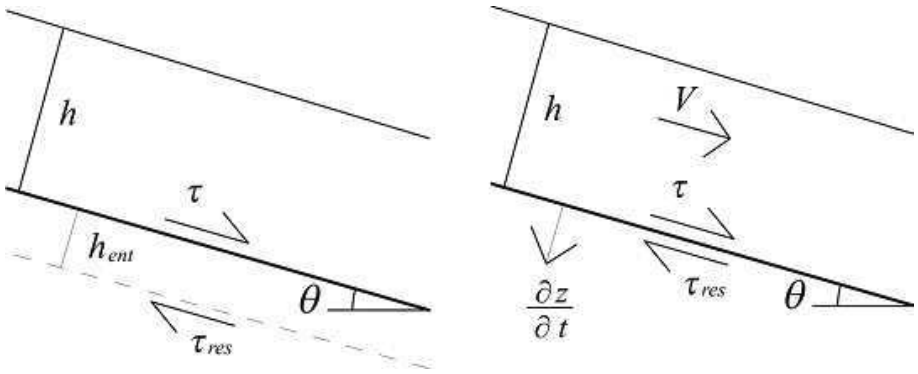

Figure 6.4: Entrainment: left static approach, right dynamic approach.

The static approach considers a static equilibrium with the terrain, in which the active forces and the resistance forces are in equilibrium. That is:

$$\tau_{res} = \tau_u, \tag{6.3.1}$$

where τ_{res} is the resistance force of the material due to the internal friction of the particles, and τ_u is the active force. If one uses the Mohr-Coulomb failure law for infinite slope, Equation 6.3.1 can be described as:

$$c + \cos\theta \left[h\rho_s - h_w\rho_w\right] g \tan\phi_{ent} = h\rho_s g \sin\theta, \tag{6.3.2}$$

in which c is the cohesion, ρ_s, ρ_w soil and water bulk densities respectively, h_w the water depth due to the water table level, and ϕ_{ent} the internal friction angle of the bed material. Because the model uses a homogeneous material, it cannot distinguish different materials (water and sediment). The water and sediment mixture is modeled solely by a bulk density ρ, even for the basal material. On the other hand, the acting forces to provoke a basal movement are the shear flow stress and the weight of the basal material that is incorporated in the flow (Figure 6.4 left). The relationship between the active and resistant forces is

$$c + \cos\theta \left[h + h_{ent}\right] \rho g \tan\phi_{ent} = \tau_f + h_{ent}\rho g \sin\theta, \tag{6.3.3}$$

where h_{ent} is the depth of the incorporated material (entrainment or erosion depth), and τ_f is the friction stress due to the flow movement (weight of the flow in the flow direction). The entrainment conditions can be established as:

$$\tau_f > c + \cos\theta h\rho g \tan\phi_{ent}, \;\; \cos\theta \tan\phi_{ent} > \sin\theta. \tag{6.3.4}$$

This implies that the active forces have to be greater than the resistance forces to provoke basal erosion. Fulfilled the condition 6.3.4 is straight to calculate h_{ent}:

$$h_{ent} = \frac{\tau_f - (c + \cos\theta h\rho g \tan\phi_{ent})}{\rho g \left(\cos\theta \tan\phi_{ent} - \sin\theta\right)}. \tag{6.3.5}$$

Once the depth of entrainment h_{ent} has been calculated, it is necessary to conserve the momentum of the cell induced by the new mass. Obviously the resultant velocity diminishes due to entrainment.

For the dynamic equilibrium approach (Figure 6.4 right), the hypothesis is nearly the same to the static approach, which assumes that the resistance of the material is Coulomb type. If the active forces are greater than the resistance, entrainment occurs. The difference is that the newly incorporated material is accelerated with the mean velocity of the flow, and then the quantity of newly incorporated mass depends on the availability of momentum, i.e.,

$$\frac{\partial z}{\partial t} = \frac{1}{\rho V}(\tau_f - \tau_{res}), \tag{6.3.6}$$

in which $\frac{\partial z}{\partial t}$ is the velocity of entrainment, τ_{res} the resistance force of the material and V the mean flow velocity. Fraccarollo and Capart (2002) represented this methodology by:

$$\frac{\partial z}{\partial t} = \frac{1}{\rho V}(\tau_f - c - (1-\lambda)\cos\theta h \rho g \tan\phi_{ent}), \tag{6.3.7}$$

where the formulation includes a parameter λ (Iverson and Denlinger, 2001) to define the pore pressure that varies between 0 (dry debris) and 1 (completely saturated debris). This parameter indicates which part of the pressure corresponds to the effective stress and which part to the pore pressure. Note that in Equation 6.3.4 the factor $(1-\lambda)$ is the multiple of $\tan\phi_{ent}$.

It is difficult to estimate values for λ, because this parameter is related to pore pressure. Pore pressure plays an important role in debris flow dynamics (Iverson and Denlinger, 2001; Savage and Iverson, 2003) and it evolves in time as well as changes from head to tail. As a consequence, the application of a constant value for λ is a rough but common approximation (Pudasaini et al., 2005). The limitations of this approach is analyzed by Savage and Iverson (2003) and Iverson and Denlinger (2001). To achieve accuracy in the calculation of λ, it is necessary to use complex equations. Thus, an advection diffusion system should be solved (Iverson and Denlinger, 2001). Due to the uncertainty in its calculation, in our model, a constant value of this parameter is used to calculate the entrainment rate. Since the values of λ are low in granular debris flow, we adopt a value of 0.3 (Pudasaini et al., 2005).

The active force in the bed is evaluated from the rheology of the material and the resistance force due to Coulomb relationship. Thus, if one uses the Coulomb model as rheology the difference between the two forces is zero. To avoid this problem, the present model uses different values for the internal friction angles of the flow and the basal material.

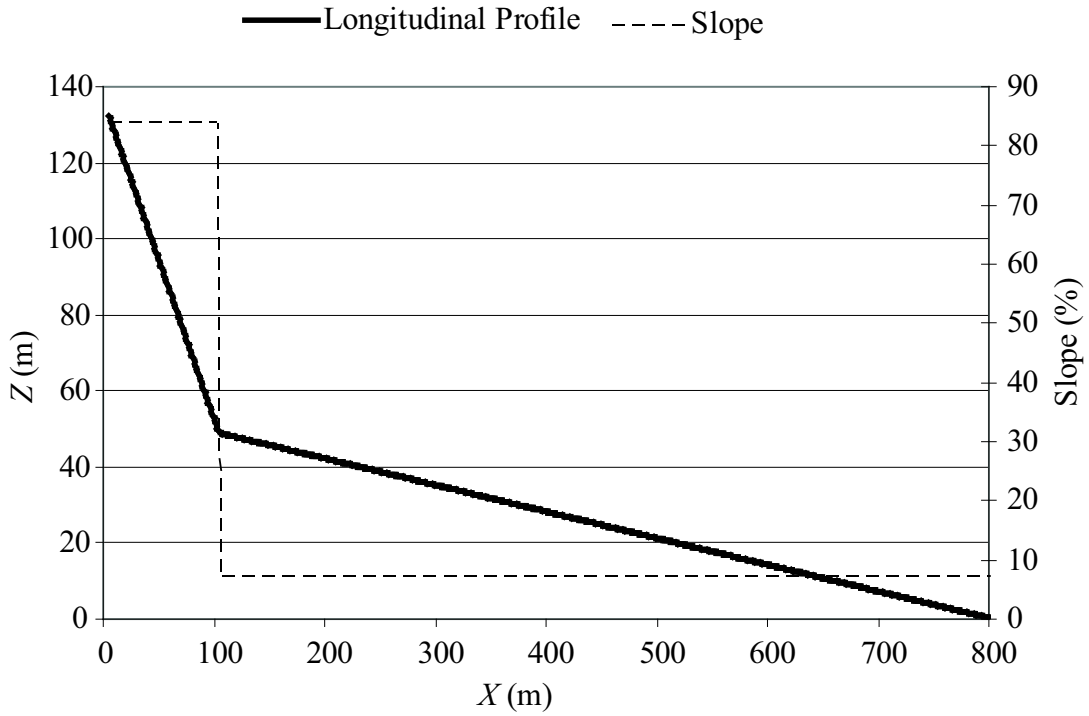

Figure 6.5: Channel used to test the entrainment computation.

To validate the dynamic approach, some preliminary computations were made using theoretical cases. A horizontally 800 m long channel was defined including in the first 100 m a steep slope with inclination of 40 ° followed by part of 4 ° inclined (Figure 6.5). The initial amount of material was 100 m^3, the material is planed at the upper part of the channel. Erosion depth is not limited at depth along the whole channel. The entrainment was tested using the Voellmy fluid model and different rheological parameters (ϕ, C).

Then the total amount of newly incorporated material from the bed was calculated for different ϕ_{ent} values. Figure 3b shows the influence of the friction angle of the bed material on the flow volume for two different Voellmy configurations. The rheology is used to calculate τ_f:

$$\text{A} \begin{cases} C = 10 \\ \tan(\phi) = 0.065 \end{cases}, \qquad \text{B} \begin{cases} C = 20 \\ \tan(\phi) = 0.065 \end{cases}. \tag{6.3.8}$$

The parameter ER (Entrainment Rate) relates the final flow volume to the initial one. In Figure 6.6 the results obtained for the A Voellmy configuration are shown, the parameter ϕ_{ent} has an important influence in the total entrainment.

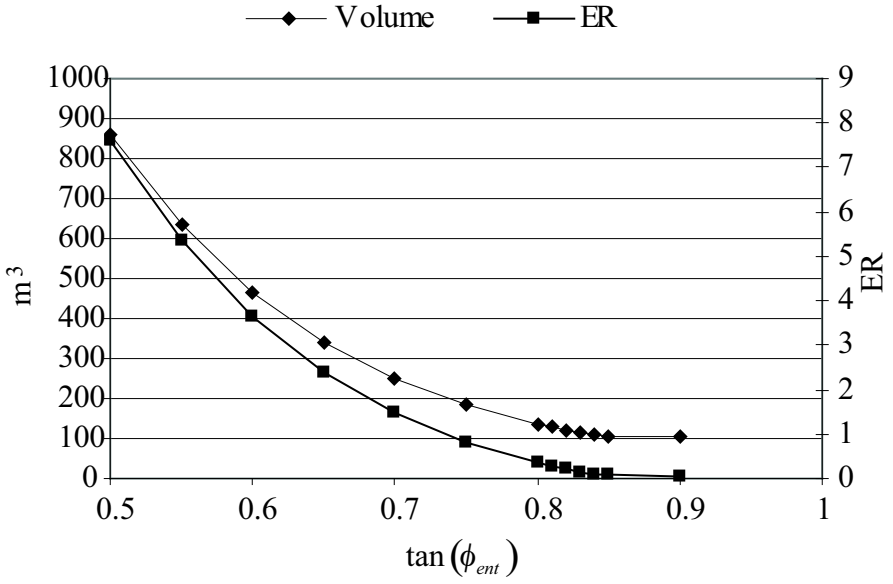

Figure 6.6: Results obtained with the configuration A, for different value of ϕ_{ent}.

The second configuration (B) results are shown in Figure 6.7, as its clear the total volumes obtained are clearly lower than the previous ones, so both, Chezy parameter and entrainment friction angle are important for the total volume.

However, it should be mentioned that, if the static approach would have been used, the entrainment angle ϕ_{ent} could not have been smaller than the slope angle θ. If this occurs, an unstable situation is reached, with a infinite amount of eroded material. In the presented case the dynamic approach was applied.

In Figure 6.8 the time evolution of the flow volume is shown, the erosion occurs at

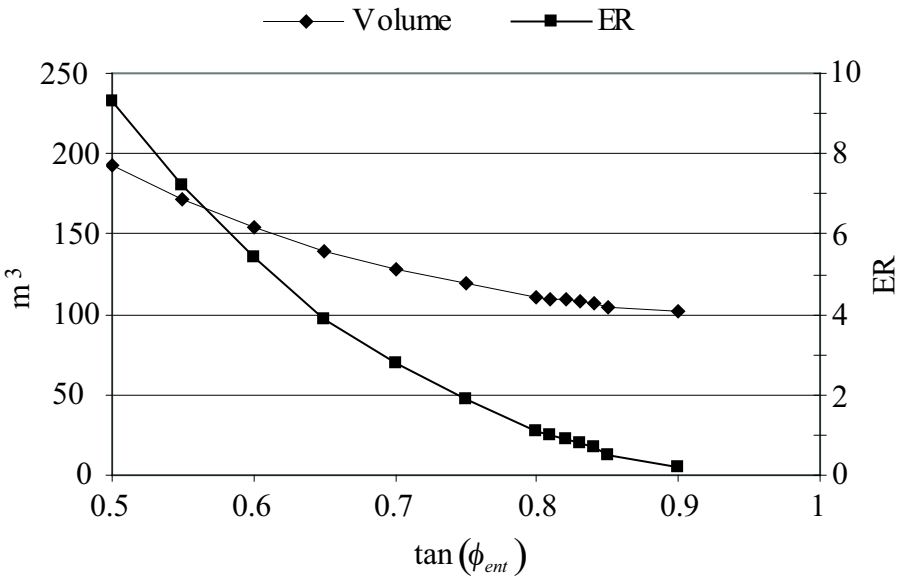

Figure 6.7: Results obtained with the configuration B, for different value of ϕ_{ent}.

the beginning of the event, so in the steeped part of the channel, the case presented is A with $\phi_{ent} = 35\,^{\circ}$, the total volume at the end of the simulation is 250 m^3.

In Figure 6.9 the eroded profile and the final deposit are presented, the maximum erosion is 2.8 meters, and it's clear that the deposition initiates when the channel slope is smaller than Voellmy configuration parameter ϕ.

Finally, the dynamic entrainment approach was tested in one test case (Cardemeller torrent at Pal), because of detailed field data on initial and final volume of the debris flow. The other two cases were simulated without the entrainment approach in order to simplify modeling.

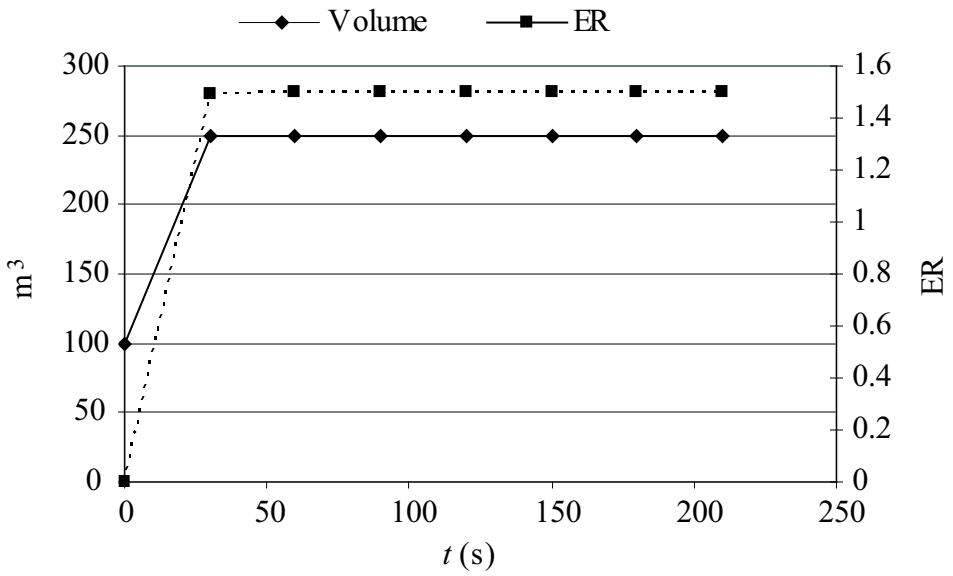

Figure 6.8: Volume evolution with the time, for the case A, with $\phi_{ent} = 35\,^{\circ}$.

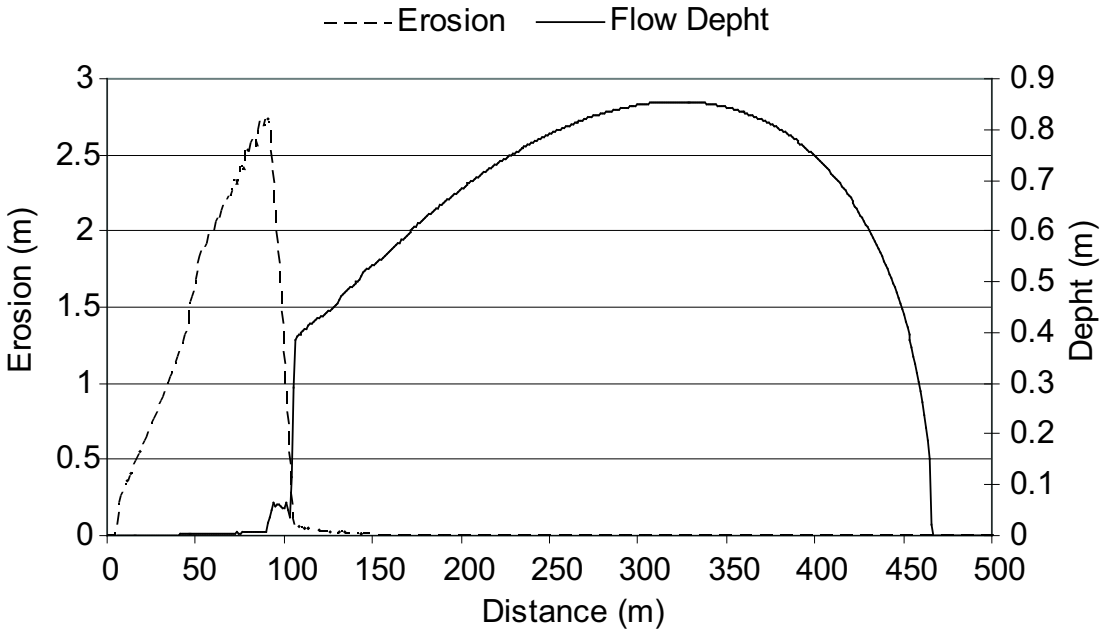

Figure 6.9: Longitudinal profile of the deposition and the basal erosion along the channel.

6.4 Rheology adaptation

If the simulations use the Voellmy rheology for numerical modeling, the front inclination of the final deposit is normally similar to the Voellmy parameter ϕ. However, ϕ-values are far from the static dry internal friction angle, ϕ_{stat}, which governs the slopes in the deposit boundaries of debris. In order to simulate this behavior the Voellmy parameter ϕ has to be changed dynamically during the simulation. This ϕ-adaptation is of crucial relevance during the accumulation phase, when the flow is near to stop. The model implements a correction of this feature increasing the ϕ-value, if flow velocity is lower than a selected limit V_1 (Figure 6.10). The magnitude of ϕ changes linearly from the initial friction angle to the static dry internal friction angle.

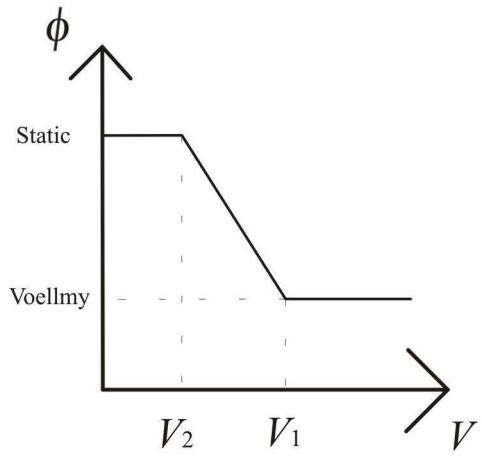

Figure 6.10: Voellmy internal friction angle ϕ evolution with the volocity.

Chapter 7

Validation Test Cases

In the previous chapter all the elements of the model have been defined, in the present chapter some calibration cases are used to validate the model. Previously to the application of the model to real cases it should be tested and calibrated. In validation process several errors and inaccuracies are found. Some of them correspond to code bugs and the remain ones belong to model theoretical background weakness. In the previous chapters several hypothesis were applied to develop and simplify the physics of the model. Every hypothesis constrains the model applicability range, specially dealing with curved surfaces.

7.1 Introduction

It is known that the analytical solutions for nonlinear SWE are only obtained for some especial cases, one dimensional flows with some restrictions on the slopes and the friction approaches. There are no analytical solution for a purely bi-dimensional debris flow. So, analytical solutions for the one dimensional cases will be used. Also an experimental results obtained in the USGS laboratory and in the UPC-GITS laboratory are used to test the model.

- Analytical, ideal, frictionless, flat, dambreak.
- Analytical one-dimensional dambreak with steep slope and friction.

- Experimental UPC-GITS bi-dimensional dambreak.
- Experimental USGS bi-dimensional debris flow.

7.2 Ideal Dambreak Scenario

The first validation test is the frictionless, flat surface, dambreak. The solution to this problem was first given by Stoker (1957), the dam is placed at the coordinate $x = 0.0$ (see Figure 7.1) and the test case initial conditions are:

$$g = 9.81,\ h_l = 1,\ hu_l = 0,\ h_r = 0.5,\ hu_r = 0,$$

where the values with the l subindex refers to the variable at the left side of the dam, on the contrary the r subindex refers to the values found in the right side of the dam. As its shown in the initial conditions, the gate at 0.5 m coordinate acts as a dam, separating the upper part of the channel, with a 1 m depth and the lower part of the channel with 0.5 m depth.

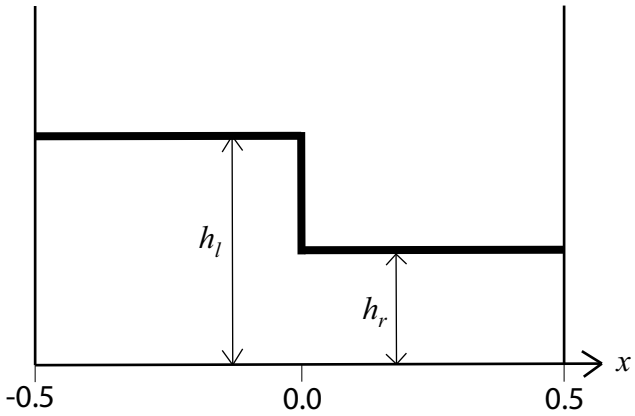

Figure 7.1: Dambreak problem used to test the Stoker analytical solution.

All the framework previously developed, related to the Riemann solver could be applied here to obtain, numerically, the solution to the proposed dambreak. In Figure 7.2 the problem is solved and the resulting waves shown, the solution is composed by two different functions, a shock in the right side and a rarefaction in the left.

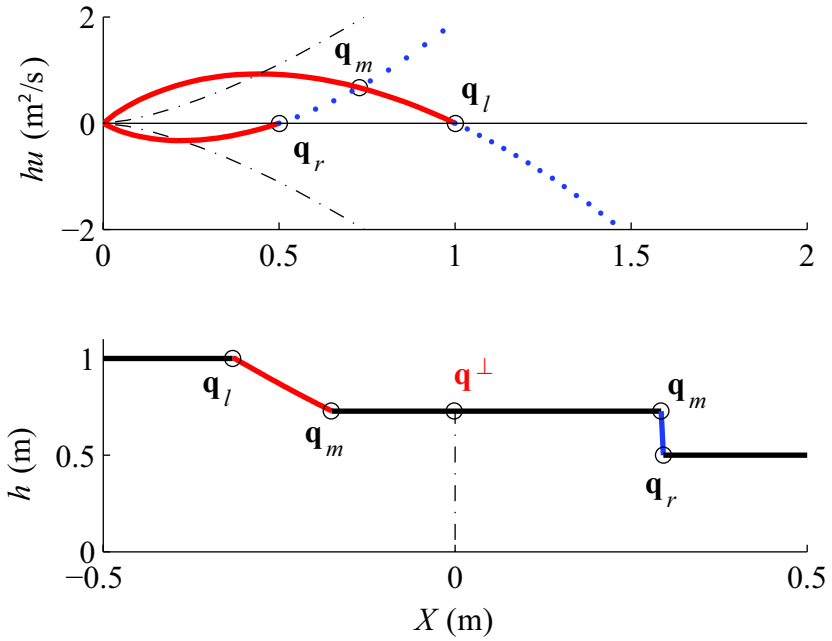

Figure 7.2: Solution to the dambreak problem proposed, a shock wave and a rarefaction are found connecting the initial states at both sides of the dam. The description of the figure curves could be found in Chapter 4.

The obtained Riemann problem solution (Whitman, 1974; Stoker, 1957)is:

$$\mathbf{q}_m = \begin{pmatrix} h_m \\ hu_m \end{pmatrix} = \begin{pmatrix} 0.7269\,\mathrm{m} \\ 0.6712\,\mathrm{m}^2/\mathrm{s} \end{pmatrix}. \tag{7.2.1}$$

Using this values is possible to compute the different velocities to construct the waves, first the shock wave velocity:

$$\lambda_2 = (hu_r - hu_m) \;/\; (h_r - h_m) = 2.9579\,\mathrm{m/s}. \tag{7.2.2}$$

As was explained in the corresponding chapter, the SWE nonlinear problem solutions, in general, could not be expressed as a waves sum, this is the case of the rarefaction presented in the left side of the solution, there is not a characteristic speed of the wave, two different velocities are found for the rarefaction instead.

$$\begin{aligned} \lambda_a &= \sqrt{gh_l}, \\ \lambda_b &= \frac{hu_m}{h_m} - \sqrt{gh_m}. \end{aligned} \tag{7.2.3}$$

These three different velocities (Equations 7.2.2, 7.2.3) define the position of the characteristic points in the solution:

$$x_a = 0.5 - \lambda_a,\ x_b = 0.5 - \lambda_b,\ x_c = 0.5 + \lambda_2. \tag{7.2.4}$$

These characteristic points and the corresponding solutions could be seen in the Figure 7.3, compared to the numerical solution obtained using the model. The version used was the first order one, the excessive diffusion of the first order discretizations appears clearly, specially in the shock neighborhood.

In the following example the second order discretization is used to avoid the excesive diffusion ad to obtain best fitting of the theoretical solution.

7.3 Dambreak Scenario With Friction And Slope

The dam-break scenario presented by Mangeney et al. (2000) involves movement of debris in a wide channel inclined by θ. The resistance to the debris flow generated on the channel bed is characterized by an angle of friction, ϕ. In Figure 7.4 the geometrical description is shown, the problem is a dambreak case, but with especial features, a slope and also basal friction.

The proposed case is similar to the previous one, but the dry situation is found in the right side of the dam, when the slope and the internal friction angle are discarded, the solution moves from the Stoker (1957) to the Ritter (1892).

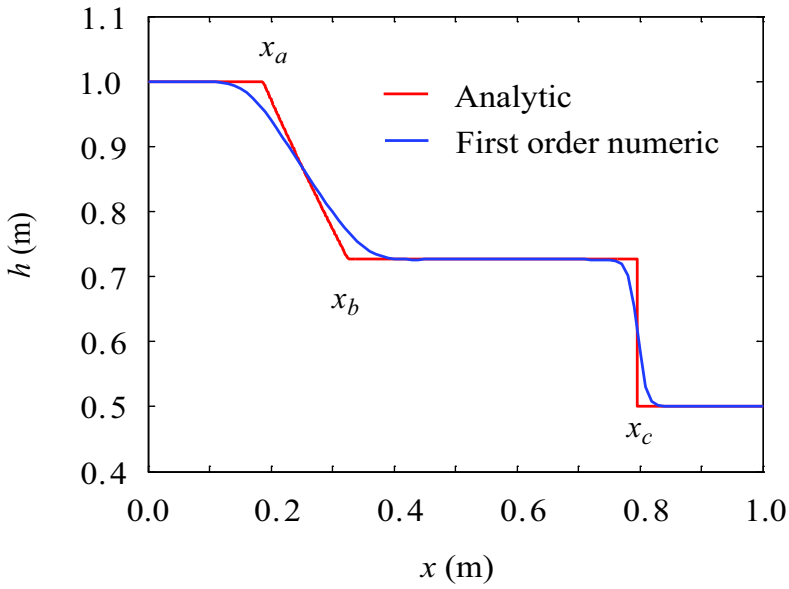

Figure 7.3: Comparison of the theoretical results to the numerical ones, the test case is the classical Stoker (1957) dambreak solution, the simulation is using the first order approach.

In Mangeney et al. (2000) the analytical solution for the problem with slope and internal friction angle is found:

$$h(t) = \begin{cases} H & x \leqslant -x_r \\ \frac{1}{9g\cos g\theta}\left(2c_0 - \frac{x}{t} - \frac{1}{2}mt\right)^2 & -x_r < x < x_l \\ 0 & x_l \leqslant x \end{cases} \tag{7.3.1}$$

Where:

$$\begin{aligned} x_r &= c_0 t + \frac{1}{2}mt^2, \\ x_l &= 2c_0 - \frac{1}{2}mt^2, \\ m &= g\left(\cos\theta\tan\phi - \sin\theta\right), \\ c_0 &= \sqrt{gH\cos\theta}. \end{aligned} \tag{7.3.2}$$

Here one principal test was carried out, where the initial depth of debris H is taken as 10 m, the channel bed inclination, θ, and the angle of friction, ϕ, are taken

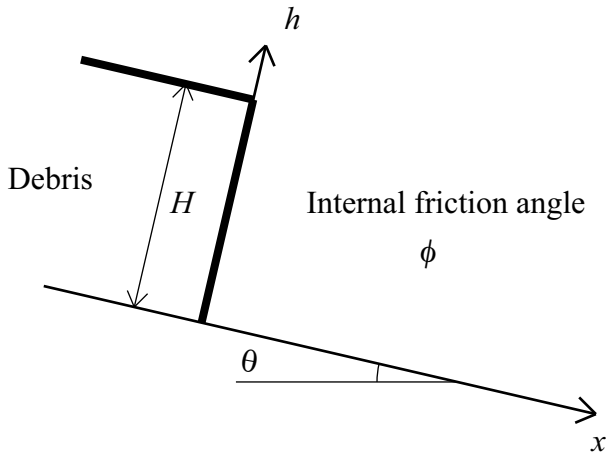

Figure 7.4: Geometrical description of the case proposed by Mangeney et al. (2000), the geometry has a constant slope θ and the material has an internal friction angle ϕ.

as $\theta = 30\,^\circ$ and $\phi = 25\,^\circ$ respectively. Simulated flow profiles were calculated at every 10-second interval, up to 30 seconds after the dam removal. Another test case was calculated to compare results for $\theta = 0\,^\circ$ and $\phi = 0\,^\circ$, but taking the initial depth as $H = 20\,\mathrm{m}$.

In our first example, flow movement was simulated for an initial depth of debris of 20 m, a horizontal channel and zero friction at the bed (Figure 7.5a). The flow profile simulated by the numerical model at 10 s indicates that numerical results are identically as the analytical ones. In our second example, the initial depth of debris was taken as 10 m, the channel inclination as $\theta = 30\,^\circ$ and the basal friction angle as $\phi = 25\,^\circ$. Figure 7.5b illustrates flow profiles at 10, 20 and 30 s indicating some minor differences between numerical and analytical results. These differences may affect maximum front velocity of a granular flow, but seem to be acceptable for our debris flow simulations. In contrast to the previous example, here the second order space corrections have been introduced to improve the results. Differences between the numerical results and analytical solution could be reduced by applying a Runge-Kutta temporal discretization.

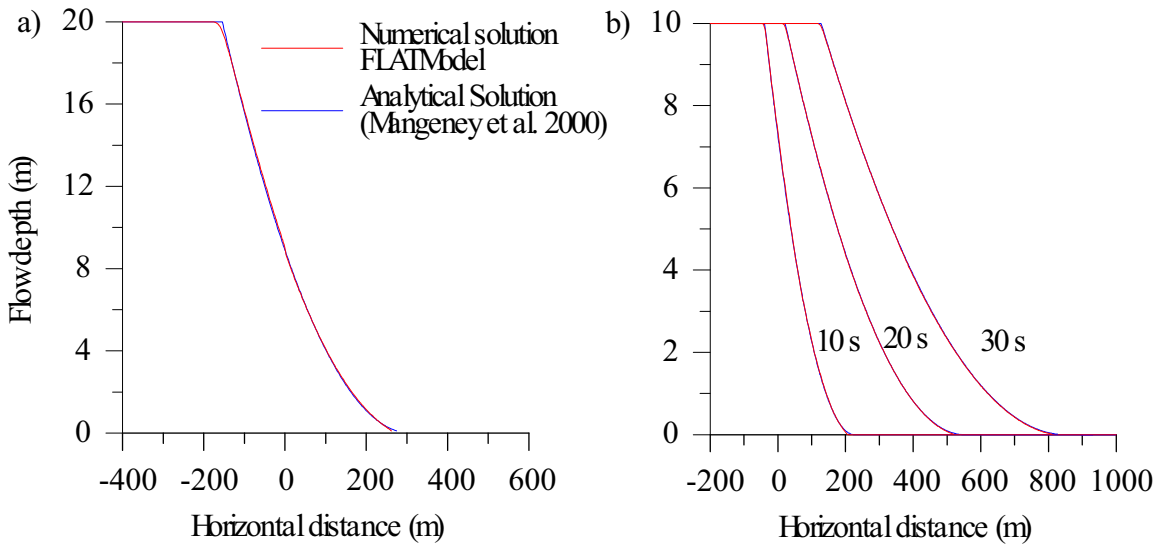

Figure 7.5: Comparison between analytical solutions of one-dimensional dam-break scenarios and numerical results calculated by the numerical model. a) Dam-break characterized by an initial flow depth of 20 m and material of zero bed friction across a horizontal surface. b) Dam-break characterized by an initial flow depth of 10 m and material of $\phi = 25\,^\circ$ bed friction across a surface inclined by $\theta = 30\,^\circ$.(Figure courtesy of M. Hürlimann)

7.4 Bi-dimensional Dambreak

In this test case an experimental dambreak with water is carried on. The configuration of the setup is adapted to evidence the bi-dimensional characteristics of the flow, more details about this experiment could be found in Bateman et al. (2006), all the experiments where developed by the UPC-GITS team Fluvial Morphodynamic Laboratory.

7.4.1 Experimental Setup

We studied the changes over time in water-surface position (height) caused by suddenly opening the gate. The experiment involved high-speed movements in the water

surface, which were recorded with two different digital cameras: a high-speed Basler camera and a medium-speed Lumenera camera.

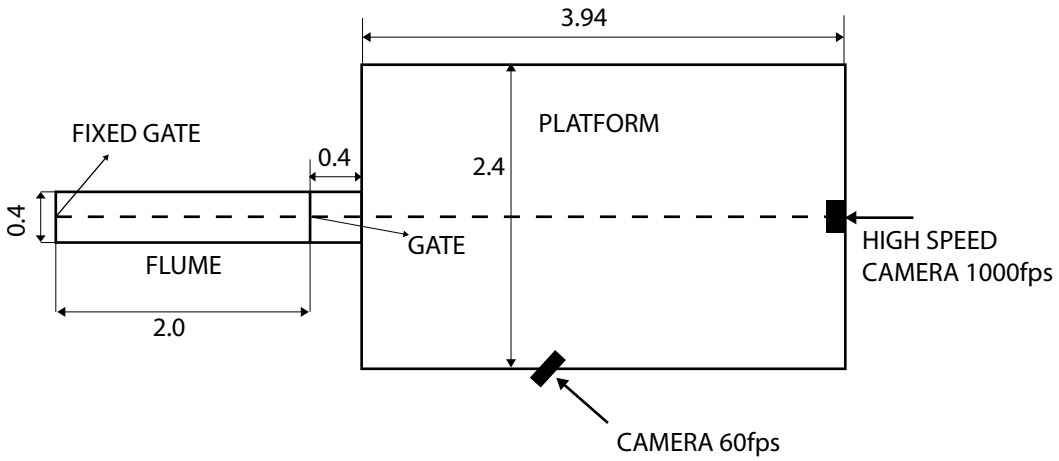

Figure 7.6: Flume and platform set-up and the positions of cameras, with dimensions in cm.

A flume filled with water was controlled by a sluice gate and connected directly to a platform, as shown in Figure 7.6. The platform was initially dry. The gate was removed manually from its original position and water flowed from the flume to the platform. The flume used in the experiment was 9 m long, 40 cm wide and 60 cm high. The flume ended at a platform 4 m long, 2.4 m wide and 60 cm tall. In this experiment, the effective flume length was just 2 m (see Figure 7.6). A fixed volume of water was held between two gates about 2 m apart. This part of the flume was connected to the platform by a manual sluice gate. A 50 cm deep volume of water was held.

Between 5 and 10 parallel laser beams were placed vertically over the platform, generating lines perpendicular to the flume axis in order to obtain cross-sections of the water surface. The water was mixed with milk at a concentration of 2% so that it would reflect the laser beams and make it possible to take photographs. Higher concentrations of milk caused more reflection, and lower concentrations allowed the light to penetrate the mixing fluid to a greater degree. We tried out different mixtures and found that the minimum concentration of milk was about 2% by volume. This

allowed us to use as little milk as possible and obtain strips of light that were not too thick, thus preventing them from overlapping.

The Basler camera can capture images at up to 1000 fps with a resolution of 1200x1000 pixels or more, depending on the frame size. The Basler camera used normal Nikon lenses that produce high-quality images without optical aberration. The Lumenera camera had higher luminescence than the Basler because its lens had higher luminescence and also because the Basler's minimum shooting frequency was higher. The Lumenera had a wide-angle lens, which caused significant image deformation, which had to be corrected. A new MATLAB code was produced to correct this aberration.

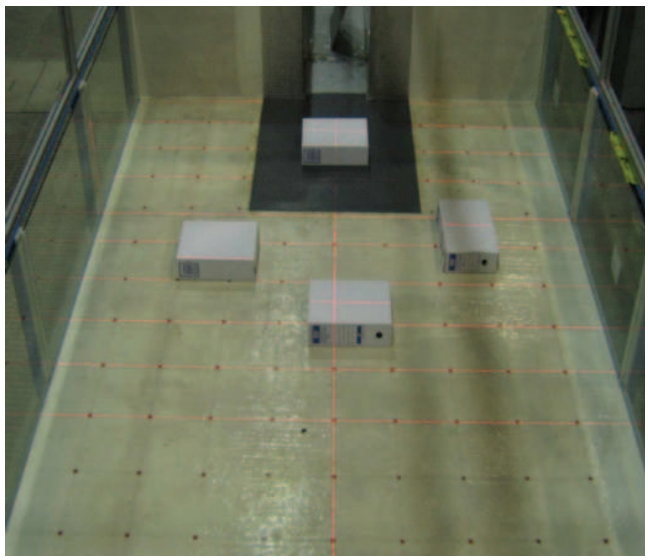

Figure 7.7: Lasers and general view of the experimental set-up in the channel platform.

A series of photographs of the light reflecting from the mixture were taken and processed. The idea was to obtain different cross-sections of the surface using the laser beams, in order to reconstruct the surface at each time step. We could not use many lasers because the beams could have overlapped and the numerical process would have failed. A minimum distance was therefore maintained between lasers.

The channel platform has a dots mesh drawn (see Figure 7.7). The lasers follow the rows defined by these dots. In the Figure 7.7 is possible to see the light and a couple of cardboard boxes used to check the calibration distances scaling.

7.4.2 Camera Position

The cameras were placed in such a way that the projection of the laser beams in the flow surface did not cross at any time. They needed to be able to perceive water-level fluctuations accurately. In our experiments, the camera angle ranged from 20 to 30°. The camera distance depended on the area being analyzed, neither the distance nor the angle mattered because the camera needed to be calibrated and there were intrinsic values throughout the process.

7.4.3 Camera Calibration

Once the aberration had been corrected, the camera needed to be calibrated. As mentioned above, at least six points must be identified in the space of known coordinates and correlated with six points in the photograph in order to determine the **M** projection matrix (Bateman et al., 2006). As a calibration object, we used a meshed box located in a known position (Figure 7.8). The points in the space used to calibrate the camera were located throughout the volume of study in order to avoid extrapolation problems that would increase the estimation error. We used a set of points taken from different positions of the meshed object in the area of interest.

7.4.4 Detection Of Laser Beams

There are various techniques for finding the pixels that belong to a laser beam in a photo. Depending on the quality of the photograph, the layout of the laser beams, the contrast of the beams, the background of the image and other factors, one technique

may be better than another. All techniques require a pre-filtering or post-filtering process. In the present analysis two different techniques were used, detection by maximum and morphological image treatment, which were applied to both cameras that observed the experiment from different positions. Frontal (Basler) and lateral (Lumenera) points of view were used in the subsequent analysis, as shown in Figure 7.6.

The frontal view had certain advantages over the lateral view. The main advantage lies in the layout of the laser beams in the photograph. It was easy to apply an intuitive technique to detect the maximum of the column of pixels (by colour index), which match up with the laser beams.

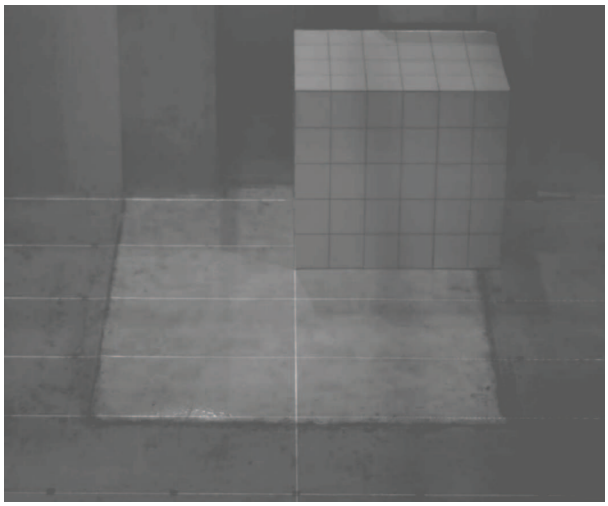

Figure 7.8: Meshed box used in the calibration procedure.

The image resolution of the Basler camera was higher than Lumenera's one. The study area occupied the entire frame and it was possible to obtain more information about the process. However, in this specific example, the frontal view presented a difficulty: the image could not describe the lateral flow depth gradients as well as images from the lateral view do.

First, we corrected the photograph by refining it. Due to the fact that the illumination condition was poor, the Basler took the photographs with an electronic gain

that introduced some noise, which appeared as fine vertical highlight lines, a low pass FIR filter was used to smooth the image, suppressing the light noise. Then a simple algorithm to detect maximums is used and the the image converted to binary, on the binary domain successive operations were carried on until the different laser pieces are connected with accuracy defining the real laser lines.

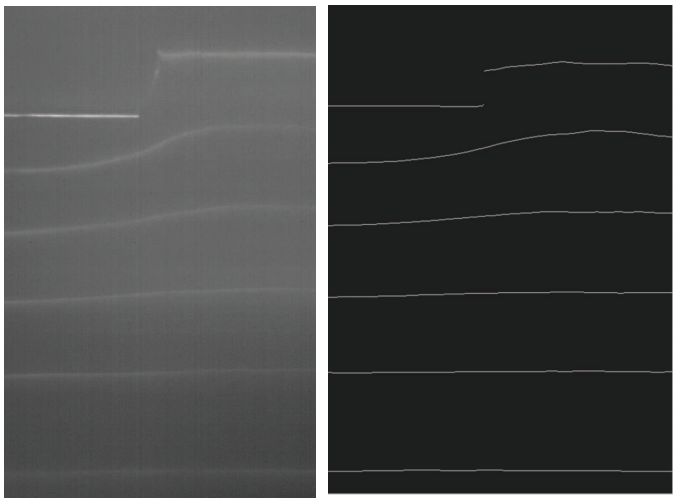

Figure 7.9: Comparison between the original Basler camera image (left) and the results obtained after filtering (right).

In the Figure 7.9 the comparison between the original image and the obtained result is shown, all the line pieces present in the image are connected forming the laser lights.

For the second camera, Lumenera, a morphological function to detect contours were used. The obtained results were very interesting for the analysis of the fan expansion area, due to the position and angle of the camera. But as will be seen in the results analysis these areas do not accomplish the SWE hypothesis, so were not useful for the comparison with the numerical results.

7.4.5 Results

After the image processing, the water free surface is obtained and the results could be compared to the experimental ones, the configuration selected for the model is:

1. Computational mesh 1 cm^2.
2. Exact SWE Riemann solver.
3. Second order in space scheme using minmod limiter (LeVeque, 2002; Toro, 2001).
4. Transversal Riemann solver to obtain complete second order in bi-dimensional flow (LeVeque, 2002).
5. Results output every hundredth of second.

The first step to compare results is to transform the local results of the image processing in full domain results, this means to interpolate the free surface from the known points to the whole domain (Figure 7.10, Figure 7.11). Splines were used to carry out this step.

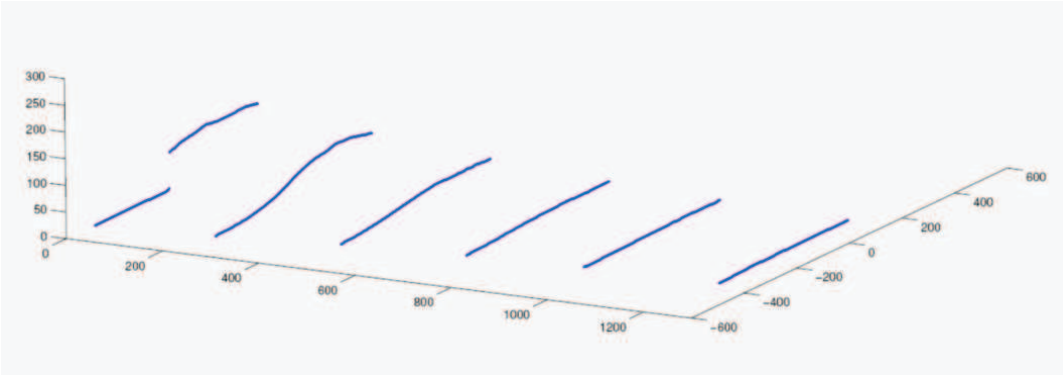

Figure 7.10: Position of the free surface obtained by the laser image processing, the results are lines.

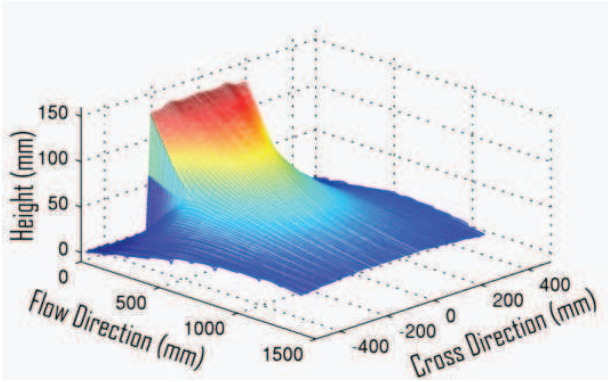

Figure 7.11: Interpolated results for the whole domain.

The next step is to compare the experimental results with the numerical ones obtained by using the model (Figure 7.12). The time step selected is 2.45 s. To compare the results two different operations were carried out. The first one is to subtract the depths between the experimental and the numeric in order to compare the differences. And the second one is to delimitate the wet area of the platform. This is important because one of the targets of the work was to validate the drying/wetting process of the model.

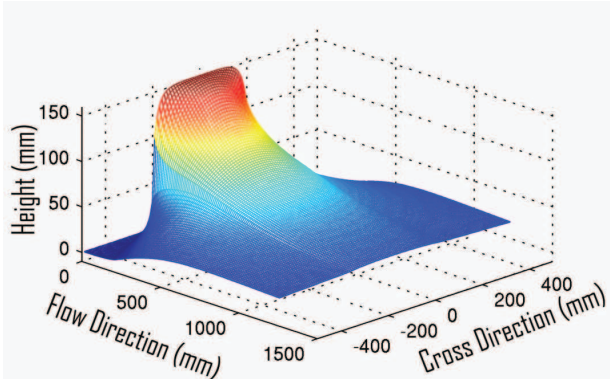

Figure 7.12: Numerical results obtained using the model.

Figure 7.13 shows the behavior of the absolute error, which is calculated as the experimental data minus the numerical data. The numerical and experimental data

fit quite good throughout the area of study. The unique regions where the results are not in agreement are those which fail to meet the SWE conditions. Two regions were defined, due to the shallowness hypothesis there are areas were the conditions are clearly not fulfilled, specially in the gate neighborhood (Figure 7.13). A threshold is defined to establish these areas, sectors with error higher than the 40% are discarded, being less than the 7% of the total area.

Nevertheless, the comparison shows that the data has a mean error of 13.9% throughout the area of study. If a new threshold of 20% is used to discard areas non SWE areas, the data that has a mean error of 9%, being the discarded area less than the 15% of the total domain.

There are especial places were, due to the flow configuration, the numerical results are far from the experimental ones. But the problem related to these points is not in the numerical solution, is in the equations system applicability. As has been stated during the equation system definition, its necessary to introduce multiple approximations to simplify the equations, these approximations are not valid in some areas of the experiment domain, specially close to the dam gate, there the flow vertical profile is complicaded, the velocities along the vertical are not parallel, so the approach of the *mean velocity* introduces large error in the results.

The mixture of water and milk flowed very quickly across the platform, producing a jet flow that increased in width from 0.4 to 2.4 m. The front of the flow moved very quickly, close to 3.42 m/s, which was much faster than the theoretical value of 2.21 m/s given by the Ritter solution.

Also the questions related to the hydrostatic pressure are complicated. There are places with an important vertical acceleration. So, in these places the flow pressures are lower than the predicted ones. It is worth to notice that in SWE framework, the pressures and the free surface dynamics are linked.

Another comparison between experimental and numerical data is carried out. This comparison concerns to flow expansion in the platform. Figure 7.14 shows all data

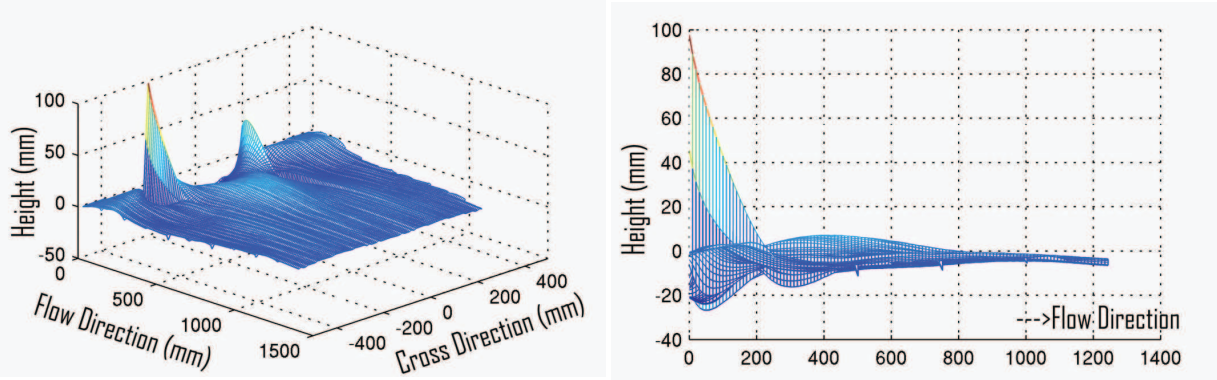

Figure 7.13: Depth difference between the experimental and numerical results, .

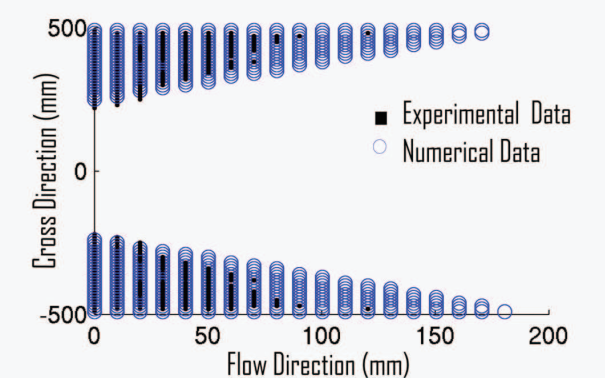

Figure 7.14: Differences in the platform in the dry condition.

below a height of 2 mm. The resulting flow expansion angles are 36 and 23° for the numerical and experimental data respectively. The experimental flow fan opens faster than the numerical one.

7.5 Experimental Debris Flow

This is the first calibration case with bi-dimensional behavior, these results were obtained in Iverson et al. (2004), to calibrate the numerical model proposed in Denlinger and Iverson (2004). In the experiment, a dambreak with sand is carried out. The

size of the sand is between 0.5-1 mm, the bulk density is 1550 kg/m^3 and the internal friction angle ϕ is 43 degrees. The flow surface during the experiment and the final deposition area is measured.

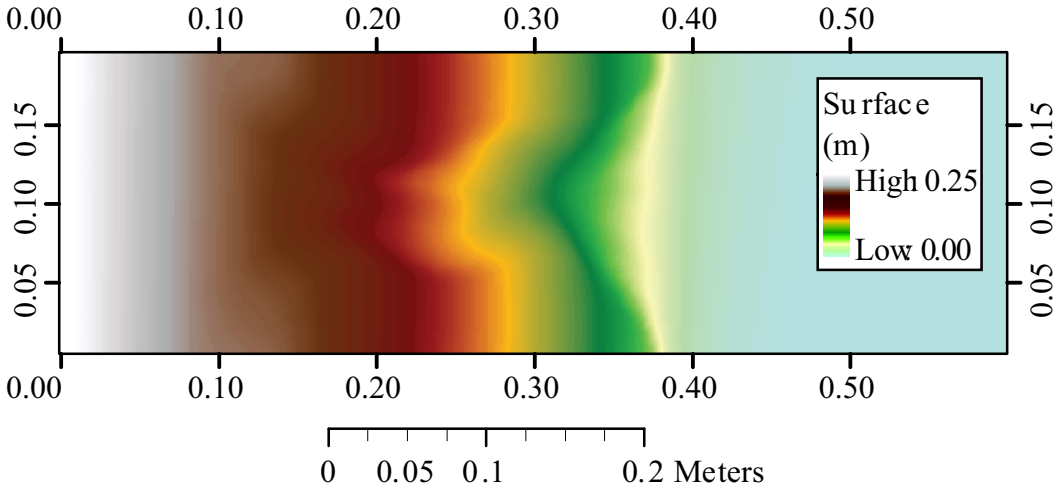

Figure 7.15: Topography of the experiment. Flow from left to right.

The channel dimensions were 0.2 meter width and 1 meter long. In the upper part, a gate exist, containing the dam 300 cm^3 of sand. The material of the channel is formica upstream to the gate. The remaining channel is made of urethane. For the basal stress computations the friction angle between the sand and the different channel materials is computed. The friction angle between urethane and sand is 19.85°. The friction angle between formica and sand is 23.47°.

In the Figure 7.15 the basal topography is shown, the maximum level is 0.25 meters high, the mean slope is 31.6°, over the friction angle between urethane and sand. The comparisons between simulation results using two different basal friction angles and data from the flume experiment are given by isopach maps of flow depth at different times (Figure 7.16). Model predictions match qualitatively well to the dynamic characteristics of the sand avalanche. Simulation results show higher fluidification mobility.

A second run was carried out introducing the active/passive pressure coefficients

(see Page 83). The implementation was simple. Passive coefficient for flow compression and active coefficient for flow expansion. The results where poor, instability was introduced due to the discontinuity in pressure. The method proposed in Hungr (1995) includes a kind of *inertia* in the pressure coefficient, avoiding the discontinuities. Similar methods are proposed in Pudasaini and Hutter (2007); Iverson et al. (2004).

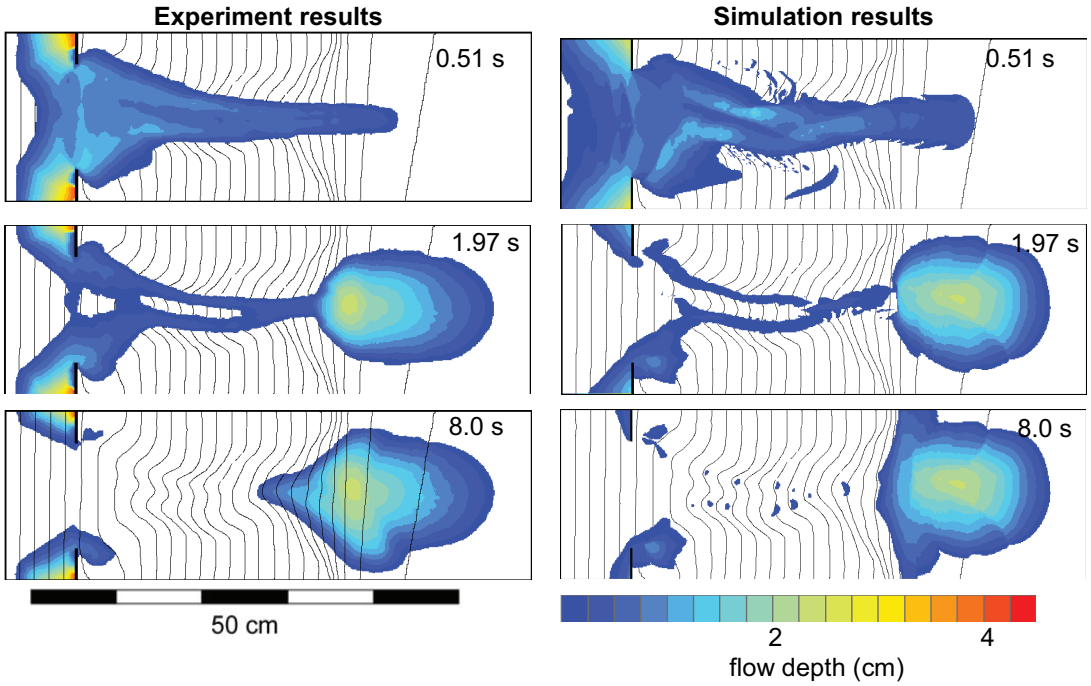

Figure 7.16: Comparison between the laboratory experiment of a sand avalanche (left column) and numerical results calculated by the model (right column). Flow depth is plotted on a topographic base with a contour interval of 1 cm.

In continuation, we present an example to see how our stop-and-go approach can be visualized for the same simulation run as described above. This is shown in Figure 7.17 where green (bright) color indicates cells in movement and red (dark) color shows cells with no movement.

The simulation times forward from left to right and from top to bottom. The time step between images is 0.12 seconds.

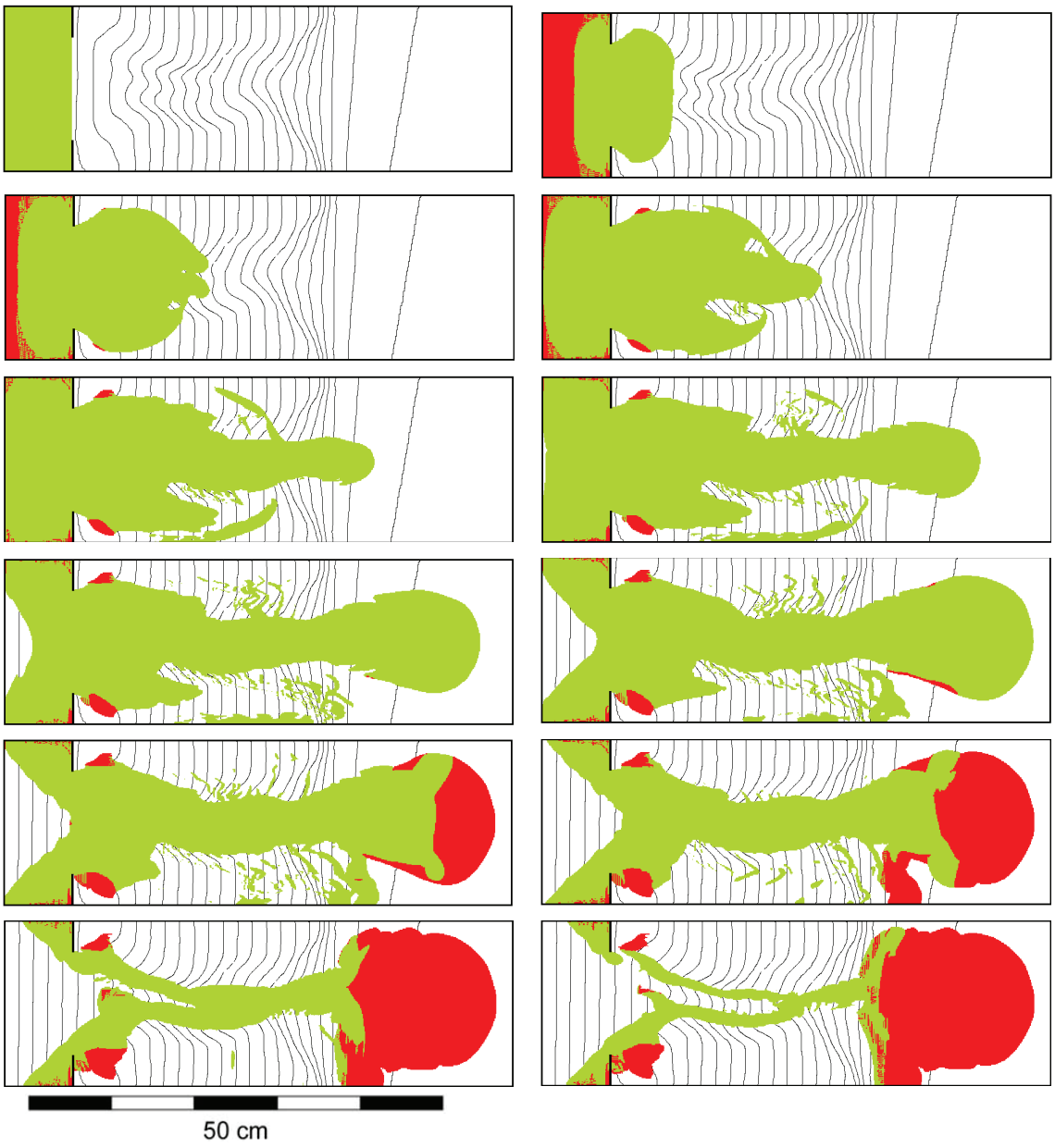

Figure 7.17: Visualization of the stop-and-go approach implemented in the model at different time steps using a basal friction angle of 19.85 °. Green (bright) color indicates cells in movement and red (dark) color shows cells with no movement.

Chapter 8

Real Cases

In this chapter some real applications of the model will be shown, all the cases belong to the Catalonia geographic space (North East Spain). The procedure carried on to apply the model consist in the "back analysis". This means that the data about the debris flow event is collected *a posteriori* and then some different configurations are testes until good agreement to the measurements is obtained.

As will be clear in the sequent, for the Catalonia environment, there is a characteristic rheology that fits the behavior of the events. This agreement allows, in a second stage, to use the model with predictive character.

8.1 Introduction

Because of the particular characteristics of the Mediterranean climate that affect the Northeastern part of the Iberian Peninsula, debris flows do not occur as frequent as in other mountainous areas. Generally, debris flows can be triggered by two different types of rainfall events:

1. Short and locally restricted rainstorms of high to very high intensity that happen during summer.

2. Rainfall episodes of moderate to high intensity that affect a large area during

one or few days in late summer and autumn (Corominas et al., 2002; Hürlimann et al., 2003).

In the present study, three events have been selected for numerical simulation of the model. They took place at different locations in the Eastern Axial Pyrenees and the Catalan Prelitoral Mountain range (Figure 8.1). These events probably represent the three most important debris flows that occurred in our study area during the last 30 years, but unfortunately field data are limited. Thus, our simulations only provide general patterns on flow dynamics of these events.

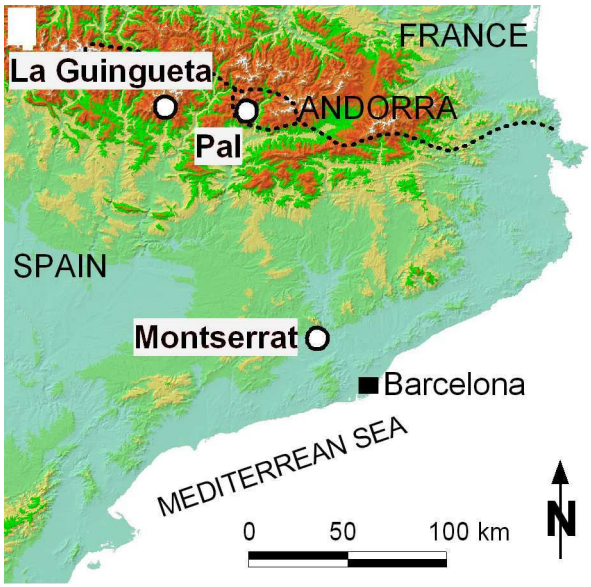

Figure 8.1: Location of the three drainage basins.(Figure courtesy of M. Hürlimann)

8.2 La Guingueta

8.2.1 Field Data

The Jou torrent near La Guingueta village drains the largest of the three selected catchments covering 4.4 km^2. The drainage basin is situated in the Eastern Axial Pyrenees (Figure 8.1) and bedrocks consist of shales. However, the basement rocks only crop out in the lower section, while the rest is covered by till deposits or periglacial materials.

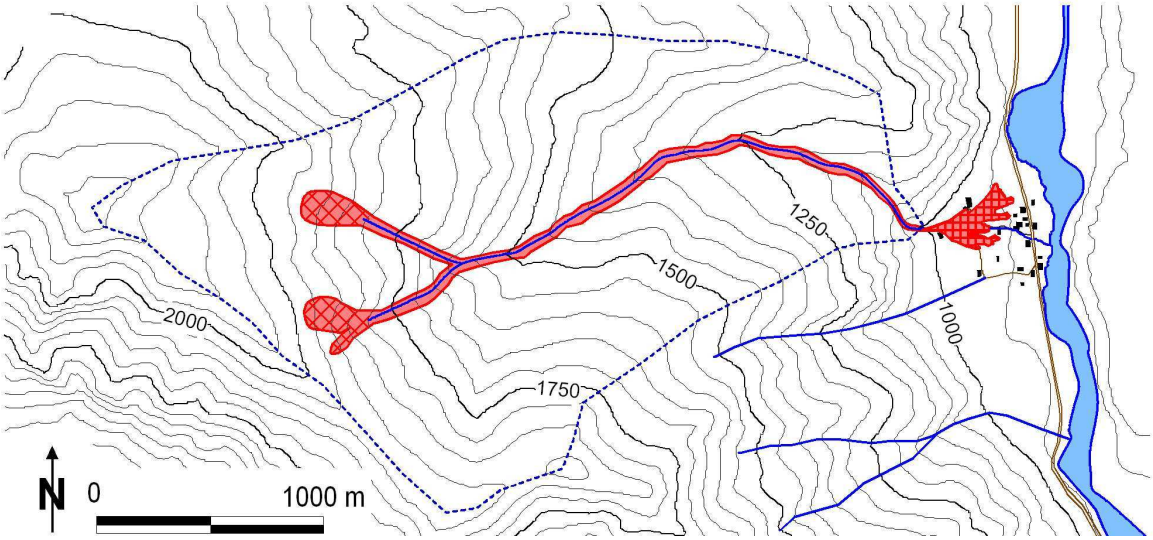

Figure 8.2: Jou Torrent at La Guingueta, topographic map indicating the surveyed flow path of the event.(Figure courtesy of M. Hürlimann)

The Jou debris flow was also provoked by the 1982 floods and a total rainfall amount of 154 mm in 24h which was measured at a nearby rain gauge. In the night from November 7 to November 8, three surges transported a total volume of about 30000 m^3 to the fan (Figure 8.2). Field data indicated that two major failures in the higher port of the catchment transformed into debris flows, but most of the accumulated material was eroded in the glacial or periglacial deposits (Bru et al., 1984). The accumulation zone of the debris flow covered a large area of the fan and damaged several houses and roads of La Guingueta village.

Figure 8.3: La Guingueta fan picture.(Photography courtesy of M. Hürlimann)

8.2.2 Simulation Results

Field data indicate that two principal initiation zones caused the debris flow (Figure 8.2). During the numerical modelling, each initial volume was released at the same moment and assumed to be 15000 m^3, which gives a total mobilized mass of 30000 m^3 (Figure 8.4 Left). The simulations were carried out over a topographic grid with a cell size of 2 m. Voellmy fluid model was applied again and the best-fit flow properties were $\mu = \tan(\phi) = 0.1$, $C = 10\,m^{1/2}/s$.

Apart from the extent and the depth of the initially mobilized mass, Figure 8.4 Left also indicates the calculated depths of the final deposit. While the extension of the inundated area obtained by the simulation coincides rather well with the one observed in the field, accumulated depths of material seem to be affected again by the uncertainties related to the DEM. As in the previous case, these errors can be explained by the fact that a DEM representing actual conditions was used for the input relief.

Such a topographic error provoked that the maximum depth computed for the final deposit was 3.4 m. However, this maximum value was only limited to one point located inside the artificial channel, which was constructed after 1982. Thus, the

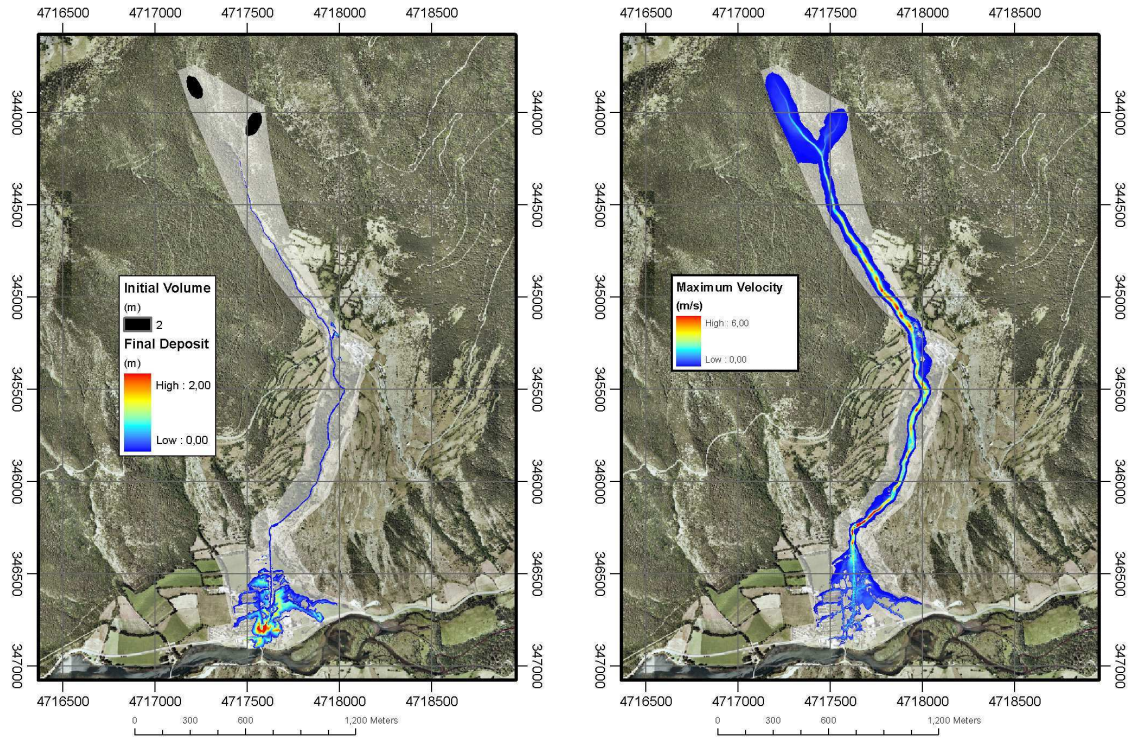

Figure 8.4: Simulation results of the debris flow occurred in the Jou torrent at La Guingueta using Voellmy fluid model $\left(\mu = \tan(\phi) = 0.1,\, C = 10\,\mathrm{m}^{1/2}/\mathrm{s}\right)$. **Left**: Depth of initiation zone and of final deposit. **Right**: Maximum flow velocity.

legend used for Figure 8.4 Left and Figure 8.6 Left ranges from 0 to 2 m. This range more or less coincides with the depth of the deposit observed after the debris-flow event. In Figure 8.4 Right, the maximum calculated flow velocity is illustrated.

Results indicate that maximum velocity is limited to the steep and strongly confined section just upstream of the fan apex. There, maximum velocity of more than 9 m/s was calculated (the legend in Figure 8.4 is limited to 6 m/s). The sensitivity analysis of the different flow resistance laws and their rheological parameters generally confirmed previous results.

Figure 8.5 Left compares the extension of the final deposit obtained on one side by the best-fit Voellmy parameters $\left(\mu = \tan(\phi) = 0.1,\, C = 10\,\mathrm{m}^{1/2}/\mathrm{s}\right)$ and on the other side by a higher ϕ-value of 0.14. As it could be supposed, the final deposit is shorter

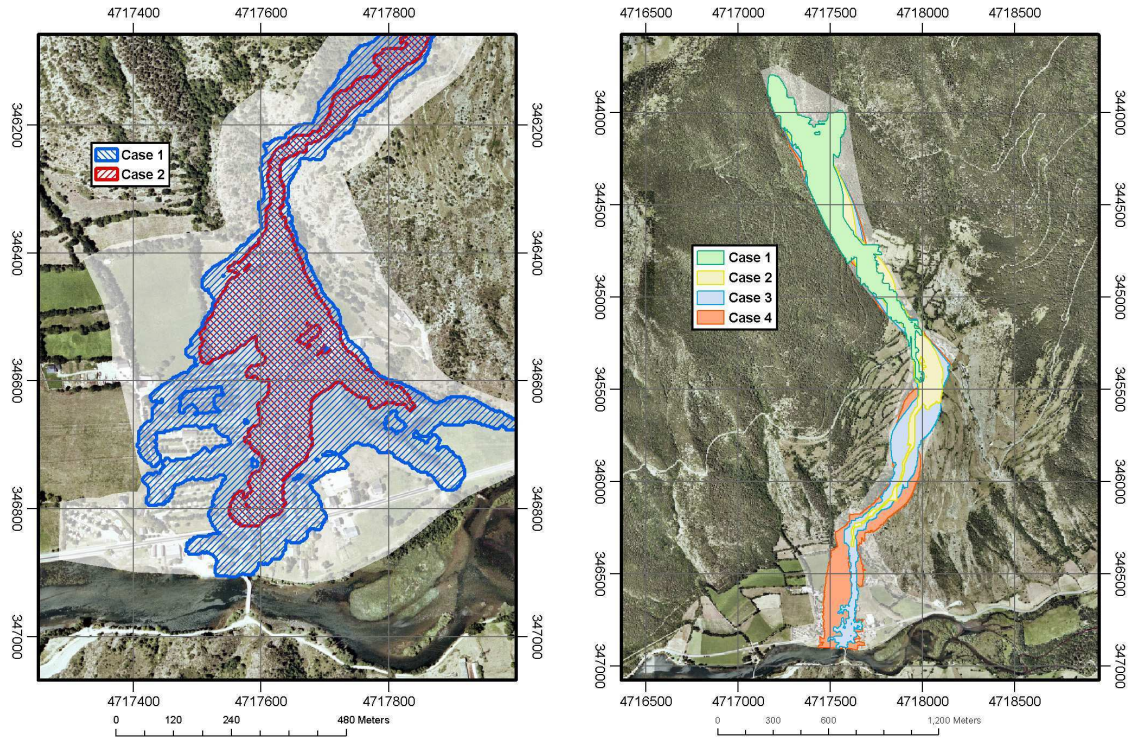

Figure 8.5: Simulation results of the debris flow occurred in the Jou torrent at La Guingueta using Voellmy fluid model. **Left**: Extensions of final deposits computed by different Voellmy parameters (Case 1: $\mu = \tan(\phi) = 0.1$, $C = 10\,\mathrm{m}^{1/2}/\mathrm{s}$; Case 2: $\mu = \tan(\phi) = 0.14$, $C = 10\,\mathrm{m}^{1/2}/\mathrm{s}$). **Right**: Zone affected by simulations using different Herschel-Bulkley parameters (Case 1: $\tau_0 = 1\,\mathrm{kPa}, k = 1\ (\mathrm{Pa\,s})^{1/3}$; Case 2: $\tau_0 = 1\,\mathrm{kPa}, k = 0.1\ (\mathrm{Pa\,s})^{1/3}$; Case 3: $\tau_0 = 0.5\,\mathrm{kPa}, k = 0.1\ (\mathrm{Pa\,s})^{1/3}$; Case 4: $\tau_0 = 0.3\,\mathrm{kPa}, k = 0.1\ (\mathrm{Pa\,s})^{1/3}$.

using a higher friction angle. So, the value of this parameter is rather delicate and strongly affects the total extension of the debris-flow deposit.

Additionally, simulation runs applying Herschel-Bulkley rheology were carried out (Figure 8.5 Right). As already observed in the Font de la Llum event, a viscous flow resistance law is not able to simulate such a type of debris-flow. Grain sizes of the till and periglacial materials include gravels to boulders in a silty matrix (Bru et al., 1984), which support the hypothesis of a granular debris flow. A large range of parameters were tested, but no good agreement was received and specially the flow cross-section

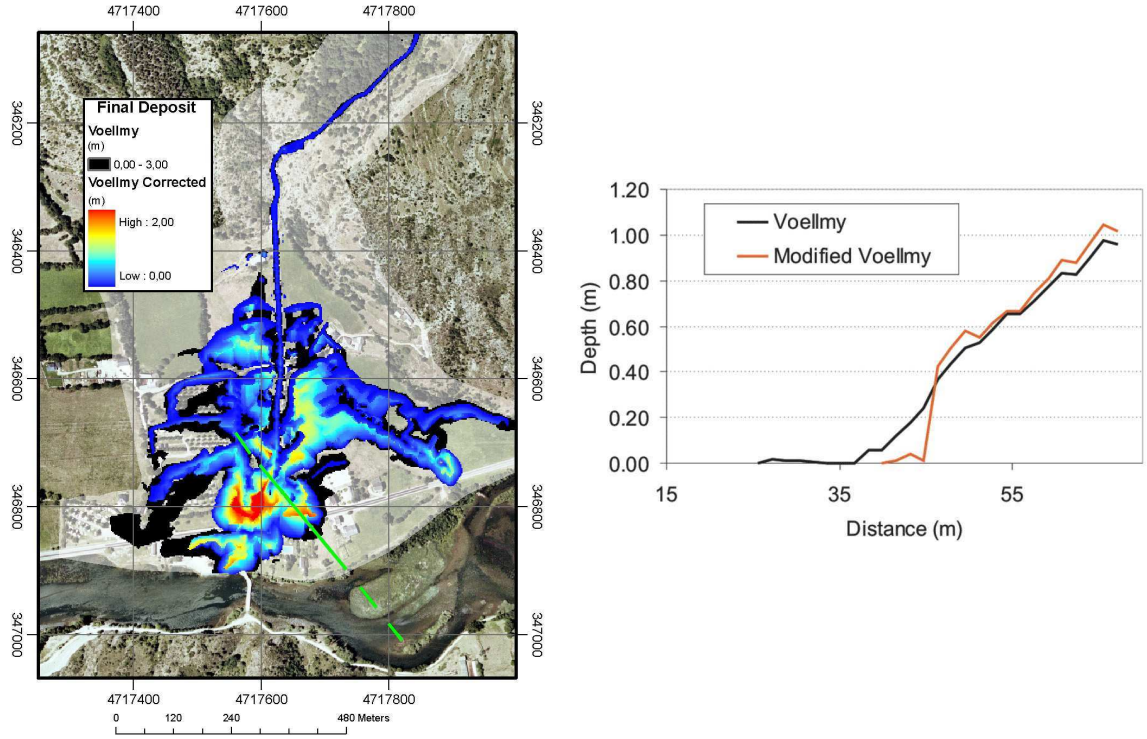

Figure 8.6: Correction of front inclination of final deposit modifying the ϕ-value (see text for detailed explanations). **Left**: Comparison of extensions of final deposit for normal Voellmy model and corrected Voellmy model using in both cases $\mu = \tan(\phi) = 0.1$, $C = 10\,\mathrm{m}^{1/2}/\mathrm{s}$. Static friction angle was $35\,^{\circ}$. **Right**: Computed depths of final deposit along the profile illustrated in Figure 8.6 Left (green line).

area and lateral expansion angle of the deposit on the fan have a behavior far from the one observed.

Finally, the simulation results obtained on the fan help to visualize the effect of the correction referring to the front slope of the final deposit. Figure 8.6 Left shows the extension of the final deposit calculated using the Voellmy fluid model without the correction (called "Voellmy" in Figure 8.6 Left) and the corrected Voellmy fluid model (called "Corrected Voellmy").

The corrected model changed the initial friction angle $\phi = 5.7,^{\circ}$ into the static frictional angle $\phi_{stat} = 35,^{\circ}$ for the critical velocities of $V_1 = 0.3$ m/s and $V_2 = 0.1$

m/s (see Figure 6.10). The improvement of this implementation is clearly visible in Figure 8.6 Right, where longitudinal profiles at the front of the final deposit profile are illustrated. Only the corrected Voellmy model can simulate the typical steep fronts that are generally visible at debris-flow deposits.

8.3 Montserrat

8.3.1 Field Data

The Font de la Llum catchment covers a small area of 0.46 km^2 at the eastern flank of Montserrat massif. The massif is situated about 30 km northwest of Barcelona in the Catalan Pre-litoral Mountain range (Figure 8.1) and maximum altitudes reach about 1250 m a.s.l. From a geological point of view, the bedrock of the drainage basin involves sequences of conglomerates, sandstones and lutites, which are locally covered by a colluvium layer. The higher part of the basin is characterized by very steep slopes with inclinations of up to 60°, while the lower part includes a smooth morphology with small slope angles (Figure 8.7).

The selected event was triggered on June 10, 2000, by an extremely intense thunderstorm, which provoked a failure of the colluvium deposit in the highest part of the massif. The advective rainstorm lasted about 4 hours including a maximum intensity of $\sim$ 80 mm/h and accumulated about 160 mm rainfall. Field observations and interpretation of aerial photographs indicate that the initially failed mass of the terrain was rapidly transformed into a flow. Another characteristic was that almost the entire superficial deposit was incorporated into the flow.

A total volume of about 10,000 m^3 was estimated in the elongated accumulation zone (Figure 8.7). The morphologic and sedimentologic characteristics observed in the field suggest that the event descended the torrent in various surges of hyperconcentrated flows and/or debris flows.

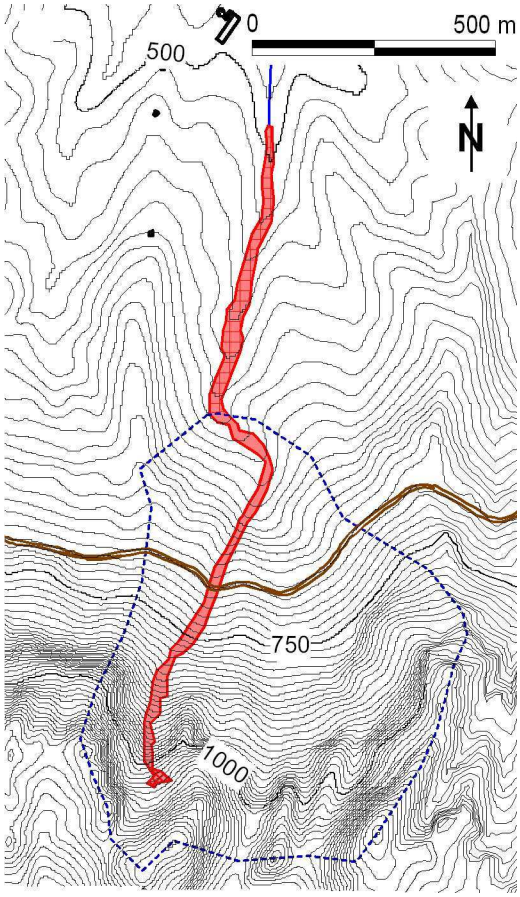

Figure 8.7: Font de la Llum torrent at Montserrat, topographic map indicating the flow path of the event simulated.(Figure courtesy of M. Hürlimann)

8.3.2 Simulation Results

The model simulated the event at Font de la Llum as one surge of 10,000 m^3. The high-quality digital elevation model available was transformed into a grid of 0.3 m cell size and runs were carried out at this precision.

First, the three flow resistance laws were compared and a sensitivity analysis of the rheological parameters was carried out. Many different simulation runs were executed and both the extension and the depth of the final deposit were compared with the data observed in the field. The results of this comparison indicate that the most realistic simulations were obtained by the Voellmy fluid model and material

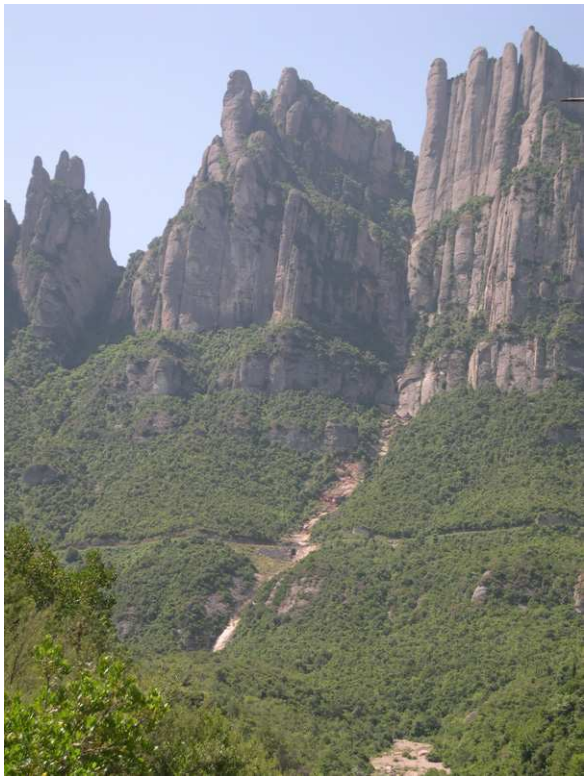

Figure 8.8: Montserrat picture.(Photography courtesy of A. Bateman)

properties of $\mu = \tan(\phi) = 0.13$, $C = 10\,\mathrm{m}^{1/2}/\mathrm{s}$ (Figure 8.9 Left). In contrast, no good agreement with the real deposit shape was obtained applying Bingham model.

Figure 8.9 Right illustrates outcomes calculated for $\tau_0 = 0.75\,\mathrm{kPa}$, $\mu_\mathrm{m} = 0.450\,\mathrm{Pa\,s}$ and $\rho = 1500\ \mathrm{kg/m^3}$. First approximations of τ_0 could be calculated using the equilibrium equation for Bingham flows (Figure 2.7). The depth of the final deposit is about 1.5 m and the slope in this area is $5.7\,^\circ$. So, an initial approximation of a value for τ_0/ρ should be about $1.4\ \mathrm{m^2/s^2}$.

Previous studies applying viscous rheology proposed values for τ_0/ρ of $0.4\ \mathrm{m^2/s^2}$ (Chen and Lee, 2002), 0.1 to $0.5\ \mathrm{m^2/s^2}$ (Rickenmann and Koch, 1997) or 0.1 to 1 $\mathrm{m^2/s^2}$ (Pastor et al., 2004). The same references also propose values for viscosity (μ_m/ρ), which should be around $0.05\ \mathrm{m^2/s}$ (in our case, the best-fit value was 0.3

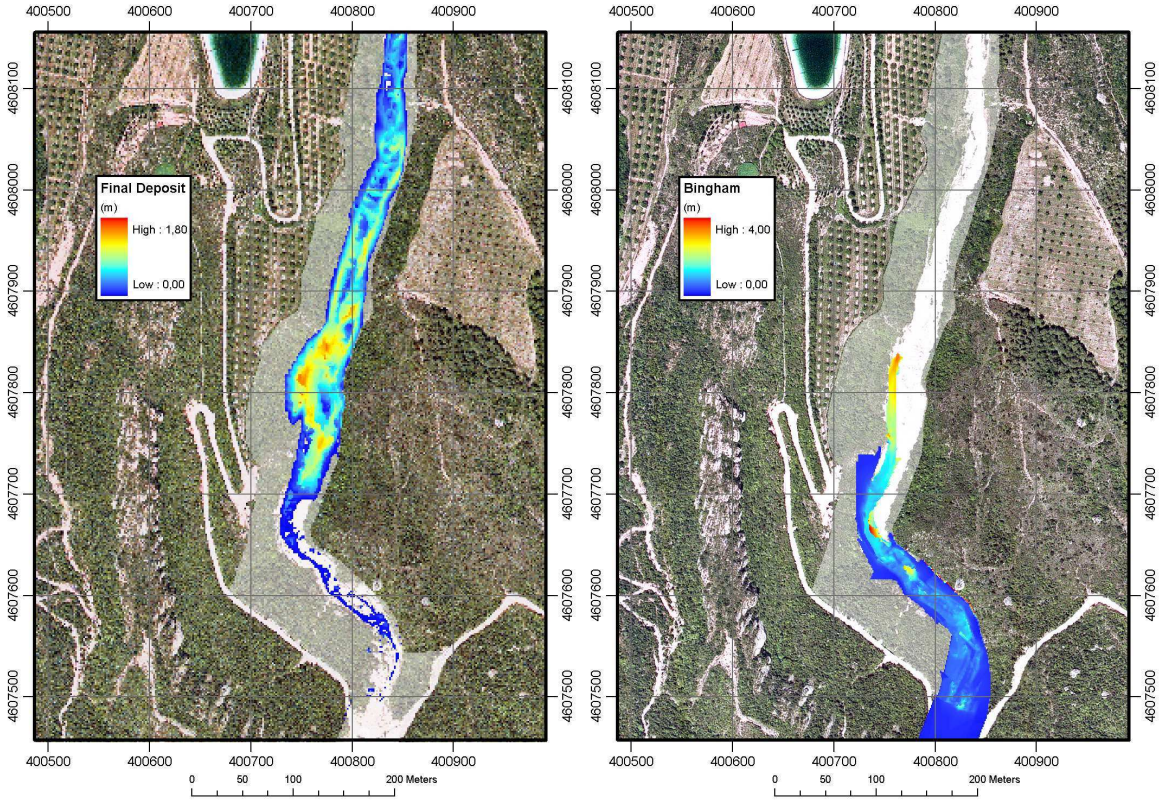

Figure 8.9: Backanalysis of the Font de la Llum event at Montserrat. **Left**:Depth of final deposit computed by best-fit Voellmy fluid model ($\mu = \tan(\phi) = 0.13$ and $C = 10\,\mathrm{m}^{1/2}/\mathrm{s}$). **Right**: Depth of final deposit computed by best-fit Bingham model ($\tau_0 = 0.75\,\mathrm{kPa}, \mu_\mathrm{m} = 0.450\,\mathrm{Pa\,s}$).

m^2/s). Finally, Herschel-Bulkley rheology was tested using parameter values proposed by previous works (Coussot et al., 1998). Once more, very poor results were computed using many different parameter combinations for Bingham and Herschel-Bulkley rheologies($\mu_\mathrm{m}/\rho = 0.1 - 1\ \mathrm{m}^2/\mathrm{s}$, $k/\rho = 0.05 - 1\ \mathrm{m}^2/\mathrm{s}^{5/3}$ and $n = 0.33$).

Although this backanalysis does not include additional information on other important data such as flow velocity or flow area observed at some points in the trajectory, the outcome indicates that the event may be characterized by a granular flow behaviour.

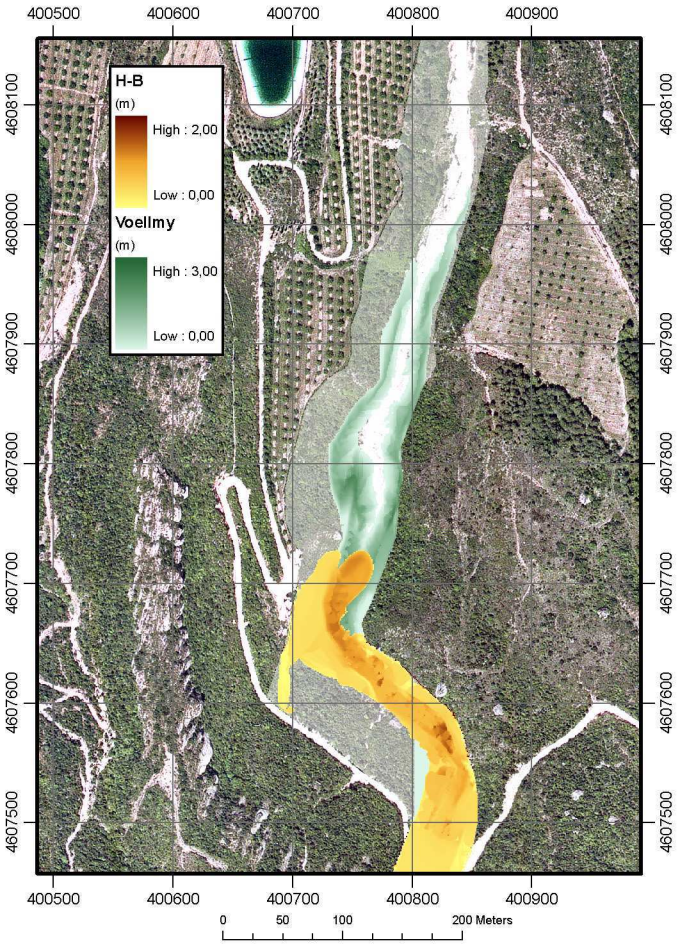

Figure 8.10: Backanalysis of the Font de la Llum event at Montserrat. Comparison between Voellmy and best Herschel-Bulkley.

Additionally, some detailed results of the Voellmy simulation are presented illustrating only the final part of the flow. This part includes the end of the steep section and the smooth section of the elongated accumulation area. Figure 8.11 Left illustrates maximum flow velocity and Figure 8.11 Right shows maximum flow depth. Simulation results reveal that the debris flow or hyperconcentrated flow reached locally a maximum velocity of about 16 m/s at the end of the steep section, while velocity strongly decreases in the lower smooth section, where accumulation starts.

This local maximum velocity slightly surpasses the estimates obtained by the

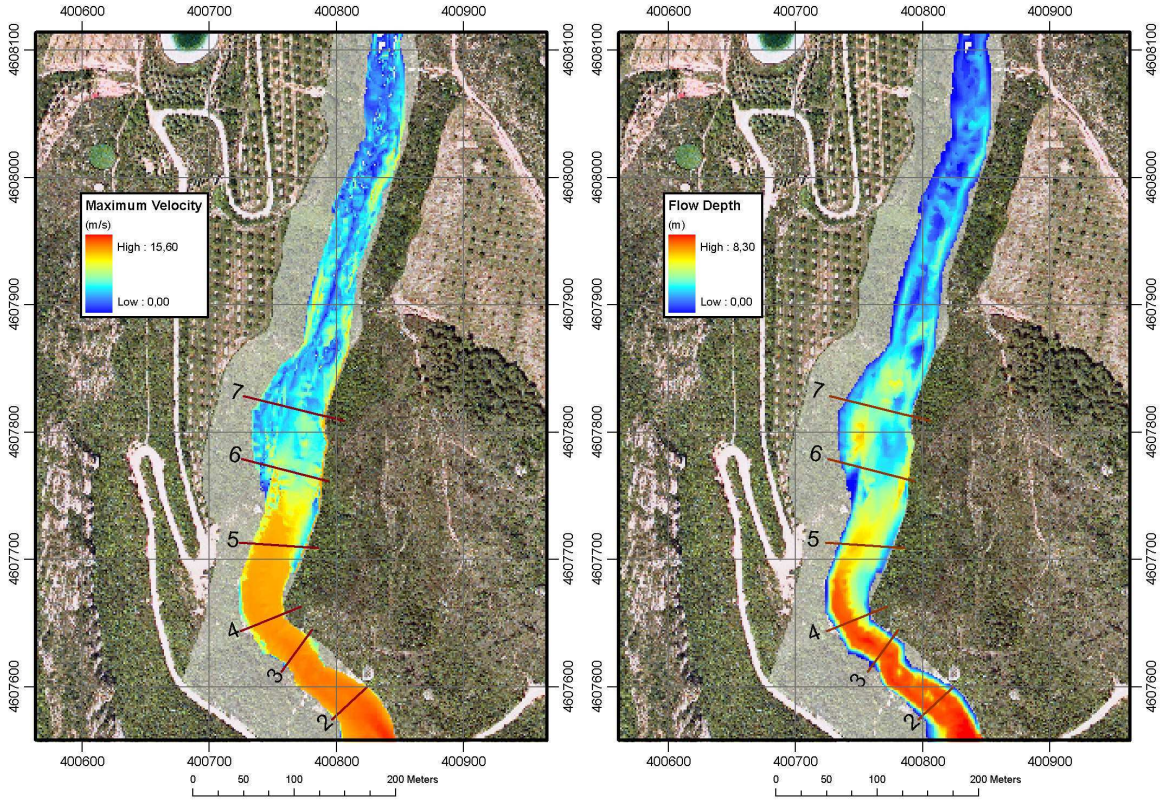

Figure 8.11: Backanalysis of the Font de la Llum event at Montserrat. **Left**: Maximum velocity applying the same Voellmy parameters as in a). **Right**: Maximum flow depth applying the same Voellmy parameters as in a). The lines and the numbers are the cross sections used to calculate hydrographs.

application of the superelevation approach (Johnson and Rodine, 1984), which gave about 12 m/s for the average front velocity at the same position. Regarding simulated flow depth, maximum values of more than 8 m were computed at the end of the steep section, where the flow is strongly confined and flow width is very small. Maximum flow depth rapidly decreases in the accumulation and values generally range from 0.2 m to 2 m. The runs of the Font de la Llum event also provided illustrative data on how the stop-and-go mechanism could be simulated by the model. Figure 8.12 shows different hydrographs at the three successive sections 5, 6 and 7. All these sections are located in the accumulation zone of the torrent, where the stop-and-go effect was clearly visible during numerical modeling.

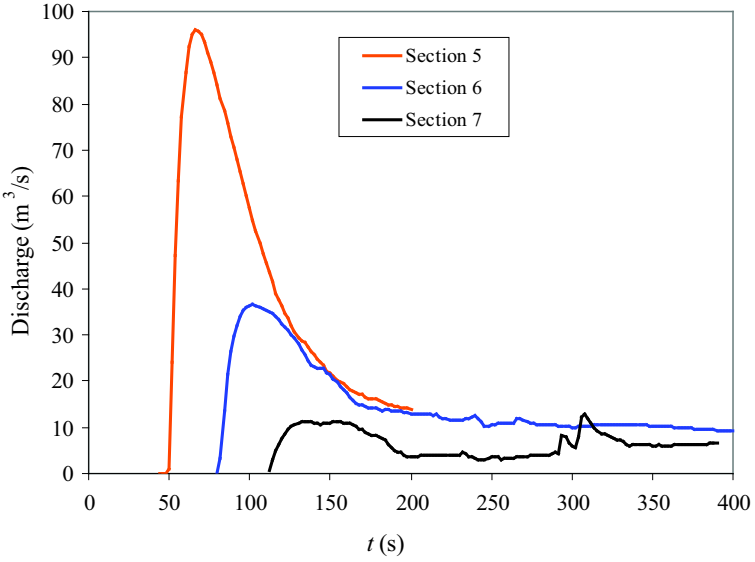

Figure 8.12: Hydrographs of Montserrat event illustrating the Stop and Go phenomena. Sections 5, 6 and 7 (see Figure 8.11).

It can be seen that flow hydrographs of the first two sections exhibit only one peak, nevertheless the hydrograph of section 7 shows two peaks. These two peaks are illustrated in Figure 8.13 together with the curve indicating the evolution of the flow area. Both peaks present discharges of ~ 12 m^3/s, but the second peak is the result of an important deposit failure upstream. The red circle in Figure 8.13 points out a small local failure, which can be clearly noted as a negative evolution of the flow area previous to the larger peak.

The La Guingueta case exhibits flow pulses in the fan area, but there were three different flow surges. In the Montserrat case there were also small pulses (see section 7) but there were not different surges. This behavior is classical in non linear flow dynamics, where the flow tends to form pulses, specially in high velocity flows.

In Figure 8.14 the hydrographs for the initial crossections are shown, its clear that the discharge peak it is reduced in few meters, the extreme value of the discharge is

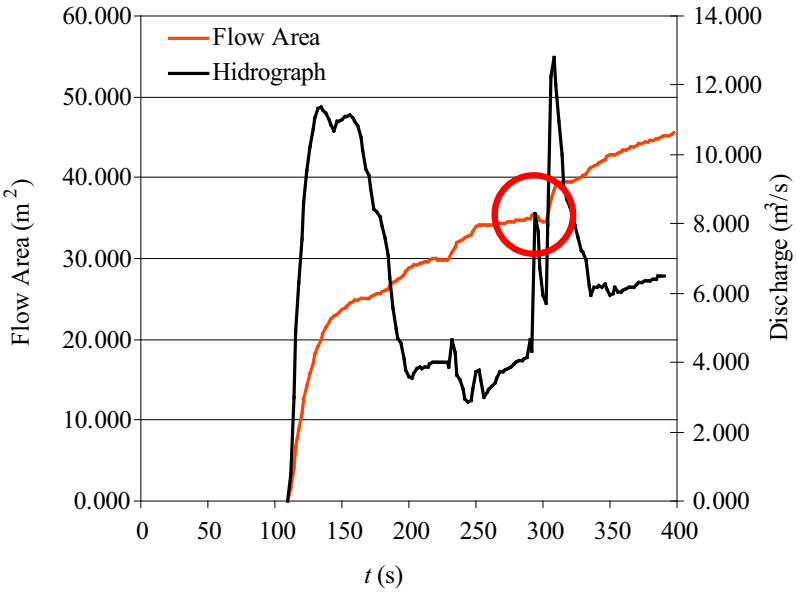

Figure 8.13: Hydrographs of Montserrat event illustrating the Stop and Go phenomena. Evolution of the flow area and the discharge at section 7 indicating remobilization of material (see Figure 8.11).

due to the very steep slope in the upper part of the stream, that provokes a very high velocity and the extreme discharge, after the upper part the velocity is rapidly reduced.

Although the peak discharge values in these sections seem to be excessive, there were data that supports these extreme values. The stream crosses a road through a kind of culvert. The road and the culvert were completely destroyed. Also the bedrock appears in the upper part of the stream as a proof of the extreme shear stresses occurred during the event. The superelevation approach indicates extreme velocities in the upper part bend.

In Figure 8.15 flow positions obtained at different time steps are shown. In the upper part of the domain the velocities are very high and the distance between the different time steps is high. In the lower part the velocity is reduced and the distances also are reduced.

In this case the model results do not fit quite well the event data. It is not clear

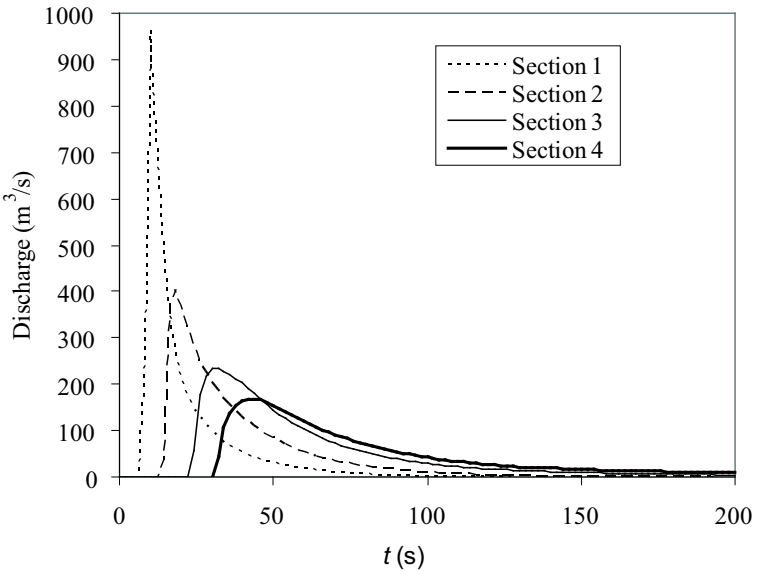

Figure 8.14: Hydrographs of Montserrat event in the first crossections of the stream (see Figure 8.11).

that the event was a pure debris flow. Probably it was a mixture of hyperconcentrated sediment transport and debris flow. It means that a single rheology is not able to model the whole event. A more sophisticated model is necessary to improve the results accuracy. The absence of channel levees in the lower part of the surveyed cross sections indicates that provably the flow was more diluted and there was an aggradation process in the channel.

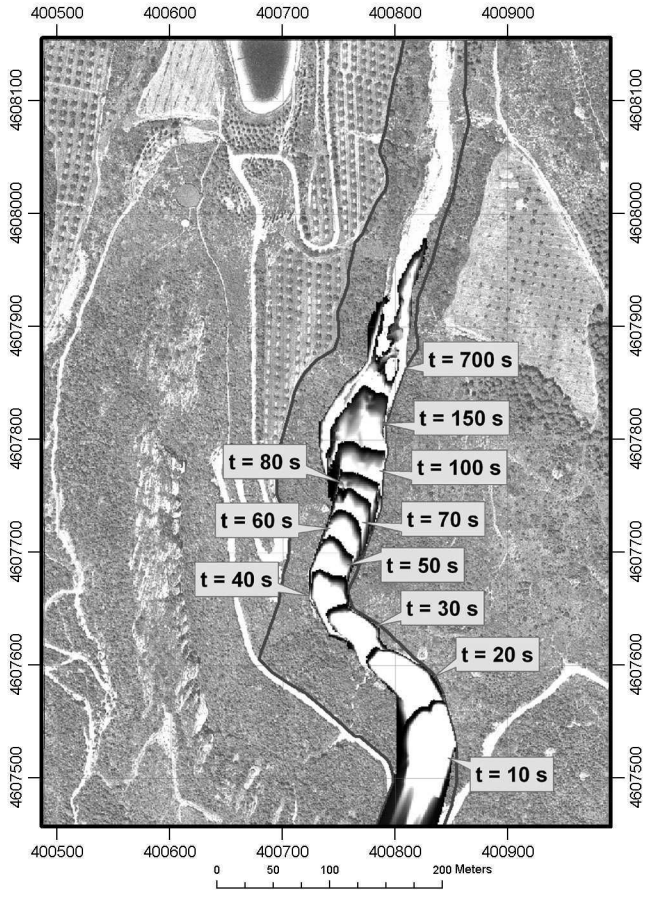

Figure 8.15: Different time steps obtained with the Voellmy best fit.

8.4 Pal

8.4.1 Field Data

The Cardemeller catchment near Pal is situated in the Principality of Andorra and covers an area of 1.7 km^2 (Figure 8.1). From a geological point of view, the drainage basin is settled in the Eastern Axial Pyrenees and the basement principally consists of Devonian and Cambro-Ordovician rocks including meta-limestones, phyllites and slates. Bedrock is generally covered by superficial deposits of glacial origin and colluvium.

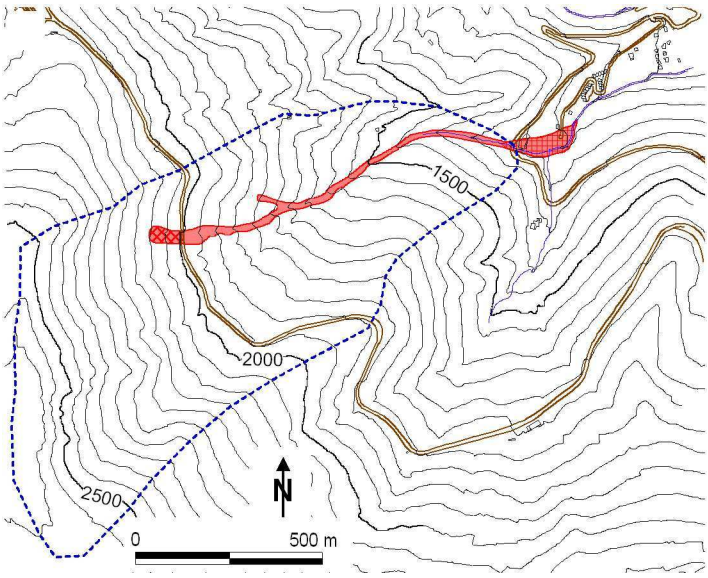

Figure 8.16: Cardemeller torrent at Pal, topographic map indicating the flow path of the event.(Figure courtesy of M. Hürlimann)

The initiation of the debris flow took place in a road cut excavated in colluvium and mobilized several hundred cubic meters (Figure 8.16). The debris flow was provoked during the widespread floods of November 7/8, 1982. A total rainfall amount of about 180 mm in 48 h was estimated for the Pal area using nearby rain gauges that unfortunately only recorded the total daily precipitation.

The initial slope failure rapidly transformed into a debris flow and strongly increased volume by important entrainment of material along the flow path. A final volume of about 5000 m^3 was calculated by field observations just after the event. The accumulation zone of the debris flow covered the higher part of the fan and destroyed the road at the fan apex (Figure 8.16).

8.4.2 Simulation Results

The main purpose of the backanalysis of the Cardemeller debris flow was the validation of the implementation of basal entrainment into the model. In each simulation a start

Figure 8.17: Picture of Cardemeller torrent at Pal .(Photography courtesy of M. Hürlimann)

volume of 500 m^3 was released at the road cut, where initial failure occurred in 1982 (Figure 8.16). The topographic grid used at this catchment included rectangular cells of 1 m size.

Preliminary simulations showed that the Voellmy fluid model provided again most reasonable results (Bateman et al., 2007). In this case, the rheological parameters of the final runs were $\mu = \tan(\phi) = 0.22$ and $C = 12\,\mathrm{m}^{1/2}/\mathrm{s}$.

Regarding the analysis on basal erosion the parameter ϕ_{ent}, which governs the entrainment condition, was assumed to be $\phi_{ent} = 31\,^\circ$. This value would correspond to a pore pressure parameter of 0.3 and an internal friction angle of $40\,^\circ$ (Equation 6.3.7), which coincide with the ones proposed by (Iverson and Denlinger, 2001) and (Pudasaini et al., 2005).

General results on the flow dynamics of the Cardemeller debris flow are presented

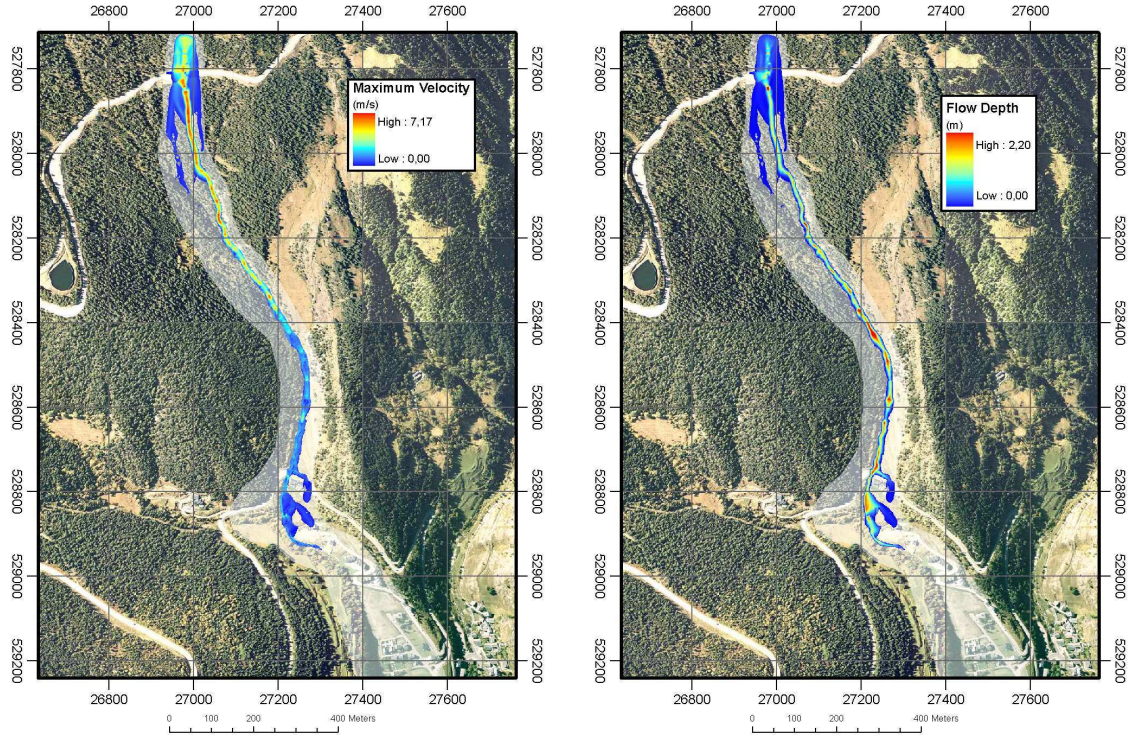

Figure 8.18: Backanalysis of the debris flow occurred in the Cardemeller torrent at Pal applying Voellmy fluid ($\mu = \tan(\phi) = 0.22$ and $C = 12\,\mathrm{m}^{1/2}/\mathrm{s}$). **Left**: Maximum flow velocity. **Right**: Maximum flow depth.

first, while the sensitivity analysis on the basal entrainment will be described later. Figure 8.18 Left shows maximum velocity and Figure 8.18 Right illustrates maximum flow depth. Maximum flow velocity reaches about 7 m/s in the higher confined section, whereas maximum flow depth greater than 2 m can be observed at several points along the flow path.

The extension of the final deposit (Figure 8.19 Left) coincides more or less with the area observed just after the event by field data (see Figure 8.16). Most differences can be explained by the topographic information used for the simulation. Since an actual digital elevation model (DEM) was incorporated, significant variation can appear between this DEM and the pre-event relief. This discrepancy especially affects the depth of the final deposit, which is strongly related to morphologic anomalies. All

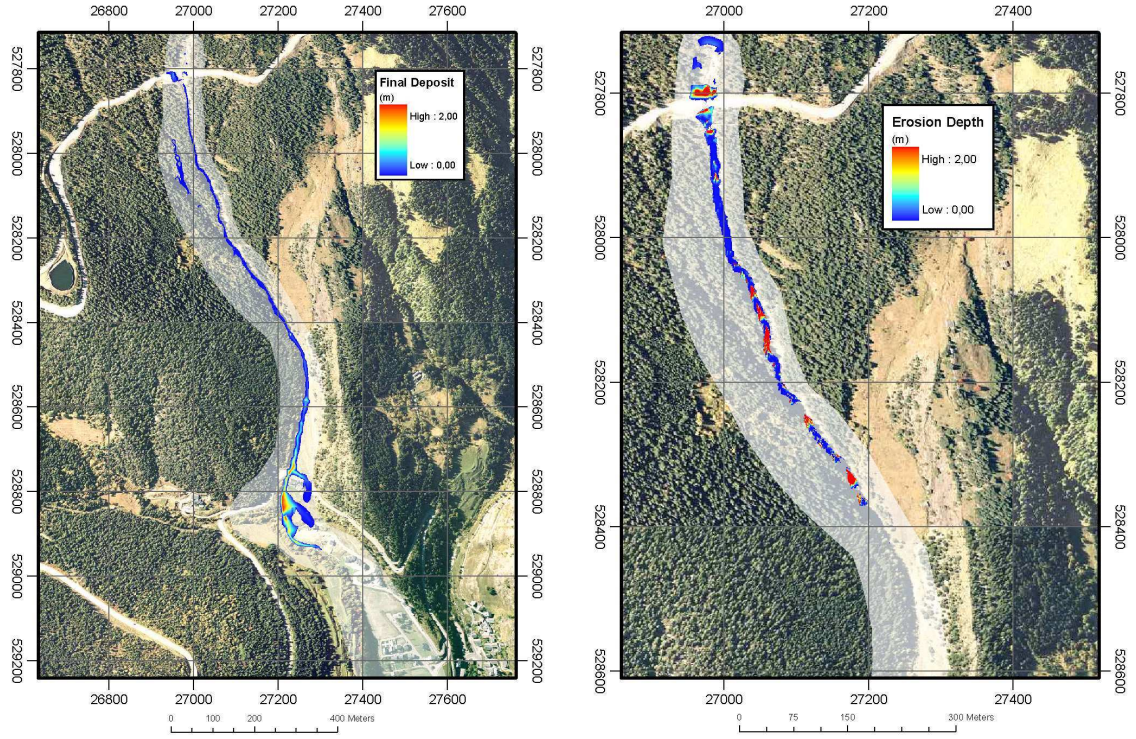

Figure 8.19: Backanalysis of the debris flow occurred in the Cardemeller torrent at Pal applying Voellmy fluid ($\mu = \tan(\phi) = 0.22$ and $C = 12\,\mathrm{m}^{1/2}/\mathrm{s}$). **Left**: Depth of final deposit. **Right**: Erosion depth calculated along flow trajectory using the dynamic approach and $\phi_{bed} = 31\,^{\circ}$.

these uncertainties, however, do not alter the runs analyzing the effect of entrainment, because erosion was limited to the higher part of the flow path.

Figure 8.19 Right shows the erosion depth computed in the higher section of the path. Simulation results indicate that maximum entrainment occurs at steep and confined points, where erosion depths of up to 2 m were calculated. A curious feature is the step-and-pool morphology, which is associated with the areas of erosion. This fact seems to be correlated with both the torrent width and some kind of retrogressive scour.

Apart from the erosion depth along the flow path, the evolution of the flow total volume with time was computed (Figure 8.20). The blue line indicates the general

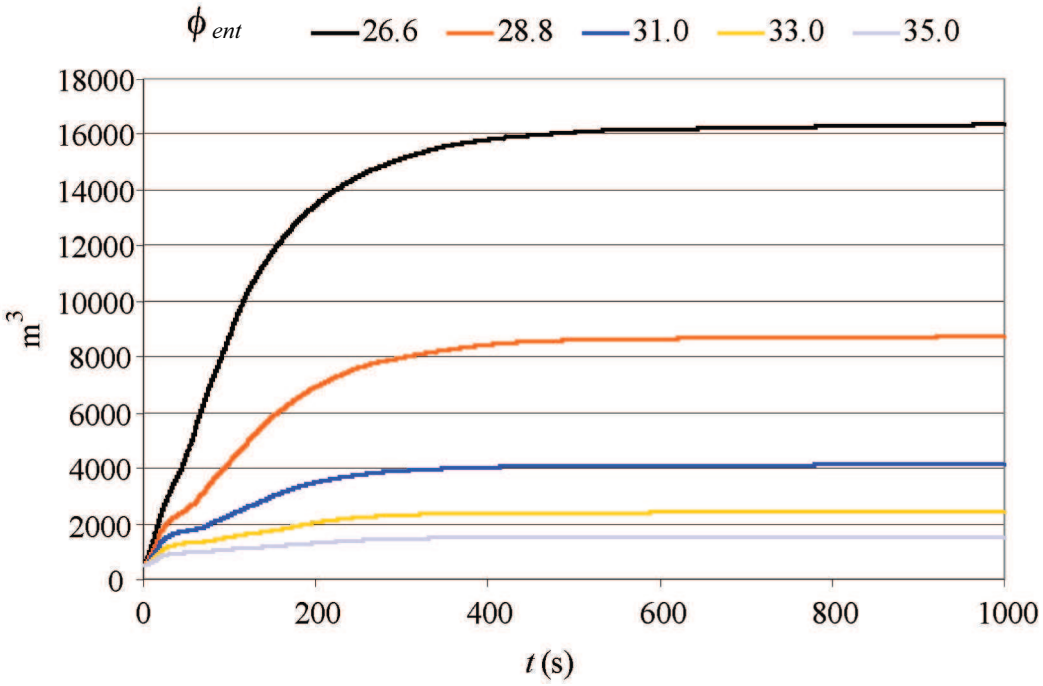

Figure 8.20: Effect of entrainment during the Cardemeller debris flow applying the dynamic approach and different values of ϕ_{ent}, evolution of debris-flow volume with time.

value of $\phi_{ent} = 31\,°$. The initial volume of 500 m^3 strongly increases in the first phase of the event, because the debris flow passes through the steep section. The principal part of the total computed volume of about 4100 m^3 was reached after only 400 seconds, while very small entrainment occurs afterwards.

The final volume underestimates the total volume after the event, but this error can be fixed by a small reduction of ϕ_{ent}-value, as we will see in the following. A sensitivity analysis of the parameter ϕ_{ent} was carried out, in order to obtain an idea of its influence on the erosion rate. Figures 8.20 compares the previously commented results using $\phi_{ent} = 31\,°$ with five other ϕ_{ent}-value and Figure 8.21 summaries the results correlating the final volume with the ϕ_{ent}-value applied.

Both Figures 8.20, 8.21 indicate the strong influence of ϕ_{ent} on the erosion rate, especially for values smaller than about $\phi_{ent} = 30\,°$. A similar non-linear behavior

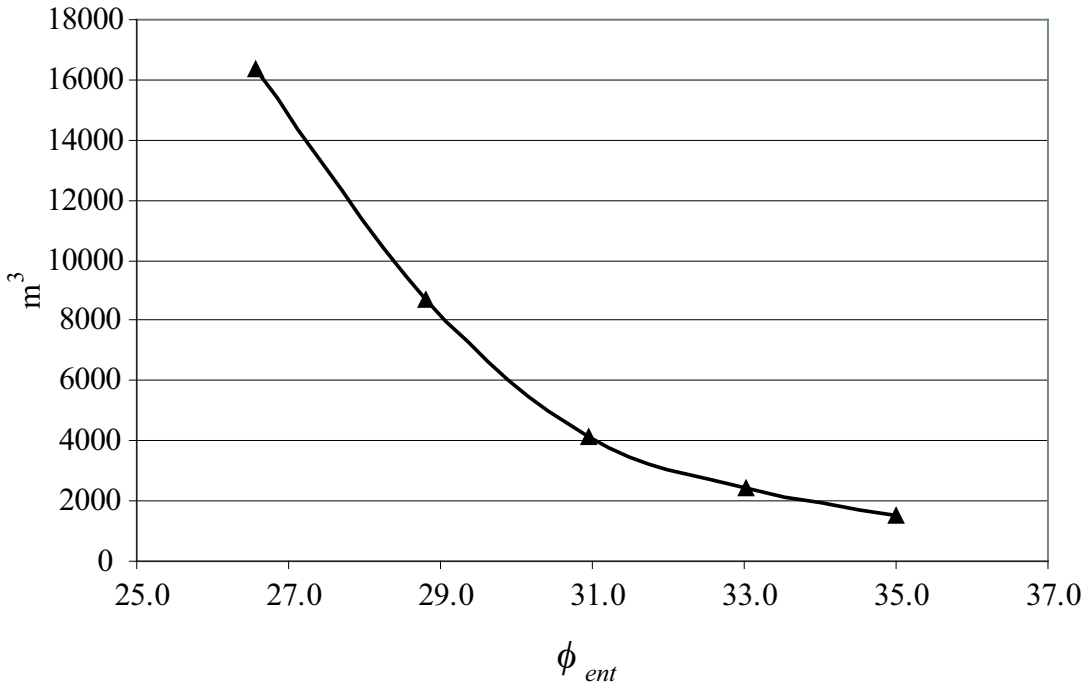

Figure 8.21: Effect of entrainment during the Cardemeller debris flow applying the dynamic approach and different values of ϕ_{ent}, relation between ϕ_{ent}, final volume of debris flow.

was already observed in the theoretical runs illustrated in Figure 6.6. As a concluding remark, we can state that a total final volume of about 5000 m^3, which was estimated for the Cardemeller debris flow, would have been computed applying a ϕ_{ent}-value of about $\phi_{ent} = 30.5\,^\circ$. Such a friction angle of the channel bed material may be rather small, but detailed laboratory or *in-situ* tests would be necessary to exactly validate this parameter.

Conclusions

A debris flow model has been developed. Different steps have been carried out: beginning with the equations definition and ending with the real test cases validation, passing through the software implementation. The proposed model is specially adapted to steep slopes scenarios. The main constrain of the model is the requirement of low ratio between terrain surface second derivatives and first derivatives. This ratio is equivalent to terrain surface low curvatures or slowly varying slopes.

Compared to the existing debris flow models, the strength of the here presented one is the simplicity in input data setup. Just a DEM (Digital Elevation Model) is necessary in order to define the topography and no preprocessor in necessary to adapt to the model coordinate system. The coordinate system used by the model is named PCS (Proposed Coordinate System) and is a particularization of the coordinates defined in Bouchut and Westdickenberg (2004).

The classical mass and momentum conservation laws are used as main modeling equations. The present model is a depth integrated model. It solves two dimensional differential equations. The complexity of model development is related to the depth integration process over general curved surfaces.

Several practical issues of the model implementation are also addressed. An algorithm for the flow stop and go mechanism (remobilization) is included in the model. Also basal entrainment calculation approaches are included among other particular features.

The validation of the model seems to be fulfilled, running different analytical,

experimental and real test cases. As is common in fluid dynamics, there is not an analytical solution for a complete debris flow problem, so simplified ones are used instead.

From every chapter a conclusions list is presented:

Regarding the coordinate system definition (Chapter 1):

1. For steep slope modeling, the terrain surface normal is selected as integration direction.

2. The proposed coordinate system (PCS), keeps the cartesian coordinates X, Y as curvilinear coordinates (u, v), and the surface is defined as $Z = h(X, Y)$.

3. In the PCS, when the second derivative of the terrain surface function are lower than the slopes (first derivative) the principal curvatures are small ($h_{ij} \ll h_i \Rightarrow \mathrm{K_G}, \mathrm{K_M} \simeq 0 \Rightarrow k_1, k_2 \simeq 0$).

4. In the PCS, when the second derivative of the terrain surface function are lower than the slopes (first derivative) the Christoffel symbols are small ($h_{ij} \ll h_i \Rightarrow \Gamma^k_{ij} \simeq 0$).

5. In the PCS, if the values of the Gaussian Curvature $\mathrm{K_G}$ and Mean Curvature $\mathrm{K_M}$ are null, being the terrain slopes not null, then the second derivatives of the terrain surface function (h_{XX}, h_{YY}, h_{XY}) are null, and, therefore, Christoffel symbols are also null:

$$(\mathrm{K}_G, \mathrm{K}_M = 0) \Leftrightarrow (h_{XX}, h_{YY}, h_{XY} = 0) \Leftrightarrow \left(\Gamma^k_{ij} = 0\right)$$

6. Discard the curvatures in the equations justifies also discarding the Christoffel symbols.

Regarding the equation system definition (Chapter 2):

1. The model equations system is defined based on the mass conservation and momentum conservation.

2. An homogeneous, constant density flow is considered, so the model approach is monophasic.

3. A non-dimensionalization of the equations system is carried out using characteristic variables of the flow:

   - A flow length L
   - A depth H
   - Curvature radius r

4. The perturbation method is used to simplify the equations.

5. In zero order approach, the vertical velocities are null for shallow flows.

6. In first order approach the velocity profile along the depth is linear for shallow flows.

$$u_0^1 = \hat{u}^1 / (1 - k_1\beta)$$
$$u_0^2 = \hat{u}^2 / (1 - k_2\beta)$$

7. In first order approach the pressure includes centripetal terms:

$$P(w) = \frac{\rho}{2}\left(h_1(0)\hat{u}^1\right)^2 \left\{ \left(\frac{1}{1-k_1 d}\right)^2 - \left(\frac{1}{1-k_1 w}\right)^2 \right\} +$$
$$+\frac{\rho}{2}\left(h_2(0)\hat{u}^2\right)^2 \left\{ \left(\frac{1}{1-k_1 d}\right)^2 - \left(\frac{1}{1-k_1 w}\right)^2 \right\} + \rho g_3 (d - w)$$

8. The dimension of the model is reduced by the depth integration.

9. Supposing small curvatures ($k_1, k_2 \simeq 0$) simplifies the integrated equation system, reduces the metric complexity:

- The velocity profile becomes constant
- The pressure becomes hydrostatic, neglecting the centripetal effects
- 2D bed surface metrics are equal to the flow 3D volume metrics: $\widehat{E} = E$, $\widehat{G} = G$, $\hat{g}_{ij} = g_{ij}$.

10. Discarding the curvature effects converts the definition of equation system in the direct application of covariant derivative to the SWE. Equal to compute SWE in curved manifolds (Rossmanith et al., 2004).

11. The equations system obtained in the model before introducing the rheology is:

$$\begin{cases} \dfrac{\partial d}{\partial t} + \dfrac{1}{\sqrt{|g|}} \dfrac{\partial \left(\sqrt{g} u^k d\right)}{\partial x^k} = 0 \\ \dfrac{\partial \left(d u_i\right)}{\partial t} + \dfrac{1}{\sqrt{|g|}} \dfrac{\partial}{\partial x^j} \left(\sqrt{|g|} T^{ji}\right) = d g_i \end{cases}$$
$$T^{ij} = d u^i u^j + \frac{g_3}{2} d^2 g^{ij}$$

12. The shallow flow hypothesis influences in the rheology, several terms of the stress tensor could be discarded through geometrical arguments. These discarded elements include internal stresses.

13. The pressure P and the bed shear stresses τ_{bi} are the terms that depend on the rheology, the first comes from the integration of τ_{ii} and the second from τ_{i3}.

Regarding the numerical methods applied to solve the equations system (Chapter 3):

1. The *Finite Volume Method* (FVM) is used to discretize the equations, the metric term is included into the flux function.

2. The *cell-edge flux functions* (Bale and LeVeque, 2002) are used in the FVM discretization.

3. A high resolution discretization is implemented, using TVD limiters: Minmod, Superbee, Van Leer and Monotonized Centered Limiter (LeVeque, 2002).

4. Linearized (Roe, HLLC, Osher) and non-linear solvers are implemented in the model (LeVeque, 2002).

5. A locally orthonormal axes are defined to solve the Riemann problem at the control volume interfaces, in these coordinates the equations system becomes equal to the SWE with a corrected gravity. So the classical SWE solver is used.

Regarding the boundary conditions introduction (Chapter 4):

1. A new method to introduce boundary conditions is described in Chapter 4.

2. It combines a filter, which ensures that only well-posed problems are defined, and a method for interpolating the unknown dependent variables in partial boundary conditions (subcritical regimes).

3. The method is based on the Riemann problem solution and is optimal for the Godunov method.

4. It allows discontinuities such as boundary conditions to be introduced.

5. The method can immediately be extended to one-dimensional Euler equations, but more research is required before it can be extended to multidimensional problems.

6. The method is computed using an exact Riemann solver because it is not computationally expensive, so the combination with approximate Riemann solvers should be researched.

Regarding the accuracy in internal boundary conditions calculation (Chapter 5):

1. When a control structure is introduced in the computational domain of the model a internal boundary condition is established, this control structure is regulated by a closure relation. In this function the smoothness is related to the maximum time step.

2. A new accuracy criterium for the internal boundary condition is introduced, allowing to guarantee the fulfillment of the structure characteristic curve.

3. This proposed criterium adds a new time step constrain to add to the Courant stability restriction.

4. The new accuracy criterium is tested and validated.

Regarding to the special features of the model (Chapter 6):

1. Three different special features are included in he model:

   (a) Stop and go mechanism: Algorithm to establish the deposition of the flow.

   (b) Entrainment process: Approach used to compute the basal entrainment of material into the flow (see Equation 6.3.7).

$$\frac{\partial z}{\partial t} = \frac{1}{\rho V}(\tau_f - c - (1-\lambda)\cos\theta h \rho g \tan\phi_{ent}) \tag{8.4.1}$$

   (c) Rheology adaptation: A filter to select between the static internal friction angle and the dynamic friction angle.

Regarding to the validation using analytical, experimental and real cases (Chapter 7):

1. Four different test cases were carried out to validate the code:

   (a) Analytical, ideal, frictionless, flat, dambreak.

   (b) Analytical one-dimensional dambreak with steep slope and friction.

(c) Experimental UPC-GITS bi-dimensional water dambreak.

(d) Experimental USGS bi-dimensional sand flow.

Being the numerical results in good agreement with the predicted ones. A problem exist in the definition of a complete bi-dimensional analytical solution for SWE. Without this analytical solution bi-dimensional models validation is not possible.

2. The agrement in the ideal dambreak analytical solutions is good, the results fit well with the predicted values. The test case was solved using first order approach in the discretization. The principal error appears in rarefaction wave due to the poor accuracy of the first order model. The values for the shock wave are accurate.

3. The dambreak test case with slope and friction is solved with a second order approach. The numerical results fit almost exact values of the analytical solution. The reason for this good agreement is related to the fact that the solution is mainly formed by a rarefaction wave, and with the second order approach these waves are well fitted.

4. A 2D validation case was carried out in the UPC-GITS experimental facilities. The free surface of the flow was captured using laser technologies.

5. The mean depth error in the numerical simulation of the experiment was 13.9%, and on the 80% of the domain the error is less than 7%.

6. In the sand flow experimental test case (USGS), the agreement in the shapes of the final deposit is good. Also the numerical transient results fit well with the experiment.

Regarding the real cases (Chapter 8):

1. Three different real cases were analyzed with the model: “La Guingueta”, Pal, Montserrat.

2. To fit the real data the back analysis technic is used.

3. Regarding “La Guingueta” case:

   - The total volume was 30000 m^3, divided in two different initiation points.
   - The selected cell size was 2 m.
   - The rheology adaptation special feature was used.
   - The best-fit results were obtained using the Voellmy rheology with the parameters $\mu = \tan(\phi) = 0.1$, $C = 10\,m^{1/2}/s$.
   - The maximum depth values were around 2 m and the maximum velocities 9 m/s.
   - The final deposit fits well the real case surveyed data.

4. Regarding Montserrat case:

   - The total volume was 10000 m^3.
   - The selected cell size was 0.3 m.
   - The best-fit results were obtained using the Voellmy rheology with the parameters $\mu = \tan(\phi) = 0.13$, $C = 10\,m^{1/2}/s$.
   - The maximum depth values were around 0.2-2 m and the maximum velocities 16 m/s, other methodologies suggest a real maximum velocity around 12 m/s.
   - The maximum discharge was over 90 m^3/s.
   - The final deposit fits well with the real case surveyed data, but indicates that probably the event was between hyperconcentrated flow and debris flow.

5. Regarding Pal case:

   - The initial volume was 500m^3.

- The entrainment approach was used in this simulation.
- The maximum erosion allowed was fixed in 2 meters.
- Regarding the analysis on basal erosion the parameter ϕ_{ent}, which governs the entrainment condition, the value was assumed to be $\phi_{ent} = 31\,^{\circ}$.
- Using this parameter the total material volume at the end of the simulation was lightly under 5000 m^3.
- The selected cell size was 1 m.
- The best-fit results were obtained using the Voellmy rheology with the parameters $\mu = \tan(\phi) = 0.22$, $C = 12\,m^{1/2}/s$.
- The maximum velocity were around 7 m/s.
- The final deposit fits well with the real case surveyed data.

Future Works

In this chapter some future research lines will be proposed. In author's opinion more effort should be given to improve the knowledge in debris flow mechanics. Numerical methods for fluids are being developed in agreement with other disciplines, but heterogeneous flows are a central point of debris flow research.

The development of computational hardware opens the door to the birth of complete 3D models, so the future of coordinate integrated models is not so clear. One of the problem is the data availability of the real phenomenon. Complete model without detailed data input is not possible.

Some future and immediate research lines should be as follows:

1. Following the debris flow experimental activities developed at the *Laboratorio de Morfodinmica Fluvial* in the UPC and from literature review (Iverson and Denlinger, 2001; Pudasaini and Hutter, 2007) it seems that pore pressure plays an important role in the debris flow phenomenon. A *state of the art* model for real events probably should include this variable, although the necessary parameters for the modeling of pore pressure requires complex elements like pressure diffusion (Baum et al., 2008). The existing literature about these parameters is limited.

2. The fact of using the constant density hypothesis reduces significantly the applicability range of the model, so the inclusion of variable density would result

in a powerful model but also would require the integration of variable-density entrainment equations and variable density rheology law.

3. The proposed cases were mainly granular flows, it seems to be necessary the introduction of dense rapid granular flows rheologies (Delannay et al., 2007; Azanza et al., 1999; MiDi, 2004), where concepts like *granular temperature* are used to model the flow mechanics. The main limitation of these models are the exclusion of water, so it comes into conflict with the pore pressure inclusion.

4. In the constitutive equations analysis, some terms of the stress tensor are discarded, this includes the internal stresses, following the methodology introduced by Iverson et al. (2004). A more complex rheological should be introduced to improve results, probably, as in the commented reference other numerical methods should be used for dealing with the complete stress tensor.

5. As it is known, using structured grids as computational mesh simplifies the data input construction but limits the flexibility of the model. In this case the real events have an associated topography, with small scale elements that should be better captured using unstructured mesh. The translation of the code to this type of meshes would increase its flexibility and accuracy.

Appendix A

Torus example

In this appendix the torus example used in Chapter 1, Section 1.6, is presented. The amount of figures and equations suggest splitting the chapter creating this appendix. Every metric element is presented as an equation with the corresponding graphical representation.

The sections presented in this appendix are:

- First Fundamental Form I_p
- Second Fundamental Form II_p
- Torus Christoffel Symbols.
- Torus Intrinsic Metrics.

Every section has a subsection for PCS and for Principal Curvatures Coordinates.

The metric intrinsic elements are:

- Mean and Gaussian curvatures.
- Principal curvatures.

All the metric intrinsic elements are common in both coordinate systems, that's why they are not associated to a particular coordinate system choice.

The equations used for torus parametrization in PCS are:

$$\begin{cases} x = X \\ y = Y \\ z = h(X,Y) = -\sqrt{r_2^2 - \left(r_1 - \sqrt{X^2+Y^2}\right)^2} \end{cases} \tag{A.0.1}$$

Where r_1, r_2 are the bend radius and the crossection shape radius.

The equations used for torus parametrization in Principal Curvatures Coordinates are:

$$\begin{cases} \mathrm{x} = (\mathrm{r}_1 + \mathrm{r}_2 \cos(\phi)) \cos(\theta) \\ \mathrm{y} = (\mathrm{r}_1 + \mathrm{r}_2 \cos(\phi)) \sin(\theta) \\ z = \mathrm{r}_2 \sin(\phi) \end{cases} \tag{A.0.2}$$

Where $\theta \in (0, \pi)$ and $\phi \in (\pi, 2\pi)$, these two coordinates define the curvature lines.

A.1 First Fundamental Form I_p

The first fundamental form I_p is related to the dot product of the curvilinear coordinates tangents, it defines the covariant metric tensor g_{ij}, and also the inverse o contravariant metric tensor $g^{ij} = (g_{ij})^{-1}$.

A.1.1 PCS

In the present case the components of this tensor in PCS are:

$$
\begin{aligned}
g_{11} = E &= \frac{r_2X^2 + r_2Y^2 - r_1^2Y^2 + 2\,r_1\sqrt{X^2+Y^2}Y^2 - Y^2X^2 - Y^4}{\left(r_2 - r_1^2 + 2\,r_1\sqrt{X^2+Y^2} - X^2 - Y^2\right)\left(X^2+Y^2\right)} \\
g_{12} = F &= \frac{\left(-r_1 + \sqrt{X^2+Y^2}\right)^2 XY}{\left(r_2 - r_1^2 + 2\,r_1\sqrt{X^2+Y^2} - X^2 - Y^2\right)\left(X^2+Y^2\right)} \\
g_{21} &= F \\
g_{22} = G &= \frac{r_2X^2 + r_2Y^2 - r_1^2X^2 + 2\,r_1\sqrt{X^2+Y^2}X^2 - X^4 - Y^2X^2}{\left(r_2 - r_1^2 + 2\,r_1\sqrt{X^2+Y^2} - X^2 - Y^2\right)\left(X^2+Y^2\right)}
\end{aligned}
\tag{A.1.1}
$$

A.1.2 Principal Curvatures Coordinates

In the present case the components of this tensor in Principal Curvatures Coordinates are:

$$
\begin{aligned}
g_{11} &= E = \left(r_1 + r_2\cos\left(\phi\right)\right)^2 \\
g_{12} &= F = 0 \\
g_{21} &= F \\
g_{22} &= G = r_2^2
\end{aligned}
\tag{A.1.2}
$$

A.2 Second Fundamental Form II_p

The second fundamental form II_p is related to the second derivatives of the curvilinear coordinates.

A.2.1 PCS

In the present case the components of this tensor in PCS are:

$$
\begin{aligned}
e = &- \left(\begin{array}{c} -{r_1}^3 Y^2 - 3 r_1 Y^4 - 3 X^2 r_1 Y^2 + r_1 r_2 Y^2 \\ + \left(X^2 Y^2 + Y^4 - r_2 Y^2 - X^2 r_2 + 3 {r_1}^2 Y^2 \right) \sqrt{X^2 + Y^2} \end{array} \right) \\
&\cdot \frac{\left(r_2 - {r_1}^2 + 2 r_1 \sqrt{X^2 + Y^2} - X^2 - Y^2 \right)^{-3/2} \left(X^2 + Y^2 \right)^{-3/2}}{\sqrt{\frac{r_2}{r_2 - {r_1}^2 + 2 r_1 \sqrt{X^2 + Y^2} - X^2 - Y^2}}}
\end{aligned}
\tag{A.2.1}
$$

$$
\begin{aligned}
f = &YX \left(\begin{array}{c} -3 X^2 r_1 - 3 r_1 Y^2 + r_1 r_2 - {r_1}^3 \\ + \left(X^2 + 3 {r_1}^2 + Y^2 \right) \sqrt{X^2 + Y^2} \end{array} \right) \\
&\cdot \frac{\left(r_2 - {r_1}^2 + 2 r_1 \sqrt{X^2 + Y^2} - X^2 - Y^2 \right)^{-3/2} \left(X^2 + Y^2 \right)^{-3/2}}{\sqrt{\frac{r_2}{r_2 - {r_1}^2 + 2 r_1 \sqrt{X^2 + Y^2} - X^2 - Y^2}}}
\end{aligned}
\tag{A.2.2}
$$

$$
\begin{aligned}
g = &- \left(\begin{array}{c} -3 X^2 r_1 Y^2 - X^2 {r_1}^3 + X^2 r_1 r_2 - 3 X^4 r_1 \\ + \left(3 {r_1}^2 X^2 - r_2 Y^2 - X^2 r_2 + X^2 Y^2 + X^4 \right) \sqrt{X^2 + Y^2} \end{array} \right) \\
&\cdot \frac{\left(r_2 - {r_1}^2 + 2 r_1 \sqrt{X^2 + Y^2} - X^2 - Y^2 \right)^{-3/2} \left(X^2 + Y^2 \right)^{-3/2}}{\sqrt{\frac{r_2}{r_2 - {r_1}^2 + 2 r_1 \sqrt{X^2 + Y^2} - X^2 - Y^2}}}
\end{aligned}
\tag{A.2.3}
$$

A.2.2 Principal Curvatures Coordinates

In the present case the components of this tensor in Principal Curvatures Coordinates are:

$$
\begin{aligned}
e &= \frac{\left({r_1}^2 + 2 r_1 r_2 \cos(\phi) + {r_2}^2 (\cos(\phi))^2 \right) \cos(\phi)\, r_2}{\sqrt{{r_2}^2 (r_1 + r_2 \cos(\phi))^2}} \\
f &= 0 \\
g &= \frac{{r_2}^2 (r_1 + r_2 \cos(\phi))}{\sqrt{{r_2}^2 (r_1 + r_2 \cos(\phi))^2}}
\end{aligned}
\tag{A.2.4}
$$

A.3 Torus Christoffel Symbols

In this section the Christoffel symbols are calculated.

A.3.1 PCS

The Christoffel symbols equations and graphical representations in PCS are:

$$\Gamma^X_{XX} = -\frac{X\left(-r_1+\sqrt{X^2+Y^2}\right)}{r_2\left(X^2+Y^2\right)^2\left(r_2-{r_1}^2+2\,r_1\sqrt{X^2+Y^2}-X^2-Y^2\right)} \cdot \begin{pmatrix} -3\,r_1X^2Y^2+X^2\sqrt{X^2+Y^2}Y^2-X^2\sqrt{X^2+Y^2}r_2-3\,r_1Y^4+ \\ +3\,\sqrt{X^2+Y^2}{r_1}^2Y^2-{r_1}^3Y^2+Y^4\sqrt{X^2+Y^2}+r_1Y^2r_2-\sqrt{X^2+Y^2}r_2Y^2 \end{pmatrix} \tag{A.3.1}$$

Graphical representation of this values are presented in the Figure A.1.

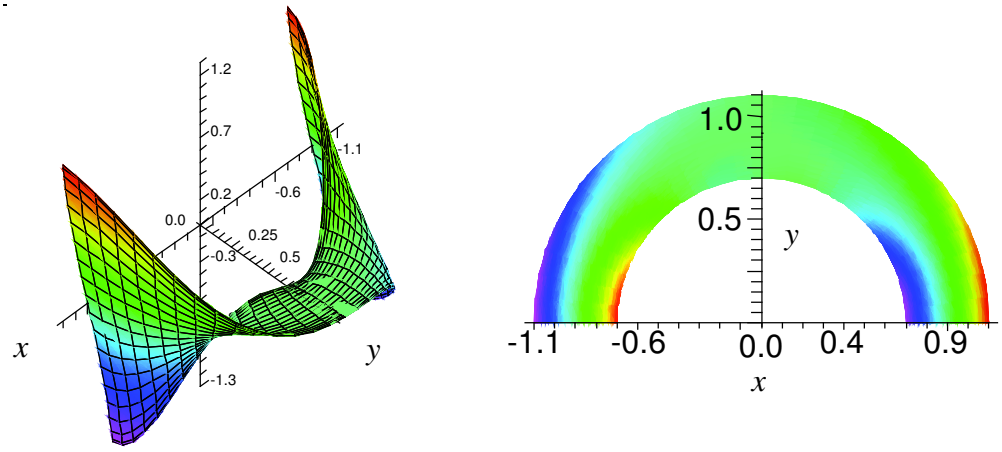

Figure A.1: Γ^X_{XX} values for torus geometry, with $r_1 = 0.9$ and $r_2 = 0.2$.

$$\Gamma^Y_{XX} = -\frac{Y\left(-r_1+\sqrt{X^2+Y^2}\right)}{r_2\left(X^2+Y^2\right)^2\left(r_2-{r_1}^2+2\,r_1\sqrt{X^2+Y^2}-X^2-Y^2\right)} \cdot \begin{pmatrix} -{r_1}^3Y^2-3r_1Y^4-3X^2r_1Y^2+r_1r_2Y^2 \\ +\left(Y^4+X^2Y^2-X^2r_2-r_2Y^2+3{r_1}^2Y^2\right)\sqrt{X^2+Y^2} \end{pmatrix} \tag{A.3.2}$$

Graphical representation of this values are presented in the Figure A.2.

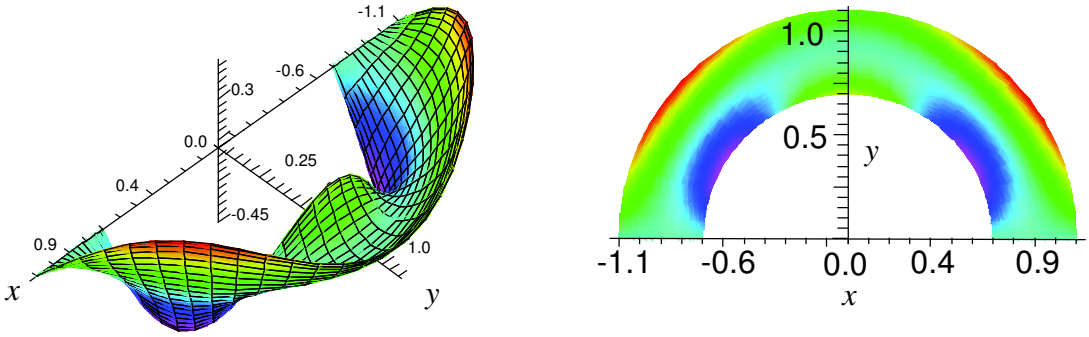

Figure A.2: Γ^{Y}_{XX} values for torus geometry, with $r_1 = 0.9$ and $r_2 = 0.2$.

$$\Gamma^{X}_{XY} = -\frac{YX^2\left(-r_1+\sqrt{X^2+Y^2}\right)}{r_2\left(X^2+Y^2\right)^2\left(r_2-{r_1}^2+2\,r_1\sqrt{X^2+Y^2}-X^2-Y^2\right)} \cdot \begin{pmatrix} -3X^2r_1-3r_1Y^2+r_1r_2-{r_1}^3 \\ \left(3{r_1}^2+X^2+Y^2\right)\sqrt{X^2+Y^2} \end{pmatrix} \tag{A.3.3}$$

Graphical representation of this values are presented in the Figure **??**.

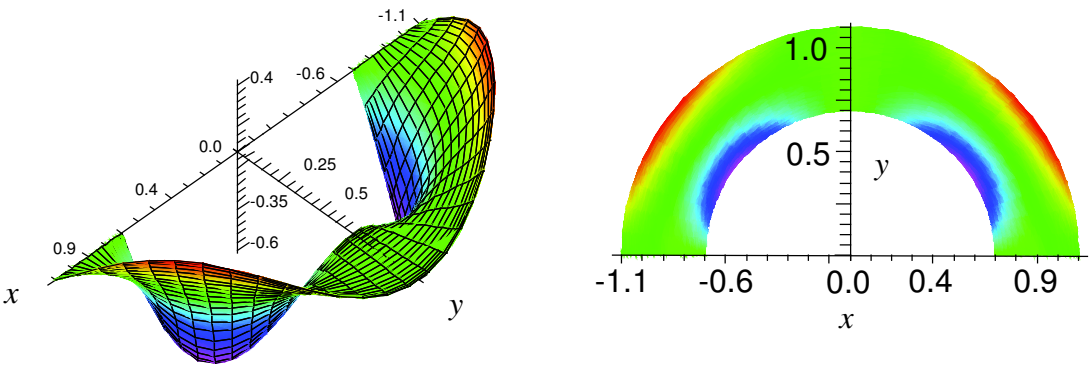

Figure A.3: Γ^{X}_{XY} values for torus geometry, with $r_1 = 0.9$ and $r_2 = 0.2$.

$$\Gamma^{Y}_{XY} = -\frac{XY^2\left(-r_1+\sqrt{X^2+Y^2}\right)}{r_2\left(X^2+Y^2\right)^2\left(r_2-{r_1}^2+2\,r_1\sqrt{X^2+Y^2}-X^2-Y^2\right)} \cdot \begin{pmatrix} -3X^2r_1-3r_1Y^2+r_1r_2-{r_1}^3 \\ \left(3{r_1}^2+X^2+Y^2\right)\sqrt{X^2+Y^2} \end{pmatrix} \tag{A.3.4}$$

Graphical representation of this values are presented in the Figure A.4.

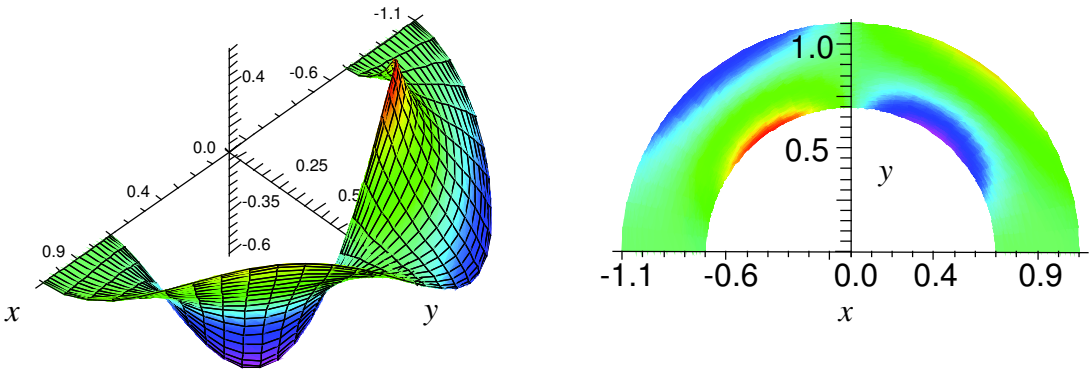

Figure A.4: Γ^{Y}_{XY} values for torus geometry, with $r_1 = 0.9$ and $r_2 = 0.2$.

$$\Gamma^{X}_{YY} = -\frac{X\left(-r_1+\sqrt{X^2+Y^2}\right)}{r_2\left(X^2+Y^2\right)^2\left(r_2-{r_1}^2+2\,r_1\sqrt{X^2+Y^2}-X^2-Y^2\right)} \cdot \begin{pmatrix} -3X^2r_1Y^2-X^2{r_1}^3+X^2r_1r_2-3X^4r_1 \\ +\left(X^4+X^2Y^2-X^2r_2+3{r_1}^2X^2-r_2Y^2\right)\sqrt{X^2+Y^2} \end{pmatrix} \tag{A.3.5}$$

Graphical representation of this values are presented in the Figure A.5.

$$\Gamma^{X}_{YY} = -\frac{Y\left(-r_1+\sqrt{X^2+Y^2}\right)}{r_2\left(X^2+Y^2\right)^2\left(r_2-{r_1}^2+2\,r_1\sqrt{X^2+Y^2}-X^2-Y^2\right)} \cdot \begin{pmatrix} -3X^2r_1Y^2-X^2{r_1}^3+X^2r_1r_2-3X^4r_1 \\ +\left(X^4+X^2Y^2-X^2r_2+3{r_1}^2X^2-r_2Y^2\right)\sqrt{X^2+Y^2} \end{pmatrix} \tag{A.3.6}$$

Graphical representation of this values are presented in the Figure A.6.

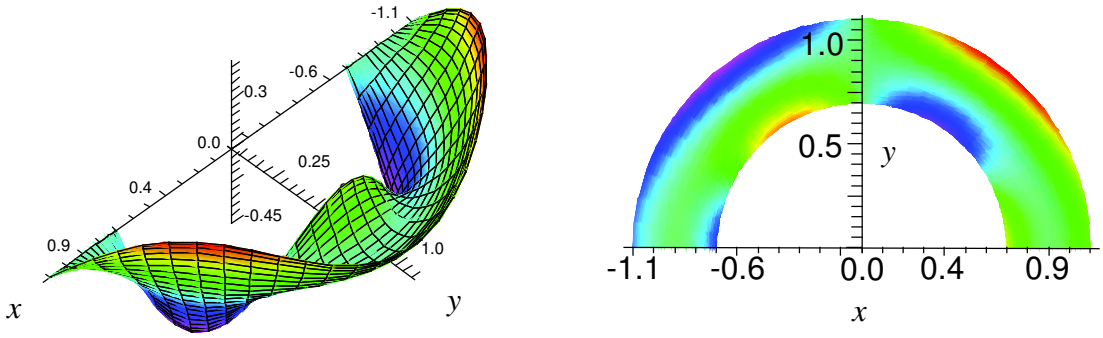

Figure A.5: Γ^X_{YY} values for torus geometry, with $r_1 = 0.9$ and $r_2 = 0.2$.

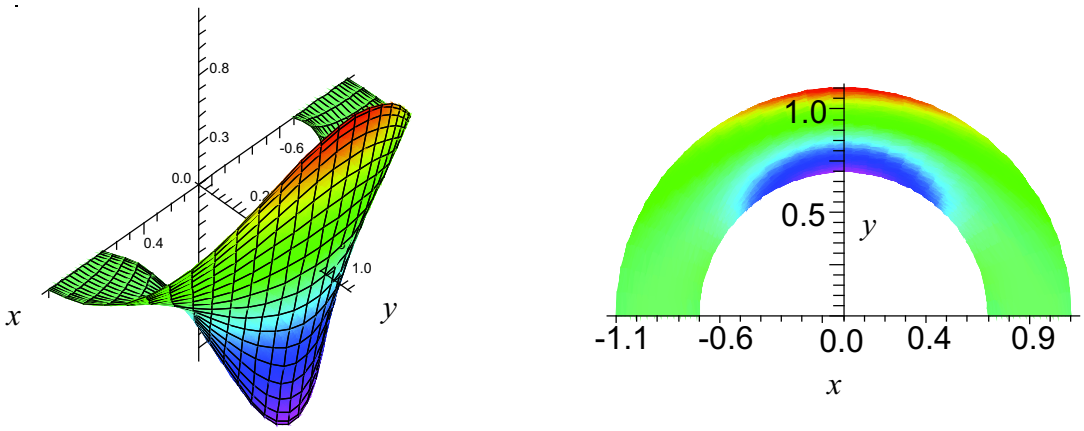

Figure A.6: Γ^Y_{YY} values for torus geometry, with $r_1 = 0.9$ and $r_2 = 0.2$.

A.3.2 Principal Curvatures Coordinates

In this case only three Christoffel symbols are different from zero, and two of them are symmetric, $\Gamma^{\phi}_{\theta\,\theta}, \Gamma^{\theta}_{\theta\,\phi}, \Gamma^{\theta}_{\phi\,\theta}$, in Figure A.7 the first one values are shown in the whole torus, for a determined case.

$$\begin{aligned}
\Gamma^{\phi}_{\theta\,\theta} &= \frac{(r_1 + r_2\cos(\phi))\sin(\phi)}{r_2} \\
\Gamma^{\theta}_{\theta\,\phi} &= -\frac{r_2\sin(\phi)}{r_1 + r_2\cos(\phi)} \\
\Gamma^{\theta}_{\phi\,\theta} &= -\frac{r_2\sin(\phi)}{r_1 + r_2\cos(\phi)}
\end{aligned} \tag{A.3.7}$$

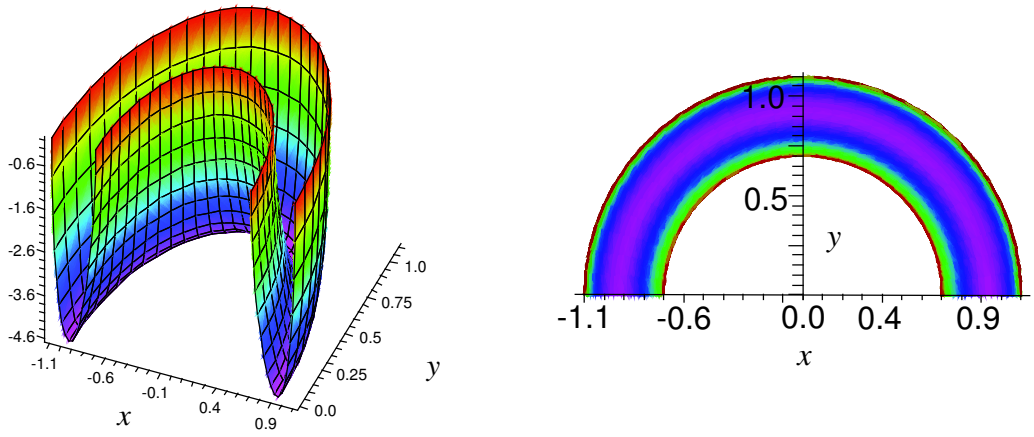

Figure A.7: Values of $\Gamma^{\phi}_{\theta\,\theta}$ in the torus $r_1 = 0.9$, $r_2 = 0.2$.

The sense of this term is the centripetal force along the longitudinal coordinate, it's clear that depends on the curvature radius of the bend. In Figure A.8 the values of $\Gamma^{\theta}_{\theta\,\phi}, \Gamma^{\theta}_{\phi\,\theta}$ are shown for the determined case.

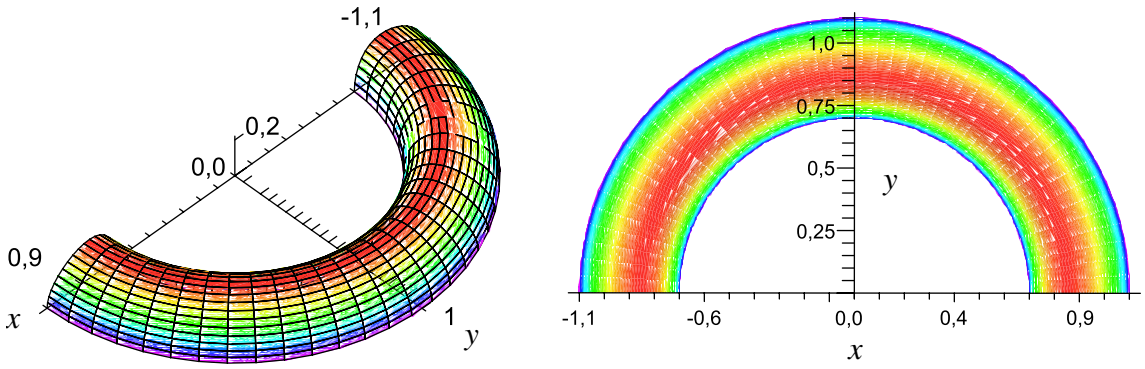

Figure A.8: Values of $\Gamma^{\theta}_{\theta\,\phi}$ in the torus $r_1 = 0.9$, $r_2 = 0.2$.

A.4 Torus Intrinsic Metrics

A.4.1 Gauss curvature

Following Equation 1.4.14 is possible to compute the Gauss Curvature for the torus using the PCS:

$$\mathrm{K}_G = -\frac{-X^2 + r_1\sqrt{X^2+Y^2} - Y^2}{r_2\left(X^2+Y^2\right)} \tag{A.4.1}$$

In the principal directions coordinate system the Gaussian Curvature is:

$$\mathrm{K}_G = \frac{\cos\left(\phi\right)}{r_2\left(r_1 + r_2\cos\left(\phi\right)\right)} \tag{A.4.2}$$

In the Figure A.9 the value of the Gauss curvature is presented, as is shown, the maximum values are achieved near the boundary. The curvature values are intrinsic, so the figures are equal for the both coordinate system, the proposed one (Equation A.4.1) and the principal curvatures one (A.4.2).

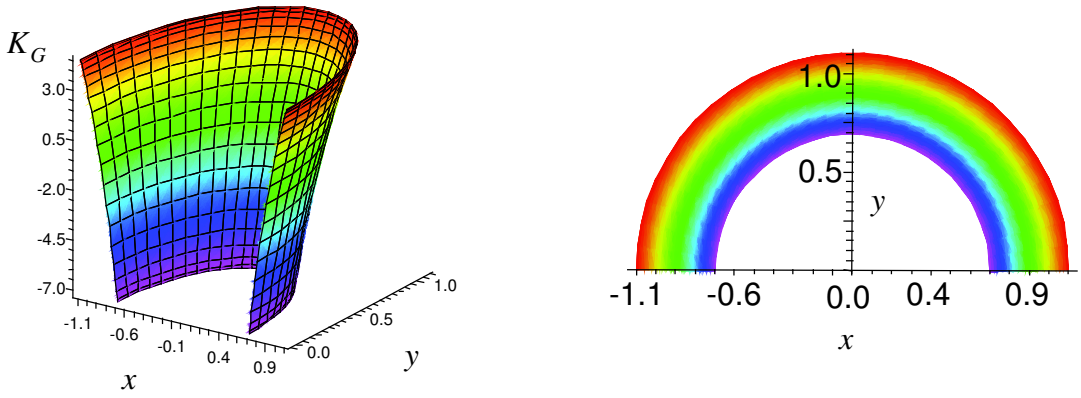

Figure A.9: Gauss curvature of the torus ($r_1 = 0.9$, $r_2 = 0.2$).

A.4.2 Mean curvature

In Equation 1.4.15 the Mean Curvature is found, and the results for the torus using the PCS are:

$$\mathrm{K}_M = -\frac{1}{2}\frac{-5r_1X^2 + 2X^2\sqrt{X^2+Y^2} - 5r_1Y^2}{\sqrt{r_2\left(X^2+Y^2\right)}\left(r_2 - r_1^2 + 2r_1\sqrt{X^2+Y^2} - X^2 - Y^2\right)} \cdot \frac{-2r_2\sqrt{X^2+Y^2} - r_1^3 + 4r_1^2\sqrt{X^2+Y^2} + r_1r_2 + 2Y^2\sqrt{X^2+Y^2}}{\sqrt{r_2\left(X^2+Y^2\right)}\left(r_2 - r_1^2 + 2r_1\sqrt{X^2+Y^2} - X^2 - Y^2\right)} \tag{A.4.3}$$

The Mean Curvature in the principal directions is:

$$\mathrm{K}_M = \frac{1}{2}\frac{2r_2\cos(\phi) + r_1}{r_2\left(r_1 + r_2\cos(\phi)\right)} \tag{A.4.4}$$

In the Figure A.10 the value of the Mean Curvature is presented, as is shown, the maximum values are achieved near the boundary. As in the previous case, it's an intrinsic property, so the results are the same in both coordinate systems (A.4.3, A.4.4).

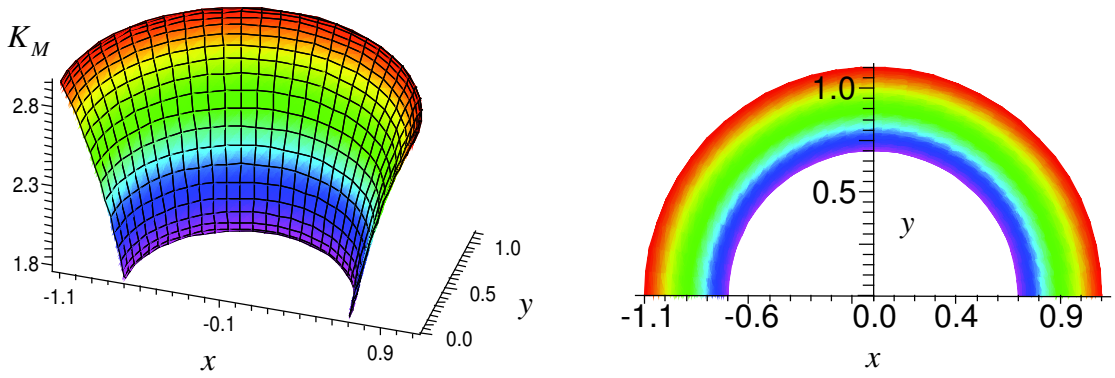

Figure A.10: Mean curvature of the torus ($r_1 = 0.9$, $r_2 = 0.2$).

A.4.3 Principal curvatures

The values of the principal curvatures obtained are:

$$k_1 = \frac{1}{r_2}$$
$$k_2 = \frac{\cos(\phi)}{r_1 + r_2\cos(\phi)} \tag{A.4.5}$$

One of the principal curvatures is related to the crossection shape radius (r_2), and the other to the radius of curvature of the bend (r_1). In the Figure A.11 the values of both principal curvatures are shown, it's important to note that the extreme values are in the shape boundary.

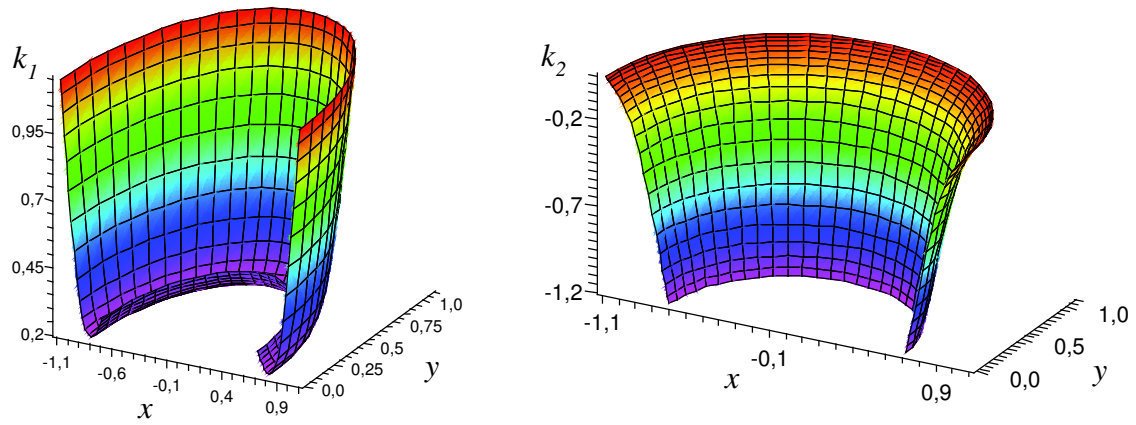

Figure A.11: Values of the principal curvatures (k_1, k_2) in the torus ($r_1 = 0.9$, $r_2 = 0.2$).

Appendix B

Gravity Vector in PCS

In this appendix an example of the gravity vector coodinates transformation in presented, the PCS is selected, so gravity vector changes from the Catersian basis to PCS basis.

The first step is to define the transformation matrix from PCS to Cartesian, this matrix is constructed usign the PCS basis vectors:

$$\mathbf{X}_u = \begin{pmatrix} 1 \\ 0 \\ h_X \end{pmatrix}, \quad \mathbf{X}_v = \begin{pmatrix} 0 \\ 1 \\ h_Y \end{pmatrix}, \quad \mathbf{N} = \frac{1}{(1 + h_X^2 + h_Y^2)^{1/2}} \begin{pmatrix} -h_X \\ -h_Y \\ 1 \end{pmatrix}. \tag{B.0.1}$$

And the transformation matrix is:

$$\mathbf{T}_{\text{PCS C}} = \begin{bmatrix} 1 & 0 & -\frac{h_X}{\left(1+h_X^2+h_Y^2\right)^{1/2}} \\ 0 & 1 & -\frac{h_Y}{\left(1+h_X^2+h_Y^2\right)^{1/2}} \\ h_X & h_Y & \frac{1}{\left(1+h_X^2+h_Y^2\right)^{1/2}} \end{bmatrix}. \tag{B.0.2}$$

The inverse transformation matrix is obtained through matrix inversion:

$$\mathbf{T}_{\mathrm{C\,PCS}} = \begin{bmatrix} \frac{h_X h_Y}{\left(1+h_X^2+h_Y^2\right)} & -\frac{h_X h_Y}{\left(1+h_X^2+h_Y^2\right)} & \frac{h_X}{\left(1+h_X^2+h_Y^2\right)} \\ -\frac{h_X}{\left(1+h_X^2+h_Y^2\right)} & \frac{1+h_X^2}{\left(1+h_X^2+h_Y^2\right)} & \frac{h_Y}{\left(1+h_X^2+h_Y^2\right)} \\ -\frac{}{\left(1+h_X^2+h_Y^2\right)^{1/2}} & -\frac{h_Y}{\left(1+h_X^2+h_Y^2\right)^{1/2}} & \frac{1}{\left(1+h_X^2+h_Y^2\right)^{1/2}} \end{bmatrix} \tag{B.0.3}$$

With the matrix B.0.3 is possible to transform the gravity vector:

$$\mathbf{g}_C = \begin{pmatrix} 0 \\ 0 \\ g \end{pmatrix}, \quad \mathbf{g}_{PCS} = \mathbf{g}_C \cdot \mathbf{T}_{C\,PCS} = \frac{g}{(1+h_X^2+h_Y^2)} \begin{pmatrix} -h_X \\ -h_Y \\ -(1+h_X^2+h_Y^2)^{1/2} \end{pmatrix}. \tag{B.0.4}$$

Bibliography

Abbott, M. B. (1966), *An introduction to the method of characteristics / [by] Michael B. Abbott*, Thames & Hudson, London :.

Abbott, M. B. (1979), *Computational hydraulics : elements of the theory of free surface flows*, Pitman Pub., Belmont, Calif.

Anderson, T. B. and Jackson, R. (1967), 'Fluid mechanical description of fluidized beds. equations of motion', *Industrial and Engineering Chemistry Fundamentals* **6**(4), 527–539.

Aris, R. (1962), *Vectors, Tensors, and the Basic Equations of Fluid Mechanics*, Prentice-Hall.

Azanza, E., Chevoir, F. and Moucheront, P. (1999), 'Experimental study of collisional granular flows down an inclined plane', *Journal of Fluid Mechanics* **400**(1), 199–227.

Bagnold, R. (1954), Experiments on a gravity-free dispersion of large solid spheres in a newtonian fluid under shear, *in* 'Proceedings of the Royal Society of London', Vol. A 225, pp. 49–63.

Bale, D. S. and LeVeque, R. (2002), 'A wave propagation method for conservation laws and balance laws with spatially varying flux functions', *SIAM J. Sci. Comput.* **24**(3), 955–978.

Barre de Saint Venant, A. (1871), 'Théorie et equations générales du mouvement non permanet des eaux courantes', *Comptes Rendus des séances de l Académie des Sciences. Paris, France* **73**, 147–154.

Bateman, A. (1993), Formación y propagación de frentes de onda en canales. Estudio teórico numérico y experimental, PhD thesis, UPC.

Bateman, A., Granados, A., Medina, V., Velasco, D. and Nalesso, M. (2006), Experimental procedure to obtain 2d time-space high-speed water surfaces, *in* 'River Flow 2006', Vol. 1, Taylor and Francis Group, London.

Bateman, A., Medina, V., Hürlimann, M. and Velasco, D. (2007), 'Modelo bidimensional para simulación de flujos detríticos: Flatmodel. aplicación a una cuenca del pirineo catalán', *Ingeniería Hidráulica en México* **XXII**(4), 5–20.

Baum, R., Savage, W. and Godt, J. (2008), TRIGRSA Fortran Program for Transient Rainfall Infiltration and Grid-Based Regional Slope-Stability Analysis, Version 2.0, Open-File Report 1159, US Geological Survey.

Benda, L. E. and Cundy, T. W. (1990), 'Predicting deposition of debris flows in mountain channels', *Can. Geotech. J.* **27**(4), 409 417.

Berger, R. C. and Carey, G. F. (1998*a*), 'Free-surface flow over curved surfaces: Part I: Perturbation analysis', *International Journal for Numerical Methods in Fluids* **28**, 191–200.

Berger, R. C. and Carey, G. F. (1998*b*), 'Free-surface flow over curved surfaces: Part II: Computational model', *International Journal for Numerical Methods in Fluids* **28**, 201–213.

Bingham, E. C. (1922), *Fluidity and plasticity*, McGraw-Hill, New York.

Bouchut, F., Mangeney-castelnau, A., Perthame, B. and pierre Vilotte, J. (2003), 'A new model of saint venant and savage-hutter type for gravity driven shallow water flows'.

Bouchut, F. and Westdickenberg, M. (2004), Gravity driven shallow water models for arbitrary topography, *in* 'in "Comm. in Math. Sci', pp. 359–389.

Bru, J., Serrat, D. and Vilaplana, J. (1984), La dinámica geomorfológica de la cuenca del torrente de jou - la guingueta (noguera pallaresa), Master's thesis, ETSECCPB, Barcelona.

Brufau, P., Garcia-Navarro, P., Ghilardi, P., Natale, L. and Savi (2000), '1d mathematical modelling of debris flow', *J. Hydrol. Res.* **38**(6), 435446.

Cao, Z., Pender, G., S.Wallis and P.A.Carling (2004), 'Computational dam-break hydraulics over erodible sediment bed', *Journal of Hydraulic Engineering* **130**(7), 689–703.

Chen, C. (1983), On frontier between rheology and mudflow mechanics, *in* H. Shen, ed., 'Frontiers in hydraulic engineering', ASCE, New York, pp. 113–118.

Chen, C. and Lee, C. (2002), 'Runout analysis of slurry flows with bingham model', *Journal of Geotechnical and Geoenvironmental Engineering* **128**(12), 1032–1042.

Clancy, L. (1975), *Aerodynamics*, Pitman Publishing, London.

Corominas, J., Moya, J. and Hürlimann, M. (2002), Landslide rainfall triggers in the spanish eastern pyrenees, *in* '4th EGS Plinius Conference "Mediterranean Storms"', Editrice, Mallorca.

Coussot, P., Laigle, D., Arattano, M., Deganutti, A. and Marchi, L. (1998), 'Direct determination of rheological characteristics of debris flow', *Journal of Hydraulic Engineering* **124**(8), 865–868.

Coussot, P. and Meunier, M. (1996), 'Recognition, classification and mechanical description of debris flows', *Earth-Science Reviews* **40**, 209–227.

Coussot, P. and Piau, J. M. (1995), 'Large-scale field coaxial cylinder rheometer for the study of the rheology of natural coarse suspensions', *Journal of Rheology* **39**(1), 105–124.

Da Cruz, F. (2004), Ecoulements de grains secs: frottement et blocage, PhD thesis, ENPC.

Delannay, R., Louge, M., Richard, P., Taberlet, N. and Valance, A. (2007), 'Towards a theoretical picture of dense granular flows down inclines.', *Nat Mater* **6**(2), 99–108.

Denlinger, R. P. and Iverson, R. M. (2004), 'Granular avalanches across irregular three-dimensional terrain: 1. theory and computation', *J. Geophys. Res.* **109**, –.

do Carmo, M. P. (1976), *Differential Geometry of Curves and Surfaces*, Prentice-Hall. 503 pages.

Egashira, S., Honda, N. and Itoh, T. (2001), 'Experimental study on the entrainment of bed material into debris flow', *Physics and Chemistry of the Earth, Part C: Solar, Terrestrial, Planetary Science* **26**, 645–650.

Engquist, B. and Osher, S. (1981), 'One-sided difference approximations for nonlinear conservation laws', *Mathematics of Computation* **36**(154), 321–351.

Ferreira, R. M. L., Leal, J. G. A. B. and Cardoso, A. H. (2003), Sediment transport by dam-break flows. a conceptual framework drawn from the theories for rapid granular flows, *in* 'Proceedings of the 3rd IMPACT Project Workshop CD-ROM', Louvain-la-Neuve, Belgium.

Fraccarollo, L. and Capart, H. (2002), 'Riemann wave description of erosional dam-break flows', *Journal of Fluid Mechanics* **461**, 183–228.

Fraccarollo, L., Capart, H. and Zech, Y. (2003), 'A godunov method for the computation of erosional shallow water transients', *Journal for Numerical Methods in Fluids* **41**, 951–976.

Fread, D. L. (1988), *The NWS DAMBRK model: Theoretical background and user documentation. HRL-258*, Hydrological Research Laboratory, National Weather Service,, Silver Spring, Md.

Godunov, S. K. (1959), 'A difference method for numerical calculation of discontinuous solutions of the equations of hydrodynamics. (russian)', *Mat. Sb. (N.S.)* **47**(89), 271–306.

Gray, J. M. N. T., Wieland, M. and Hutter, k. (1999), Gravity driven free surface flow of granular avalanches over complex basal topography, *in* 'Proc. R. Soc. Lond. A', Vol. 455, Math. Phys. Eng. Sci., p. 18411874.

Greve, R., Koch, T. and Hutter, k. (1994), Unconfined flow of granular avalanches along a partly curved surface. part i: Theory, *in* 'Proc. R. Soc. Lond. A', Vol. 445, Math. Phys. Eng. Sci., p. 399413.

Hameiri, E. and Shimshoni, I. (2003), 'Estimating the principal curvatures and the darboux frame from real 3-d range data.', *IEEE Trans Syst Man Cybern B Cybern* **33**(4), 626–637.

Harten, A. (1983), 'High resolution schemes for hyperbolic conservation laws', *J. Comput. Phys.* **49**(2), 357393.

Harten, A., Lax, P. D. and van Leer, B. (1983), 'On upstream differencing and godunov-type schemes for hyperbolic conservation laws', *SIAM Review* **25**(1), 35–61.

Henderson, F. M. (1966), *Open Channel Flow*, MacMillan Company, New York, USA.

Herschel, W. and Bulkley, R. (1926), Measurement of consistency as applied to rubber-benzene solutions, *in* 'Proceeding of American Society of Testing Material, Part II', number 26, p. 621633.

Hinch, E. J. (1991), *Perturbation methods*, Cambridge texts in applied mathematics, Cambridge University Press, Cambridge, New York.

Hübl, J. and Steinwendtner, H. (2001), 'Two-dimensional simulation of two viscous debris flows in austria', *Physics and Chemistry of the Earth, Part C: Solar, Terrestrial & Planetary Science* **26**(9), 639 – 644.

Hungr, O. (1995), 'A model for the runout analysis of rapid flow slides, debris flows and avalanches', *Canadian Geotechnical Journal* **32**(4), 610–623.

Hungr, O. and Evans, S. (2004*a*), 'Entrainment of debris in rock avalanches; an analysis of a long run-out mechanism', *Geol Soc Am* **116**, 12401252.

Hungr, O. and Evans, S. (2004*b*), 'Entrainment of debris in rock avalanches: An analysis of a long run-out mechanism', *Geological Society of America Bulletin* **116**(9-10), 1240–1252.

Hürlimann, M., Corominas, J., Moya, J. and Copons, R. (2003), Debris-flow events in the eastern pyrenees. preliminary study on initiation and propagation, *in* D. Rickenmann and C. Chen, eds, '3rd Int. Conf. on Debris-Flow Hazards Mitigation', Millpress, pp. 115–126.

Hutter, K., Wang, Y. and Pudasaini, S. P. (2005), 'The savage-hutter avalanche model: how far can it be pushed?', *Philos Transact A Math Phys Eng Sci* **363**(1832), 1507–1528.

Imran, J., Parker, G., Locat, J. and Lee, H. (2001), '1d numerical model of muddy subaqueous and subaerial debris flows', *Journal of Hydraulic Engineering* **127**(11), 959–968.

Iverson, R. (1997), 'The physics of debris flows', *Rev. Geophys.* **35**, 245–296.

Iverson, R. and Denlinger, R. (2001), 'Flow of variably fluidized granular masses across three-dimensional terrain 1. coulomb mixture theory', *J. Geoph. Res.* **106**, 537–552.

Iverson, R. M., Logan, M. and Denlinger, R. P. (2004), 'Granular avalanches across irregular three-dimensional terrain: 2. experimental tests', *J. Geophys. Res.* **109**, –.

Jin, M. and Fread, D. (1997), One-dimensional routing of mud/debris flows using nws fldwav model, *in* '1st Int. Conf. on Debris-Flow Hazards Mitigation', pp. 687–696.

Johnson, A. and Rodine, J. (1984), *Debris flow*, Slope Stability, John Wiley and Sons, New York.

Keller, J. B. (2003), 'Shallow-water theory for arbitrary slopes of the bottom', *Journal of Fluid Mechanics* **489**(-1), 345–348.

Lax, P. D. (1972), Hyperbolic systems of conservation laws and the mathematical theory of shock waves, *in* 'SIAM Regional Conference Series in Applied Mathematics', Vol. 11.

Lax, P. D. and Richtmyer, R. D. (1956), 'Survey of the stability of linear finite difference equations', *Communications on Pure and Applied Mathematics* **9**(2), 267–293.

LeVeque, R. J. (2002), *Finite volume methods for hyperbolic problems*, Cambridge texts in applied mathematics, Cambridge University Press, Cambridge, New York.

Locat, J. (1997), Normalized rheological behaviour of fine muds and their flow properties in a pseudoplastic regime, *in* 'Proc., 1st Int. Conf., ASCE', Reston, Va., p. 260269.

Mangeney, A., Bouchut, F., Thomas, N., Vilotte, J. P. and Bristeau, M. O. (2007), 'Numerical modeling of self-channeling granular flows and of their levee-channel deposits', *Journal of Geophysical Research (Earth Surface)* **112**(11), 2017–+.

Mangeney, A., Heinrich, P. and Roche, R. (2000), 'Analytical Solution for Testing Debris Avalanche Numerical Models', *Pure and Applied Geophysics* **157**, 1081–1096.

May, C. L. (1998), Debris flow characteristics associated with forest practices in the central Oregon Coast Range, M. s. thesis, Oreg. State Univ., Corvallis.

McDougall, S. and Hungr, O. (2004), 'A model for the analysis of rapid landslide motion across three-dimensional terrain', *Canadian Geotechnical Journal* **41**, 1084–1097.

MiDi, G. D. R. (2004), 'On dense granular flows.', *Eur Phys J E Soft Matter* **14**(4), 341–365.

Misner, C., Thorne, K. and Wheeler, J. (1973), *Gravitation*, Freeman, San Francisco.

Mitasova, H. and Mitas, L. (1993), 'Interpolation by regularized spline with tension: I. theory and implementation'.

Nakagawa, H., Takahashi, T., Sawada, T. and Ishibashie, A. (1999), 'Estimation of a debris flow hydrograph and analysis of evacuation action using gis', *J Hydrosci. Hydraul. Eng.* **17**(1), 73–85.

OBrien, J., Julien, P. and Fullerton, W. (1993), 'Two dimensional water flood and mudflow simulation', *Journal of Hydraulic Engineering ASCE* **119**(2), 244–261.

Papa, M., Egashira, S. and Itoh, T. (2004), 'Critical conditions of bed sediment entrainment due to debris flow', *Nat Hazards Earth Syst Sci* **4**(3)), 469474.

Pastor, M., Quecedo, M., Gonzalez, E., Herreros, M. I., Merodo, J. A. F. and Mira, P. (2004), 'Simple approximation to bottom friction for bingham fluid depth integrated models', *Journal Of Hydraulic Engineering* **130**(2), 149–155.

Pitman, E. B. and Le, L. (2005), 'A two-fluid model for avalanche and debris flows.', *Philos Transact A Math Phys Eng Sci* **363**(1832), 1573–1601.

Pitman, E., Nichita, C., Patra, A., Bauer, A., Sheridan, M. and Bursik, M. (2003), 'Computing granular avalanches and landslides', *Physics of Fluids* **15**(12).

Pons, J., Font, J., Ibáez, J., Martí, J. and Miralles, J. (1998), 'General relativistic hydrodynamics with special relativistic riemann solvers', *Astron. Astrophys.* **339**, 638642.

Pope, B., S. (2000), *Turbulent Flows*, Cambridge University Press, 770 pp.

Pudasaini, S. and Hutter, K. (2003), 'Rapid shear flows of dry granular masses down curved and twisted channels', *Journal of Fluid Mechanics* **495**, 193–208.

Pudasaini, S. and Hutter, K. (2007), *Avalanche dynamics: dynamics of rapid flows of dense granular avalanches*, Springer Verlag.

Pudasaini, S. and Kr
"oner, C. (2008), 'Shock waves in rapid flows of dense granular materials: Theoretical predictions and experimental results', *Physical Review E* **78**(4), 41308.

Pudasaini, S., Wang, Y. and Hutter, K. (2005), 'Rapid motions of free-surface avalanches down curved and twisted channels and their numerical simulation', *Philosophical Transactions of the Royal Society A: Mathematical, Physical and Engineering Sciences* **363**(1832), 1551.

Quecedo, M. and Pastor, M. (2003), 'Finite element modelling of free surface flows on inclined and curved beds', *Journal of Computational Physics* **189**, 45–62.

Rickenmann, D. and Koch, T. (1997), Comparison of debris flow modeling approaches, *in* C. Chen, ed., '1st Int. Conf. on Debris-Flow Hazards Mitigation', San Francisco, pp. 576–585.

Rickenmann, D., Laigle, D., McArdel, B. and Hbl, J. (2006), 'Comparison of 2d debris-flow simulation models with field events', *Computational Geosciences* **10**, 241–264.

Rickenmann, D., Laigle, D., McArdell, B. W. and Hbl, J. (2006), 'Comparison of 2d debris-flow simulation models with field events', *Computational Geosciences* **10**(2), 241–264.

Rickenmann, D., Weber, D. and Stepanov, B. (2003), Erosion by debris flows in field and laboratory experiments, *in* D. Rickenmann and C. Chen, eds, '3rd Int. Conf. on Debris-Flow Hazards Mitiga-tion', Millpress, Davos, pp. 883–894.

Ritter, A. (1892), 'Vereine die fortpflanzung der wasserwellen', *Deutscher Ingenieure Zeitswchrift* **36**(33), 947–954.

Roe, P. L. (1981), 'Approximate riemann solvers, parameter vectors, and difference schemes', *Journal of Computational Physics* **43**(2), 357–372.

Rossmanith, J. A. (2006), 'A wave propagation method for hyperbolic systems on the sphere', *Journal of Computational Physics* **213**, 629–658.

Rossmanith, J. A., Bale, D. S. and Leveque, R. J. (2004), 'A wave propagation algorithm for hyperbolic systems on curved manifolds', *Journal of Computational Physics* **199**, 631–662.

Sarra, S. (2003), 'The method of characteristics with applications to conservation laws.', *Journal of Online Mathematics and Applications (JOMA)* **3**.

Savage, S. B. and Hutter, K. (1989), 'The motion of a finite mass of granular material down a rough incline', *Journal of Fluid Mechanics* **199**(-1), 177–215.

Savage, S. B. and Hutter, K. (1991), 'The dynamics of avalanches of granular materials from initiation to run-out', *Acta. Mech.* **86**(-1), 201223.

Savage, S. B. and Iverson, R. M. (2003), Surge dynamics coupled to pore pressure evolution in debris flow, *in* D. Rickenmann and C. Chen, eds, '3rd Int. Conf. on Debris-Flow Hazards Mitigation', Millpress, Davos, p. 503514.

Scheidl, C. and Rickenmann, D. (2009), Comparison of different simulation models to estimate the runout of alpine debris flows., *in* 'EGU General Assembly 2009. Geophysical Research Abstracts', Vol. Vol. 11.

Shannon, C. E. (1949), Communication in the presence of noise, *in* 'Proc. Institute of Radio Engineers', Vol. 37, p. 1021.

Sivakumaran, N. and Dressler, R. (1989), 'Unsteady density-current equations for highly curved terrain', *Journal of the Atmospheric Sciences* **46**(20), 3192–3201.

Sivakumaran, N. S., Hosking, R. J. and Tingsanchali, T. (1981), 'Steady shallow flow over a spillway', *Journal of Fluid Mechanics Digital Archive* **111**(-1), 411–420.

Spinewine, B. and Zech, Y. (2002), Dam-break waves over movable beds: a flat bed test case, *in* 'Proceedings 2nd Project Workshop, Mo-i-Rana, Norway, 12-13 September 2002', EC Contract EVG1-CT-2001-00037 IMPACT Investigation of Extreme Flood Processes and Uncertainty.

Stoker, J. J. (1957), *Water waves: The mathematical theory with applications*, Vol. IV of *Pure and Applied Mathematics*, Interscience Publishers, Inc., New York.

Takahashi, T. (1991), *Debris flow.*, Balkema, Rotterdam.

Takaoka, H., Hashimoto, H., Ikematsu, S. and Hikida, M. (2006), Prediction of landslide-induced debris flow hydrograph: the atsumari debris flow disaster in japan, *in* G. Lorenzini, C. Brebbia and D. Emmanouloudis, eds, 'Monitoring, Simulation, Prevention and Remediation of Dense and Debris Flows', WIT Press.

Toro, E. (2001), *Shock-Capturing Methods for Free-Surface Shallow Flows*, Wiley and Sons Ltd.

Toro, E. F. (1999), *Riemann solvers and numerical methods for fluid dynamics - A practical introduction - 2nd edition*, Springer, Berlin.

Toro, E. F., Spruce, M. and Speares, W. (1994), 'Restoration of the contact surface in the hll-riemann solver', *Journal of Shock Waves* **4**(1), 25–34.

Travis, M., Elsner, G., Iverson, W. and Johnson, C. (1975), Viewit computation of seen areas, slope and aspect for landuse planning, Gen. Techn. PSW 11/1975, US Department of Agriculture Forest Service, Pacific Southwest Forest and Range Experimental Station, Berkley, California, USA.

Voellmy, A. (1955), 'ber die zerstrungskraft von lawinen', *Schweizerische Bauzeitung* **73**, 212–285.

Vreugdenhil, C. B. (1990), 'Numerical methods for shallow water flow', *VKI, Computational Fluid Dynamics, Volume 1 48 p (SEE N90-27989 22-34)* **1**.

Wang, Y., Hutter, K. and Pudasaini, S. (2004), 'The savage-hutter theory: A system of partial differential equations for avalanche flows of snow, debris, and mud', *ZAMM* **84**, 507–527.

Whitman, G. B. (1974), *Linear and nonlinear waves*, Wiley, New York.

Whittaker, J. (1935), *Interpolatory function theory.*, (Cambridge Tracts in Math. a. Math. Phys. 33) London: Cambridge Univ. Press. 107 p. .

Zienkiewicz, O. C. and Taylor, R. L. (2000), *The finite element method*, 5th ed edn, Butterworth-Heinemann, Oxford.